Dissertation

submitted to the

Combined Faculty of Natural Sciences and Mathematics

of the Ruperto-Carola University of Heidelberg, Germany

for the degree of

Doctor of Natural Sciences

Put forward by

Artur Hahn

born in Drushba, Kazakhstan

Oral examination: July 6th, 2021

Artificial magnetic resonance contrasts based on microvascular geometry:

A numerical basis

Artificial magnetic resonance contrasts based on microvascular geometry: A numerical basis

Magnetic resonance imaging (MRI) is highly versatile, offering many contrast settings inherently sensitivity to tissue microstructure at the sub-voxel scale (below the imaging resolution). Since its invention, images produced with MRI have mainly been based on classical reconstructions, with contrast determined by the signal attenuation from local tissue and MRI sequence design. In the advent of machine learning becoming practical, wide availability of computational power and high-resolution imaging such as laser scanning microscopy, new processing techniques involving MRI interpretations based on comparisons with known signals and ground-truth microstructure can be explored. Data-driven signal classifications enable model-less predictions of tissue properties on a single voxel level, offering artificial MRI contrasts. In this thesis, groundwork is laid for the exploration of such contrasts and suitable MRI sequences, with a demonstration of the feasibility of such an approach based on transverse relaxation for brain tumor detection. The thesis is focused on the role of microvascular geometry on reversible transverse relaxation in the context of tumor imaging. Comprehensive quantifications of cancer-induced vessel remodeling are provided, and the effects thereof studied with MRI simulations. Consequently, a numerical framework was developed for correlations of MRI signal properties with underlying microstructure for further exploration of artificial contrasts.

Künstliche Kontraste für die Magnetresonanztomographie basierend auf mikrovaskulärer Geometrie: Numerische Grundlagen

Magnetresonanztomographie (MRT) bietet viele Gewebekontraste mit inhärenter Sensitivität gegenüber Mikrostruktur und Dynamik unterhalb der Bildgebungsauflösung. Bisher beruhte der Kontrast in MRT Aufnahmen weitestgehend auf klassischen Signalgewichtungen basierend auf dem Einfluss von lokalem Gewebe auf die messbare Signalintensität unter den Einstellungen einer MRT Sequenz. Mit der zunehmenden Verfügbarkeit von Rechenleistung, praktikabler künstlicher Intelligenz und der Möglichkeit zur hochauflösenden, großskaligen Bildgebung echter Gewebemikrostruktur, beispielsweise mithilfe der Laser-Scanning-Mikroskopie, eröffnen sich neue Möglichkeiten der MRT Signalinterpretation durch Fokus auf erlernbare Signalsignaturen einzelner Bildpunkte (Voxel) unter verschiedenen MRT-Sequenzen. Maschinelles Lernen ermöglicht eine Modell-lose Interpretation komplexer Signalsignaturen zur Schätzung gewisser Gewebeeigenschaften auf Voxel-Ebene für eine Art künstlichen MRT Kontrast durch einen Vergleich mit bekannten Signalformen. In dieser Dissertation wurden numerische Werkzeuge entwickelt, um hochaufgelöste 3D Daten echter Mikrovaskulatur umfassend mit geometrischen und topologischen Maßen zu quantifizieren und deren Einfluss auf MRT Messungen zu simulieren. Dies wurde in eine skalierbare numerische Prozessierung verpackt, um MRT Signaleigenschaften mit Charakteristiken der zugrundeliegenden Gefäßarchitektur in großskaligen, datenbasierten Untersuchungen zu korrelieren. Die Gefäßgeometrie und -topologie in gesundem Hirngewebe und hochgradig malignen Hirntumoren wurde umfassend untersucht und es konnte gezeigt werden, dass der kollektive Einfluss von tumorgeschuldeten Gefäßremodellierungen auf die transversale Relaxation in MRT eine Klassifizierung von Tumorsignalen auf Voxel-Ebene theoretisch ermöglicht.

For Alexander Hahn

Contents

1 Introduction

Since its invention in the 1970s, magnetic resonance imaging (MRI) has become a powerful and multifaceted tool in medical practice, enabling the diagnosis and monitoring of diverse pathologies previously undetectable with non-invasive methods. In contrast to X-ray imaging, it is not based on the transmission and absorption of ionizing radiation through tissue and therefore minimizes harmful effects on patients. Compared with nuclear medical imaging methods such as positron emission tomography (PET) and single-photon emission computed tomography (SPECT), the signal generated and measured in MRI does not only contain spatial information about its origin within the body. Based on the principles of nuclear magnetic resonance (NMR), the MRI signal can encode useful information about the microscopic environment of the tissue it originated from. Different MRI pulse sequence designs, pertaining to the radiofrequency (RF) radiation used to excite and manipulate the spin system generating the NMR signal, can be used to emphasize specific aspects of the tissue microenvironment.

The multitude of factors influencing the measurable NMR signal combines internal, tissue-inherent properties and external, hardware-specific conditions. Pertinent microscopic tissue characteristics include thermodynamic degrees of freedom, *e.g.*, vibrational and rotational states, which affect the relaxivity of the excited spin system, macroscopically described by the relaxation times T_1 and T_2 (details in section 1.2.3). Besides the sheer local spin density, usually referring to the proton density PD, the molecular environment has different effects. Atoms proximal to the spin-bearing nuclei, especially in nearby chemical bonds, can cause a so-called chemical shift of the Larmor frequency by characteristically altering the electronic orbital shielding of the nuclei from the external magnetic field [1, 2]. Also, magnetization transfer can occur between different spins, changing the excited spin pool composition, relaxation characteristics and on-resonance [3–5]. On mesoscopic length scales, the NMR signal is altered by magnetic susceptibility variations within the tissue, which cause field deformations and Larmor frequency inhomogeneities in their surroundings. Diffusion of spin-bearing nuclei due to Brownian motion counters this effect by effectively averaging local Larmor frequencies. Dynamic macroscopic conditions such as perfusion and physiological motion also affect MRI in characteristic ways, often causing artifacts if not dealt with correctly.

In conjunction with the tissue properties just described, external factors from the MRI scanner determine the measurable NMR signal. Influential scan parameters include the external field strength B_0, applied field gradients G, and the RF-pulse sequence design; *i.e.*, oscillating field amplitudes B_1 and pulse durations with corresponding flip angles α, as well as the timings between RF-pulses, namely the echo time T_E, repetition time T_R, and inversion time T_I for inversion recovery sequences [1]. Throughout the

1

years, unceasing technological improvements and new theories have sharpened our intuition of "action" and "reaction" in the context of MRI. Actions with certain RF and gradient pulses cause characteristic NMR signal reactions, which are determined by the local constellation of aforementioned microscopic conditions and tissue characteristics. Throughout the years, our technical comprehension, hardware engineering, and ability to describe different factors mathematically have continuously improved, ultimately enabling the brilliant imaging and diverse contrasts available today.

1.1 Motivation

Theoretical treatments since the 1990s have brought forth analytical descriptions of the NMR signal evolution in certain idealized tissue microenvironments, predicting the detailed course of transverse relaxation, *i.e.*, the signal decay with relaxation times T_2 and T_2^* (see section 1.2.3 for elaboration), in the presence of distinct magnetic susceptibility inclusions. Approximate and exact mathematical solutions for the transverse relaxation evolution have been found for tissue-embedded spheres (modeling, *e.g.*, pulmonary alveoli in lung tissue [6] or paramagnetic marker particles [7, 8]), filled cylinders (modeling, *e.g.*, straight blood vessels [9–13]), spheroids (modeling, *e.g.*, red blood cells or marrow within trabecular bones [14]), and nested cylindrical shells (modeling myelinated axons [15]). Such analytical treatments, detailed in section 1.2.4, have shown that the transverse relaxation from a macroscopic MRI voxel (three-dimensional (3D) pixel) is influenced by the geometric properties of microscopic susceptibility inclusions within that voxel, far below the MRI resolution, in a well-defined manner.

Exact mathematical solutions of these problems yield highly complex signal forms, as demonstrated for the long cylindrical vessel model in section 1.2.4. In practice, fitting such complex functions to real MRI data to determine the vessel radius and tissue volume fraction is infeasible, especially with signal noise. Furthermore, idealized geometries allow for an analytical solution, but oversimplify most organic tissue structures such as capillary networks in the brain. This motivated a new, data-driven approach to the problem of microstructure estimation through MRI, which I begin to pursue in this thesis. I conjecture that characteristic microstructures in certain organs and tissue types should produce recognizable NMR signatures, which can be learned using methods of artificial intelligence for inference about microstructural anomalies within macroscopic MRI voxels. It should be possible to learn healthy signal forms corresponding to certain tissue types and specific pulse sequences by training classifiers for a machine aided detection of deviations thereof. This way, each MRI voxel could be interpreted individually by a trained classifier based on a combination of acquired signal intensities from tailored pulse sequences - an impossible task for humans but well-fit for machine

learning. Since neighboring voxel signals in MRI are virtually independent, local clusters of anomalously classified voxels may point out meaningful problems, even if they are too small to be recognizable on an anatomical level by radiologists.

At this point, a random search for appropriate sequence designs or the direct use of randomized sequences, mixing a range of NMR contrasts (as can be used for magnetic resonance fingerprinting (MRF) [16]), should be avoided for multiple reasons. For one, it would waste precious scan time on real MRIs. An ethical justification for such overkill measurements would be hard to advocate before a basic proof-of-principle and a prior search for sequence types useful for the detection of certain, characteristic tissue anomalies. Moreover, different contrasts and sequence types are not standardized across vendors, MRI scanners and RF coils. In consequence, the absolute signal intensities of different contrasts depend on hardware and sequence design, complicating an inclusion of different fundamental contrasts for the definition of a healthy tissue signature generalizable across hardware. Therefore, within this thesis, I focus on a single contrast type, namely the reversible transverse relaxation, typically associated with the relaxation time $T_2' = 1/R_2'$, where $R_2' = R_2^* - R_2$ (see section 1.2.3). This choice for a starting point is motivated by the referenced theoretical studies [9–13].

A numerical approach is taken here to provide a proof-of-principle for a voxel-by-voxel signal classification using the T_2' evolution in the context of brain tumor diagnosis. The MRI physics were implemented numerically to enable the production of a large range of virtual measurements without wasting valuable scan time on real MRIs, while having exact knowledge about the ground truth microstructure underlying each virtual MRI voxel [17, 18]. The feasibility test is based on the influence of microvascular deformations associated with tumor growth, grounded on the effects of naturally present deoxyhemoglobin within blood [19]; the phenomenon behind the blood oxygenation level dependent (BOLD) effect [20, 21].

The vascular compartment was isolated for this proof-of-concept because of its omnipresence in living tissue, the strong remodeling effects of tumor growth on the capillary network [22–25], and its observed consequences for BOLD-type measurements [26, 27] (see section 1.2.5). Further, the blood susceptibility represents an externally alterable factor, which can be manipulated by inhalation of special oxygen and carbon dioxide mixtures, inducing hyperoxia or hypercapnia [28, 29], or by intravascular contrast agent injection, *e.g.*, with gadolinium chelates or superparamagnetic iron-oxide nanoparticles (SPIONS) [30]. This offers an additional degree of freedom to alter during MRI to probe perfusion characteristics through transverse relaxation, should endogenous conditions not suffice. Such means are taken in dynamic susceptibility contrast (DSC) imaging [31, 32] and specialized techniques, like vessel size imaging (VSI) [33, 34] and vessel architectural imaging (VAI) [35–37].

The BOLD effect is most prominently known from its use in functional MRI (fMRI), where active brain regions show increased metabolic demands and associated dips of the capillary blood oxygenation, temporarily changing local T_2 and especially T_2^* values [38]. Throughout a cycle of typically around ten seconds, the local blood oxygen saturation initially drops, following neuronal activation, and is quickly compensated by a vascular response through so-called neurovascular coupling, resupplying the region with freshly oxygenated blood [39, 40]. Repeating $T_2^{(*)}$-weighted MRI acquisitions over the course of several seconds thus exposes regions with heightened neuronal and glial activity [17, 41]. Similarly to fMRI, which tracks transverse relaxation rate changes over several seconds, most DSC methods sample T_2 and T_2^* throughout the relatively long time course of a contrast agent bolus pass-through [34, 42]. Such relaxation rate comparisons from separate MRI acquisitions present several intricacies. Patient movement and physiological dynamics between acquisitions can complicate a voxel registration and ascription of signal variations to individual aspects. In a related manner, signal-impeding conditions such as B_0 inhomogeneities can change with varying anatomic conditions and further hinder a correct interpretation of inter-acquisition signal changes.

The approach investigated in this thesis focuses on the intra-voxel NMR behavior on much shorter time scales well below a second. As numerous theoretical, numerical, and experimental studies have shown, transverse relaxation is not monoexponential in heterogeneous tissues, exhibiting Gaussian and multiexponential decay forms [14, 43, 44]. Assuming most physiological conditions to be approximately constant over the time course of typical transverse magnetization decay in biomedical imaging (below $0.5\,\text{s}$), this signal range should be strongly influenced by static microstructural conditions like the local capillary geometry. In this time range, vessel constrictions and dilations, as well as oxygenation changes and pulsatile flow effects should be minimal [39, 45–47]. In contrast to BOLD fMRI and DSC measurements, which probe physiological dynamics, in this thesis, signatures of the intra-voxel MRI signal are analyzed for static physiological conditions. It is investigated whether the collective effects of tumor-induced vessel remodeling and angiogenesis theoretically alter the extravascular component [18] of the integrated MRI voxel signal with endogenous T_2' contrast clearly enough to be used for automated tumor voxel classification.

A well-known difficulty in the interpretation of BOLD signal dynamics stems from the fact that local blood oxygen fluctuations in the brain are normally accompanied by cerebral blood volume (CBV) variations due to vessel constrictions and dilations [17, 39]. Furthermore, analytical treatments of dephasing effects in the cylindrical vessel model, detailed in section 1.2.4, have shown that the blood oxygen saturation and vessel radius have strongly correlated effects on transverse relaxation, which are difficult to disentangle without additional constraining measurements of the blood oxygenation.

This predicament calls for more sophisticated vessel models, involving new parameters in addition to the vessel radius and CBV to describe the capillary geometry. A more realistic vessel network model may help solve degeneracies in the inverse problem of inferring on capillary structure from macroscopic NMR signal characteristics.

Especially in the context of detecting pathological remodeling of capillary beds, an understanding of the geometric and topological peculiarities of microvasculature associated with certain diseases is important. The sheer ability to classify differences in signal forms is not very useful if the origin of these differences remains unknown. In addition to the achievable classification accuracy, it is crucial to identify which aspects of the vasculature are distinct in which sense. Therefore, a large part of this thesis is dedicated to the extensive quantification of large vascular networks in healthy and pathological tissue. Full cerebrovascular networks of unprecedented extent, concerning the combination of sample size and resolution, were analyzed comprehensively to parametrize and quantify the differences between healthy and tumor-bearing brain tissue on a large scale and attain statistically significant results from entire tissue specimens in a mouse model. For this purpose, generalizable, automated, and highly scalable quantifications of vessel geometry and topology were custom-written for use with high-performance computation clusters or standard desktop computers, depending on availability, to analyze 3D acquisitions of ground-truth microvasculature, *e.g.*, from fluorescence light sheet microscopy [48, 49] or multiphoton microscopy [50].

With the numerical toolkits developed in the course of this thesis, real microvascular architectures acquired, *e.g.*, with laser scanning microscopy [51, 52] or micro-computed tomography (μCT) techniques [53], or created artificially [54, 55] can be used as a substrate for MRI simulations with simultaneous quantifications of the underlying geometric and topological parameters. The custom-developed programs can automatically process arbitrarily large and arbitrarily shaped tissue sections in a partitioned manner and resume progress where left off, should processing be interrupted at some point. This allows for asymptotic studies, where virtual MRI voxels are sampled from the specified tissue in a randomized way and preliminary results can be summarized in statistics at any point. This framework is suitable for the generation of training, validation, and test data for data-driven approaches of microvascular characterization from macroscopic MRI signals using machine learning. This builds the basis for continuing studies of the influence of microvascular architectures on MRI, *e.g.*, to attempt regressions of the quantified microvascular properties from T_2' evolutions. Using the developed toolkits, different approaches can be taken to identify plausible connections between characteristic signal changes and certain vessel remodeling aspects. This may even aid in the development of new vessel models incorporating relevant model parameters which are distinctive in tumor-affected tissue and other pathologies.

Data-driven approaches may open up new avenues of signal interpretation, where artificial contrasts can be defined, based on the signal form from a tailored sequence, which has been learned for different tissue microenvironments. To begin this journey, I conjecture that a promising approach should be the voxel-wise interpretation of MRI signals from a fixed sequence type with variable echo times T_E. With a fixed underlying contrast used for the signal acquisition, *e.g.*, T_2, T_2^*, or certain diffusion weighting, hardware-specific effects on the signal intensity, such as coil sensitivity and B_0 and B_1 inhomogeneities, can be circumvented, since they should be equal for a particular sequence type, independent of its echo time. A processing based on relative signal intensities at different echo times, normalized to the signal at a defined reference time, with better adapted fit models, should generalize well for a vendor-independent method. A basis for exploring suitable sequence and contrast types for different tissues, organs, and pathologies is provided in this thesis and demonstrated for brain tumor effects on the geometry and topology of the capillary bed.

1.2 Background

Although it maintains striking analogies to angular momentum, explaining the origin of its name, *spin* is a fundamental property of elementary particles. In theory, it follows as an inherent field characteristic from solutions of the Dirac equation, which combines quantum mechanical operator correspondence to the observables of energy and impulse (inspired by the Schrödinger equation) with the relativistic energy-impulse relationship as postulated by Albert Einstein's special relativity [56]. In the standard model of particle physics, elementary particles can be divided into two families: fermions with half-integer spin quantum numbers ($s \in \{\frac{1}{2}, \frac{3}{2}, \frac{5}{2}, ...\}$) and bosons with full-integer spin ($s \in \{0, 1, 2, 3, ...\}$). Fermions obey the Pauli exclusion principle, which forbids a degeneracy of quantum mechanical states in a system, while bosons allow for an unlimited number of particles in the same state. In consequence, our intuitive understanding of matter, which "takes up" space, refers to fermion compositions (usually from stable spin-$\frac{1}{2}$ fermions), while interactions are mediated by so-called gauge bosons (fundamental spin-1 fields which couple to the fermions; *i.e.*, photons, gluons, and W and Z bosons). Currently, gravity is the only known fundamental force which is still best-described separately by general relativity without the need for force-mediating bosons, while particle mass itself can be explained by coupling to the Higgs field; responsible for the only experimentally-observed elementary particle with zero spin (the Higgs boson).

Every atom is made up of a nucleus (containing protons and neutrons) and surrounding electrons for neutral charge. The compact nucleus holds most of the atomic mass and the electrons are responsible for chemical bonds between different atoms to form molecules.

As composite particles made up of quarks and gluons, protons and neutrons each carry spin-$\frac{1}{2}$. Different isotopes of elements have distinct nuclear spin quantum numbers, which depend on the combination of proton and neutron spins in a complex way and can range from $s=0$ to $s=8$ in naturally occurring isotopes. A general property of spin is its quantization along one spatial direction (without loss of generality, usually referred to as the z-axis). Quantum mechanical spin operators $\hat{S}_i$ obey the angular momentum commutator relations [56]:

$$[\hat{S}_i, \hat{S}_j] = i\hbar\varepsilon_{ijk}\hat{S}_k \qquad \text{and} \qquad [\hat{\vec{S}}^2, \hat{S}_i] = 0 \qquad \text{with } i, j, k \in \{1, 2, 3\}, \qquad (1.1)$$

corresponding to axes $\{x, y, z\}$, respectively, and using Einstein notation for sums. In the bra-ket notation, the eigenstates $|s, s_z\rangle$ of operators $\hat{\vec{S}}^2 = \hat{S}_x^2 + \hat{S}_y^2 + \hat{S}_z^2$ and $\hat{S}_z$ yield the following eigenvalues equations: $\hat{\vec{S}}^2|s, s_z\rangle = s(s+1)\hbar^2|s, s_z\rangle$ and $\hat{S}_z|s, s_z\rangle = \hbar s_z|s, s_z\rangle$. The spin orientation is quantized in one direction between $-s$ and s in unit steps; *i.e.*, $s_z \in \{-s, -s+1, ..., s-1, s\}$. A transition between these states is only possible through interaction with a vector boson (with spin $s=1$), such as a photon. In NMR, these fundamental principles are taken advantage of for interrogations of diverse microscopic conditions in spin-bearing samples and imaging with variable contrasts and resolution.

1.2.1 Basics of NMR

The particle spin $\vec{s} = (s_x, s_y, s_z)$ is associated with a magnetic moment $\vec{\mu} = \gamma\vec{s}$ through the gyromagnetic ratio γ [1]. In an external magnetic field $\vec{B}_0$, there is a dipole interaction energy $E = -\vec{\mu} \cdot \vec{B}_0$, which explains the Zeeman effect; *i.e.*, the splitting of quantized energy states and spectral lines in a magnetic field. The direction of the external field $\vec{B}_0$ breaks the rotational symmetry of a system, leading to the quantization of the spin component s_z along $\vec{B}_0$. In consequence, an ensemble of particles with spin quantum number s will undergo an energy splitting, with each particle's energy offset being determined by the spin's z-component s_z, leading to $(2s + 1)$ different potential energy levels. Transitions between neighboring energy levels occur under absorption or emission of a photon with the frequency ω_L and energy $E = \hbar\omega_L = 2|\vec{\mu} \cdot \vec{B}_0|$ with Planck's reduced constant $\hbar = h/2\pi$. The frequency ω_L is called Larmor frequency [1].

NMR is commonly conducted with protons because they are most abundant in organic tissue and have the convenient spin quantum number $s = 1/2$. Thus, there are two quantization states: $s_z = \pm 1/2$ with corresponding Zeeman energies $E = -(\pm\gamma\hbar B_0/2)$ at field strength $B_0 = |\vec{B}_0|$. The transition is achieved with photons at Larmor frequency $\omega_L = \gamma|\vec{B}_0|$ with $\gamma \approx 2.67522 \cdot 10^8\,\mathrm{rad} \cdot \mathrm{s}^{-1} \cdot \mathrm{T}^{-1}$ for protons [57]. High spin abundance produces superior NMR signals with better signal-to-noise ratio (SNR). This is further influenced by the field strength B_0 and sample temperature T. More specifically, the

sum of individual magnetic moments $\vec{\mu}_i$ of spins at location $\vec{r}$ compose the magnetization $\vec{m}(\vec{r}) = \frac{1}{V} \cdot \sum_i \vec{\mu}_i$ in volume V, which is parallel to $\vec{B}_0$ in equilibrium. Using Maxwell-Boltzmann statistics as an approximation for the high-temperature limit of Fermi-Dirac statistics, it can easily be derived that the equilibrium magnetization $\vec{m}_0$ is given by [1]:

$$\vec{m}_0(\vec{r}) = \rho(\vec{r})\hbar^2\gamma^2\frac{s(s+1)}{3k_BT}\vec{B}_0 \qquad (1.2)$$

with local spin density $\rho(\vec{r})$ and Boltzmann constant k_B. This finding corresponds to Curie's law [1]. With protons ($s = 1/2$) at body temperature ($T \approx 37°$C), a little less than 1 out of 10 million spins more are in the lower-energetic state (parallel to $\vec{B}_0$) than in the antiparallel, higher-energy state per Tesla field strength B_0. Because the energy scales of the Zeeman effect are so minor and $k_BT \gg \hbar\omega_L$, the thermal disturbance is strong in clinical NMR environments, which is why high spin densities ρ and field strengths B_0 are desirable for a clear signal. After all, the sample magnetization $\vec{m}$ is responsible for inducing a measurable current in the reception coils around the sample (*e.g.*, a human patient) through the electromagnetic waves it produces and the amplitude of these waves is proportional to the magnetization magnitude $\vec{m}_0$.

In magnetic resonance (MR), the magnetization $\vec{m}$ is manipulated with on-resonant RF radiation at the Larmor frequency to create mixed states of up and down spins. The system dynamics can be derived entirely within quantum mechanics or semi-classically, without any quantization principles - a fascinating property of NMR, lying at the interface of quantum and statistical physics [58]. Using the Heisenberg picture, where the time evolution of an observable operator is given by its commutator with the system's hamiltonian $\hat{H}$, and the Hamilton operator for the Zeeman effect given by $\hat{H} = -\vec{B} \cdot \hat{\vec{\mu}} = -\gamma\vec{B} \cdot \hat{\vec{S}}$, one finds for the magnetic moment operator $\hat{\mu}_k = \gamma\hat{S}_k$:

$$\begin{aligned}
\frac{\mathrm{d}}{\mathrm{d}t}\hat{\mu}_k &= \frac{\mathrm{i}}{\hbar}\left[\hat{H}, \hat{\mu}_k\right] = \frac{-\mathrm{i}}{\hbar}\left[\gamma\vec{B}\cdot\hat{\vec{S}}, \gamma\hat{S}_k\right] & |\sum_{j=1}^{3} B_j\hat{S}_j \mathrel{\hat{=}} B_j\hat{S}_j \ \ (\text{Einstein notation}) \\
&= \frac{\gamma^2}{\mathrm{i}\hbar}B_j\left[\hat{S}_j, \hat{S}_k\right] & |\text{ with Eq. (1.1)} \\
&= \gamma^2\varepsilon_{ijk}B_j\hat{S}_i \\
&= \gamma(\hat{\vec{\mu}}\times\vec{B})_k\,. & (1.3)
\end{aligned}$$

According to the Ehrenfest theorem, the above equations are equally valid for the expectation values of the magnetic moment components $\langle\mu_k\rangle = \langle\psi|\hat{\mu}_k|\psi\rangle$ [56].

For many-particle systems, the quantum mechanical density matrix formalism can be used to derive the expectation values for all components of the magnetic moment operator $\hat{\vec{\mu}}$ for a two-state system [59]. It interestingly yields the dynamics of the magnetic moment expectation value, also in the presence of an oscillating magnetic

field $\vec{B}(t) = \vec{B}_0 + \vec{B}_1(t)$ with static field $\vec{B}_0 = (0, 0, B_0)$ and dynamic component $\vec{B}_1(t) = (B_1 \cos(\omega_L t), B_1 \sin(\omega_L t), 0)$ with circular polarization [1, 59]:

$$\langle \mu_x \rangle = \frac{\gamma^2 \hbar^2 B_0}{4 k_B T} \sin(\omega_1 t) \sin(\omega_L t) \,,$$

$$\langle \mu_y \rangle = \frac{\gamma^2 \hbar^2 B_0}{4 k_B T} \sin(\omega_1 t) \cos(\omega_L t) \,,$$

$$\langle \mu_z \rangle = \frac{\gamma^2 \hbar^2 B_0}{4 k_B T} \cos(\omega_1 t) \,,$$

where $\omega_L = \gamma B_0$ and $\omega_1 = \gamma B_1$. It follows from first principles that excitation photons need to be circularly polarized and close to the Larmor frequency for absorption. Further, the coherent excitation of an entire spin ensemble allows for a superposition of spin states in which the expectation values of all spin components are determined, resulting in a precession of the components transverse to the external magnetic field $\vec{B}_0$. The ratio and relation between up- and down-quantized spins can be tuned through the power and duration of the oscillating field $\vec{B}_1(t)$ to facilitate a quasi-continuous transition between longitudinal magnetization (parallel to $\vec{B}_0$) and transverse components.

It follows that the magnetization $\vec{m} = \frac{1}{V} \sum \vec{\mu}$ of a many-particle spin system in volume V can be tipped out of equilibrium with a circularly polarized, oscillating magnetic field $\vec{B}_1(t)$ at the Larmor frequency in a continuous way. The flip angle α of the magnetization $\vec{m}$ is given by $\alpha = \omega_1 \tau = \gamma B_1 \tau$, where τ is the duration of application of the oscillating field $\vec{B}_1$; *i.e.*, the RF pulse length [1]. Because only the transverse magnetization precesses and causes oscillating electromagnetic fields, a popular choice for initial excitation is the 90°-pulse with $\alpha = 90°$, which produces maximal transverse magnetization by tipping the entire longitudinal magnetization $\vec{m}_0$ perpendicular to $\vec{B}_0$. Another common RF-pulse is the 180°-pulse, which inverts the longitudinal magnetization to be antiparallel to $\vec{B}_0$ and mirrors the transverse magnetization components. This is done for inversion recovery sequences and spin echo production (see details in section 1.2.3).

As mentioned, the above results can also be derived without quantum mechanics [58]. The first classical description of NMR was published by Felix Bloch in 1946 [60], introducing the famous Bloch equations, which can be summarized in vector form:

$$\frac{\mathrm{d}}{\mathrm{d}t} \vec{m}(t) = \gamma \, \vec{m}(t) \times \vec{B} + \frac{1}{T_1} \left(m_0 - m_z(t) \right) \vec{e}_z - \frac{1}{T_2} \vec{m}_\perp(t) \tag{1.4}$$

with the equilibrium magnetization m_0 pointing along the z-axis with unit vector $\vec{e}_z$, longitudinal magnetization component m_z and transverse magnetization $\vec{m}_\perp$. The relaxation times T_1 and T_2 are variables of utmost importance in clinical imaging, which will be elaborated in section 1.2.3. In addition to the first term on the right-hand side,

which stands in analogy to Eq. (1.3), Bloch identified the two fundamental relaxation mechanisms with T_1 and T_2, often referred to as longitudinal (or spin-lattice) and transverse (or spin-spin) relaxation [1].

Conceptually, the relaxation mechanisms can be understood as follows. Longitudinal relaxation with T_1 is an energy-driven process which gradually rebuilds the equilibrium magnetization $\vec{m}_0$ by emitting photons (at the Larmor frequency) which transport off energy from an excited spin system and distribute it to the surroundings; *i.e.*, the "lattice". Transverse relaxation with T_2 relates to the exchange of energy between individual spins, which leads to a loss of the coherence within the many-particle system. In consequence, the summed volume magnetization $\vec{m} = \frac{1}{V} \sum \vec{\mu}$ decays due to interactions between the magnetic moments μ and the resulting loss of phase coherence. Typically, T_2 decay occurs much faster than T_1 relaxation, which is additionally incorporated in the T_2 mechanism. This is why NMR measurements including multiple excitations traditionally demand long repetition times T_R between excitations (on the order of seconds), until longitudinal magnetization is sufficiently restored, even if the transverse magnetization has long diminished and there is no more signal from the last excitation.

The NMR signal is measured by induction of a current in a receiving coil, typically surrounding the sample to be examined, through Lenz's law [61]. The magnetic field fluctuations at the coil, which is often also used for RF transmission, are induced from electromagnetic radiation from the entire excited sample simultaneously [1]. In principle, these are the de-excitation photons escaping the spin system as part of the T_1 relaxation mechanism. The signal $S(t)$ received from an excited sample with volume V is proportional to the integral transverse magnetization within that volume:

$$S(t) \propto \vec{M}_\perp(t) = \int_V \vec{m}_\perp(\vec{r}, t) \, \mathrm{d}^3 r \tag{1.5}$$

The signal $S(t)$ is complex with two components, which can be measured in quadrature, either with two perpendicular coils or artificially separated by signal-processing [1]. Since only the transverse magnetization $\vec{m}_\perp$ composes the signal, a description using complex numbers of the form $m_\perp = m_x + \mathrm{i} m_y$ is convenient for most applications.

In the most basic NMR experiment, following an ideal 90° excitation pulse at time $t = 0$ without any additional manipulations in the form of RF pulses or magnetic field gradient applications, the magnetization $M_\perp(t)$ will undergo a so-called free induction decay (FID). In this case, Eq. (1.5) can be concretized as follows [1]:

$$S_{FID}(t) \propto M_\perp(t) = \int_V m_0(\vec{r}) \cdot \mathrm{e}^{-t/T_2(\vec{r})} \cdot \mathrm{e}^{-\mathrm{i}\omega_L(\vec{r})t + \phi_0} \, \mathrm{d}^3 r \,, \tag{1.6}$$

with initial phase ϕ_0 in the complex plane and ignoring varying, location-dependent transmit and receive coil sensitivities.

1.2.2 From NMR to MRI

As outlined above, basic NMR measurements do not inherently contain spatial information but rather offer a signal mixed from an entire sample within the magnetic field B_0. The transition to imaging with NMR is clever and quite simple. The basic concept enabling imaging with NMR is the application of magnetic field gradients $\vec{G} = (G_x, G_y, G_z)$ for a linear dependence of the Larmor frequency on the location $\omega_L(\vec{r}) = \gamma B_0(\vec{r}) = \gamma[B_0 + \vec{G} \cdot \vec{r}] = \gamma[B_0 + G_x x + G_y y + G_z z]$. Depending on how many dimensions the imaging should encompass, there are different methods that can be combined for spatial encoding of the NMR signal.

For 2D imaging, which is common in clinical application, only a planar slice of the sample within the scanner is excited with on-resonant RF radiation. This is achieved by applying a field gradient normal to the plane of imaging, *e.g.*, gradient $\vec{G} = (0, 0, G_z)$ in the z-direction for a static field strength $B_0(z) = B_0 + G_z z$ during RF irradiation. The RF excitation pulse is designed with a certain band width of frequencies to contain the Larmor frequencies $\omega_L(z) = \gamma B_0(z)$ within a slice of desired thickness. For instance, for a box-profile slice, the RF pulse would have the form of a sync function in the time domain, attained by Fourier transformation of the box profile in the frequency domain.

Once transverse magnetization has been created in the imaging slice, Eq. (1.6) governs its evolution in absence of further RF irradiation. With a new magnetic field gradient in the imaging plane, *e.g.*, $\vec{G} = (G_x, 0, 0)$, Eq. (1.6) takes the following form:

$$
\begin{aligned}
S(t) \propto M_\perp(t) &= \int_V m_0(\vec{r}) \cdot \mathrm{e}^{-t/T_2(\vec{r})} \cdot \mathrm{e}^{-\mathrm{i}(\omega_L(\vec{r})t + \phi_0)} \, \mathrm{d}^3 r \\
&= \int_x \int_y \int_{\Delta z} m_0(x, y, z) \cdot \mathrm{e}^{-t/T_2(x,y,z)} \cdot \mathrm{e}^{-\mathrm{i}\gamma[B_0 + G_x x]t - \mathrm{i}\phi_0} \, \mathrm{d}z \, \mathrm{d}y \, \mathrm{d}x \quad (1.7) \\
&= \mathrm{e}^{-\mathrm{i}(\gamma B_0 t + \phi_0)} \cdot \int_x \left[\int_y \int_{\Delta z} m_0(x, y, z) \cdot \mathrm{e}^{-t/T_2(x,y,z)} \, \mathrm{d}z \, \mathrm{d}y \right] \mathrm{e}^{-\mathrm{i}\gamma G_x x t} \, \mathrm{d}x \\
&= \mathrm{e}^{-\mathrm{i}(\gamma B_0 t + \phi_0)} \cdot \int_x P_{y,\Delta z} \left[m_\perp(\vec{r}, t) \right] \cdot \mathrm{e}^{-\mathrm{i}\gamma G_x t x} \, \mathrm{d}x \\
&= \mathrm{e}^{-\mathrm{i}(\gamma B_0 t + \phi_0)} \cdot \int_x P_{y,\Delta z}[m_\perp](x, k_x) \cdot \mathrm{e}^{-\mathrm{i}k_x x} \, \mathrm{d}x \, .
\end{aligned}
$$

With the variable substitution $k_x(t) := \gamma G_x t$, the signal $S(k_x) \hat{=} S(t)$ is apparently the Fourier transformed of the transverse magnetization $m_\perp(\vec{r}, t) = m_0(\vec{r}) \, \mathrm{e}^{-t/T_2(\vec{r})}$, projected over the z-slice thickness Δz and the y-direction of the imaging field-of-view (FOV): $P_{y,\Delta z}[m_\perp](x, k_x) \hat{=} P_{y,\Delta z}[m_\perp(\vec{r}, t)] = \int_y \int_{\Delta z} m_0(x, y, z) \cdot \mathrm{e}^{-t/T_2(x,y,z)} \, \mathrm{d}z \, \mathrm{d}y$. The transverse magnetization $m_\perp(\vec{r}, t)$, or more specifically, the initial magnetization $m_0(\vec{r})$, is proportional to the local spin density $\rho(\vec{r})$, which can be inferred upon through inverse Fourier transformation of $S(k_x)$. This one-dimensional (1D) spatial encoding of the NMR signal origin, which lets k_x progress with the signal evolution time t, is called frequency encoding.

To achieve spatial encoding along an additional, linearly independent direction, such as the y-axis, it does not suffice to apply a frequency encoding gradient like $\vec{G} = (G_x, G_y, 0)$, since this would yield 1D frequency encoding on the diagonal between the x- and y-axes. Instead, an analogous $k_y := \gamma G_y \tau$ needs to be incremented with an independent time parameter τ. This can be done through so-called phase encoding. Before the application of a frequency encoding gradient $\vec{G}_f = (G_x, 0, 0)$, a phase encoding gradient $\vec{G}_p = (0, G_y, 0)$ is applied for a duration τ after spin excitation. This offsets the initial phase ϕ_0 of the transverse magnetization to a y-dependent value, which alters Eq. (1.7) as follows:

$$
\begin{aligned}
S(t, \tau) \propto M_\perp(t, \tau) &= \int_V m_0(\vec{r}) \cdot e^{-(t+\tau)/T_2(\vec{r})} \cdot e^{-i(\omega_L(\vec{r})t + \phi_0(y, \tau))} \, d^3r \\
&= \int_x \int_y \int_{\Delta z} m_\perp(\vec{r}, t, \tau) \cdot e^{-i(\gamma[B_0 + G_x x]t + \gamma[B_0 + G_y y]\tau)} \, dz \, dy \, dx \\
&= e^{-i\gamma B_0(t+\tau)} \int_x \int_y \left[\int_{\Delta z} m_\perp(\vec{r}, t, \tau) \, dz \right] e^{-i\gamma(G_x xt + G_y y\tau)} \, dy \, dx \\
&= e^{-i\gamma B_0(t+\tau)} \int_y \left[\int_x P_{\Delta z} \left[m_\perp(\vec{r}, t, \tau) \right] e^{-i\gamma G_x tx} \, dx \right] e^{-i\gamma G_y \tau y} \, dy \\
&= e^{-i\gamma B_0(t+\tau)} \int_y \left[\int_x P_{\Delta z}[m_\perp](x, k_x, y, k_y) \cdot e^{-ik_x x} \, dx \right] e^{-ik_y y} \, dy.
\end{aligned}
$$

For simplicity of the intinsic T_2 decay parametrization, the phase encoding gradient G_y was assumed to follow immediately after excitation, with direct subsequent switching to the frequency encoding gradient G_x. The 2D signal $S(t, \tau) \mathrel{\widehat{=}} S(k_x, k_y)$, attained through multiple acquisition repetitions with different gradient strengths G_y or durations τ for varying phase encoding, can yield a map of the local transverse magnetization projection within the slice $P_{\Delta z}[m_\perp(\vec{r}, t, \tau)]$, proportional to the spin density $\rho(\vec{r})$ by two independent Fourier back transformations along k_x and k_y. The raw measurements before inverse transformation are said to be acquired in k-space.

Phase encoding can be applied multiple times with independent gradients in different directions, using different time interval variables in analogy to τ. This enables true 3D imaging, which omits the slice selection gradient during excitation but typically incorporates two phase encoding directions with one frequency encoding axis. The number of frequency encoding repetitions needed for such 3D imaging quickly increases, scaling multiplicatively with the number of desired voxels in the y- and z-direction (with frequency encoding along the x-direction). This is why, in practice, 2D imaging with multiple slices is often used for a 3D coverage when a limited FOV along z suffices. In some mostly experimental applications, such as spectroscopic imaging, frequency encoding is omitted in place of phase encoding of all spatial directions [62]. This can be done to avoid drowning inherent Larmor frequency off-resonances with artificial field gradients in order to probe microscopic and metabolic conditions in more detail [63–65].

1.2.3 Fundamental MRI constrasts

The combination of RF pulses and magnetic field gradient applications used for an MRI measurement is called an MRI sequence. It determines the way the spin system in a static magnetic field B_0 is manipulated to produce signals as a type of answer to certain interrogations. The "answer" signal from the sample depends on microscopic tissue properties and the way the "question" is asked, *i.e.*, the sequence design. It is possible to emphasize different tissue characteristics with distinct aspects of sequence design, tuning the so-called MRI contrast to weigh particular properties. The first mathematical description of NMR already included the most fundamental contrast types, parametrized by T_1 and T_2; cf. the Bloch equation, Eq. (1.4). In the following, the most elemental contrasts are introduced in order to put the contrast studied in this thesis (namely the T_2' evolution), as well as the aim for creating artificial MRI contrasts, into context.

Longitudinal relaxation was briefly discussed towards the end of section 1.2.1, following the introduction of Eq. (1.4). It describes the process of the excited spin system returning to thermal equilibrium, where the net magnetization $\vec{m}_0 \parallel \vec{B}_0$ is recovered (see Eq. (1.2)). This process is driven by the principle of energy minimization and gradual de-excitation of nuclear spin states. This de-excitation is stimulated by fluctuating magnetic fields from the microscopic and atomic environment due of thermal motion, *i.e.*, rotational and vibrational states. Since this is effectively a coupling of the excited spins to the atomic "lattice", longitudinal relaxation with T_1 is often called spin-lattice relaxation [1]. The energy-driven process is described by a limited exponential regrowth, which solves the longitudinal component $m_z(t)$ of the Bloch equation (1.4):

$$m_z(t) = m_z(0)\, \mathrm{e}^{-t/T_1} + m_0 \left(1 - \mathrm{e}^{-t/T_1}\right) ,$$

where $m_z(0)$ is the initial value immediately after the application of an RF pulse at time $t = 0$ and m_0 is the magnitude of the equilibrium magnetization as in Eq. (1.2).

The longitudinal magnetization component m_z does not contribute to the induction of a measurable NMR signal because it is parallel to the external field $\vec{B}_0$ and does not precess. The T_1 contrast is classically tuned with the repetition time T_R of an MRI sequence involving multiple excitation pulses. If an excitation pulse is applied without sufficient temporal spacing T_R to the last excitation, regions with long T_1 will exhibit weaker transverse magnetization and a hypointense signal because there was not much longitudinal magnetization to be flipped, as opposed to regions with short T_1 that would already be closer to equilibrium $\vec{m}_0$ at the time of the next excitation. Thus, relatively short repetition times T_R in an MRI sequence emphasize T_1 contrast. Since T_1 contrast is not a subject of this thesis, it will not be elaborated further.

The second fundamental NMR contrast, which already appears in the Bloch equation (1.4), relates to transverse relaxation; *i.e.*, the decay of transverse magnetization $m_\perp$. Spin-spin relaxation with T_2 originates from a similar microscopic mechanism as T_1 relaxation, but with interactions and energy exchanges between excited and ground-state spins [1]. The coherence in the system is gradually lost, even though energy does not leave it. This T_2 decay also occurs within so-called isochromats or spin packets, *i.e.*, local ensembles of individual spins with equal Larmor frequency that form a "classical" magnetization vector $\vec{m} = \frac{1}{V}\sum\vec{\mu}$, which is not subject to Heisenberg's uncertainty principle (in contrast to the magnetic dipole moment $\vec{\mu}$ of an individual spin with only one determinable component μ_z). As such, intrinsic spin-spin relaxation with T_2 is not reversible and commences as soon as transverse magnetization has been created. According to Eq. (1.4), it resembles a mono-exponential decay, while $\vec{m}$ precesses around $\vec{B}_0$ at the frequency $\omega_L = \gamma B_0$, following an RF excitation at $t = 0$ which creates a transverse component $m_\perp > 0$:

$$m_\perp(t) = m_\perp(0)\,e^{-t/T_2} \qquad \text{(in the rotating frame with } \omega_L = \gamma B_0\text{).}$$

Both T_1 and T_2 depend on the thermal degrees of freedom of the molecular and atomic environment, as well as the field strength B_0 and the gyromagnetic ratio γ (when working with nuclei other than hydrogen). Spin de-excitation is most stimulated when the local electromagnetic field fluctuations from movements of magnetic and electric dipole moments due to thermal motion lie at frequencies close to the Larmor frequency. At a typical field strength of $B_0 = 1.5\,\text{T}$ and human body temperature (37°C), longitudinal relaxation times T_1 within the body lie somewhere between several hundreds and several thousands of milliseconds, while T_2 values mostly range more within several tens to several hundreds of milliseconds (see **Tab.** 1.1 for some representative values). The observed differences are due to the varying molecular structure and excited thermal degrees of freedom in each tissue on a microscopic scale.

Tissue	T_1 **(ms)**	T_2 **(ms)**
Gray matter	950	100
White matter	600	80
Muscle	900	50
Fat	250	60
Cerebrospinal fluid	4500	2200
Blood	1200	100 (venous) - 200 (arterial)

Table 1.1: Approximate relaxation time values in different healthy tissue types, typically observed at $B_0 = 1.5\,\text{T}$ and human body temperature of 37°C. The T_2 time of blood depends on its oxygen saturation and the given values are exemplary for typical voxels in a vein or an artery. Table reproduced from [1], p. 56.

In addition to intrinsic spin-spin relaxation with T_2, transverse magnetization from an entire sample or imaging voxel undergoes an additional decay due to so-called spin dephasing. In practice, magnetic field inhomogeneities on small length scales cause the distribution of Larmor frequencies within a volume otherwise assumed to be homogeneous, to broaden, resulting in deviations from a δ-peak at $\omega_0 = \gamma B_0$ with external field strength B_0. In the simplest case, this broadening has a Lorentzian profile shape, leading to an additional exponential signal attenuation, commonly parametrized with the relaxation rate $R_2' = 1/T_2'$. This concretizes Eq. (1.6), describing the integral FID signal from volume V after an ideal $90°$ excitation from equilibrium $\vec{m}_0$, as follows:

$$
\begin{aligned}
S_{FID}(t) \propto M_\perp(t) &= \int_V m_0(\vec{r}) \cdot \mathrm{e}^{-t/T_2(\vec{r})} \cdot \mathrm{e}^{-\mathrm{i}\omega_L(\vec{r})t + \phi_0} \, \mathrm{d}^3 r \\
&= M_0 \cdot \mathrm{e}^{-R_2 t} \cdot A_d(t) \cdot \mathrm{e}^{-\mathrm{i}\Omega(t)} \\
&= M_0 \cdot \mathrm{e}^{-R_2 t} \cdot \mathrm{e}^{-R_2' t} \cdot \mathrm{e}^{-\mathrm{i}\Omega(t)} = M_0 \cdot \mathrm{e}^{-R_2^* t} \cdot \mathrm{e}^{-\mathrm{i}\Omega(t)}.
\end{aligned}
\tag{1.8}
$$

More generally, the dephasing attenuation $A_d(t) = |\langle \mathrm{e}^{\mathrm{i}\phi(t)} \rangle|$, with individual spin packet phase $\phi(t) = \int_0^t \omega_L(\vec{r}(t')) \, \mathrm{d}t' + \phi_0$ during diffusion on the path $\vec{r}(t')$ and ensemble average $\langle \cdot \rangle$, can take arbitrary forms with a nonlinear phase evolution $\Omega(t)$ of the integral magnetization $M_\perp(t)$. This is demonstrated in section 1.2.4. In the mono-exponential approximation, $A_d(t) \approx \mathrm{e}^{-R_2' t}$, the relaxation rates R_2 and R_2' are typically summarized with $R_2^* = R_2 + R_2'$ and the associated relaxation time $T_2^* = 1/R_2^*$ [1].

In NMR imaging, the T_2 or T_2^* weighting of the signal is tuned with the echo time T_E. For a standard T_2^*-weighted image, the frequency encoding described in section 1.2.2 is used to produce a so-called gradient echo at time T_E after excitation. For this purpose, a gradient in the frequency encoding direction is applied prior to signal acquisition in order to offset the excited spin system to an initial value $-k_0$ in k-space. During acquisition, the frequency encoding gradient, also called read gradient, will lead the system towards k-space center with $k = 0$ and typically beyond it to $k = k_0$. At the moment of reaching $k = 0$, a gradient echo is formed, corresponding to a signal maximum, where artificial dephasing through gradient applications is reversed (modulo diffusion effects). The gradient echo amplitude at time $t = T_E$ is T_2^*-weighted with respect to the spin excitation at $t = 0$ [1]. Thus, T_E controls the impact of T_2^* on the local signal intensities.

Another type of echo that can be summoned in NMR is the famous spin echo, first described by Erwin Louis Hahn in 1950 [66]. A spin echo forms at echo time T_E if a $180°$ RF pulse is applied to a sample with transverse magnetization $m_\perp(t = 0) > 0$ at time $t = T_E/2$. With correct B_1 polarization in the transverse magnetization plane, this leads to a complex conjugation of the transverse magnetization in the complex description [1]. Conceptually, the $180°$ pulse mirrors the phase accumulated by each

spin packet up to time $t = T_E/2$, making it negative (when the coordinate axes and $\phi = 0$ are defined accordingly). Without diffusion, *i.e.*, the random movement of spins, all dephasing effects would be reversed at time $t = T_E$, given that the magnetic fields have not changed, even microscopically. This leads to a signal maximum at echo time T_E, of which the envelope is T_2 weighted. For this reason, the T_2' component of transverse relaxation is said to be reversible, while T_2 decay is irreversible. In practice, diffusion hinders a perfect rephasing of spin packets at T_E, but a maximum of transverse magnetization with minimal dephasing effects is observed nonetheless. When T_E is very short in combination with a long T_R, the signal intensity is mainly influenced by the local spin density, commonly referred to proton density weighting in clinical imaging.

MRI is fundamentally affected by the structure and dynamics of the tissue it images. Besides thermal motion and the molecular environment, pertinent factors include the strength, barriers and isotropy of diffusion, as well as the distribution of magnetic field inhomogeneities within the object being imaged. Inhomogeneities of the B_0 field can be owed to bad shimming, but they are also caused by spatial variations of the imaged sample's magnetic susceptibility χ. In medical imaging, such variations appear on different length scales. In the human head, for instance, the susceptibility χ differs significantly between the soft tissue within the skull and the air in the nasal cavity or the skull itself (cf. Table 1 in [67]). In MRI at high field strengths, macroscopically, such sudden susceptibility variations can cause artifacts around the material boundaries because B_0 is altered characteristically on a large scale and these regions become off-resonant, which reduces the absorption rate of RF radiation at frequency $\omega_0 = \gamma B_0$ and therefore the pulse efficacy and initial transverse magnetization $m_\perp(t = 0)$.

On mesoscopic and microscopic length scales, below the dimensions of an MRI voxel, blood vessels represent prevalent susceptibility inclusions within living soft tissue, which otherwise approximately has the magnetic susceptibility of water. In comparison, hemoglobin, the main protein in red blood cells, is slightly diamagnetic when binding oxygen (oxyhemoglobin, $\chi \lesssim \chi_{water}$) and notably paramagnetic without oxygen (deoxyhemoglobin, $\chi > \chi_{water}$) (see, *e.g.*, Table 1 in [67]). This is the basis of the BOLD effect [20, 38]. Decreasing blood oxygenation makes vessels and capillaries more paramagnetic, which causes stronger field inhomogeneities within MRI voxels. This, in turn, invokes additional spin dephasing and affects $A_d(t)$ from Eq. (1.8). The motivation of this thesis is rooted in the fact that $A_d(t)$ is typically not mono-exponential in heterogeneous media and multi-compartmental tissues [14, 43, 44]. Analytical and numerical treatments of this problem have shown that the vessel geometry far below the MRI resolution can theoretically be inferred upon through suitable modeling of the dephasing attenuation $A_d(t)$. In the following section, the most prominent classical treatments with analytical methods are introduced for different conditions.

1.2.4 Classical models of spin dephasing around vessels

A theoretical treatment of the dephasing effects caused by blood-filled vessels is possible under some simplifying assumptions. A representation of blood vessels to first approximation is given by the single capillary model (SCM), which has been studied extensively, as demonstrated in the following. Motivated by Krogh's approach of describing the oxygen supply of tissue [68], the model can be used to describe a sparse, regular arrangement of parallel vessels. With infinitely long, straight cylinders, the problem can be reduced to 2D. The SCM describes regularly perfused tissue with a hexagonal closest-packed arrangement of parallel vessels by focusing on only one representative cell. The hexagonal supply cell surrounding the vessel can be approximated by a round cylinder (cf. **Fig.** 1.1). The tissue between the vessel with radius R_C and supply cell boundary at radius R_D, containing the signal-composing spins, is called dephasing volume. The fractional blood vessel volume $\eta = fVV$ in this model is given by $\eta = R_C^2/R_D^2$.
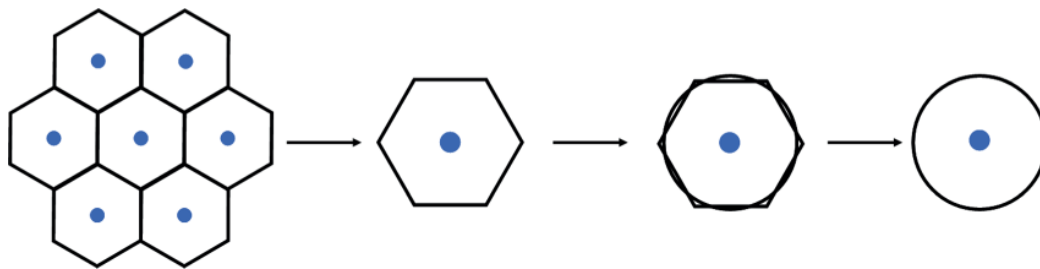
Figure 1.1: Transition scheme between a regular, hexagonal vessel arrangement to the single capillary model (SCM), adapted without change from [13] with kind permission from the American Physical Society. In this 2D representation, vessels are blue circles, surrounded by their supply/dephasing tissue.

In an external magnetic field $\vec{B}_0$ perpendicular to the cylindrical axis, a 2D-dipole field forms around the vessel, which is paramagnetic due to a homogeneous distribution of deoxyhemoglobin or contrast agent (see **Fig.** 1.2). The local Larmor frequency offset $\omega_{2D}(\vec{r})$, resulting from this paramagnetic susceptibility inclusion, is given by [69]:

$$\omega_{2D}(r, \phi) = \delta\omega R_C^2 \frac{\cos(2\phi)}{r^2}, \tag{1.9}$$

where the position $\vec{r}$ is described by the distance $r = |\vec{r}|$ and angle ϕ (see **Fig.** 1.2,b). The characteristic off-resonance $\delta\omega = \omega(r = R_C, \phi = 0) = \gamma\Delta\chi/2\, B_0 \sin^2\theta$ incorporates the gyromagnetic ratio γ, effective perpendicular field strength $B_0 \sin^2\theta$, and the magnetic susceptibility difference between vessel interior and exterior $\Delta\chi$.
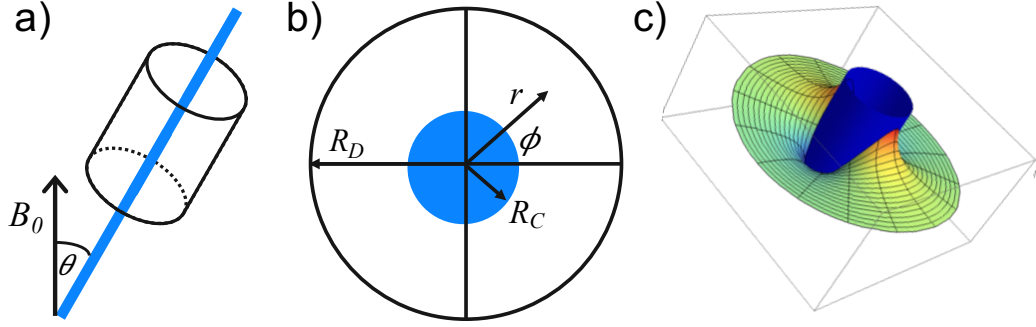
Figure 1.2: Sketches of **a)** vessel cylinder (blue) with surrounding dephasing cylinder in an external field $\vec{B}_0$, **b)** cross section of a vessel with capillary radius R_C and dephasing cylinder radius R_D, **c)** surface plot of 2D-dipole field distortions around a paramagnetic cylinder with perpendicular field component B_0.

Strictly seen, the original Bloch equation, as presented in Eq. (1.4), only describes NMR under static conditions without any physical movement of the spin-bearing particles. An extension of the Bloch equation, incorporating spin diffusion, was introduced in 1956 and named the Bloch-Torrey equation [70]. In the following considerations, T_1-relaxation is omitted since it only affects the longitudinal magnetization separately. The Bloch-Torrey equation for the local transverse magnetization $m_\perp(\vec{r}, t)$, which is denoted as $m(\vec{r}, t)$ in this section for notational simplicity, reads:

$$\frac{\partial}{\partial t} m(\vec{r}, t) = \left[D\Delta - \mathrm{i}\omega(\vec{r}) - \frac{1}{T_{2,0}} \right] m(\vec{r}, t). \tag{1.10}$$

Here, D is the diffusion coefficient of the spin-bearing atoms or molecules (usually water), $\Delta = \nabla^2$ is the Laplace operator, and $T_{2,0}$ is the intrinsic spin-spin relaxation time (see section 1.2.3).

Since transverse relaxation in MRI is typically assumed to be mono-exponential with $M(t) = M_\perp(t) \approx M_0\, \mathrm{e}^{-t/T_2^*}$, the so-called mean relaxation time approach can be used to calculate the relaxation time T_2^* [69]:

$$T_2^* = \int_0^\infty \frac{M(t)}{M_0}\, \mathrm{d}t. \tag{1.11}$$

For clearer notation in the following, the total relaxation rate $R_2^* = 1/T_2^*$ can be divided into intrinsic component $R_{2,0}$ and a contribution from dephasing ΔR_2^*:

$$\begin{aligned}
R_2^* &= R_{2,0} + \Delta R_2^* \\
&= \frac{1}{T_{2,0}} + \frac{1}{\Delta T_2^*}.
\end{aligned}$$

Analogous relationships exist for spin echo measurements. On top of intrinsic spin-spin relaxation with $R_{2,0}$, an additional spin echo attenuation with ΔT_2 occurs when the signal-composing protons diffuse through inhomogeneous magnetic fields:

$$R_2 = R_{2,0} + \Delta R_2$$
$$= \frac{1}{T_2} = \frac{1}{T_{2,0}} + \frac{1}{\Delta T_2}.$$

Again, the mean relaxation time approach can be used to calculate the effective relaxation time T_2 from the spin echo amplitude $M_{SE}(t)$:

$$T_2 = \int_0^\infty \frac{M_{SE}(t)}{M_0}\,\mathrm{d}t. \tag{1.12}$$

In the treatments to follow, internal spin-spin relaxation with $T_{2,0}$ is omitted because this mono-exponential decay can simply be superimposed onto the dephasing effects, which are the focus within this thesis.

Approximating solutions using the cylindrical vessel model

Many approaches have been taken to solve the Bloch-Torrey equation (1.10) for symmetrical model geometries such as the SCM. Since the 1990's, several approximate solutions for different diffusion regimes have been introduced and around twenty years later, an exact solution valid for all diffusion conditions was presented [13, 71]. The most prominent approximate solutions on the way to the most general one are briefly introduced in the following in order to demonstrate the form of the dephasing attenuation from a cylindrical vessel in different diffusion regimes; *i.e.*, no diffusion, slow diffusion, and fast diffusion of the signal-composing spins in the extravascular space around the vessel.

Static dephasing regime

The first successful analytical treatment of dephasing effects of local field inhomogeneities in the SCM was published in 1994 [9]. In their considerations of the time, the authors neglected diffusion of the water molecules in an attempt to solve the original Bloch equation (1.4) with 2D dipole field inhomogeneities as in Eq. (1.9). Due to the complete omission of diffusion effects, this solution is said to be valid in the static dephasing regime. Such conditions can be approximately fulfilled by very large vessel diameters, weak off-resonance magnitudes (arterial blood with high oxygen saturation and/or low field strength B_0), and/or very weak diffusion.

For the total magnetization $M(t)$ as determined from the volume integral in Eq. (1.5), Yablonskiy and Haacke found the following description of the FID caused by a single vessel [9, 72]:

$$M_{SCM,0}(t) = \frac{h(\eta \delta \omega t) - \eta h(\delta \omega t)}{1 - \eta} = \frac{\eta}{1 - \eta} \int_\eta^1 J_0(x \delta \omega t) \frac{dx}{x^2}, \tag{1.13}$$

where $h(x)$ is the extended hypergeometric function:

$$h(x) = {}_1F_2\left(\left\{-\frac{1}{2}\right\}; \left\{\frac{1}{2}, 1\right\}; -\frac{x^2}{4}\right).$$

Also known as the Barnes extended hypergeometric function, ${}_pF_q$ is defined in the following way [73]:

$$\,_pF_q\left(\{a_1, ...a_p\}; \{b_1, ..., b_q\}; z\right) = \sum_{k=0}^\infty \frac{(a_1)_k (a_2)_k \cdots (a_p)_k}{(b_1)_k (b_2)_k \cdots (b_q)_k} \frac{z^k}{k!} \tag{1.14}$$

with Pochhammer symbols $(x)_k$, given by

$$(x)_k = \frac{\Gamma(x + k)}{\Gamma(x)}.$$

The alternative representation includes an integral over the first order Bessel function with index zero, J_0. The validity of this solution for the static dephasing regime of the SCM is marked by the subscript on the integral transverse magnetization in Eq. (1.13).

The authors also extended their considerations to infinitely long, cylindrical vessel distributions with small tissue volume fraction $\eta = N \pi R_C^2 / V$ and random orientation angles. In the hypothetical limit of infinitely many vessels $N \to \infty$ (but constant η) and a uniform distribution of angles, the following was found by averaging over vessel orientations [74]:

$$M_{RVM,0}(t) = \exp\left[-\frac{\eta}{3} \int_0^1 (2 + u)\sqrt{1 - u} \frac{1 - J_0(\delta \omega t u)}{u^2} du\right] \tag{1.15}$$

$$= \exp\left[-\eta \cdot {}_1F_2\left(\left\{-\frac{1}{2}\right\}; \left\{\frac{3}{4}, \frac{5}{4}\right\}; -\frac{\delta \omega^2 t^2}{4}\right) - 1\right]. \tag{1.16}$$

Approximating this "random vessel model" (RVM) solution in static dephasing by a mono-exponential decay with relaxation rate $\Delta R_{2,RVM,0}^*$ with the mean relaxation approach as in Eq. (1.11), the decay rate contribution from dephasing is given by [13]:

$$\Delta R_{2,RVM,0}^* = \frac{1}{\Delta T_{2,RVM,0}^*} = \frac{2\eta \delta \omega}{1 + \eta}. \tag{1.17}$$

It should be noted that the capillary radius R_C does not appear in the solutions of this model directly, but only through the blood volume ratio η. Spin echo considerations in the static dephasing regime are trivial for temporally constant field inhomogeneities, since no dephasing attenuation of the echo amplitude is observed with static conditions and perfect rephasing. The static dephasing approximation provides good predictions for scenarios where the length scale of local field inhomogeneities is much greater than the diffusion distance expected during time t. In the cylinder model, this corresponds to large vessels with $R_C \gg \sqrt{D}t$ and/or low off-resonance magnitude $\delta\omega$.

Approximations including diffusion effects

Linear local field approximation

The first successful incorporation of spin packet diffusion through magnetic field perturbations from randomly oriented vessel cylinders was achieved by considering purely linear local field variations [75]. This is a good approximation when diffusion effects are relatively weak in comparison to the variance of local field strength. The authors showed that, with water diffusion coefficient D, the complex transverse magnetization can be approximated by the following ensemble average:

$$M(t) = \left\langle \exp\left(-\mathrm{i}\omega(\vec{r})t - \frac{D}{3}[\nabla\omega(\vec{r})]^2 t^3\right)\right\rangle,$$

leading to the final result:

$$M_{KP}(t) = \mathrm{e}^{\left(-\frac{\eta}{2}\int_0^\pi \sin\theta\,\mathrm{d}\theta \int_0^1 \left[1-\exp\left(-\frac{4D}{3R_C^2}\delta\omega^2 t^3 u^3 \sin^4\theta\right)J_0(\delta\omega t u \sin^2\theta)\right]\frac{\mathrm{d}u}{u^2}\right)}$$

with nomenclature as before and the subscript KP standing for the original authors, Kiselev and Posse. The result for spin echo measurements can be found in [75].

To treat fast diffusion, the authors solved the Bloch-Torrey equation using second order perturbation theory. Strong diffusion leads to an averaging of the field inhomogeneities seen by each spin packet, slowing down the signal decay. This leads to a reduced linewidth and more Lorentzian shape of the Fourier transformed of the total magnetization time series $M(t)$. For this reason, the fast diffusion case was coined the "motional narrowing" or "diffusion narrowing" regime (DNR) [74]. For fast diffusion limit, the linear field approximation leads to the same solution as the Gaussian phase approximation, introduced in the following.

Gaussian phase approximation

In the early 2000's, Sukstanskii and Yablonskiy approached the problem with fast

diffusion by assuming Gaussian probability distributions of the spin packet phases for permeable [76] and impermeable cylindrical vessels [77]. Here, only the impermeable cylinder treatment is presented, since this conforms with the simplifications of the simulations presented in publications I and V. Gaussian phase distributions allows for the following formulation [74]:

$$M(t) = \exp\left(-\frac{1}{2}\langle\phi^2(t)\rangle\right)$$
$$= \exp\left(-\int_0^t K(t')(t - t')\,dt'\right)$$

with the two-point frequency correlation function $K(t)$:

$$K(t) = \langle\omega(\vec{r})\omega(\vec{r}_0)P(\vec{r}, \vec{r}_0, t)\rangle. \tag{1.18}$$

Here, $P(\vec{r}, \vec{r}_0, t)$ is the probability of a spin packet diffusing from position $\vec{r}_0$ to $\vec{r}$ in time t. In the case of unhindered diffusion, this would be a Gaussian distribution. In Eq. (1.18), the angular brackets denote an averaging over spin packet positions $\vec{r}$ and $\vec{r}_0$, vessel positions, and vessel orientations.

An evaluation of these averages leads to the following signal attenuation [77]:

$$M_{SY}(t) = \exp\left(-\frac{128\eta\delta\omega^2 R_C^4}{15\pi^2 D^2}\int_0^\infty \frac{g(\nu^2 Dt/R_C^2)}{\nu^9\left[J_2'^2(\nu) + N_2'^2(\nu)\right]}\,d\nu\right),$$

where $J'(\nu)$ and $N'(\nu)$ are derivates of the Bessel functions of the first and second kind, respectively. For the FID, the function $g(x)$ is given by:

$$g_{FID}(x) = e^{-x} + x - 1,$$

whereas dephasing during spin echo experiments with a 180° RF pulse at time $t = T_E/2$ can be attained by inserting

$$g_{SE}(t, x) = 2\exp\left(-\frac{x^2 DT_E}{2R_C^2}\right) + 2\exp\left(-\frac{x^2 D(2t + T_E)}{2R_C^2}\right) - \exp\left(-\frac{x^2 D(t + T_E)}{R_C^2}\right)$$
$$+ \frac{x^2 D(t + T_E)}{R_C^2} - 3.$$

Strong collision approximation

An approach that is valid across the entire range of diffusion regimes [74] is known as the "strong collision approximation", which was introduced by Bauer and colleagues in 1999 [78, 79] and later extended [80]. The strong collision approximation replaces the diffusion

operator in the Bloch-Torrey equation, $D\Delta$ in Eq. (1.10), with a stochastic Markov process, enabling an evaluation of the integral magnetization $M(t)$. The model was originally derived for parallel capillaries as an approximation in the healthy myocardium, where capillaries are approximately parallel over relatively long distances [79].

As a Markov process, the transition rate between different states of the system due to diffusion only depends on the equilibrium probability of the final state. A major consequence from the strong collision approximation is that the signal decay including diffusion, $M(t)$, can be connected to the solution for an equivalent geometry without diffusion $M_0(t)$ via their respective Laplace transforms $\hat{M}(s)$ and $\hat{M}_0(s)$ [78]:

$$\hat{M}(s) = \frac{\hat{M}_0(s + \tau^{-1})}{1 - \tau^{-1}\hat{M}_0(s + \tau^{-1})}, \tag{1.19}$$

with the Laplace transformation of a function $f(t)$ given by:

$$\hat{f}(s) = \int_0^\infty f(t)\,\mathrm{e}^{-st}\,\mathrm{d}t.$$

The correlation time τ for infinitely long cylinders can be determined using the correlation function $K(t)$ and, in the cylindrical model, was shown to be [78]:

$$\tau_C = -\frac{R_C^2}{4D}\frac{\ln\eta}{1-\eta}. \tag{1.20}$$

The Laplace transformed $\hat{M}_0(s)$ of the static dephasing magnetization $M_{SCM,0}(t)$ for infinitely long cylinders, as given in Eq. (1.13), can be expressed as:

$$\hat{M}_{SCM,0}(s) = \frac{1}{(1-\eta)s}\left[H_C\left(\frac{s}{\eta\delta\omega}\right) - \eta H_C\left(\frac{s}{\delta\omega}\right)\right]$$

with the geometry-specific H-function for parallel cylinders:

$$H_C(y) = \sqrt{1 + \frac{\sin^4\theta}{y^2}}. \tag{1.21}$$

The H-function can be averaged over vessel orientations θ to the external $\vec{B}_0$ field to determine H_{RC} for randomly oriented cylinders [74]:

$$H_{RC}(y) = \int_0^\pi \frac{\sin\theta}{2}\sqrt{1 + \frac{\sin^4\theta}{y^2}} = {}_3F_2\left(\left\{-\frac{1}{2},\frac{1}{2},1\right\},\left\{\frac{3}{4},\frac{5}{4}\right\};-\frac{1}{y^2}\right), \tag{1.22}$$

again, leading to the hypergeometric function as defined in Eq. (1.14).

In general, the transverse magnetization $M(t)$ can be attained by inverse Fourier transformation of the frequency density of states $p(\omega)$:

$$M_{SC}(t) = \rho \int_{-\infty}^{\infty} p(\omega)\, \mathrm{e}^{\mathrm{i}\omega t}\, \mathrm{d}\omega$$

with spin density ρ, assumed to be constant throughout the extravascular volume. Naturally, the density of states $p(\omega)$ is the Fourier transformed of the signal $M(t)$, thus:

$$\begin{aligned}
p(\omega) &= \frac{1}{2\pi\rho} \int_{-\infty}^{\infty} M(t)\mathrm{e}^{-\mathrm{i}\omega t}\, \mathrm{d}t \\
&= \frac{1}{2\pi\rho} \left| \hat{M}(\mathrm{i}\omega) + \hat{M}^*(\mathrm{i}\omega) \right| = \frac{1}{\pi\rho} \left| \mathrm{Re}\hat{M}(\mathrm{i}\omega) \right|.
\end{aligned} \tag{1.23}$$

With the strong collision approximation, by inserting Eq. (1.19), it follows that:

$$\begin{aligned}
p(\omega) &= \frac{1}{\pi\rho} \left| \mathrm{Re} \left\{ \frac{\hat{M}_0(\mathrm{i}\omega + \tau^{-1})}{1 - \tau^{-1}\hat{M}_0(\mathrm{i}\omega + \tau^{-1})} \right\} \right| \\
&= \frac{\tau}{\pi} \left| \mathrm{Re} \left\{ \left[\int_V \frac{\mathrm{d}^3 r}{1 + \mathrm{i}\tau[\omega - \omega(\vec{r})]} \right]^{-1} - \rho \right\}^{-1} \right|.
\end{aligned}$$

With the 2D-dipole distribution of Larmor frequencies from Eq. (1.9), it can be shown that for cylindrical geometries, the frequency density of states $p(\omega)$ is given by the following for all diffusion regimes [72]:

$$p(\omega) = \frac{\tau}{\pi\rho} \left| \mathrm{Re} \left\{ \frac{H\left(\frac{1+\mathrm{i}\tau\omega}{\eta\tau\delta\omega}\right) - \eta H\left(\frac{1+\mathrm{i}\tau\omega}{\tau\delta\omega}\right)}{\frac{1-\eta}{\rho}(1 + \mathrm{i}\tau\omega) - H\left(\frac{1+\mathrm{i}\tau\omega}{\eta\tau\delta\omega}\right) + \eta H\left(\frac{1+\mathrm{i}\tau\omega}{\tau\delta\omega}\right)} \right\} \right|, \tag{1.24}$$

where the H-function should be substituted by H_C from Eq. (1.21) for parallel capillaries and H_{RC} from Eq. (1.22) for random vessel orientations. Once the total magnetization $M_{SC}(t)$ is attained through Fourier transformation of Eq. (1.24), the magnetization time evolution expected from a spin echo experiment, $M_{SC,SE}(t)$, can be found as [72]:

$$M_{SC,SE}(t) = \mathrm{e}^{-t/\tau} + \frac{\mathrm{e}^{-t/\tau}}{\tau} \int_0^t \mathrm{e}^{\xi/\tau} \left| M\left(\frac{\xi}{2}\right) \right|^2 \mathrm{d}\xi. \tag{1.25}$$

The validity of each approximating theory has been tested and compared [74]. Monte Carlo simulations of spin dephasing around cylindrical vessels with different radii were conducted to emulate different diffusion regimes. In **Fig.** 1.3, adapted from [74], the relaxation rates ΔR_2^* and ΔR_2, determined from mono-exponential fits to the simulated signal attenuations, were plotted with the theoretical predictions from each treatment introduced above. Each theory predicts dephasing quite well in its own range of validity.
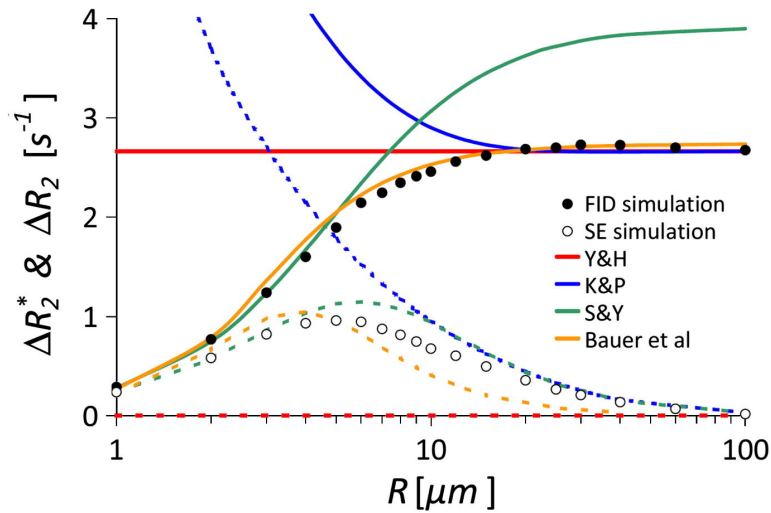
Figure 1.3: Relaxation rates ΔR_2^* and ΔR_2 accountable to dephasing effects during FID and spin echo experiments, adapted from [74] with the kind permission of Elsevier. Simulations were compared with analytical predictions, with solid lines for FID and dotted lines for spin echoes. In the legend, abbreviations refer to: Y&H - static dephasing regime, K&P - linear local field approximation, S&Y - Gaussian phase approximation, and Bauer et al - strong collision approximation. The simulations were conducted with blood volume fraction $\eta = 0.03$ and blood oxygenation $Y = 0.6$.

The introduced theories show that even an approximating analytical treatment of spin dephasing, despite very simple geometric assumptions, proves to be quite cumbersome. For completeness, the exact solution of the Bloch-Torrey equation in the SCM, introduced in 2012 by Ziener and colleagues [71] is briefly presented in the following. This solution served as a ground truth for validations of the precision of the dephasing simulations implemented for publication I (in 2D) and publication V (in 3D).

Exact solution of the cylindrical vessel model

The linearity of the Bloch-Torrey equation (1.10) concerning the local magnetization $m(\vec{r}, t) = m(r, \phi, t)$ allows for a factorization ansatz, segregating the dependencies on vector magnitude r and angle ϕ of the location $\vec{r}$ relative to the capillary center, as well as time t:

$$m(r, \phi, t) = T(t)R(r)\Phi(\phi). \tag{1.26}$$

For the individual functions, new differential equations follow from the Bloch-Torrey equation, which have been studied before. In summary, solutions of these individual equations are identified and used in an eigenfunction expansion to form a full solution of the present problem [71].

The angle-dependent part is governed by the Mathieu differential equation:

$$\frac{\partial^2}{\partial \phi^2}\Phi_m(\phi) + \left[k_m^2 - \mathrm{i}\tau\delta\omega\cos(2\phi)\right]\Phi_m(\phi) = 0,$$

where k_m is the angular eigenvalue to eigenfunction Φ_m. Due to the symmetry of the 2D-dipole field in Eq. (1.9), only the π-periodic, even Mathieu functions ce_{2m} can appear in the expansion of the sought solution:

$$\Phi_m(\phi) = \mathrm{ce}_{2m}(\phi, \mathrm{i}\tau\delta\omega/2).$$

The angular eigenvalue k_m is determined by the characteristic value a_{2m} of the Mathieu function ce_{2m}:

$$k_m^2 = a_{2m}(\mathrm{i}\tau\delta\omega/2).$$

The radial part $R(r)$ has to obey the Bessel differential equation, solved by the eigenfunctions $R_{nm}(r)$:

$$\frac{\partial^2}{\partial r^2}R_{nm}(r) + \frac{1}{r}\frac{\partial}{\partial r}R_{nm}(r) + \left[\frac{\lambda_{nm}^2}{R_C^2} - \frac{k_m^2}{r^2}\right]R_{nm}(r) = 0 \tag{1.27}$$

with radial eigenvalues λ_{nm}^2. Reflecting boundary conditions on the inner capillary cylinder and outer dephasing cylinder are assumed for periodic solutions. This is formulated by $\partial_r R_{nm}(r)|_{r=R_C} = \partial_r R_{nm}(r)|_{r=R_D} = 0$ for all eigenfunctions R_{nm} and has the consequence that the solutions R_{nm} can be expressed as linear combinations of Bessel functions J and Neumann functions Y with their derivatives denoted by a prime:

$$R_{nm}(r) = Y'_{k_m}(\lambda_{nm})J_{k_m}\left(\frac{\lambda_{nm}}{R_C}r\right) - J'_{k_m}(\lambda_{nm})Y_{k_m}\left(\frac{\lambda_{nm}}{R_C}r\right).$$

The radial eigenvalues λ_{nm} are forced to fulfill the following transcendental equation:

$$Y'_{k_m}(\lambda_{nm})J'_{k_m}\left(\frac{\lambda_{nm}}{\sqrt{\eta}}\right) = J'_{k_m}(\lambda_{nm})Y'_{k_m}\left(\frac{\lambda_{nm}}{\sqrt{\eta}}\right), \tag{1.28}$$

The indices of the Bessel and Neumann functions are given by the angular eigenvalue k_m and Eq. (1.28) was solved numerically with complex root finding algorithms [13].

For the time-dependent part of the local magnetization in Eq. (1.26), the separation ansatz with the Bloch-Torrey equation (1.10) yields:

$$\frac{R_C^2}{D}\left[\frac{\partial}{\partial t} + \frac{1}{T_2}\right]T_{nm}(t) = -\lambda_{nm}^2 T_{nm}(t),$$

which is solved by:

$$T_{nm}(t) = \exp\left[-t\left(\frac{\lambda_{nm}^2 D}{R_C^2} + \frac{1}{T_{2,0}}\right)\right].$$

(1.29)

Intrinsic spin-spin relaxation with $1/T_{2,0}$ is included trivially in this solution, representing a mere factor $\mathrm{e}^{-t/T_{2,0}}$.

The full solution for the local magnetization $m(\vec{r}, t)$ follows from Eq. (1.26):

$$\frac{m(r,\phi,t)}{m_0} = \mathrm{e}^{-\frac{t}{T_{2,0}}} \sum_{m=0}^{\infty} \sum_{n=1}^{\infty} c_{nm} \mathrm{ce}_{2m}\left(\phi, \mathrm{i}\frac{\delta\omega R_C^2}{2D}\right) \cdot R_{nm}(r)\mathrm{e}^{-\lambda_{nm}^2\frac{D}{R_C^2}t},$$

(1.30)

where m_0 is the equilibrium magnetization which is flipped into the transverse plane by a 90°-excitation pulse at time $t = 0$. The expansion coefficients c_{nm} are given by [71]:

$$\frac{c_{nm}}{2\pi} = \frac{A_0^{(2m)}\lambda_{nm}^2 J'_{k_m}\left(\frac{\lambda_{nm}}{\sqrt{\eta}}\right)\left[J'_{k_m}(\lambda_{nm})s'_{1,k_m}\left(\frac{\lambda_{nm}}{\sqrt{\eta}}\right) - J'_{k_m}\left(\frac{\lambda_{nm}}{\sqrt{\eta}}\right)s'_{1,k_m}(\lambda_{nm})\right]}{\left[J'_{k_m}(\lambda_{nm})\right]^2\left[\lambda_{nm}^2 - \eta k_m^2\right] - \left[J'_{k_m}\left(\frac{\lambda_{nm}}{\sqrt{\eta}}\right)\right]^2\left[\lambda_{nm}^2 - k_m^2\right]}$$

(1.31)

with S'_{1,k_m} denoting the first derivative of the Lommel function and J'_{k_m} again referring to the derived Bessel function. $A_0^{(2m)}$ is the first Fourier coefficient of the even Mathieu function ce_{2m} and it, like the eigenvalues k_m, exhibits a dependence on $\delta\omega R_C^2/D$. This product is a dimensionless scalar that parametrizes the impact of diffusion effects in the SCM. Low values of $\delta\omega R_C^2/D \lesssim 1$ describe strong diffusion phenomena with a significant averaging effect on the local Larmor frequencies seen by spin packets, whereas high values of $\delta\omega R_C^2/D$ indicate that the diffusivity of water is weak compared to the local field inhomogeneities. With increasing values, the resulting dephasing behavior increasingly resembles the static dephasing regime [13].

An integration over the dephasing volume containing the spin packets with local transverse magnetization $m(r, \phi, t)$, the total signal evolution from the integral magnetization $M(t)$ can be found to be given by [13]:

$$\frac{M(t)}{M_0} = \int_0^{2\pi}\int_{R_C}^{R_D} \frac{m(r,\phi,t)}{m_0} r\,\mathrm{d}r\,\mathrm{d}\phi$$

$$= \mathrm{e}^{-t/T_{2,0}} \sum_{m=0}^{\infty}\sum_{n=1}^{\infty} d_{nm}\exp\left[-\lambda_{nm}^2\frac{D}{R_C^2}t\right]$$

(1.32)

with the expansion coefficients

$$d_{nm} = \frac{8\eta}{1-\eta}\frac{\left[A_0^{(2m)}\right]^2\left[J'_{k_m}(\lambda_{nm})s'_{1,k_m}\left(\frac{\lambda_{nm}}{\sqrt{\eta}}\right) - J'_{k_m}\left(\frac{\lambda_{nm}}{\sqrt{\eta}}\right)s'_{1,k_m}(\lambda_{nm})\right]^2}{\left[J'_{k_m}(\lambda_{nm})\right]^2\left[\lambda_{nm}^2 - \eta k_m^2\right] - \left[J'_{k_m}\left(\frac{\lambda_{nm}}{\sqrt{\eta}}\right)\right]^2\left[\lambda_{nm}^2 - k_m^2\right]}.$$

Details about the functions, eigenvalues and expansion coefficients appearing in the solutions in Eqs. (1.30) and (1.32) can be found in the original publications [71] and [13]. Discussions about the Mathieu functions and their characteristic values with imaginary arguments can be found in [81] and an in-depth treatment of the modified Lommel functions in this context is provided in [82].

Despite the crude simplifications of vessel geometry, the dephasing solutions take very complicated forms, clearly deviating from mono-exponential decay with $A_d(t) \approx e^{-R_2' t}$. The solutions found, incorporating the cylindrical radius R_C and tissue volume fraction η, are too complex to be used for real signal fitting, especially with noise on the measurable signal. Yet, it is inspiring to find that the mapping from microvascular geometry to a macroscopic NMR signal is well-defined for this geometric model and can even be solved exactly. This motivates the search for a dephasing-based method to characterize microvascular properties and/or anomalies using T_2'-weighted MRI signals with variable echo times to sample the voxel-wise dephasing attenuation $A_d(T_E)$. A promising first application for such developments is cancer imaging, since tumors are known to have dramatic remodeling effects on microvasculature.

1.2.5 Cancer imaging and its unsolved problems

Cancer is a prevalent pathology and responsible for many deaths each year. The time of diagnosis and how far a malignant tumor has developed (tumor stage) have a great impact on the prognosis and viable treatment options for the patient. Malignant brain tumors, specifically the most commonly occurring, glioblastoma multiforme, typically have very bad prognoses and often, are discovered too late for a promising treatment. A medical imaging technique sensitive to early tissue alterations due to a growing tumor on small length scales would be of enormous relevance to oncology.

Microstructural changes to tissue accompany different pathologies, including most malignant tumor types. Neoplasia usually brings forth a modified cell mass composition, density, and extracellular matrix, coinciding with altered diffusion properties, as well as characteristic vascular adjustments to suit the metabolic needs of a growing tumor [83–86]. Such changes to tissue microstructure, manifesting on length scales of several micrometers or even nanometers, cannot be resolved directly with current medical imaging techniques used for diagnosis and treatment monitoring in a non-invasive way. Reliable tumor grading still demands invasive biopsies with histologic examinations; a laborious process which only facilitates sampling of small tissue sections and is unpleasant for the patient [87, 88].

The development of non-invasive imaging techniques sensitive to specific aspects of the tissue microenvironment has been an ambition of the MRI community for decades. This has brought forth a wealth of techniques to probe biological, chemical, and physical properties or surrogate biomarkers thereof for tumor diagnosis and phenotyping through indirect imaging and sophisticated modeling [89–91]. An introduction of the available methods, even just superficially, would blow the scope of this thesis and detour too much from the focus of this study, but the most established medical imaging modalities were summarized in a recent review of modern techniques sensitive to different aspects of tissue malformations related to cancer; see **Fig.** 1.4 and the original publication [92].
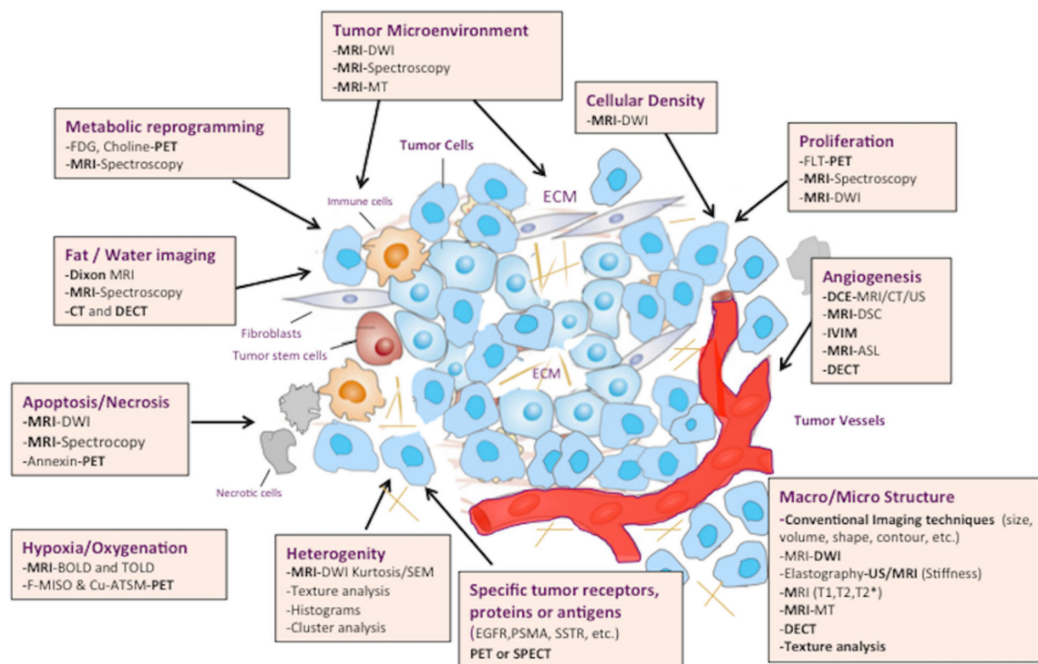
Figure 1.4: Clinical imaging techniques sensitive to different aspects of tumor biology and microstructure (see [92] for elaboration). This image was adapted without changes from García-Figueiras et al. [92], published under the Creative Commons Attribution 4.0 International License (http://creativecommons.org/licenses/by/4.0/).

In brief, diffusion weighted and diffusion tensor imaging (DWI and DTI) use magnetic field gradients to attenuate the local signal depending on diffusion in the gradient direction [93]. This enables a quantification of voxel-wise diffusion strength and anisotropy [94], but also advanced interpretations of non-Gaussian diffusion [95, 96] and microstructural quantifications in certain tissue types [97, 98]. Molecular imaging facilitates the detection and concentration assessment of certain molecules, gene expressions, and metabolic processes based on spectroscopic imaging [99]. Magnetization transfer MRI (MT-MRI) [5] has shown promising potential in cancer therapy monitoring [100, 101]

and chemical exchange saturation transfer (CEST) MRI [102, 103] has successfully been tested, *e.g.*, for classification of IDH mutations [104], glioblastoma imaging [105], and metastasis detection [106]. Tissue stiffness can be measured with MR elastography (MRE), which images shear wave propagations with phase-sensitive MRI [107, 108] and is well-applicable for tumor imaging [109, 110]. Despite the diversity of techniques having been developed based on endogenous conditions, contrast enhanced MRI with intravascular contrast agent administration still plays an important role in clinical imaging of cancers based on altered tissue perfusion and vessel permeability [111–114].

Although dynamic contrast techniques remain as the clinical gold standard for non-invasive measurements of microvascular anomalies [34, 115, 116], it is generally favorable to avoid the use of exogenous contrast agents; for one, due to patient comfort but also due to the high cytotoxicity of the commonly used gadolinium and possible long-term depositions within the body [117, 118]. Currently, the contrast agent-free MRI techniques closest to clinical use for assessing microvascular anomalies are arterial spin labeling (ASL) [119] and intravoxel incoherent motion (IVIM) imaging [120]. Both of these methods allow for quantitative estimations of voxel-wise blood volume and blood flow, with possible applications for cancer diagnostics and tumor grading [121–124].

The BOLD effect is another promising candidate to replace intravascular contrast agent administration, involving endogenous blood susceptibility variations. The link between the activation of a brain region and associated blood oxygen fluctuations, causing T_2^* and T_2 variations, is described by so-called neurovascular coupling [125, 126]. In healthy subjects, a drop of oxygen saturation is quickly compensated by fresh, oxygen-rich blood, which restores the microscopic field homogeneity and local T_2- and T_2^*-weighted signal intensities. The interpretation of such signal dynamics enables time-resolved, in-vivo, non-invasive measurements of neuronal and metabolic activities within the brain. Interestingly, brain tumors have been found to disrupt the neurovascular system and function locally and nonlocally, also affecting the connectivity of different brain regions [26, 27].

A comprehension of which types of anomalies of the neurovascular response system are associated with brain tumors would offer entirely new possibilities for non-invasive diagnoses and possibly even tumor grading. Unfortunately, the brain's regional activation patterns and functional connectivity can vary quite significantly among different individuals [127, 128] and be altered by many factors; *e.g.*, personal fitness, emotional state and arousal, but also neurological and psychiatric disorders [129–131]. Due to the brain's sheer complexity and the myriad of influential factors at play, a detailed understanding of intra- and interpersonal fMRI signatures is still very far away. In addition, there are many types of malignant brain tumors with distinct metabolic characteristics and infiltration patterns that can affect different brain regions, commu-

nication pathways, and neurovascular coupling very individually. Thus, a robust and generalizable use of BOLD-based fMRI measurements for tumor-diagnostic purposes is, at this point, an unrealistic goal as ambitious as it would be groundbreaking.

Technically, what complicates a diagnostic abstraction of fMRI methodology are several aspects; mainly being the temporal and spatial scales of necessary MRI measurements for a functional interpretation, in combination with the physiological complexity and dynamics at these time and length scales. The neurovascular response within individual voxels is typically measured over relatively long timescales on the order of $3-10\,\mathrm{s}$, with the sampling increment determined by the sequence repetition time T_R (usually $0.5-3\,\mathrm{s}$). Over the sampling timeframe of several seconds, microscopic conditions within a voxel are influenced by external, macroscopic processes, such as heart beats, pulsatile blood flow, breathing, significant vessel constrictions and dilations, dynamic structural adaptation, and metabolic demands elsewhere [47, 132–134]. All of these factors can influence the local BOLD signal. Further, besides the functional connectivity of different brain regions, the anatomical connectivity of the cerebrovascular network can lead to complex BOLD changes within voxels distant to neural activation sites, which are directly connected through the vascular network topology but do not necessarily have a functional link [135–137]. Interpreting functional connectivity from temporal correlations of BOLD signal changes in different brain regions is complicated by many physiological factors, of which the detailed interactions can further vary individually, depending on age, health, fitness, and lifestyle [138, 139].

Many of the difficulties just mentioned may be evaded by reducing the relevant time and length scales for an advanced MRI signal interpretation. Within time intervals of less than around $200\,\mathrm{ms}$, most physiological conditions within an MRI voxel (typical side lengths of around $1\,\mathrm{mm}$) are constant to good approximation. This includes structural properties of the vasculature and local blood oxygenation. As malignant tumors are known to promote vascular remodeling, involving vessel cooption, occlusion, and angiogenesis [140–144], the microvascular geometry in afflicted tissue is often peculiar in comparison to healthy tissue. In fact, the degree of this deformation has been suspected to correlate with tumor malignacy [145–148]. In regions of tumor growth, the microvascular properties which are approximately constant and minimally influenced by external, physiological factors over short time scales should be distinctive and recognizable. A successful voxel-wise characterization of microvasculature may enable an improved prognosis of future tumor development and possibly assist in non-invasive tumor grading. Moreover, a comparison of signal intensities within single voxels minimizes unknown and disregarded nonlocal effects that may influence functional connectivity and lead to a misinterpretation of signals from different tissue regions, as would be interpreted in "classic" fMRI.

While it makes sense to start vessel characterization for tumor diagnostics at the single voxel level, a better understanding of the nonlocal connectivity of the cerebrovascular network is of great importance for multiple reasons. For one, to understand a large transport network, it does not suffice to concentrate on the small constituents or patches of it. A vascular networks needs to be modeled and seen as such in order to comprehend its function and different aspects of its design. Only once healthy brain vasculature has been characterized as a network, *e.g.*, with the principles of graph theory [149], the effects of tumor growth on vascular connectivity can be studied. Such foundations may pave the way towards a better understanding of the effects of brain tumor development on fMRI and the phenomenon of neurovascular uncoupling. This was the motivation for large-scale quantifications of the network topology of entire brain hemispheres and a comparison with vascular networks in glioblastoma models, which is presented in publication IV. To my best knowledge, these are the first comprehensive vessel network quantifications of this kind, spanning the length scale of an entire brain at single capillary resolution.

An overview of pertinent literature describing past structural imaging endeavors of tumor vasculature is provided in the introductions and discussions of publications II, III, and IV. A major contribution of the original research works in this thesis is the development of a processing pipeline, which directly extracts quantitative, physical information from large microscopic datasets of vessel networks of arbitrary resolution, size, and shape. While publication III is focused around the determination of classical, local, geometric features of real vessel architectures, in publications II and IV, topological paradigms were applied to model the vasculature as a large system of many constituents, forming one entity that can be parametrized with nonlocal quantities. These publications offer new perspectives on large cerebrovascular networks and the remodeling effects of glioblastoma multiforme.

With the numerical tools developed in the course of this thesis and introduced in the following publications, the heterogeneous effects of tumor growth on tissue vasculature can be studied individually, given the availability of 3D image data, *e.g.*, from laser scanning microscopy or microCT [150]. With an increasing prevalence of high-resolution, large-scale imaging modalities and the ability to image vasculature selectively with specialized contrasts or markers, the developed tools are hoped to assist in further characterizations of organ-specific microvascular structures and characteristic effects of different pathologies. Perhaps, this data-driven approach will elucidate new perspectives on vascular pathologies, inspire the development of therapies to target specific aspects, or identify new quantities with a well-defined influence on the macroscopic MRI signal in order to devise more realistic vessel models [54, 151], incorporating, *e.g.*, connectivity or distributive characteristics.

2 Thesis overview

This thesis is presented in cumulative format in accordance with the regulations of the Department of Physics and Astronomy of the Ruperto-Carola University of Heidelberg. It comprises five articles published in internationally acclaimed peer-reviewed journals. Within this thesis, the individual manuscripts are referred to by roman numerals. I am the first and principal author of publications II, IV, and V, shared first author of publication III, and co-author of publication I. Conform with faculty regulations, the publications with principal authorship have not been used and will not be used for any other dissertation. The articles have been reproduced in this thesis with the kind permissions of Elsevier (publications I and II), Sage Publishing (publication III), Springer Nature (publication IV), and John Wiley & Sons, Ltd. (publication V). In section 2.2, each publication is summarized in the context of this thesis. Copyright information and individual author contributions to the articles are provided in chapter 3, preceding each publication.

2.1 List of publications

Publication I

F. T. Kurz, C. H. Ziener, M. Rückl, <u>A. Hahn</u>, V. J. F. Sturm, K. Zhang, L. R. Buschle, M. Bendszus, S. Heiland, H.-P. Schlemmer, W. R. Bauer & T. Kampf. *The influence of spatial patterns of capillary networks on transverse relaxation.* **Magnetic Resonance Imaging** 40:31-47 (2017). https://doi.org/10.1016/j.mri.2017.03.012

Publication II

<u>A. Hahn</u>, J. Bode, T. Krüwel, L. R. Buschle, V. J. F. Sturm, K. Zhang, B. Tews, H.-P. Schlemmer, S. Heiland, M. Bendszus, C. H. Ziener, M. O. Breckwoldt & F. T. Kurz. *Gibbs point field model quantifies disorder in microvasculature of U87-glioblastoma.* **Journal of Theoretical Biology** 494:110230 (2020). https://doi.org/10.1016/j.jtbi.2020.110230

Publication III

<u>A. Hahn</u>, J. Bode, A. Alexander, K. Karimian-Jazi, K. Schregel, D. Schwarz, A. C. Sommerkamp, T. Krüwel, A. Abdollahi, W. Wick, M. Platten, M. Bendszus, B. Tews, F. T. Kurz & M. O. Breckwoldt. *Large-scale characterization of the microvascular geometry in development and disease by tissue clearing and quantitative ultramicroscopy.* **Journal of Cerebral Blood Flow & Metabolism** 271678X20961854 (2020). https://doi.org/10.1177/0271678X20961854

Publication IV

<u>A. Hahn</u>, J. Bode, T. Krüwel, G. Solecki, S. Heiland, M. Bendszus, B. Tews, F. Winkler, M. O. Breckwoldt & F. T. Kurz. *Glioblastoma multiforme restructures the topological connectivity of cerebrovascular networks.* **Scientific Reports** 9:11757 (2019). https://doi.org/10.1038/s41598-019-47567-w

Publication V

<u>A. Hahn</u>, J. Bode, S. Schuhegger, T. Krüwel, V. J. F. Sturm, K. Zhang, J. M. E. Jende, B. Tews, S. Heiland, M. Bendszus, M. O. Breckwoldt, C. H. Ziener & F. T. Kurz. *Brain tumor classification of virtual NMR voxels based on realistic blood vessel-induced spin dephasing using support vector machines.* **NMR in Biomedicine** e4307 (2020). https://doi.org/10.1002/nbm.4307

2.2 Thematic summary

2.2.1 Publication I

In publication I, it was investigated how different spatial arrangements and degrees of irregularity in capillary arrays affect transverse relaxation. This study provides extensions of the results formerly attained for perfectly periodic and regular, or completely random arrangements of cylindrical vessels, using the traditional models applied previously for analytical and numerical treatments, as described in section 1.2.4. Specifically, the infinite cylindrical vessel model was embedded into different spatial arrangements and the consequences for spin dephasing were compared with those of increasingly varying capillary radii in a regular lattice and blood oxygen saturation changes. Theoretical foundations were combined with numerical calculations to add a distributive dimension to the models and compare the magnitude of their dephasing effects with those of vessel geometric variations and blood oxygen fluctuations.

The dephasing process around a single, infinitely long, cylindrical vessel in the Krogh model (see section 1.2.4) was compared with that of different periodic arrangements of cylinders. In analogy to the description of crystal structures using a Bravais lattice, unit cells were used to produce highly regular, periodic replications of capillaries with hexagonal and square, planar arrangements. The effects of each pattern on the sub-voxel Larmor frequency distribution were studied numerically. Further, the gap between a perfect crystalline regularity and complete spatial randomness was bridged with a continuous model, parametrizing the degree of disorder. Initially, spatial irregularity was first introduced and tuned through random displacements of capillary centers from a hexagonal lattice (using Gaussian distributed offsets with vanishing mean and standard deviations $\sigma_P \in [0, 2.5]\,\mu$m with a regular inter-capillary distance of $16.5\,\mu$m) and the effects were compared with those of increasingly varying capillary radii (also Gaussian distributed around a mean value $\mu_R = 1.94\,\mu$m with standard deviations $\sigma_R \in [0.1, 0.5]\,\mu$m). The findings justified further analyses with a constant capillary radius throughout the arrays.

In search of a simple model to quantify the irregularity of capillary distributions with a continuous parameter, not bound by any characteristic length scales or radius-dependent limits, a plasma model from statistical physics was adopted in this study. The two-dimensional (2D) one-component plasma (OCP) has previously been used to parametrize the coronary capillary regularity, successfully differentiating heart muscle tissue with different forms of cardiomyopathy [152]. Such an adaptation of the 2D-OCP, traditionally describing the repulsion of identically charged particles within a plasma in the canonical ensemble [153], is particularly motivated by a striking mathematical analogy to the differential equation describing the distribution of oxygen sources in a

tissue plane being supplied by concentration-driven oxygen diffusion, with perturbing factors to an ideal placement being summarized in a type of temperature parameter (see *Appendix A2* of publication II for elaboration). Macroscopic states of the 2D-OCP are fully determined by a single, dimensionless parameter $\Gamma \in [0, \inf)$, describing the balance between energy minimization and entropy maximization for a given state.

In this publication, it was investigated how the order parameter Γ affects the transverse relaxation rate R_2' accountable to capillary distributions. It was chosen as a candidate for the continuous parametrization of spatial regularity in capillary networks to bridge the gap between a perfect hexagonal lattice ($\Gamma \to \infty$) and uniform, random distribution ($\Gamma = 0$). Numerical simulations were used to produce 2D point fields using the 2D-OCP model with a range of Γ values. The point distributions produced this way were used as the positions of parallel capillary segments in a plane. Motivated by the traditional cylindrical vessel model commonly treated in the past (see section 1.2.4), the vessels were approximated by infinite cylinders to enable a treatment in 2D. The effects of random vessel orientations were analyzed for the limiting cases of completely random capillary distributions ($\Gamma = 0$) and the hexagonal lattice ($\Gamma \to \infty$) with an analytical averaging technique used in similar studies [9], revealing slower dephasing from randomly oriented vessels.

A conclusion of this study was that the definition of an artificial MRI contrast parametrizing microvascular disorder based on reversible transverse relaxation would not be straight-forward using the cylindrical vessel paradigm. Starting with a hexagonal lattice arrangement, the effects of varying vessel radii on intra-voxel Larmor frequency distributions were found to be similar to those of increasing random deviations of capillary positions from the crystal lattice, although the former were less pronounced in comparison. With relatively disordered vessel positions, an additional Gaussian radius distribution did not significantly change the signal shape any further, as compared with uniform radii. Thus, the influence of the singular vessel geometry on transverse relaxation depends on the distributive properties of the vessel network, having similar effects on the intra-voxel frequency density of states $\rho(\omega)$, *i.e.*, the histogram of Larmor frequency offsets. The magnitude of these vessel-induced frequency deviations scales linearly with the characteristic off-resonance $\delta\omega = 2\pi\chi_{do} \cdot (1 - Y) \cdot \text{Hct} \cdot \gamma B_0$, where χ_{do} is the magnetic susceptibility difference between deoxygenated and oxygenated hemoglobin, $Y \in [0, 1]$ is the blood oxygenation ratio, and Hct is the hematocrit.

An inclusion of diffusion effects, omnipresent in living tissue, yielded interesting results with the 2D-OCP model. Water diffusion in the extravascular space smooths off-resonance distributions and yields frequency histograms reminiscent of Lorentzian profiles, smearing the characteristic asymmetry found for hexagonal vessel lattices (see **Fig. 10, c** of publication I). Increasingly disordered vessel arrangements have a

similar effect on $\rho(\omega)$ in the extravascular volume (see **Fig. 8** of publication I). With diffusion, the relaxation rate R_2' from exponential fitting scales approximately with $2\delta\omega$, as opposed to just linearly with $\delta\omega$, as for static dephasing.

The relaxation rate R_2' exhibited a peculiar dependence on the order parameter Γ with varying off-resonance magnitude $\delta\omega$, but only under the inclusion of water diffusion (cf. **Fig. 12** and **Tab. 2** in publication I). With dynamic dephasing, low values of $\delta\omega$ (weak fields B_0 and/or low blood susceptibility χ) would cause stronger R_2' relaxation in the 2D-OCP model than in the regular hexagonal lattice, whereas large $\delta\omega$ (high B_0 and/or blood susceptibility) would show the opposite, with faster relaxation in the regular hexagonal capillary arrangement. This finding suggests that dynamic susceptibility contrast (DSC) may offer an effective handle on the capillary regularity, as the transition between these opposing cases is expected to be continuous. The effects of spatial irregularity in the capillary network on DSC MRI must be studied in more detail, ideally with real vessel architectures, to validate a separability from other vessel geometric and structural properties.

2.2.2 Publication II

As mentioned above, the 2D-OCP, used in publication I to model artificial capillary distributions with different degrees of regularity, was first applied to the myocardium [152], where capillary arrangement is known to be quite regular [154]. There, it was found that an attribution of the order parameter Γ to tissue sections, *e.g.*, as part of a histopathologic examination, may aid the diagnosis of different causes of heart-failure, such as dilated cardiomyopathy, ischemic cardiomyopathy, or inflammatory cardiomyopathy. In publication I of this thesis, it was investigated whether a non-invasive estimate of Γ values would theoretically be possible for individual MRI voxels, based on intra-voxel spin dephasing typically characterized by R_2'.

In publication II, the applicability of the 2D-OCP was analyzed for the identification of malignant brain tumors in a mouse model. Brain tissue naturally presents more intricate capillary beds with higher perceived disorder than myocardial tissue, especially in areas overlapping multiple brain regions or white and grey matter. This investigation was based on large, highly-resolved 3D image datasets acquired using fluorescence light sheet microscopy, following the fluorescent labeling of vessel lumen with an intravascular marker perfusion and subsequent tissue clearing [155], which had already been conducted in this case for a previous study [49]. Single plane illumination microscopy (SPIM) [156] yielded image stacks of the vasculature of entire mouse brains with $3.25\,\mu$m in-plane resolution and $5\,\mu$m image spacing. The vessels were segmented using the segmentation toolkit `ilastik`, based on interactive training and a random forest pixel classification, which incorporates 3D intensity, edge, and texture information with variable smoothing

[157, 158]. The segmented 3D vessel architecture was post-processed with custom-written codes to correct for artifacts and masked manually to exclude badly imaged tissue due to blurring on the edges of the field of view.

To emulate the voxel placement in realistic MRI acquisitions, the post-processed SPIM image volumes were subdivided into 3D matrices of macroscopic cubes with $0.5\,\text{mm}$ side length, representing virtual MRI voxels. The capillary centerline centroids in each imaging plane and voxel were used for a Voronoi tessellation [159], subdividing the tissue planes into polygons vaguely representing oxygen supply regions. Geometric properties of the Voronoi polygons and nearest neighbor distances of capillary centerlines were used to make Γ estimates for each imaging plane and virtual MRI voxel, following the original methodology of Karch et al. [152], by comparing with the statistical properties of simulated 2D-OCP realizations.

This was done for three healthy mouse brains and six entire glioblastoma xenografts from the U87MG tumor cell line [49]. The automated pipeline estimated $27\,489$ Γ values in healthy brain tissue and $18\,209$ values entirely within solid tumors. The resulting sample means with standard errors were $\langle \Gamma_H \rangle = 4.9 \pm 0.4$ in healthy tissue and $\langle \Gamma_G \rangle = 2.1 \pm 0.4$ in glioblastoma. It should be noted that the virtual MRI voxels from healthy tissue included partial volume effects of white and grey matter and different brain regions, without any specific placement or usage of a brain atlas. Tumor voxels used for analysis were made sure to lie entirely within tumor tissue, as marked by trained radiologists by manual mask drawing.

It was found that the 2D-OCP model may facilitate an identification of tumor tissue within individual MRI voxels, based on an attribution of Γ values. A non-negligible overlap of estimated Γ value ranges in healthy and pathologic voxels (cf. **Fig. 4** of publication II) is expected to originate from specific brain regions, where healthy tissue naturally exhibits higher microvascular disorder, *e.g.*, covering different tissue type boundaries. Tumor detection based on estimated voxel Γ values is expected to improve by additionally considering voxel neighborhoods and anatomical location, tempering the effects of false positive classifications based on lower capillary regularity due to partial volume effects.

2.2.3 Publication III

The findings of publication I, that varying vessel radius distributions and the capillary regularity have similar effects on transverse relaxation, which are not separable based on the cylindrical vessel model, motivated the search for a more comprehensive picture of real microvasculature for NMR modeling. The laser scanning microscopy data used in publication II visually suggested that tumor-induced vascular remodeling did not only affect the spatial distribution of capillaries but also the individual vessel geometry.

As has been found in previous studies, the orientational anisotropy of microvessels is altered locally through tumor growth [160], while bifurcation angles, hierarchical diameter scaling, and fractal properties can also be changed [83, 161–166]. Vessel radii and tortuosity are typically elevated but individual manifestations are various and depend on tumor type, malignacy, stage, and region [23–25, 146, 167].

Extending the codes written for the numerical processing of 3D fluorescence microscopy data to estimate Γ values for real tissue in publication II, the determination of a range of geometric parameters of the vasculature was implemented to characterize the ground truth data. In publication III, the created code base is presented with several possible applications, including the investigation of tumor growth (reusing the raw data from publication II), comparison of vascular geometry in different brain regions, and fundamental developmental studies. The quantitative parameters determined for arbitrarily shaped (masked) tissue volumes included fractional vessel volume fVV (CBV in intracranial applications), microvascular density MVD (number of vessel segments per unit tissue volume), vessel surface area density ρ_A (lumen surface per unit tissue volume), and vessel length density ρ_L (total vessel length sum per unit tissue volume). These scalar measures quantify the perfusion density of tissue volumes.

In addition, the segmented vasculature was subdivided into vessel branches, *i.e.*, individual segments between branching or end points, which can be approximated by separate, tube-like geometries. Each vessel segment was labeled and characterized with the following measures: mean radius $\bar{r}$, branch length l, segment surface area A, and tortuosity τ. The tortuosity $\tau = l/d$ was determined as a simple measure of vessel curvature using its length l and end point separation d [168]. The lumen area A was calculated from finite elements using a mesh obtained from the 3D intensity gradients of the segmented image volumes. The nontrivial estimation of vessel radii for realistic, warped structures was implemented as a custom-developed combination of two methods, described in the Supplementary Material of publication III (see Supplemental Methods and **Supplemental Fig. 1**). The accuracy of radius estimates for different segment orientations was validated in the same material.

The automated quantification algorithms were implemented in a 3D tiling box manner. Arbitrarily shaped and large tissue volumes with auxiliary 3D masking, optionally including holes, are autonomously subdivided into cuboids of predefined dimensions (tunable depending on the resolution and the size of the imaged structures to enable sensibly fast processing). The cuboids are labeled sequentially and processed individually, optionally in random order, to enable so-called asymptotic analyses, where extremely large datasets can be partially quantified, preliminary results can be combined intermediately, and a convergence towards certain statistical distributions can be checked. The vessel properties within the cuboids are determined and artificially

divided segments through partitioning are recovered in a subsequent steps, combining the results from each segment piece. This allows for a characterization of large volumes in a parallel or sequential manner, according to the available computer hardware. Should processing be interrupted, the algorithm will pick up where left off in processing of the individual cuboids. Additionally, this method separately quantifies the vasculature within individual cuboids in analogy to the volume partitioning used in publication IIto emulate macroscopic MRI voxels.

With image data reused for different biological studies, the utility of the developed numerical toolkit was demonstrated with various SPIM datasets of mouse brains and embryos. This methodological paper was aimed at sharing the developed quantification algorithms with the research community, presenting its flexibility in different scenarios. Despite the availability of expensive licenses for several highly professional and versatile computer programs for the analysis of microscopy data to scientific standards, we decided to develop our own custom processing codes, specialized for our desired quantifications of vascular geometry in amorphous 3D vasculature. Considering the size of our datasets (several Gigabytes per acquisition in minimal 8-bit format, with several cubic millimeters of imaged tissue at single micrometer resolution, containing order $10^5 - 10^6$ vessel segments), resourceful and incremental processing needed to be implemented to enable analyses on standard PCs. My custom-developed Matlab code, presented in publication III, facilitated the aspired analyses on regular desktop computers with optional parallelization, with the processible image size being limited only by the addressable random access memory (RAM) available to Matlab.

2.2.4 Publication IV

The numerical processing pipeline introduced in detail in publication III was applied to large, intact cerebrovascular networks in a mouse model in publication IV. Without differentiating particular brain regions, the vascular geometry in six entire healthy brain hemispheres was compared with two distinct models of glioblastoma, namely from the U87 and the GL261 cell lines. All experimental animal data for this study had also already been acquired for previous investigations [48, 49]. The objective here was to extensively characterize the hallmarks of brain tumor microvasculature in order to identify individual aspects to focus on in the search for new models of the capillary architecture that could effectively discriminate healthy and cancerous brain tissue. To the best of my knowledge, this article presents the first-ever graph theoretical quantifications to this extent on real cerebrovascular networks in a mammal. These were the largest vascular networks quantified this comprehensively to date.

It was found that the capillary geometry in the studied tumor xenografts was so heterogeneous, that differences of the vessel segment geometry were difficult to

formulate from the grand statistical consideration of entire tumors. High heterogeneity and variance in different tumor regions smeared definite, local remodeling aspects to the point of dissipation in the statistical comparison with entire brain hemispheres. Only the perfusion density parameters fVV and MVD presented significant differences in the large statistical comparison of entire GL261 tumors with healthy brain tissue, whereas U87 tumors only exhibited significant differences within the tumor core. Notable differences of the statistics of individual vessel geometric properties were only observed between tumor cores and healthy brain tissue, while an inclusion of entire tumor volumes counterbalanced the differences in the core to resemble healthy statistics in total (see **Fig. 1, b-g** in publication IV). An explicit comparison of tumor cores with tumor peripheries was previously provided in publication III (see **Fig. 3** therein).

To augment the geometric quantifications of these cerebrovascular networks, I implemented a comprehensive topological characterization in addition to the numerical processing presented in publication III. This involved an automated mapping of the vascular network to an undirected graph, describing vessel segments as connections (edges) between branching and end points (nodes). The network topology was quantified with a wide range of fundamental measures, including the network size (number of nodes and edges), node density (per unit tissue volume), mean and maximum node degree (number of connections to a node), and clustering coefficients, which parametrize the interconnectedness of topologically neighboring nodes (see **Tab. 2** of publication IV for a summary).

The degree distributions exhibited nontrivial forms, because the networks were imaged at a resolution comparable to the radii and lengths of the smallest capillary segments (see **Fig. 1, d-e** in publication IV). This had a coarsening effect on the real networks, where bifurcations less than $\sim 3 - 5\,\mu$m apart were summarized into a branching node with degree $k > 3$ (whereas a simple bifurcation would have degree $k = 3$). In graph theory, adjacent nodes without an edge connection in between are again summarized into a single larger node [149], which resulted in high degree nodes with $k > 10$. Indeed, this makes sense in an analysis of large vascular networks, since branching points separated by distances shorter than the smallest vessel diameters can be considered as single intersection points in the context of a large network (see the discussion in publication IV).

To further study the network structure on larger length scales, a community unfolding algorithm was applied to the basic graphs to reveal hierarchical clustering structures and modularity within the networks. The employed Louvain algorithm [169] uncovered vessel communities by maximizing intra-community clustering with minimal inter-community connectivity. The communities were modeled as the nodes of a meta-network with weighted connections, determined by the number of basic inter-community edges (see

Fig. 3 of publication IV for illustration). Community structures were compared and their connectivity was characterized with similar topological measures as the basic networks. Additionally, the scaling of community size distributions, neighboring community degree relationships, and mean shortest paths and network diameters in a topological sense were analyzed (see **Fig. 4** and **Tab. 4** of publication IV).

All vascular networks presented interesting statistical distributions of node degrees k, exhibited scale-free network characteristics, following a power law $P(k) \sim k^{-\gamma}$ for high degrees. Mean clustering coefficients C also followed a power law scaling with node degrees k (see **Fig. 2** and **Tab. 2** of publication IV). All topological analyses indicated a rather slight deformation of network structure from healthy brain tissue to U87 tumors, but profound alterations in GL261 tumors. Tumor cores deviated from healthy vasculature most dramatically in virtually every aspect. Perhaps most notably, brain tumors were found to decompose large modular vessel communities of the healthy mouse brain (in publication IV, see **Fig. 3, b-d**), presumably affecting the brain oxygen regulation and neurovascular coupling [55, 139]. These findings are highly relevant for building advanced models of vascular networks for MRI modeling, especially when including hemodynamic effects and oxygen variations. The detrimental effects of tumor growth on the network topology may further help explain neurovascular uncoupling and aid a more reliable interpretation of BOLD fMRI aberrations for tumor diagnosis [26].

2.2.5 Publication V

After an extensive characterization of the real vascular networks imaged with high-resolution laser scanning microscopy in publications II, III, and IV, the focus is taken back to the influence of microvascular architecture on MRI. A fast and effective numerical implementation of the dephasing process for arbitrary susceptibility distributions in 3D was custom-written in `C++` with local CPU multithreading using OpenMP (see https://www.openmp.org/). The simulations incorporate water diffusion in the extravascular space for arbitrary virtual voxel dimensions with cuboid shape, with the possibility to calculate spin dephasing during FID, gradient echo, and spin echo measurements with optional field gradient pulses, *e.g.*, for diffusion weighting. The focus in publication V remained on dephasing during T_2' weighted MRI acquisitions, motivated by the theoretical studies summarized in section 1.2.4 and for direct comparability with publication I.

To enable large-scale imaging simulations in feasible time frames, a numerical framework was written for Unix-type operating systems using Bash shell scripting and Python 3 (see https://www.python.org/) for an orchestration of virtual voxel processing from large, masked 3D datasets, as were analyzed in publications II - IV. A 3-level hierarchical parallelization scheme was developed for quick deployment of highly parallelized and

automated analyses on high performance computing (HPC) systems, conducting NMR simulations and vessel quantifications in matching virtual MRI voxels with variable dimensions (see **Fig. 1** of publication V). The calculations were conducted on the tier 3 HPC cluster "bwForCluster MLS&WISO Production", generously supported by the state of Baden-Württemberg through the bwHPC and bwHPC-C5 projects, as well as the German Research Foundation (Deutsche Forschungsgemeinschaft, DFG) with grant INST 35/1134-1 FUGG and extensions thereof. I applied for access to this cluster shortly after beginning this doctoral project in order to enable the planned research activities.

Custom bash scripts were written to invoke the scheduling system of the compute cluster for parallel processing of individual microscopy datasets according to availability of computational power. The message passing interface (MPI) [170] was implemented for a parallelized treatment of virtual MRI voxels from each dataset across different compute nodes, as specified flexibly by the user. The cores of each node were further exploited fully through multithreading in the dephasing simulations and parallelization of quantification and field calculation steps in Matlab (see **Fig. 1** of publication V for a graphical summary). Following an automated partitioning of each 3D dataset, intra-voxel off-resonance distributions were calculated through an efficient convolution in Fourier space, serving as the basic input to the `C++` dephasing simulations, similar to previous implementations [171, 172]. Different fit models were applied to dephasing attenuation curves from each virtual voxel to produce fit parameter sets for all tissue groups. The available SPIM datasets of the healthy mouse brain, U87, and GL261 glioblastoma were processed this way.

The fit parameters from simulated dephasing curves were used to test the feasibility of classifying the voxel signal to differentiate healthy brain tissue from glioblastoma tissue with different virtual voxel sizes. Support vector machine (SVM) classifiers were created with varying numbers of training signals, which were altered to produce so-called learning curves. These curves showed the classification accuracy, sensitivity and specificity in dependence on the number of training signals. Training and prediction testing was conducted with separate image datasets from different mice, with permutations in prediction data and training data. This proof-of-principle study yielded promising results despite limitations in the amount of data availability as well as imaging and segmentation quality differences between mice. Even with bad signal-to-noise ratios of the NMR signal, good classification accuracies well above 70% were reached. In the range of testing, with 100 - 400 μm side length, larger voxels facilitated better classifications, whereas the GL261 tumors were generally better detected (cf. **Figs. 2** and **4** of publication V). The results were motivating, considering that there was no information about the voxel origins, nor any voxel neighborhood comparisons.

The numerical simulations implemented in 2D for publication I, as well as the more general 3D simulations implemented for publication V were both validated using the well-understood Krogh model with the exact analytical solution of the FID evolution [13]. Different model geometries were created in 2D and 3D with specific cylinder radii and tissue volume fractions in the physiological range. Numerical simulation results were compared with exact solutions in each case, considering the magnetization magnitude and phase evolution. The temporal and spatial discretization error estimates implemented with the simulation allowed for a quick determination of sufficient time step and field lattice spacings for an excellent agreement of the numerical simulations with the exact solutions for each model geometry (see Supplemental Fig. S1 of publication V). The time step discretization and field grid spacing for simulations with real capillary networks was chosen using an analogous error estimation for general geometries, implemented with the `C++` simulations.

3 Publications

In this chapter, the original articles are reproduced with kind permission from the respective copyright holders and publishers, with supplementary information included for the sake of completeness. The article formats are retained in their original forms, while supplemental material is partially reformatted for better referencing within this thesis.

Publication I:
Microvascular regularity influence
on transverse relaxation

Title: The influence of spatial patterns of capillary networks on transverse relaxation

Authors: Felix T. Kurz, Christian H. Ziener, Martin Rückl, <u>Artur Hahn</u>, Volker J. F. Sturm, Ke Zhang, Lukas R. Buschle, Martin Bendszus, Sabine Heiland, Heinz-Peter Schlemmer, Wolfgang R. Bauer and Thomas Kampf

Contributions: F.T.K., C.H.Z., and T.K. conceptualized this study. A.H., M.R., V.J.F.S, K.Z., and T.K. collaboratively wrote numerical tools and simulations for data production and analysis. F.T.K., C.H.Z., M.R., L.R.B., and T.K. conducted analytical work. F.T.K., C.H.Z., M.R., A.H., and T.K. wrote the manuscript with contributions from M.B., S.H., HP.S., and W.R.B. All authors contributed to proof-reading and revisions.
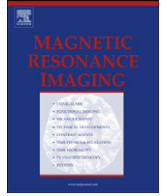
Original contribution

The influence of spatial patterns of capillary networks on transverse relaxation

F.T. Kurz [a,b,*,1], C.H. Ziener [a,b,1], M. Rückl [c], A. Hahn [a], V.J.F. Sturm [a,b], K. Zhang [a,b], L.R. Buschle [a,b], M. Bendszus [a], S. Heiland [a], H.P. Schlemmer [b], W.R. Bauer [d], T. Kampf [e,f]

[a] Heidelberg University Hospital, Department of Neuroradiology, Heidelberg, Germany
[b] German Cancer Research Center, Radiology E010, Heidelberg, Germany
[c] Humboldt University Berlin, Department of Physics, Berlin, Germany
[d] University Hospital Würzburg, Department of Internal Medicine I, Würzburg, Germany
[e] University Hospital Würzburg, Division of Neuroradiology, Würzburg, Germany
[f] University of Würzburg, Department of Physics V, Würzburg, Germany

ARTICLE INFO

ABSTRACT

Tissue-inherent relaxation parameters offer valuable information about the arrangement of capillaries: in an external field, capillaries act as magnetic perturbers to generate local inhomogeneous fields due to the susceptibility difference of deoxygenated blood and the surrounding tissue. These field inhomogeneities influence the free induction decay in a characteristic way, and, conversely, the above tissue parameters can be recovered by multi-parametric fits of adequate theoretical models to experimentally sampled free induction decays. In this work we study the influence of different spatial patterns of capillary positions on the free induction decay. Starting from the standard single capillary approximation (Krogh cylinder) for a symmetric array of capillaries, the free induction decay is analyzed for increasingly random capillary positions, using a previously described Gibbs point field model. The effects of diffusion are implemented with a flexible and fast random walk simulation. We find that the asymmetric form of the obtained frequency distribution is more robust against variations of capillary radii than against shifts of capillary positions, and further that, for an inclusion of diffusion effects, the single capillary approximation models the uniform alignment of capillaries in the hexagonal lattice to great accuracy. An increase in randomization of capillary positions then leads to a significant change in relaxation times. This effect, however, is found less pronounced than that of changes in the off-resonance field strengths which are controlled by the oxygen extraction fraction, thus indicating that observed changes in BOLD imaging are more likely to be attributed to changes in oxygenation than to capillary alignment.

© 2017 Elsevier Inc. All rights reserved.

1. Introduction

The quantitative evaluation of subtle tissue changes that involve microscopically small structures such as capillaries and cells is useful in assessing the form, extent and dynamic change of pathophysiological processes that are usually well below the resolution of MR scanning devices in clinical routine. For example, Karch et al. demonstrated a relationship between the degree of irregularity of capillary arrangements in cardiac tissue and some cardiac pathologies [1]. Likewise, techniques that are based on the BOLD

(blood oxygen level-dependent) effect [2] can be used to evaluate microstructural changes that are associated with hemodynamic and metabolic pathology-related alterations in brain tissue (see [3] for a review of some theoretical models). The range of applications is large and stretches from diagnostic to monitoring and even therapeutic purposes [4,5]. With regard to magnetic resonance imaging it is therefore important to know how much information about microstructural patterns in a voxel can actually be extracted from the corresponding MR signal.

On a microscopic scale, two intrinsic tissue properties dominate the MR signal decay: the spatial pattern of magnetic susceptibility inclusions in the tissue (e.g. the arrangement of capillaries in muscle tissue that contain blood with paramagnetic properties [2]), and the mobility of spins that surround these susceptibility inclusions. The first effect can be described in terms of a local Larmor frequency $\omega(\mathbf{r})$ that encodes information about the shape of the microscopically small

magnetic perturbers (which generate local magnetic field inhomogeneities in an external field). The second effect is usually modeled as a diffusion process that is characterized by the diffusion coefficient D and boundary conditions that are imposed by the spatial arrangement of the perturbers. The time evolution of the local transverse magnetization is then determined by the solution of the Bloch-Torrey equation (see below) that takes into account both susceptibility and diffusion effects [6]. For capillary networks, several deterministic analytical models about MR signal behavior were brought forward recently [7–13], see also [14] and references therein. Most approaches accurately describe the limiting regimes of static dephasing, where diffusion effects are negligible, and the regime of strong diffusion effects: the motional narrowing limit (see also [15,16]). They either rely on assumptions on the spin phase distribution [8], an approximation of the NMR signal in weak fields [9], second order perturbation theory for low diffusion effects [10], or stochastic approximations of diffusion-mediated field fluctuations [17]. One recent approach provides a solution of the Bloch-Torrey equation for the specific spatial pattern of symmetrically positioned capillaries [12,13] that is based on a single capillary approximation in analogy to Krogh's cylinder model [18]: in this geometrical model, it suffices to study (restricted) diffusion in the Krogh cylinder around one capillary. The Krogh model divides the biological tissue into independent parallel cylindrical unit cells that each host one capillary in their center. This necessarily leads to a loss of structural information, see also Fig. 1. It was shown recently, however, that the signal evolution of the magnetization inside a unit cell differs for quadratic and circular shapes [19]. In addition, the single capillary approximation may be adequate for some tissues (e.g. muscle tissue [20–22]), but most tissues do not display a uniform regular capillary position arrangement (e.g. the heterogeneous construction of a capillary supply network for pathological tumor growth [23], brain capillaries [14] or pathology-related capillary arrangements in cardiac tissue [1]).

In this work, we numerically evaluate and compare the influence of simplified model geometries on the frequency distribution in one MR voxel for square lattices, hexagonal lattices, the Krogh model and, eventually, the transition towards irregularly arranged capillaries (termed plasma) with the help of an entropy point field model that was proposed recently [24]. The effects of diffusion of spin-carrying particles are implemented with a random walk simulation. We show that irregular patterns of capillaries have a substantial influence on transverse relaxation times.

2. Methods

In this work, capillary arrangement patterns that cover the whole tissue space are assumed as being either based on a square lattice, a hexagonal lattice or a random positioning of capillaries (multi-capillary models; Fig. 1b–d), whereas the Krogh model represents the single capillary approximation where the study of the whole capillary network is reduced to the study of axial spin diffusion inside the concentric Krogh cylinder around one capillary (see also Table 1 for a comparison of capillary-tissue volume fractions and capillary densities in the different geometries). The volume elements in which dephasing processes of spin-carrying particles occur are then aligned as either quadratic prisms or hexagonal prisms (as in the cross-section of a face-centered cubic Bravais lattice), see Fig. 1c,d. This prevents remaining residual space between volume elements. Here, we only consider the two-dimensional planes of capillary cross-sections (see Fig. 1a–b); however, the results can easily be generalized to three dimensions and are the same as long as the capillaries remain parallel. This assumption may be reasonable for muscle tissue [22], yet, in the Krogh model, a (spatially equally distributed) randomization of vessel orientations can be achieved by considering the integration of the local frequency over the distribution function of the tilt angle β for randomly oriented cylinders, i.e. $\sin(\beta)/2$ (see also Section 3.5 below). In the following we will briefly introduce the Krogh model and its implications on the frequency distributions for static and dynamic dephasing processes. We will then evaluate the frequency distributions for square and hexagonal lattices to compare them with that of the Krogh model for different volume fractions.

2.1. Single capillary approximation: the Krogh model

The transition to the Krogh model or single capillary approximation consists in replacing the quadratic and hexagonal prisms with cylinders of equal volume, see Fig. 1e–g. In this process, neighboring
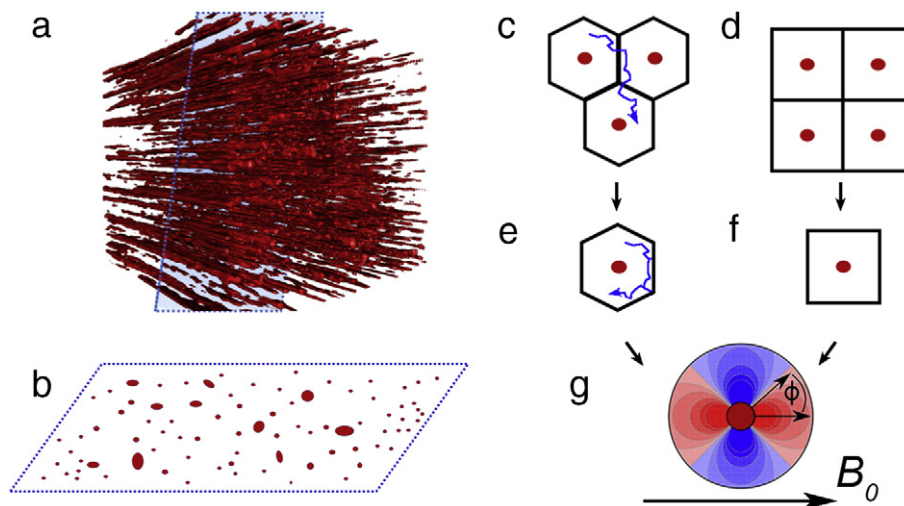

Fig. 1. Capillary arrangement patterns for biological tissue. (a) Microscopic blood vessels in the brain cortex, provided courtesy of B. Tews, National Center for Tumor Diseases, Heidelberg, Germany. (b) Schematic view of the cross section area (dotted blue line in (a)) with a random arrangement of capillary positions with variable radii. (c–d) Simplified spatial pattern of the capillaries in (b) in a hexagonal lattice (c) and a square lattice (d): the underlying assumption is that bulk tissue can be divided into simple, uniform and independent unit cells that each contain a single capillary. (e–f) Simplification steps for the transition of the hexagonal and the square lattice to the Krogh model: diffusion of magnetization between the unit cells is modeled by reflective boundaries of the unit cells (exemplified in the blue trajectory for the hexagonal lattice). (g) The unit cell in the Krogh model is simplified as a cylinder that co-axially surrounds a cylindriform capillary with radius R_C. The two-dimensional dipolar off-resonance field, as given in Eq. (1) with polar coordinates (r, ϕ), is portrayed in the Krogh cylinder with red (positive) and blue (negative) field portions.

Table 1
Capillary volume fraction η for different spatial patterns of capillary arrangements. R_D: radius of the Krogh cylinder (see below or Fig. 1g), ICD: intercapillary distance; for the two-dimensional one-component plasma (2D-OCP; see below): A = area of the simulation box, m = number of capillaries within the simulation box.

	Capillary volume fraction η
Square lattice	$\frac{\pi R_C^2}{\text{ICD}^2}$
Hexagonal lattice	$\frac{2\pi R_C^2}{\sqrt{3}\text{ICD}^2}$
Krogh model	$\frac{R_C^2}{R_D^2}$
2D-OCP	$\frac{m\pi R_C^2}{A}$

cylinder surfaces necessarily overlap and should thus be considered as mathematical entities and not as actual physical boundaries. A detailed explanation and justification of this approach is detailed in Refs. [25–27]. The Krogh model assumes that the tissue is built of independent parallel cylindrical unit cells, each containing a coaxial single blood filled cylindrical capillary (Fig. 1g) that supplies the unit cell with oxygen and nutrients. In an external magnetic field, each capillary then induces the local off-resonance field [28]

$$\omega(r,\phi) = \delta\omega \, R_C^2 \frac{\cos(2\phi)}{r^2} \tag{1}$$

in the surrounding supply area where diffusion and dephasing of the magnetization take place, with polar coordinates $\mathbf{r} = (r, \phi)$ in a plane perpendicular to the capillary axis. The capillary radius is denoted as R_C and $\delta\omega = \omega(r = R_C, \phi = 0)$ is the characteristic frequency shift on the surface of the capillary. The transverse dynamic magnetization (in complex notation), $m(r, \phi, t) = m_x(r, \phi, t) + im_y(r, \phi, t)$, can eventually be obtained as the solution of the transverse part of the Bloch-Torrey equation [6]:

$$\frac{\partial}{\partial t} m(r, \phi, t) = [D\Delta - \mathrm{i}\,\omega(r,\phi)]\, m(r, \phi, t), \tag{2}$$

and the measurable MR signal of the transverse magnetization $M(t)$ follows as

$$M(t) = \int_V \mathrm{d}^3\mathbf{r}\, m(r, \phi, t) \tag{3}$$

$$= \int_{-\infty}^{+\infty} \mathrm{d}\omega\, \rho(\omega) \mathrm{e}^{\mathrm{i}\omega t}, \tag{4}$$

where $\rho(\omega)$ is denoted as the frequency distribution

$$\rho(\omega) = \frac{1}{V} \int_V \mathrm{d}^3\mathbf{r}\, \delta(\omega - \omega(\mathbf{r})), \tag{5}$$

with $\delta(\omega)$ as the Dirac-Delta function and dephasing volume V. The application of the single capillary approximation in this case is meaningful since it allows a closed-form solution of the Bloch-Torrey Eq. (2) in terms of an eigenfunction expansion [12,13]. With the help of such a solution, fundamental effects of spin dephasing in a dipole field can be investigated and understood. We provide further details about this solution and its computational implementation in Appendix A. It will be used to evaluate the accuracy of the random walk algorithm by comparing theoretical and simulated free induction decay in the Krogh model (see Section 3.3).

If diffusion is negligible, then $\rho(\omega)$ corresponds to the local Larmor frequency distribution, and, within the Krogh model, an analytical expression can be given as [29]:

$$\rho(\omega) = \begin{cases} \frac{\eta}{1-\eta}\, \frac{\delta\omega}{\pi\omega^2} \sqrt{1 - \left(\frac{\omega}{\delta\omega}\right)^2} & \text{for } |\omega| \geq \eta\delta\omega \\ \frac{\eta}{1-\eta}\, \frac{\delta\omega}{\pi\omega^2} \left[\sqrt{1 - \left(\frac{\omega}{\delta\omega}\right)^2} - \sqrt{1 - \left(\frac{\omega}{\eta\delta\omega}\right)^2} \right] & \text{for } |\omega| \leq \eta\delta\omega \\ 0 & \text{for } |\omega| > \delta\omega, \end{cases} \tag{6}$$

where capillary volume fraction $\eta = R_C^2/R_D^2$ and R_D represents the radius of the Krogh cylinder. Generally, single spins can diffuse from one supply area to the next one (see Fig. 1c). This problem is met with reflecting boundary conditions that are imposed on the outer boundary of the supply cylinder [30], see Fig. 1e. Reflecting boundaries are also imposed on the surface of the capillary as is common practice in theoretical modeling [26,31].

However, the radial symmetry of the original Krogh model is broken by the angular dependence of the off-resonance field (see Eq. (1) and Fig. 1). Furthermore, the reduction to one single capillary neglects the contribution of the surrounding capillaries on the off-resonance field in the original supply volume, see also [32]. While typically small volume fractions $\eta \lesssim 0.1$ for some biological tissues may justify this neglection [7,26], both issues (angular symmetry and neighboring capillary contribution) can lead to serious problems when reassembling the bulk signal from the signal of the independent unit cells.

2.2. Multi-capillary model

In contrast to the single capillary model, the multi-capillary model assumes that the tissue is build up from (rectangular) unit cells containing a single or multiple capillaries. The unit cell is supposed to be aligned with the capillaries to allow the reduction of the problem to two dimensions, as discussed above. Each of the unit blocks contains the same number of capillaries with the same spatial distribution. In order to meaningfully represent bulk tissue by a single unit cell, Eq. (2) has to be solved with periodic boundary conditions. This requires a periodic behavior of both, diffusion and off-resonance field, see also Appendix B and Fig. 2. The specific properties of the microstructure are given by the capillary distribution inside the unit cell. For the highly regular square or hexagonal lattice we can use a simple unit cell that contains only one or two capillaries, respectively. However, for irregularly arranged capillary positions, it is necessary to account for a larger number of capillaries inside the unit cell to ensure sufficient statistical averaging.

2.2.1. Unit cell tilt for square and hexagonal lattices

As the tissue is build up from rectangular unit blocks, the off-resonance field of a single capillary can be written as (in Cartesian coordinates)

$$\omega(x, y) = \delta\omega \, R_C^2 \frac{[x^2 - y^2]\cos(2\alpha) - xy\sin(2\alpha)}{[x^2 + y^2]^2}, \tag{7}$$

where α is the tilt angle of the external magnetic field B_0 against the x-axis of the coordinate system, see also Fig. 2. For non-zero tilt angles α, the field at the border between two unit cells becomes discontinuous; however, by including the (long-range field) contributions of the surrounding capillaries, the off-resonance field becomes periodic. Further details can be found in Appendix B.1.

In our simulations, we first calculated fields in a unit cell of size 15.36μm × 15.36μm with a resolution of $\Delta x = 0.02$μm with off-resonance field frequency distribution $\rho(\omega)$ from Eq. (5). Capillary
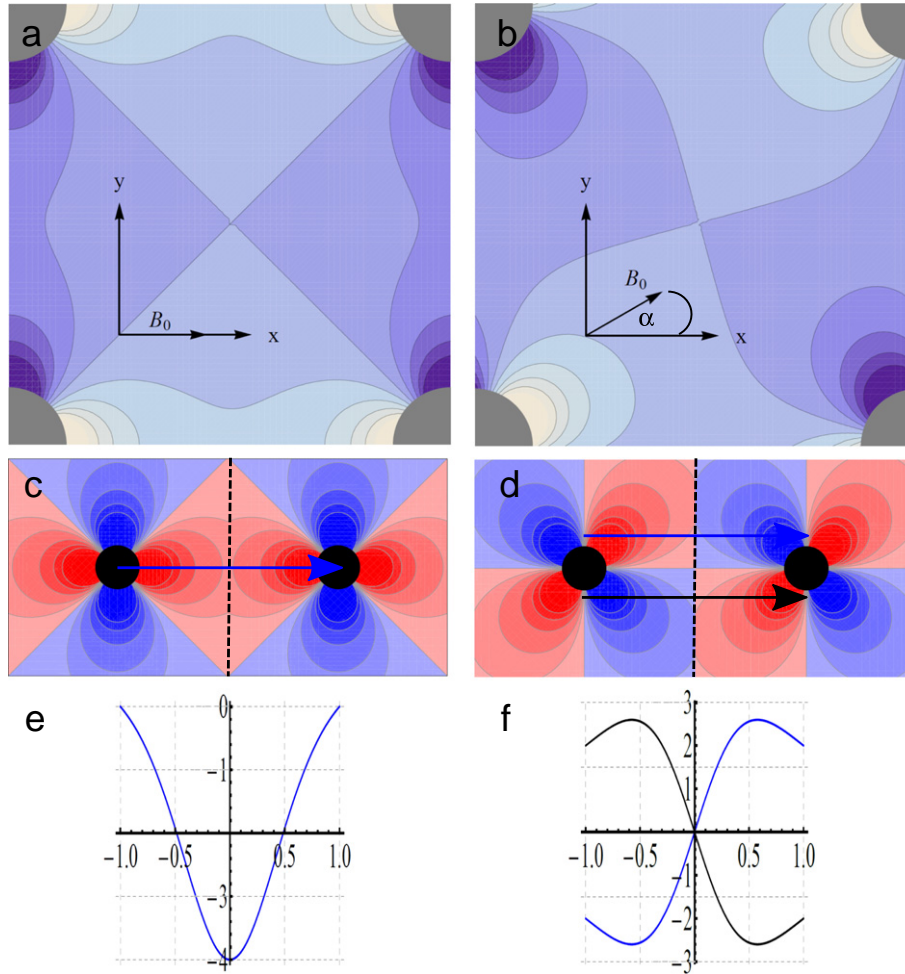
Fig. 2. Influence of the tilt angle α of a unit cell (or simulation box) against the external field B_0. (a–d) Off-resonance field distribution for zero tilt $\alpha = 0°$ (a) and a tilt of $\alpha = 30°$ (b) between capillaries in a square lattice. (c–f) Schematic field representation for two capillaries in a square lattice. The field at the border between the unit cells is continuous for a zero tilt (c,e), but not so for the tilted unit cell (d,f); in the latter case it changes the sign of ω (y-axis in (e,f)) as a trajectory of a spin-carrying particle crosses the border from one capillary at -1 to the capillary at $+1$ (represented by the arrows in (c,d)). For $\alpha = 0°$, the field at the border of a unit cell that hosts one capillary is continuous, though its normal derivative is not (see blue arrow in (c) and corresponding curve in (e)). The field then becomes discontinuous for $\alpha > 0°$ (here: $\alpha = 45°$): the black and blue curves in (f) represent the black and blue arrows in (d), respectively. This problem is circumvented by including the contributions of the surrounding capillaries. The off-resonance field is then periodic at the boundaries of a unit cell (see also Appendix B).

radii were chosen such that volume fraction $\eta = 0.05$ (see also Table 1 for a comparison of the capillary volume fractions within the four model geometries). Rectangular unit cells bases with area $|\mathbf{a}_1| \cdot |\mathbf{a}_2|$ then produce $N = |\mathbf{a}_1||\mathbf{a}_2|/\Delta x^2$ area elements where the areas inside of capillaries were not considered (in line with previous works, see e.g. [14] and references therein), such that off-resonance distributions could be constructed from $N' = N[1 - \eta]$ points (square lattice: $N' \approx 560,000$, hexagonal lattice: $N' \approx 325,000$), see also Fig. 18 in Appendix B. Tilt angles α were evaluated in steps of $1°$ from $0°$ to $45°$. Higher tilt angles follow from symmetry considerations (see also the Results section). Further details about the field calculation are provided in Appendix B.

2.2.2. Two-dimensional one-component "plasma" as a descriptor of irregular capillary positions

The irregularity of capillary positions changes the off-resonance field distribution significantly, see Fig. 3. It can be quantified through a recently proposed model by Karch et al. [24] who used a Gibbs point field model to interpret the irregular pattern of capillaries. Briefly, in this model, the capillary arrangement is allocated a "potential energy" that is lowest for a purely uniform arrangement (in a hexagonal lattice) and increases for deviations from this state. To

continue this analogy to statistical mechanics, changes in capillary constellations can then be considered as "thermal" disturbances of a system of identical point charges (capillaries) that exhibit a weak repulsive interaction. Thus, capillaries arrange like charged particles in a two-dimensional one-component plasma (2D-OCP) (see also [33,34]). In such a picture, the potential energy $\phi_{ij}(r)$ between two point charges (with charge q each) at points $\mathbf{r}_i$ and $\mathbf{r}_j$ is given as

$$\phi_{ij}(r) = -q^2 \ln(r_{ij}/L),\tag{8}$$

where $r_{ij} = |\mathbf{r}_i - \mathbf{r}_j|$ is the distance between the charges and L an arbitrary scaling length. The equilibrium state of the plasma can then be characterized by a single dimensionless constant

$$\Gamma = \frac{q^2}{k_B T},\tag{9}$$

where k_B represents the Boltzmann constant. The parameter Γ is thus a measure of the "thermal" disturbance of the whole system due to its temperature T. In this model, the system state at $T = 0$ corresponds to the state where the sum of potential energies between all system point charges is minimal, i.e. a perfectly uniform alignment
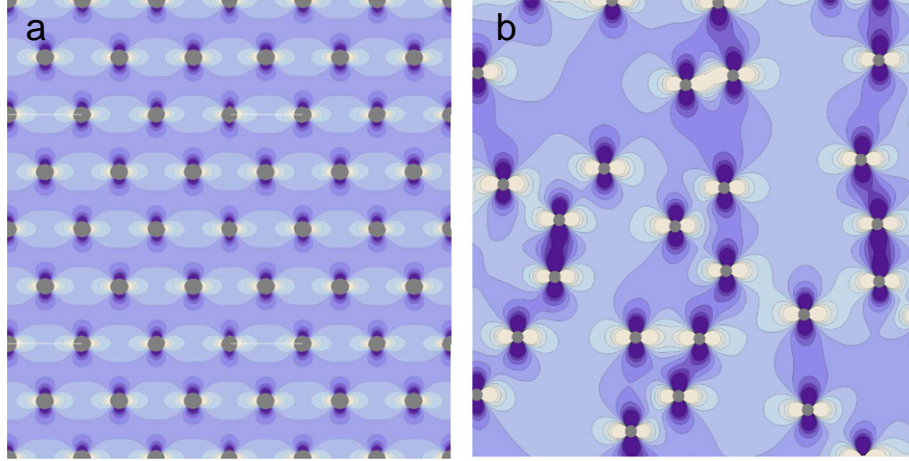
Fig. 3. Off-resonance field distribution for the transition from (a) regular capillary positions in a hexagonal lattice to (b) an irregular capillary position pattern in a two-dimensional one-component "plasma" (2D-OCP). The degree of irregularity can be characterized through one single parameter Γ [24]: high values of Γ signify highly ordered (symmetric) spatial patterns (Γ = ∞: maximum regularity), whereas low values of Γ correspond to a significant "disturbance" of the regular arrangement.

of capillaries. When $T > 0$, the system deviates from the potential energy minimum, and for $T \to \infty$ or $\Gamma = 0$, the system corresponds to a purely random capillary arrangement. To determine the "potential energy" U of a system of N capillaries, i.e. of N particles in the Gibbs point field model, in a unit cell spanned by vectors $\mathbf{a}_1$ and $\mathbf{a}_2$, we follow the methodology proposed in Karch et al. and apply Ewald's method of separating the potential energy U into terms with short-range and a long-range interactions such that [24,34]

$$U = \sum_{i=1}^{N-1} \sum_{j=i+1}^{N} \phi_{ij}(r_{ij}) \tag{10}$$

$$= \frac{q^2}{4} \sum_{\mathbf{n}} \sum_{i,j}^{N} {}' E_1\left(\zeta^2[\mathbf{r}_{ij} + \mathbf{n}]^2\right)$$

$$+ \frac{\pi}{A} \sum_{\mathbf{k} \neq 0} \frac{\exp\left(-\frac{|\mathbf{k}|^2}{4\zeta^2}\right)}{|\mathbf{k}|^2} \left| \sum_{j=1}^{N} \exp(\mathrm{i}\,\mathbf{k}\mathbf{r}_j) \right|^2 + U_{\mathrm{const}} . \tag{11}$$

The first term in this sum represents the short-range interaction energy contribution to the potential energy, with exponential integral

$$E_1(z) = \int_z^\infty \frac{\exp(-x)}{x} \, \mathrm{d}x , \tag{12}$$

and the summation index $\mathbf{n}$ running over all lattice vectors $\mathbf{n}$ with $\mathbf{n} = n_1 \mathbf{a}_1 + n_2 \mathbf{a}_2$, $n_1, n_2 \in \mathbb{N}$. The prime indicates that the term for $i = j$ is excluded for $\mathbf{n} = (0,0)$. The parameter ζ represents an adjustable parameter that controls the rate of convergence of the two terms in Eq. (11); in analogy to [24], it was set to $\zeta = 6/b$ (b: side length of the simulation box). The second term represents the long-range (Coulomb) interactions as a sum in Fourier space over all (reciprocal) lattice vectors $\mathbf{k} = m_1 \mathbf{b}_1 + m_2 \mathbf{b}_2$, where $\mathbf{b}_1 = \frac{2\pi}{a_1}\hat{\mathbf{a}}_1$ and $\mathbf{b}_2 = \frac{2\pi}{a_2}\hat{\mathbf{a}}_2$ ($m_1, m_2 \in \mathbb{N}$, $\hat{\mathbf{a}}_i = \frac{\mathbf{a}_i}{a_i}$). The cutoff value in Fourier space was chosen as in [24]: $[|\mathbf{k}|/|\mathbf{k}|_{\min}] \leq 200$. Parameter A represents the area of the hexagonal simulation box. The last term U_{const} represents a possible energy contribution from a uniform background charge. The simulations were then performed by the Metropolis Monte Carlo method [35]. The change in potential energy, $\Delta U = U_{\mathrm{pre}} - U_{\mathrm{post}}$, during the variation in position of a single particle can be allocated the following probability

$$p(\Delta U) = \min\left(\exp\left(\frac{\Delta U}{T}\right), 1 \right) , \tag{13}$$

($k_B \equiv 1$ without loss of generality). If a modification of the system leads to a reduction in potential energy ($\Delta U \geq 0$), we find $p(\Delta U) = 1$, and the modification of the system is kept in the simulations. In contrast, an increase in potential energy ($\Delta U < 0$) leads to $0 \leq p(\Delta U) \leq 1$; with a random number $x \in [0,1]$ we accept the modification of the system for $x \leq p$ and reject it for $x > p$. The probability p to change into an energetically unfavorable configuration thus diminishes exponentially with larger energies. Eventually, the system reaches thermal equilibrium where only changes occur between microstates associated with one temperature T, i.e. Γ, that represents the macrostate.

Physiologically, the model is consistent in that it assumes that capillaries spatially distribute such that the oxygen supply of the surrounding tissue is maximized so that capillaries will predominantly grow in areas with lower capillary density and, therefore, will be distributed evenly in homogeneous tissue. One advantage of this model is its simplicity: only one single parameter Γ governs the degree of irregularity with $\Gamma = \infty$ corresponding to maximum
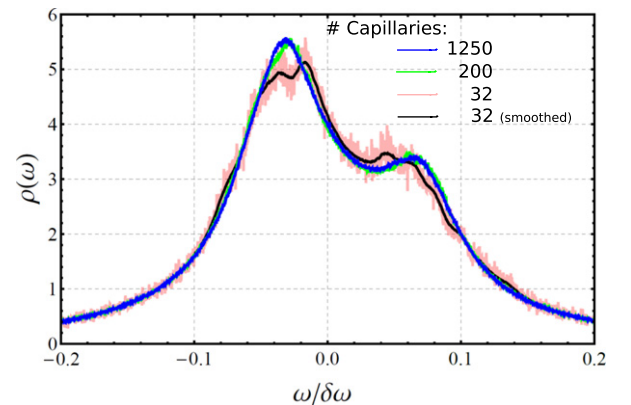

Fig. 4. Simulated frequency distributions for different numbers of capillaries. The distributions correspond to 32 capillaries (light red curve; smoothed as black curve), 200 capillaries (green curve) and 1250 capillaries (blue curve) are depicted for a standard deviation of 1μm of their positions around a regular arrangement, and $\eta = 0.05$. A substructure in the frequency distribution becomes apparent for the lowest number of capillaries due to the individual arrangement of capillaries. The curves demonstrate that there is no significant error to expect from a number of capillaries that is greater than 200, as used in [24] and in our simulations.

regularity. For instance, for capillaries in cardiac muscle tissue the Γ values were found to range between $\Gamma \approx 2$–5 [24].

Frequency distributions for the 2D-OCP were calculated according to Eq. (5). To circumvent artifacts that were generated by a too low number of capillaries within a simulation box, we tested constellations for different numbers of capillaries, see Fig. 4. Based on these results, we chose a lower threshold of 200 capillaries for the 2D-OCP, leading to unit cells of about 250μm × 430μm (ICD = 25μm).

The influence of individual capillary positions increases for a decrease in the total number of capillaries to end in the characteristic frequency distribution of a single capillary for one simulation box (similar to the shape of that for the (square and hexagonal) lattice and Krogh models). Boxes with only one (large) capillary were already studied extensively in [19,36].

2.2.3. Random walk model

To study the effects of different capillary arrangements, an efficient discrete-time continuous-space random walk was implemented. This implementation provides the necessary flexibility to adapt the algorithm to various boundary conditions, geometries, diffusion coefficients and off-resonance frequencies. Further details

about the implementation can be found in Appendix B.2. Briefly, a recursive search tree was used to detect collisions of random walk trajectories with capillary surfaces. The endpoints of steps into the capillary interior were then mirrored along the radial direction in accordance with Neumann boundary conditions. A similar treatment was implemented for the outer boundary of the simulation box; however, the outer boundary was either implemented as reflecting (of Neumann-type) for the Krogh model or cyclic (of inhomogeneous Neumann-type) for the square and hexagonal lattice as well as the 2D-OCP.

3. Results

3.1. Frequency distribution and free induction decay for regular spatial capillary patterns

For negligible diffusion effects $D \rightarrow 0$, i.e. in the limit of static dephasing, the frequency distribution of local off-resonance frequencies coincides with the Fourier transform of the free induction decay $M(t)$ [29]. For instance, an exact monoexponential decay is generated by a Lorentzian frequency distribution. Significant
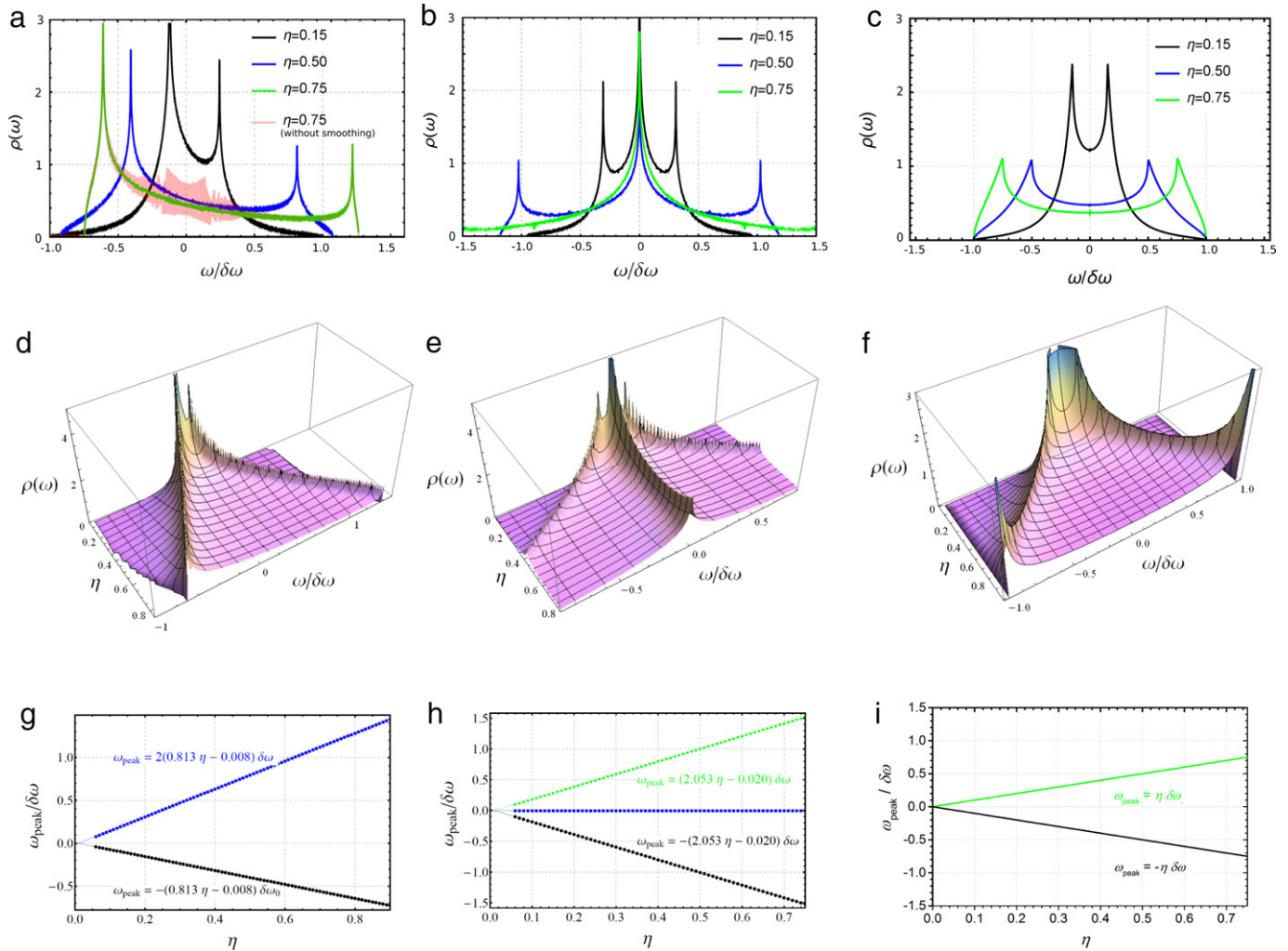
Fig. 5. Frequency distribution for the hexagonal lattice (a,d,g), the square lattice (b,e,h) and the Krogh model (c,f,i). (a–c) Frequency distributions for three different volume fractions $\eta = 0.15$ (black curve), $\eta = 0.5$ (blue curve), and $\eta = 0.75$ (green curve; non-smoothed curve in beige for the hexagonal lattice). The corresponding frequency distributions with a continuous dependency on volume fraction η are shown in the row below (d–f). (g–h) Positions of the peaks for the above distributions in dependence on η (blue, black and green dots) and corresponding curves (solid lines) based on empirical formulas (see main text). For the hexagonal lattice, two peaks are found that are located at approximately $\omega_1 \approx \frac{8}{5}\eta\delta\omega$ and $\omega_2 \approx -\frac{4}{5}\eta\delta\omega$. In the case of the square lattice, two peaks are symmetrically arranged around a major peak at $\omega_1 = 0$: these peaks are approximately located at $\omega_{2,3} \approx \pm 2\eta\delta\omega$ (h). The Krogh model exhibits two peaks at $\omega_{1,2} = \pm\eta\delta\omega$ according to Eq. (6).

changes in frequency distributions caused by different spatial capillary arrangements therefore reflect measurable changes in the free induction decay. In Fig. 5, the simulated frequency distributions for the hexagonal lattice, the square lattice and the Krogh model are given for the different volume fractions $\eta = 0.15, 0.5$, and 0.75 (Fig. 5a–c) and in a three-dimensional representation for volume fractions $\eta = 0.05 - 0.9$ (Fig. 5d–f; $\alpha = 0$). The maximum volume fraction for the square lattice (where $R_C = \text{ICD}/2$) is $\eta_{max} = \pi R_C^2/[4R_C^2] = \pi/4 \approx 0.78$, and for the hexagonal lattice (where also $R_C = \text{ICD}/2$) we find $\eta_{max} = 2\pi R_C^2/[4\sqrt{3}R_C^2] \approx 0.9$, see also Table 1 and [37]. While the peak positions within the frequency distribution for the Krogh model can be determined analytically as $\omega_{1,2} = \pm\eta\delta\omega$ (see Fig. 5c,f,i), i.e. symmetrically located around $\omega = 0$, distribution peaks for the square lattice model were numerically found at $\approx 2\eta\delta\omega$ (see Fig. 5b,e,h). For both lattices, numerical relations between peak frequency and volume fraction can be obtained (see Fig. 5g,h); the hexagonal lattice displays two peaks in the frequency distribution that are located at $\omega_1 = 2[0.813\eta - 0.008]\delta\omega$ and $\omega_2 = -[0.813\eta - 0.008]\delta\omega$, whereas the three peaks for the square lattice are located at $\omega_1 = 0$ and $\omega_{2,3} = \pm[2.053\eta - 0.020]\delta\omega$. Due to the superposition of fields of individual capillaries, the maximum off-resonance is always higher than $\delta\omega$, likewise for the hexagonal lattice. The latter shows artifacts in the low frequency range (Fig. 5a, pink curve) due to the specific regular field sampling along the interpolation lattice (see Appendix B). However, these discretization errors disappear for the simulation with dynamic dephasing since the random walk algorithm replaces the regular field sampling through random points.

Rotation of the lattices results in a dependence of the frequency distributions on the tilt angle α, as discussed above, see Fig. 6. For increasing $\alpha > 0$, the negative peak in the frequency distribution for hexagonal lattices splits into two peaks of which the peak closer to $\omega = 0$ approaches the positive peak with which it unites for $\alpha = 30°$, see Fig. 6a. For $\eta = 0.1$, the peak positions can then be determined numerically in dependence on the title angle α as $\omega_1 = 0.081\delta\omega\cos(2\alpha)$, $\omega_2 = [0.16\alpha - 0.04]\delta\omega$, and $\omega_3 = 0.081\cos(2[\alpha + \pi/3])$. The square lattice, however, keeps its symmetrically arranged peaks, see Fig. 6b, and one can provide their positions for $\eta \approx 0.06$ as $\omega_1 = 0$, $\omega_{2,3} = 0.11\cos(2[\alpha + \pi/4] \pm \pi/2)\delta\omega$. In both lattices, it suffices to only study tilt angles $\alpha = 0 \ldots 30°$ (hexagonal lattice) or $\alpha = 0 \ldots 45°$ (square lattice) due to the rotational symmetry of the field distribution; e.g., the frequency distribution of the hexagonal (square) lattice for $30°$–$60°$ ($45°$–$90°$) is the mirrored frequency distribution of 0–$30°$ (0–$45°$) around the ω-axis at $30°$ ($45°$) in Fig. 6.

3.2. Introduction of irregularity in capillary positions and radii

We first examined the influence of (normally distributed) deviations of capillary radii on the statistical frequency distribution for capillaries within a hexagonal lattice, see Fig. 7a. For a mean radius of $\mu_R = 1.94\mu m$, normal distributions were constructed with standard deviations σ_R that increased step-wise ($\Delta\sigma_R = 0.1\mu m$) from $\sigma_R = 0.1\mu m$ (black line in Fig. 7a) to $\sigma_R = 0.5\mu m$ (light gray line in Fig. 7a). Clearly, the characteristic peaks for purely uniform radii approach each other for increasing standard deviations of the radius distribution, but the distribution keeps its asymmetry. A similar effect, though more pronounced, was observed for capillaries with uniform radii in a hexagonal lattice whose positions were randomly displaced from their standard position, where the displacement followed a normal distribution with standard deviation $\sigma_P = 0$–$2.5\mu m$ that was step-wise increased with $\Delta\sigma_P = 0.5\mu m$ (ICD = $16.5\mu m$), see Fig. 7b. The resulting frequency distribution is similar to a Lorentzian distribution. A comparison of both effects may lead to the conclusion that deviations from uniform radii are less significant than deviations from the standard position in a regular lattice. Indeed, for a typical value of the thermal disturbance in the 2D-OCP for capillaries in
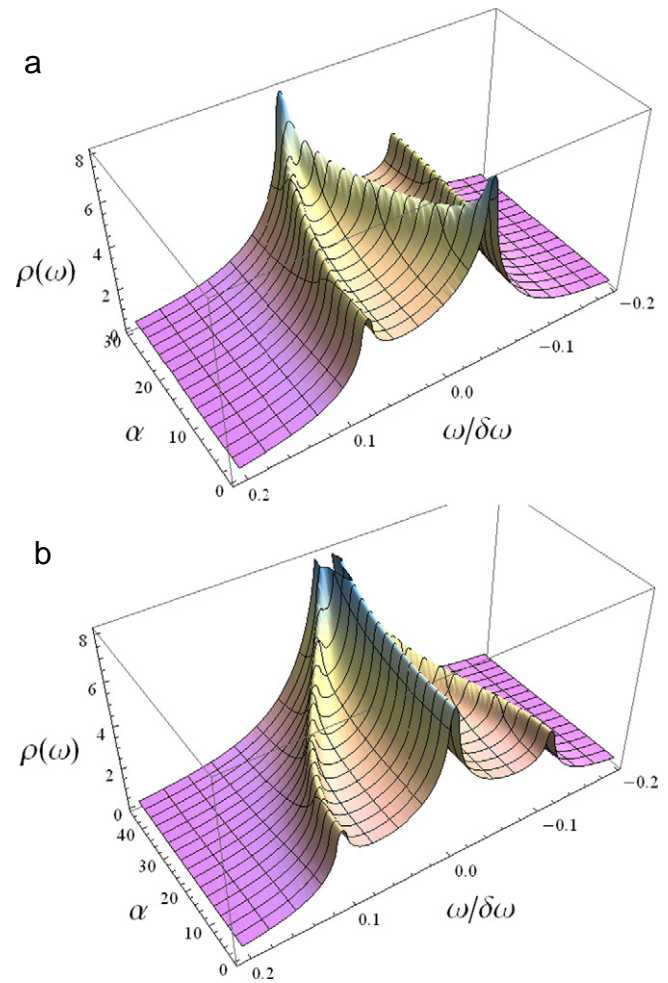

Fig. 6. Frequency distribution $\rho(\omega)$ in dependence on tilt angle α for a hexagonal lattice (a) and a square lattice (b). For the hexagonal (square) lattice, it suffices to only display tilt angles $\alpha = 0 \ldots 30°$ ($\alpha = 0 \ldots 45°$) due to the rotational symmetry. While the frequency distribution of the square lattice for increasing tilt angles α is symmetric around $\omega = 0$ where it maintains its main peak, the tilt in the hexagonal lattice produces an additional peak.

muscle tissue, $\Gamma = 4$ [24], and a normal distribution of radii around μ_R with $\sigma_R = 0.5\mu m$, the resulting frequency distribution is almost identical to that resulting for uniform radii μ_R, cf. the black and red lines in Fig. 7c. Based on this result, and owing to the fact that biological tissues are usually prone to small blood volume fractions $\eta < 0.1$ and rather small deviations of capillary radii in one imaging voxel [7,26], the following analysis uses uniform radii.

To further comprehend the effects of randomized capillary positions in the 2D-OCP, we obtained the frequency distributions in the static dephasing regime for different values of the parameter Γ between 2 and 800, see Fig. 8a (results were averaged over 10 realizations of the same 2D-OCP, each hosting 200 capillaries). As the plasma crystallizes in the hexagonal lattice structure, i.e. $\Gamma \to \infty$, the two (asymmetric) peaks of the hexagonal lattice frequency distribution are recovered (Fig. 5b). In the opposite limit, the frequency distribution of the plasma resembles that of a Lorentzian distribution (as in Fig. 7c). The transition point at which the asymmetric characteristic shape of the hexagonal lattice frequency distribution vanishes can be determined as $\Gamma \approx 140$, see the gray plane in Fig. 8b. Conversely, coming from a "heated" plasma with increased Γ values, the transition point represents a "crystallization" of the 2D-OCP. Naturally, as diffusion effects become important, this transition point
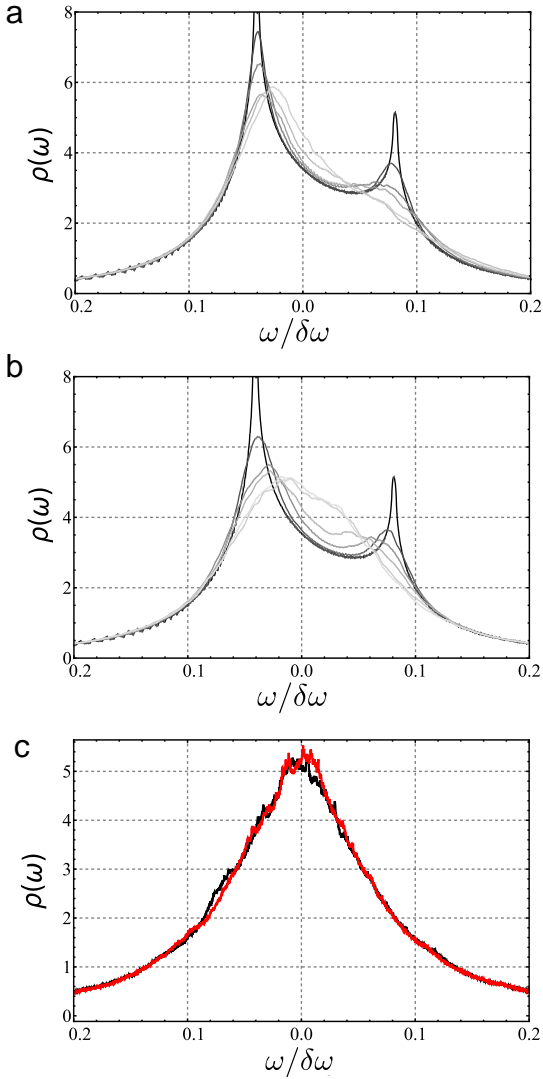
Fig. 7. Frequency distributions of the hexagonal lattice for (a) a normal distribution of capillary radii with mean radius $\mu_R = 1.94\mu m$ and a step-wise increase of the standard deviation ($\Delta\sigma_R = 0.1\mu m$) from $\sigma_R = 0.1\mu m$ (black line) to $\sigma_R = 0.5\mu m$ (light gray line); and (b) for a random displacement of capillaries around their initial position in the original hexagonal lattice, where the width of the displacement is normally distributed and the direction is random, with a step-wise increase in the standard deviation from 0 to 2.5μm ($\Delta\sigma_P = 0.5\mu m$). The peaks for the regular arrangement move towards a peak at $\omega = 0$ for an increase in standard deviation for both distributions; however, the asymmetric form of the frequency distribution is more robust against variations of radii than against randomization of capillary positions. The resulting profile of the frequency distribution is similar to that of a Lorentzian distribution. (c) Frequency distribution for the 2D-OCP with $\Gamma = 4$ (typical for capillaries in myocardium [24]), $\eta = 0.06$, and ICD = 16.5μm for a normal distribution of radii around μ_R (red line; $\sigma_R = 0.5\mu m$) and for constant radii μ_R (black line). Evidently, a normal distribution of radii does not have a significant effect on the frequency distribution for a 2D-OCP with low Γ values, but can, instead, be neglected.

shifts to larger Γ values since diffusion effects produce an increased smear of the frequency distribution curves.

To further examine the influence of different unit cell tilt angles α on our analysis, we simulated 2D-OCP frequency distributions for different tilt angles $\alpha = 0°, 10°, 20°, 30°$ at $\Gamma = 10$ and $\Gamma = 100$, see Fig. 9. Each frequency distribution represents an averaged curve over 10 simulations ($\eta = 0.06$, ICD = 16.5μm). While there is still a small effect of large tilt angles at $\Gamma = 100$, as indicated by a slight shift of the frequency distribution at $\alpha = 30°$ (blue solid line) towards

the frequency distribution at $\alpha = 0°$ (red solid line), this shift is non-existent at $\Gamma = 10$. However, since realistic (physiological and pathological) Γ values in the myocardium are usually $\Gamma < 5$, as shown in [24], we can safely neglect the effects of the unit cell tilt angle in further analyses. The inclusion of diffusion effects will also produce an additional smear of the frequency distributions around their center peak, see below, therefore further diminishing the shift in frequency distribution curves with large tilt angles at larger Γ values.

3.3. Inclusion of diffusion effects

Diffusion effects were included in our simulations through a random walk algorithm as described above and in Appendix B.2. To test the accuracy of the algorithm, the transverse magnetization decay for the Krogh model geometry was compared with the expected magnetization decay from the closed-form solution in the Krogh model according to Eq. (A7) [12,13], see Fig. 10a. The coincidence of both curves is evident; a closer look reveals that the expected statistical error, that results from the summation of residual phase errors for each time step of the random walk, is in the same range as the absolute difference of simulated and analytical magnetization decay, see Fig. 10b, thus demonstrating the robustness of the implemented algorithm. An upper limit for the expected error can be given as $|\Delta M(t)| \leq \Delta\omega_{max}\Delta t\sqrt{\frac{m}{N}} = 4.74\cdot10^{-3}$ for typical values of $\Delta\omega_{max} \leq 150s^{-1}$ at $\Delta t = 0.1ms$ (representing biologically reasonable values of $\delta\omega \leq 1000s^{-1}$ and $D \leq 2\mu m^2/ms$), $m = 10\,000$ and $N = 100\,000$ (see Eq. (B6) in Appendix B.2).

The change of the frequency distribution for the hexagonal lattice for varying diffusion constants D is shown in Fig. 10c: the characteristic asymmetric shape is apparent for $D = 0$. However, for increasing diffusion effects, the frequency distribution is increasingly smeared around the origin. Already, for $D \approx 1\mu m^2/ms$, the frequency distribution is only vaguely reminiscent of its anticipated asymmetric shape but rather appears Lorentzian with a mean value that is only slightly different from zero. With an additional randomization of capillary positions with low values of Γ in the 2D-OCP, the mean value approaches zero due to the statistical effects of the random positioning.

3.4. Effect of spatial capillary irregularity on relaxation times

For the regime of static dephasing, the free induction decay follows as the Fourier transform of the frequency distribution $\rho(\omega)$. The imaginary part of the free induction decay, $Im(M(t))$, is generally non-zero since $\rho(\omega)$ is not necessarily symmetric around $\omega = 0$ for large values of Γ or for the hexagonal lattice. Monoexponential fitting can be effected with the absolute value of $M(t)$, or with the real part of $M(t)$ provided the frequency distribution is almost symmetric around $\omega = 0$ (which may be the case for low values of Γ or strong diffusion effects, see Figs. 8 and 10). In Fig. 11 we show the effect of increasing Γ-values on the inverse relaxation time $R'_2 = \frac{1}{T'_2}$ for both monoexponential fitting routines. The fitting routines work well for plasmas that exhibit a quasi-Lorentzian frequency profile, but diverge when the plasma crystallizes at $\Gamma \approx 140$, see also Fig. 8b. The asymmetry of the frequency distribution then produces non-negligible imaginary parts of $M(t)$ which lead to changes of the free induction decay that can be better fitted with smaller relaxation rates. Relaxation time values in Table 2 were acquired as averages over both fitting routines.

With the inclusion of diffusion effects, the relaxation rates R'_2 do not scale linearly with the off-resonances as in the static dephasing regime. Therefore, simulations were performed for different frequency shifts $\delta\omega$ in different external fields, see Fig. 12 for both a typical 2D-OCP ($\Gamma = 4$) and a hexagonal lattice ($\Gamma = \infty$).
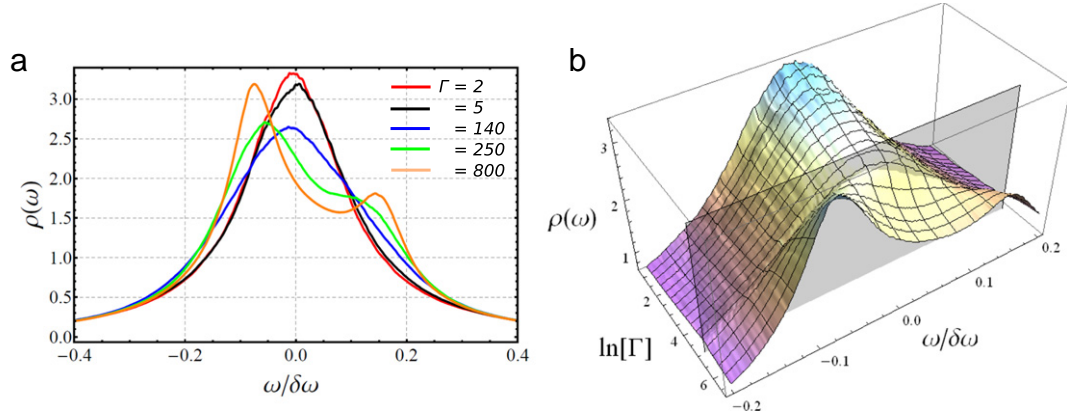
Fig. 8. Frequency distributions for randomized capillary positions in the 2D-OCP model; $\eta = 0.1$, ICD = 16.5μm. (a) Frequency distribution $\rho(\omega)$ in the 2D-OCP model in dependence on the parameter Γ that represents the "thermal" disturbance of the system and is a measure of the entropy of the spatial arrangement of capillaries. The two peaks for high values of Γ ($\Gamma = 250, 800$) vanish for decreasing Γ-values and merge into one single peak around $\omega \approx 0$ (see the red curve for $\Gamma = 2$). (b) Three-dimensional representation of the frequency distribution in dependence on ln(Γ). The distribution splits into two peaks for increasing values of Γ at $\Gamma \approx 140$ (gray plane), that correspond to the two peaks of the frequency distribution for the hexagonal lattice in Fig. 5a.

Relaxation times were then extracted with a monoexponential fitting routine to the real part of the free induction decay (black and green curves in Fig. 12). Interestingly, low off-resonance frequencies cause a faster relaxation in the 2D-OCP when compared with the hexagonal lattice (Fig. 12a), whereas high off-resonance frequencies produce an inverse effect with a faster relaxation in the hexagonal lattice (Fig. 12b), an effect that is due to the inclusion of diffusion into the simulations. Table 2 lists relaxation times for different realization of the 2D-OCP in the regime of static dephasing and for additional diffusion effects for typical values of off-resonance strengths $\delta\omega = 100$–1000s^{-1}. For instance, capillary blood with an oxygen extraction fraction of 0.4 and a hematocrit of 0.45 corresponds to $\delta\omega = 2\pi\Delta\chi_{\text{do}} \cdot OEF \cdot \text{Hct} \cdot \gamma B_0$ [7], with $\Delta\chi_{\text{do}} = 0.27\text{ppm}$ [38] (do: deoxygenated-oxygenated) and gyromagnetic ratio $\gamma = 2.675 \cdot 10^8 \text{s}^{-1}\text{T}^{-1}$, giving $\delta\omega = 160\text{s}^{-1}$ for 1.5T and $\delta\omega = 730\text{s}^{-1}$ for 7T.

Relaxation times differ for all plasma realizations; specifically, a trend of decreasing T_2' for increasing order parameter Γ at fixed $\delta\omega$ can be observed in the static dephasing regime [39]. Here, the averaged (relative) deviation from a 2D-OCP at $\Gamma = 800$ (hexagonal lattice) towards a plasma at $\Gamma = 2$ is $31.92\% \pm 0.04\%$. In the dynamic dephasing case, the averaged deviation of relaxation times of 2D-OCP at $\Gamma = 4$ from the hexagonal lattice is $21.65\% \pm 4.06\%$. However, the trend of increasing relaxation rates for increasing off-resonance frequencies $\delta\omega$ is stronger in the dynamic dephasing case: whereas all

2D-OCP relaxation rates scale with $\delta\omega$ in the static dephasing regime, they scale with $\sim 2\delta\omega$ for dynamic dephasing.

3.5. Randomly oriented angle β between capillary axis and B_0

Intra-voxel capillaries in biological tissues are usually randomly oriented against the B_0-field vector. To describe and include this effect in our analysis we have to integrate the angle-dependent transverse magnetization $M(t)$ over an adequate angle distribution function. As shown in [7], the distribution function $P(\beta)$ for an angle β between B_0 and the capillary axis corresponds to $P(\beta) = \sin(\beta)/2$, and the magnetization $\hat{M}(t)$ for a randomized angle orientation (RAO) reads:

$$\hat{M}(t) = \int_0^\pi d\beta \, \frac{\sin(\beta)}{2} \, M(t) = \int_0^\pi d\beta \, \frac{\sin(\beta)}{2} \langle e^{\hat{\Phi}(r,\phi,\beta)t} \rangle_{r,\phi} \quad (14)$$

where the Bloch-Torrey operator $\hat{\Phi}(r,\phi,\beta) = D\Delta_{r,\phi} - i\omega(r,\phi)\sin^2(\beta)$ from Eq. (2), $\Delta_{r,\phi}$ and $\langle \cdots \rangle_{r,\phi}$ represents integration over the dephasing volume. In our case, the dipole field $\omega(r,\phi)$ of cylindrical capillaries can be taken from Eq. (1) as

$$\omega(r,\phi) = \delta\omega \frac{R_C^2}{r^2} \cos(2\phi) \quad (15)$$

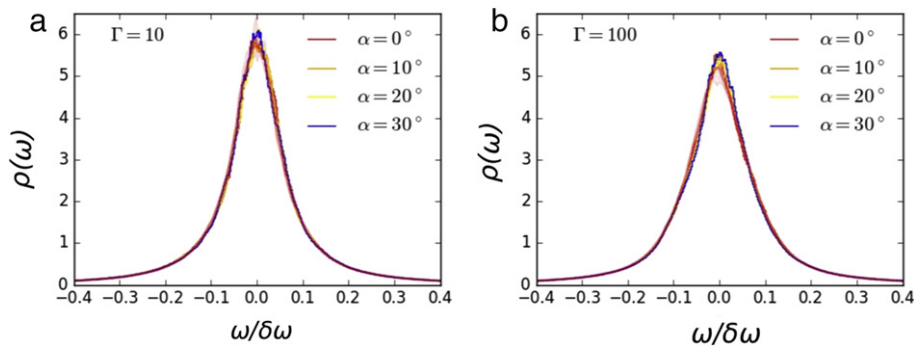$$= 2\pi\Delta\chi_{\text{do}}[1 - Y]\text{Hct}\gamma B_0 \frac{R_C^2}{r^2} \cos(2\phi), \quad (16)$$

Fig. 9. Frequency distributions in the 2D-OCP at different tilt angles α. Frequency distributions averaged over 10 simulations each are shown for $\Gamma = 10$ (a) and $\Gamma = 100$ (b) for $\alpha = 0°, 10°, 20°, 30°$. It can be seen that there is only a small shift of the frequency distribution for $\alpha = 30°$ (blue solid line in (b)) towards the curve at $\alpha = 0°$ (red solid line). This effect vanishes at $\Gamma = 10$. An inclusion of diffusion effects would produce an additional smear of the frequency distributions around the origin, therefore further diminishing effects of large tilt angles α.
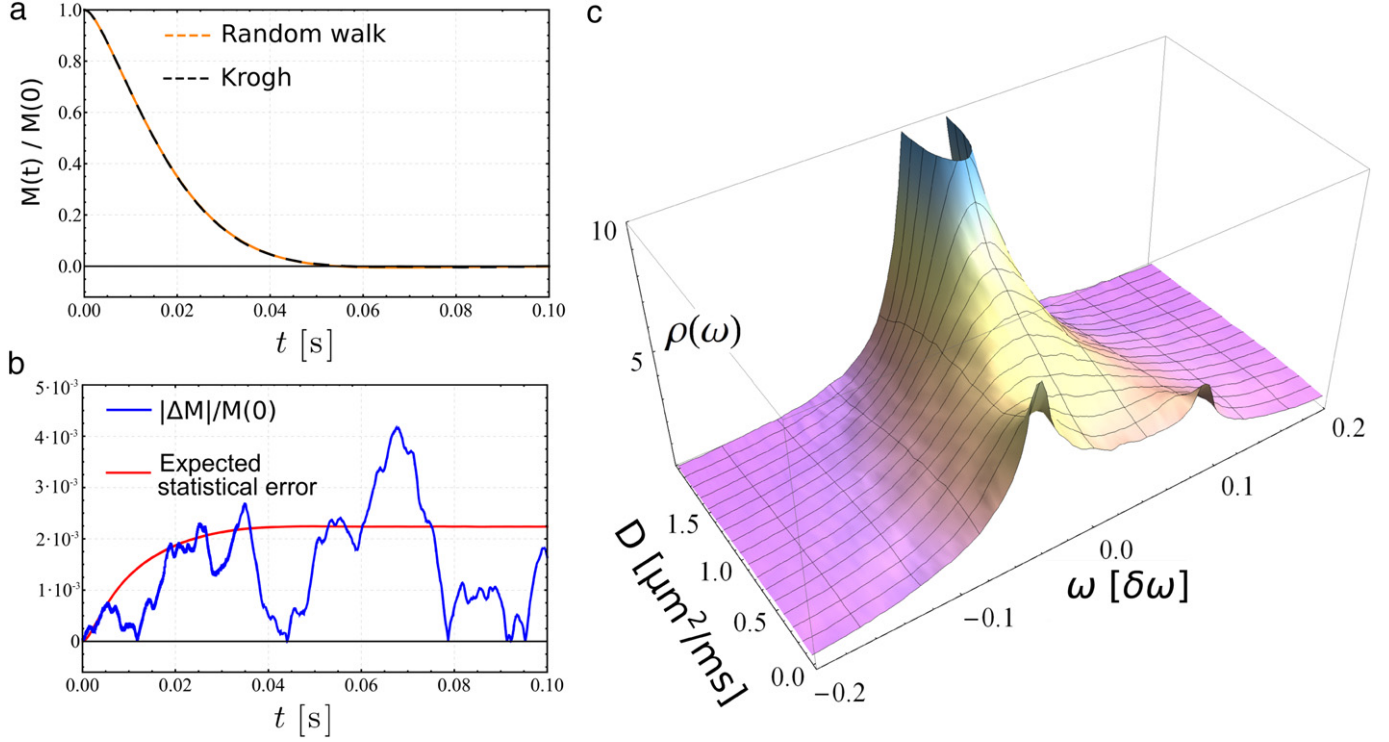
Fig. 10. Theoretical and simulated FID for the Krogh model and diffusion-dependent off-resonance frequency distribution for the hexagonal lattice. (a) Theoretical FID (dashed blacked line), as calculated from Eqs. (A1) and (3), and random walk simulation (dashed orange line) show an excellent agreement. (b) The error analysis of the absolute difference $|\Delta M|/M(0)$ of theoretical and simulated FID (blue curve) reveals errors that are in the range of the expected statistical error of the simulation (red curve; see Eq. (B6) in Appendix B.2). $\delta\omega = 936 \text{s}^{-1}$, $D = 1\mu\text{m}^2/\text{ms}$, $R_C = 2\mu\text{m}$, $\eta = 0.0533$ and $N = 100\,000$. (c) Frequency distribution and diffusion effects (hexagonal lattice). The static dephasing limit with its two characteristic peaks is recovered at $D = 0\mu\text{m}^2/\text{ms}$. The peaks at $D = 1\mu\text{m}^2/\text{ms}$ approach each other for increasing diffusion.

where we have inserted the susceptibility difference $\Delta\chi$ between capillary interior and surrounding tissue, $\Delta\chi = 4\pi\Delta\chi_{do}[1 - Y]\text{Hct}$, with $\Delta\chi_{do} = 0.27\text{ppm}$ as above [38], hematocrit Hct and oxygen extraction fraction $[1 - Y]$ (Y: fraction of oxygenated blood), see also [7].

Interestingly, the Krogh model allows us to derive a closed-form solution for $\hat{M}(t)$ in the static dephasing regime. By inserting Eq. (15) into Eq. (14), the magnetization decay in the Krogh model for the above angle orientation distribution function can be obtained as (subindex "K" denotes the Krogh model)

$$\frac{\hat{M}_K(t)}{M_0} = \frac{1}{\pi[R_D^2 - R_C^2]}\int_0^\pi d\beta\,\frac{\sin(\beta)}{2}\int_V dV\,e^{-i\omega(r,\phi)\sin^2(\beta)t} \tag{17}$$

$$= \frac{1}{\pi R_C^2}\frac{\eta}{1-\eta}\int_0^\pi d\beta\int_0^{2\pi}d\phi\int_{R_C}^{R_D}r\,dr\,\frac{\sin(\beta)}{2}e^{i\delta\omega t\frac{R_C^2}{r^2}\cos(2\phi)\sin^2(\beta)} \tag{18}$$
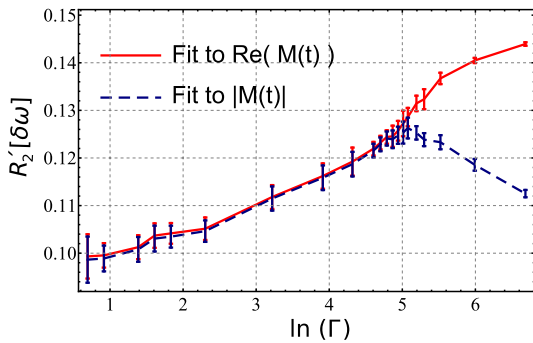
Fig. 11. Differences in fitting routines for the free induction decay $M(t)$ in the static dephasing regime. For low (realistic) values of Γ, a monoexponential fit to the real part of the magnetization, Re($M(t)$) (red curve), and the absolute value, $|M(t)|$ (blue-dashed curve), yield similar results. The free induction decay follows from a Fourier transform of the frequency distribution $\rho(\omega)$. A frequency distribution that is not purely symmetric around $\omega = 0$ leads to a non-zero imaginary part of $M(t)$ which in turn leads to differences in the fitting behavior for real and absolute values of the transverse magnetization. The inverse relaxation rates R_2' then peak for the monoexponential fit with $|M(t)|$ at $\Gamma \approx 140$ or $\ln(\Gamma) \approx 5$, corresponding to the "crystallization" of the 2D-OCP, see Fig. 8b. Values in Table 2 were acquired as averages over both fitting routines.

Table 2
Relaxation times for static and dynamic dephasing. For static dephasing, differences in T_2' between randomly positioned and highly ordered capillaries are most pronounced for small frequency shifts $\delta\omega$ and low fields. Note also the differences in relaxation times for the increases in $\delta\omega$ at fixed Γ. The differences in T_2' for dynamic dephasing are less pronounced and correspond to a change of approximately 15% of the value of highly ordered capillaries ($\Gamma = \infty$).

		T_2' [ms] (1.5 T)		T_2' [ms] (7 T)	
	$\delta\omega$ [s^{-1}]	100	200	500	1000
Static	$\Gamma = 2$	100.4	50.2	20.1	10
	$\Gamma = 5$	96.6	48.3	19.3	9.7
	$\Gamma = 800$	68.3	34.2	13.7	6.8
Dyn	$\Gamma = 4$	395	111	25	10
	$\Gamma = \infty$	502	126	21	7

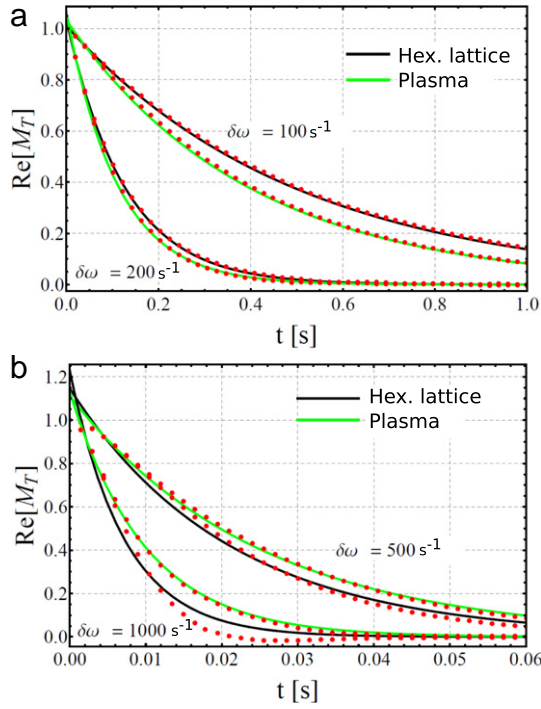**Fig. 12.** Simulated free induction decay and monoexponential fits for diffusion $D = 1\mu m^2 ms^{-1}$ in a hexagonal lattice ($\Gamma = \infty$) and realistic plasma ($\Gamma = 4$) at (a) $B_0 = 1.5$T and (b) $B_0 = 7$T. Simulation data are shown as red dots. For low off-resonance frequencies $\delta\omega$, the signal from the randomized capillary distribution of the plasma decays faster than that of the hexagonal lattice (cf. green and red curves in (a)). This behavior reverses for larger off-resonance frequencies (b). The imaginary part of $M(t)$ is in all cases smaller than 0.1. Further parameters: ICD $= 17\mu m$, $\eta = 0.01$, $R_C = 2.82\mu m$. The respective relaxation rates R'_2 for monoexponential fits are provided in Table 2.

$$= \frac{1}{R_C^2} \frac{\eta}{1-\eta} \int_{R_C}^{R_D} r\, dr \int_0^\pi d\beta \sin(\beta) J_0\left(\delta\omega t \frac{R_C^2}{r^2} \sin^2(\beta)\right) \quad (19)$$

$$= \frac{\pi}{\sqrt{2} R_C^2} \frac{\eta}{1-\eta} \int_{R_C}^{R_D} r\, dr\, J_{\frac{1}{4}}\left(\frac{R_C^2}{r^2}\frac{\delta\omega t}{2}\right) J_{-\frac{1}{4}}\left(\frac{R_C^2}{r^2}\frac{\delta\omega t}{2}\right) \quad (20)$$

$$= \frac{\pi}{2\sqrt{2}} \frac{\eta}{1-\eta} \int_\eta^1 \frac{dx}{x^2} J_{\frac{1}{4}}\left(x\frac{\delta\omega t}{2}\right) J_{-\frac{1}{4}}\left(x\frac{\delta\omega t}{2}\right), \quad (21)$$

with Bessel functions $J_\nu(x)$, total initial magnetization $M_0 = m_0 V$ and local magnetization m_0 at $t = 0$, and radius R_D of the Krogh cylinder with $\eta = R_C^2/R_D^2$. The last integral can be solved analytically to give

$$\frac{\hat{M}_K(t)}{M_0} = \frac{\pi}{6\sqrt{2}} \frac{H(\eta\delta\omega t) - \eta H(\delta\omega t)}{1-\eta}, \quad (22)$$

where

$$H(x) = J_{\frac{1}{4}}\left(\frac{x}{2}\right)\left[2[x^2+1]J_{-\frac{1}{4}}\left(\frac{x}{2}\right) - x J_{\frac{3}{4}}\left(\frac{x}{2}\right)\right]$$
$$+ x J_{-\frac{3}{4}}\left(\frac{x}{2}\right)\left[J_{-\frac{1}{4}}\left(\frac{x}{2}\right) - 2x J_{\frac{3}{4}}\left(\frac{x}{2}\right)\right]. \quad (23)$$

The frequency distribution for a randomized angle orientation, $\hat{\rho}(\omega)$, can eventually be obtained as the Fourier transform of the free induction decay $\hat{M}(t)$ from Eq. (22). In Fig. 13a, for different blood volume fractions η, we compare the numerically obtained frequency distributions $\hat{\rho}(\omega)$ with the frequency distributions for the angle $\beta = \pi/2$, i.e. perpendicular to the direction of B_0. While the traditional frequency distributions in the Krogh model have two peaks at
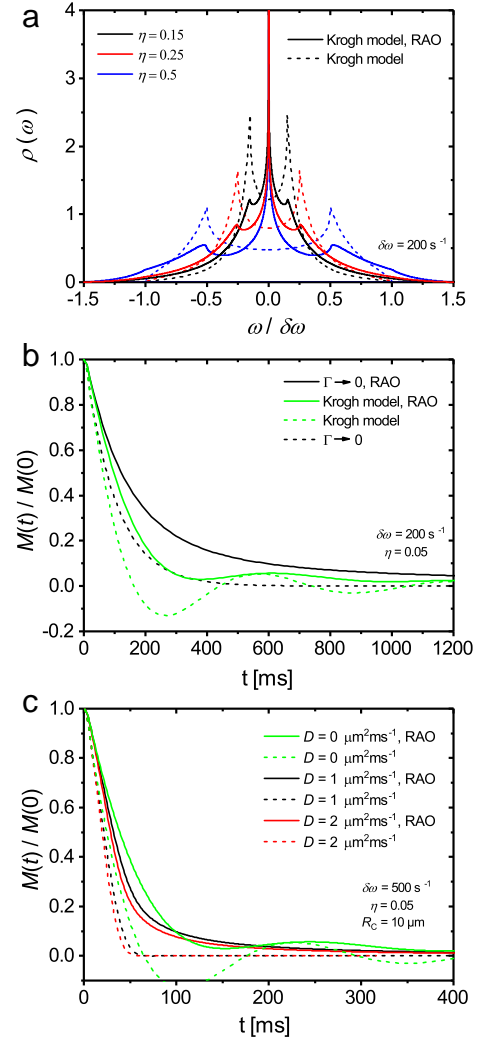
Fig. 13. Frequency distributions $\rho(\omega)$ and free induction decay $M(t)$ for randomized angle orientation (RAO). (a) Frequency distributions in the traditional Krogh model (dashed line; the capillary axis is perpendicular to B_0, see also Eq. (6)) and for RAO (solid line, based on the Fourier transform of Eq. (22)), for different blood volume fractions η. Both distribution forms exhibit symmetric peaks at $\omega = \pm\delta\omega$, but the RAO distributions possess an additional peak at zero frequency. (b) FID of the RAO Krogh model (dashed line; Eq. (22)) and the RAO 2D-OCP for $\Gamma\rightarrow 0$ (solid line; Eq. (24)). Both models show a shift towards slower decay rates in their RAO form. ($\delta\omega = 200$s^{-1}, $\eta = 0.05$). (c) FID for different diffusion constants, based on the local gradient approximation (Eq. (28); $\delta\omega = 500$, $\eta = 0.05$, $R_C = 10\mu m$), for RAO and perpendicular angle as above. The systematic RAO shift towards slower decay rates prevails for an increase in diffusion effects.

$\omega = \pm\eta\delta\omega$ (see Fig. 5c and Eq. (6)), the frequency distributions in the Krogh model for randomized angle orientations exhibit an additional peak at $\omega = 0$.

The 2D-OCP for randomized vessel positions, or $\Gamma\rightarrow 0$, is given as [7]:

$$\frac{M(t)}{M_0} = \exp\left(\eta[1 - H_0(\delta\omega t)]\right), \quad (24)$$

with the generalized hypergeometric function

$$H_0(y) = {}_1F_2\left(-\frac{1}{2}; \frac{1}{2}, 1; -\frac{y^2}{4}\right). \quad (25)$$

We compare the effect of vessel orientation randomization on both the Krogh model and the 2D-OCP in Fig. 13b for $\delta\omega = 200$s^{-1} and

blood volume fraction $\eta = 0.05$. It can be seen that vessel orientation randomization leads to a shift of similar proportion in both models towards lower relaxation rates, i.e. the effect of RAO on the relaxation rate does not change the relative differences in relaxation rates between a uniform capillary arrangement and that of a 2D-OCP with low Γ values.

To add diffusion effects to the local magnetic field, we can make use of the local gradient approximation that was first suggested by [11]. It provides an expression for the short-time local magnetization decay in terms of a small "effective" linear gradient

$$\gamma G \rightarrow \sqrt{\frac{1}{V} \int_V dV \, [\nabla \omega(\mathbf{r})]^2}$$

that represents the spatial average over the local dipole field $\omega(r, \phi)$, see also [31] and Eq. (47) in [22]:

$$\frac{m_{LGA}(r, \phi, t)}{m_0} = \exp(-i\omega(\mathbf{r})t) \frac{1}{V} \int_V d^3\mathbf{r} \exp\left(-\frac{Dt^3[\nabla\omega(\mathbf{r})]^2}{12}\right) \quad (26)$$

$$\approx \exp\left(-i\omega(\mathbf{r})t - \frac{D\gamma^2 G^2 t^3}{12}\right) \quad$$

$$= \exp\left(-i\omega(\mathbf{r})t - \frac{Dt^3}{12}\delta\omega^2 \frac{\eta[\eta+1]}{R_C^2}\right), \quad (27)$$

where we have replaced the integral on the right-hand-side in Eq. (26) by its first order term.

As in the case of static dephasing, the total magnetization in the dephasing volume of an imaging voxel follows from Eq. (14) as

$$\frac{M_{LGA}(t)}{M_0} = \frac{M_K(t)}{M_0} \exp\left(-\frac{t^3}{12}\frac{\delta\omega^2}{\tau}\eta[\eta+1]\right), \quad (28)$$

with characteristic diffusion time $\tau = R_C^2/D$ and static dephasing magnetization decay $M_K(t)$:

$$\frac{M_K(t)}{M_0} = \frac{H_0(\eta\delta\omega t) - \eta \, H_0(\delta\omega t)}{1 - \eta}, \quad (29)$$

where $H_0(y)$ corresponds to the hypergeometric function as given in Eq. (25). Of note is the similarity between Eq. (29) for parallel capillaries perpendicular to B_0 and Eq. (22) for randomized angle orientations. The magnetization decays $\hat{M}_{LGA}(t)$ for different diffusion constants D can then be obtained by numerical integration over the angle orientation distribution as in Eq. (14), see Fig. 13c. The systematic RAO shift towards slower relaxation rates prevails for an increase in diffusion effects.

3.6. Blood oxygenation and model extension to three dimensions

So far we have only incorporated a fixed oxygen extraction fraction within our model. However, blood-filled capillaries are prone to changing oxygen saturations that modify the susceptibility gradient of the capillaries to the surrounding tissue. To adapt our two-dimensional model to the changing oxygen characteristics in a capillary network, we have to average the effects of different blood oxygenation levels along a capillary axis, see Fig. 14a: the fraction of oxygenated blood, Y, changes from the arterial to the venous end of a capillary from approximately $Y \approx 1$ to $Y \approx 0.5$.

Every slice along the capillary axis possesses a specific off-resonance value and is characterized by its thickness $d = \sqrt{2D \cdot 2T_2^*}$, i.e. the average distance that a magnetization package covers during the relaxation time. For $T_2^* < T_2 \approx 50$ ms and $D \approx 1.5\mu m^2/ms$ we find $d \approx 17\mu m$. For a capillary length of $100\mu m$ we therefore
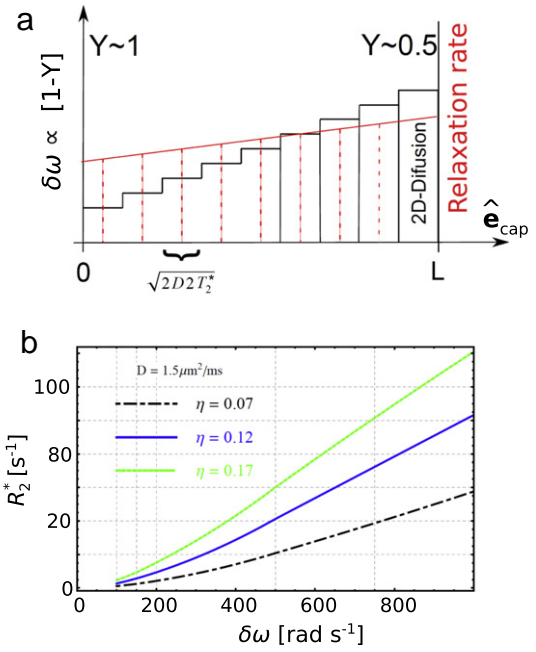
Fig. 14. (a) Schematic increase of off-resonance frequency $\delta\omega = 4\pi\Delta\chi_{do}Hct\gamma B_0 OEF$ (see also Eq. (16)), with oxygen extraction fraction $OEF = 1 - Y$ (Y: fraction of oxygenated blood), along a capillary axis $\hat{\mathbf{e}}_{cap}$ of length L. The increase in Y from the arterial to the venous end can be approximated by slices of thickness $d = \sqrt{4DT_2^*}$ (the average distance that a magnetization package covers during the relaxation time), such that each slice can be modeled in the 2D-OCP. (b) Relaxation rate R_2^* versus off-resonance frequency $\delta\omega$ for different volume fractions η. There is an approximate linear increase of relaxation rates for larger values of $\delta\omega$. $D = 1.5\mu m^2/ms$.

have approximately 5–10 different slices. We thus find for the total magnetization

$$\frac{M_{3D}(t)}{M_0} \approx \frac{1}{N} \sum_{j=1}^{N} \exp\left(-R_{2,j}^* \cdot t\right), \quad (30)$$

with index j running over the slices and $R_{2,j}^*$ corresponding to the (simulated) relaxation rates for the respective off-resonance frequencies. Since the relaxation rate approximately increases linearly for increasing off-resonance frequencies, see Fig. 14b, we can assume for the magnetization along the capillary axis with length L:

$$\frac{M_{3D}(t)}{M_0} \approx \frac{d}{L} \sum_{j=1}^{\lceil L/d \rceil} \exp\left(-\hat{R}_2^*(jd) \cdot t\right) \quad \text{with} \quad (31)$$

$$\hat{R}_2^*(l) = \frac{l}{L}\left[R_{2,ven}^* - R_{2,art}^*\right] + R_{2,art}^*, \quad (32)$$

where $R_{2,art}^*$ and $R_{2,ven}^*$ represent the relaxation rate at the arterial and venous end of the capillary, respectively.

The sum in Eq. (31) can be converted into an integral for infinitesimally small slices such that

$$\frac{M_{3D}(t)}{M_0} = \frac{1}{L} \int_0^L dl \, \exp\left(-\hat{R}_2^*(l) \cdot t\right) \quad (33)$$

$$= \frac{\exp\left(-R_{2,ven}^* \cdot t\right) - \exp\left(-R_{2,art}^* \cdot t\right)}{\left[R_{2,art}^* - R_{2,ven}^*\right] \cdot t}. \quad (34)$$

When we assume a monoexponential decay for $M_{3D}(t)$ with relaxation rate $R_{2,3D}^*$, we can determine an estimate of $R_{2,3D}^*$ by minimizing

$$\min \left\| \frac{\exp\left(-R_{2,\text{ven}}^* \cdot t\right) - \exp\left(-R_{2,\text{art}}^* \cdot t\right)}{\left[R_{2,\text{art}}^* - R_{2,\text{ven}}^*\right] \cdot t} - \exp\left(-R_{2,3D}^* \cdot t\right) \right\| \qquad (35)$$

on $t \in [0, \infty[$ to arrive at

$$R_{2,3D}^* = \frac{1}{6}\left[R_{2,\text{art}}^* + R_{2,\text{ven}}^* + \sqrt{R_{2,\text{art}}^{*\,2} + 14 R_{2,\text{art}}^* R_{2,\text{ven}}^* + R_{2,\text{ven}}^{*\,2}} \right]. \qquad (36)$$

Interestingly, even for large differences between $R_{2,\text{art}}^*$ and $R_{2,\text{ven}}^*$, the difference between $R_{2,3D}^*$ from Eq. (36) and the arithmetic mean between $R_{2,\text{art}}^*$ and $R_{2,\text{ven}}^*$, $R_{2,\text{mean}}^* = \frac{1}{2}[R_{2,\text{art}}^* + R_{2,\text{ven}}^*]$, remains small as also shown in Fig. 15. For instance, for a typical $R_{2,\text{ven}}^* \approx 80 s^{-1}$ at 7T (see Table 2 in [13]), we see for a difference of $70-80 s^{-1}$ between the arterial end ($R_{2,\text{art}}^* = 0-10 s^{-1}$) and the venous end, that the (interpolated) quotient of $R_{2,3D}^*/R_{2,\text{mean}}^* \approx 0.95$ at $R_{2,\text{mean}}^* = 40-45 s^{-1}$. The differences at 1.5T are even smaller, e.g. $R_{2,\text{ven}}^* \approx 30 s^{-1}$ and $R_{2,\text{art}}^* = 0-5 s^{-1}$ lead to a quotient of approximately 0.98. The respective magnetization decays of $R_{2,3D}^*$ and $R_{2,\text{art}}^*$ are then practically the same, see also below or Fig. 16.

A comparison of Krogh model and 2D-OCP can be accomplished by setting

$$\delta\omega(l) = \frac{l}{L}[\delta\omega_{\text{ven}} - \delta\omega_{\text{art}}] + \delta\omega_{\text{art}}, \qquad (37)$$

in analogy to Eq. (32), where we recall that $\delta\omega$ has a linear dependence on blood oxygen fraction Y: $\delta\omega \propto [1 - Y]$. The integration for infinitesimally thin slices, similar to the procedure in Section 3.5, eventually yields

$$\frac{M_{3D,K}(t)}{M_0} = \frac{1}{L}\frac{1}{1-\eta}\int_0^L dl \ [H_0(\eta\delta\omega(l)t) - \eta H_0(\delta\omega(l)t)] \qquad (38)$$

$$= \frac{1}{4}\frac{1}{1-\eta}\frac{\delta\omega_i G(\eta\delta\omega_i t) - \eta\delta\omega_i G(\delta\omega_i t)}{\delta\omega_{\text{ven}} - \delta\omega_{\text{art}}}\bigg|_{\delta\omega_i = \delta\omega_{\text{art}}}^{\delta\omega_i = \delta\omega_{\text{ven}}}, \qquad (39)$$

where "K" denotes the Krogh model, and

$$G(y) = [1 + 2y^2]J_0(y) + yJ_1(y) - [1 + y^2] \,_1F_2\left(\frac{1}{2}; 1, \frac{3}{2}; -\frac{y^2}{4}\right). \qquad (40)$$

The transverse magnetization decay from Eq. (39) is similar to Eq. (22) (angle orientation randomization) and Eq. (29) (two-dimensional Krogh model). In Fig. 16a we compare the transverse
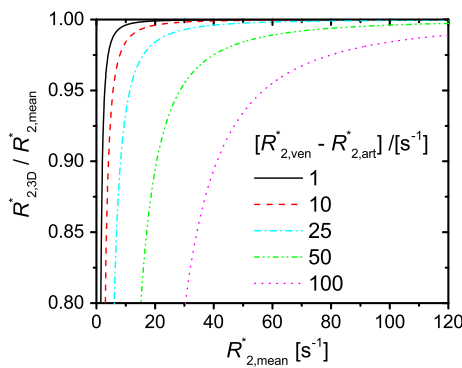
Fig. 15. Relaxation rate estimation for an oxygen gradient along capillary axis. The $R_{2,3D}^*$ relaxation rate can be obtained from an integration over infinitesimally thin 2D-OCP slices along the capillary length, see Eq. (36). The differences to the arithmetic mean between arterial and venous end are very small for typical relaxation rates at 1.5 and 7 T, see main text.
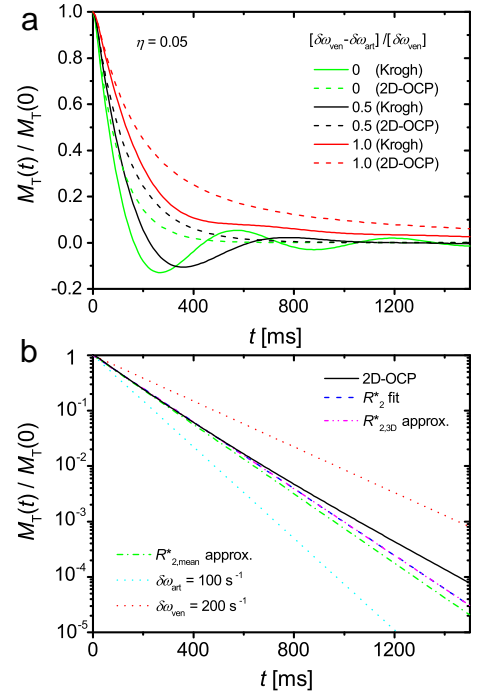
Fig. 16. Transverse magnetization decay for differences in $\delta\omega$ along the capillary axis. (a) Magnetization decays in the Krogh model and the 2D-OCP ($\Gamma \rightarrow 0$) are shown for relative differences $\Delta_{\delta\omega} = [\delta\omega_{\text{ven}} - \delta\omega_{\text{art}}]/\delta\omega_{\text{ven}} = 0, 0.5, 1.0$. There is a relaxation rate decrease for an increase in $\Delta_{\delta\omega}$ (details see main text). (b) Magnetization decay for $\Delta_{\delta\omega} = 0.5$ in the 2D-OCP and approximative measures. Remarkably, the mono-exponential fit to the 2D-OCP magnetization decay curve ($R_{2,\text{fit}}^* = 6.93 s^{-1}$) coincides with the approximate magnetization decay with $R_{2,3D}^*$ from Eq. (36) as obtained from $R_{2,\text{fit,art}}^* = 4.76 s^{-1}$ and $R_{2,\text{fit,ven}}^* = 9.51 s^{-1}$. There are only slight differences to the monoexponential decay with relaxation rate $R_{2,\text{mean}}^*$.

magnetization decays in the three-dimensional Krogh model, based on Eq. (39), and the extension of the 2D-OCP to blood oxygenation fraction, based on Eq. (24) and obtained by numerical integration in analogy to Eq. (38), for (relative) differences between $\delta\omega_{\text{art}}$ and $\delta\omega_{\text{ven}}$ at $\eta = 0.05$ and $\delta\omega_{\text{ven}} = 200 s^{-1}$. For an increase in the difference $\Delta_{\delta\omega}$ between $\delta\omega_{\text{ven}}$ and $\delta\omega_{\text{art}}$, $\Delta_{\delta\omega} = [\delta\omega_{\text{ven}} - \delta\omega_{\text{art}}]/\delta\omega_{\text{ven}}$, the relaxation rates decrease. For instance, the monoexponentially fitted relaxation rates in the 2D-OCP increase from $R_{2,\text{fit}}^* = 9.47 s^{-1}$ at $\Delta_{\delta\omega} = 0$ to $R_{2,\text{fit}}^* = 6.93 s^{-1}$ at $\Delta_{\delta\omega} = 0.5$ and $R_{2,\text{fit}}^* = 3.28 s^{-1}$ at $\Delta_{\delta\omega} = 1$. The respective relaxation rates in the Krogh model are increased in comparison, e.g. $R_{2,\text{fit}}^* = 10.89 s^{-1}$ at $\Delta_{\delta\omega} = 0$ in the Krogh model versus $R_{2,\text{fit}}^* = 6.93 s^{-1}$ in the 2D-OCP. The relation of these fitted values with the approximate $R_{2,3D}^*$ from Eq. (36) and the arithmetic mean, $R_{2,\text{mean}}^*$, are shown in Fig. 16b on a logarithmic scale. We used the monoexponentially fitted relaxation rates $R_{2,\text{fit,art}}^* = 4.76 s^{-1}$ (from $\delta\omega_{\text{art}} = 100 s^{-1}$) and $R_{2,\text{fit,ven}}^* = 9.51 s^{-1}$ (from $\delta\omega_{\text{ven}} = 200 s^{-1}$) to obtain the arithmetic mean $R_{2,\text{mean}}^* = 7.14 s^{-1}$ and $R_{2,3D}^* = 6.93 s^{-1}$ from Eq. (36). Remarkably, $R_{2,3D}^*$ and the actual fit value, $R_{2,\text{fit}}^*$, are identical which is also reflected in the coincident curves in Fig. 16b (magenta dash-dotted line and dashed blue line, respectively). The deviation from the $R_{2,\text{mean}}^*$ decay (green dash-dotted line) is also very small, indicating a useful approximative measure.

4. Discussion

In this work we investigate the influence of spatial patterns of capillaries in biological tissue in an external magnetic field on the

free induction decay through numerical simulations, using standard symmetric capillary arrangements and a recently proposed Gibbs point field model to accommodate deviations from uniform capillary positions [24]. The effects of diffusion of spin-carrying particles are incorporated through a robust random walk algorithm. We extensively study the free induction decay in the static dephasing regime through its inverse Fourier transform, the off-resonance frequency distribution, and provide numerical relations of the distribution peak positions in dependence on the blood volume fraction for the regular square and hexagonal lattices and the Krogh model. We find that differences in the peak positions of the frequency distributions become negligible for small blood volume fractions (as also discussed in [26,30,40]), which is appropriate for capillary networks in many types of biological tissue (e.g. brain and muscle tissue [7,10]).

We further show that the influence of non-uniform capillary radii on the off-resonance frequency distribution is lower than that of increasingly randomized capillary positions within a 2D-OCP model that is characterized by the order parameter Γ. A highly irregular 2D-OCP leads to a frequency distribution that, in contrast to the asymmetric frequency distribution of a regular hexagonal lattice, is increasingly smeared around the zero frequency while adopting a profile similar to that of a Lorentzian distribution. In fact, such a distribution shape for randomly distributed objects was also found by Yablonskiy et al. in the static dephasing regime [7].

This effect is important when considering the presence of diffusion that causes an additional smear of the frequency distribution around the zero frequency: increasingly symmetric or Lorentzian profiles justify the use of monoexponential fitting routines to obtain relaxation times, as one can also easily verify by taking a Lorentzian frequency distribution $\rho(\omega)$ to obtain the magnetization signal decay from Eq. (4), see also [36].

It is also demonstrated that relaxation times for irregularly arranged capillaries deviate around 20%–30% from a highly regular configuration. However, this effect is weaker for dynamic dephasing processes that involve statistical averaging and diffusion effects. In addition, it is less pronounced than the effect of changes in relaxation rates that scale with off-resonance strength $\delta\omega$ (see Table 2). For instance, the oxygen extraction fraction in brain tissue ranges between 35% and 60% [41], leading to the range $\delta\omega = 107s^{-1}$–$184s^{-1}$ (for $B_0 = 1.5T$ and Hct = 0.45). For dynamic dephasing at 1.5T, however, this range produces changes of about 60% in relaxation times (see Table 2) which is about three times higher than the effect of capillary irregularity. Therefore, when we translate this result to the context of evaluating capillarity heterogeneity as a biomarker for pathology-associated tissue alterations (as exemplified for cardiac tissue in [24]), a precise knowledge of tissue oxygen extraction is necessary, e.g. through quantitative BOLD or quantitative susceptibility mapping techniques [41,42]. Furthermore, the results indicate that notable voxel-inherent signal changes in BOLD imaging are likely to be attributed to alterations in the oxygenation status as opposed to the geometric arrangement of capillaries.

Acknowledgments

Appendix A. Analytical solution of the Krogh model

The solution of the Bloch-Torrey equation for spin dephasing in the Krogh model was derived in [12,13]. For the local magnetization, it is given in terms of the series expansion

$$\frac{m(r,\phi,t)}{m_0} = \sum_{m=0}^{\infty} \sum_{n=1}^{\infty} c_{nm} ce_{2m}\left(\phi, \frac{i}{2}\frac{\delta\omega R_C^2}{D}\right) e^{-\lambda_{nm}^2 \frac{D}{R_C^2} t}$$
$$\times \left[Y'_{k_m}(\lambda_{nm}) J_{k_m}\left(\frac{\lambda_{nm}}{R_C}r\right) - J'_{k_m}(\lambda_{nm}) Y_{k_m}\left(\frac{\lambda_{nm}}{R_C}r\right) \right], \quad (A1)$$

with Bessel functions J and Y of the first and second kind, respectively, with index k_m that represents the characteristic value a_{2m} of the corresponding π-periodic even Mathieu function ce with

$$k_m^2 = a_{2m}\left(\frac{i}{2}\frac{\delta\omega R_C^2}{D}\right), \quad (A2)$$

see also [43] (with the polar coordinates r and ϕ, diffusion coefficient D, capillary radius R_C, and capillary surface frequency shift $\delta\omega$). The eigenvalues λ_{nm} solve the eigenvalue equation

$$Y'_{k_m}(\lambda_{nm}) J'_{k_m}\left(\frac{\lambda_{nm}}{\sqrt{\eta}}\right) = J'_{k_m}(\lambda_{nm}) Y'_{k_m}\left(\frac{\lambda_{nm}}{\sqrt{\eta}}\right), \quad (A3)$$

where η represents the blood volume fraction, and the expansion coefficients c_{nm} are given as

$$c_{nm} = 2\pi A_0^{(2m)} \lambda_{nm}^2 J'_{k_m}\left(\frac{\lambda_{nm}}{\sqrt{\eta}}\right)$$
$$\times \frac{J'_{k_m}(\lambda_{nm}) s'_{1,k_m}\left(\frac{\lambda_{nm}}{\sqrt{\eta}}\right) - J'_{k_m}\left(\frac{\lambda_{nm}}{\sqrt{\eta}}\right) s'_{1,k_m}(\lambda_{nm})}{\left[J'_{k_m}(\lambda_{nm})\right]^2 \left[\lambda_{nm}^2 - \eta k_m^2\right] - \left[J'_{k_m}\left(\frac{\lambda_{nm}}{\sqrt{\eta}}\right)\right]^2 \left[\lambda_{nm}^2 - k_m^2\right]}, \quad (A4)$$

where the first derivative of the Lommel function s_{1,k_m} can be written as [44]

$$s'_{1,k_m}(x) = \frac{2x}{4 - k_m^2} \,_1F_2\left(2; 2 - \frac{k_m}{2}, 2 + \frac{k_m}{2}; -\frac{x^2}{4}\right) \quad (A5)$$

with generalized hypergeometric function $_pF_q$ for $p = 1$ and $q = 2$. The parameter $A_0^{(2m)}$ denotes the first Fourier coefficient of the Mathieu function:

$$A_0^{(2m)} = \frac{1}{2\pi} \int_0^{2\pi} d\phi \, ce_{2m}\left(\phi, \frac{i}{2}\frac{\delta\omega R_C^2}{D}\right). \quad (A6)$$

The transverse magnetization $M(t)$ can eventually be found as [13,45]:

$$\frac{M(t)}{M_0} = \sum_{m=0}^{\infty} \sum_{n=1}^{\infty} d_{nm} e^{-\lambda_{nm}^2 \frac{D}{R_C^2} t} \quad (A7)$$

with expansion coefficients

$$d_{nm} = \frac{8\eta}{1-\eta}\left[A_0^{(2m)}\right]^2$$
$$\times \frac{\left[J'_{k_m}(\lambda_{nm}) s'_{1,k_m}\left(\frac{\lambda_{nm}}{\sqrt{\eta}}\right) - J'_{k_m}\left(\frac{\lambda_{nm}}{\sqrt{\eta}}\right) s'_{1,k_m}(\lambda_{nm})\right]^2}{\left[J'_{k_m}(\lambda_{nm})\right]^2 \left[\lambda_{nm}^2 - \eta k_m^2\right] - \left[J'_{k_m}\left(\frac{\lambda_{nm}}{\sqrt{\eta}}\right)\right]^2 \left[\lambda_{nm}^2 - k_m^2\right]}. \quad (A8)$$
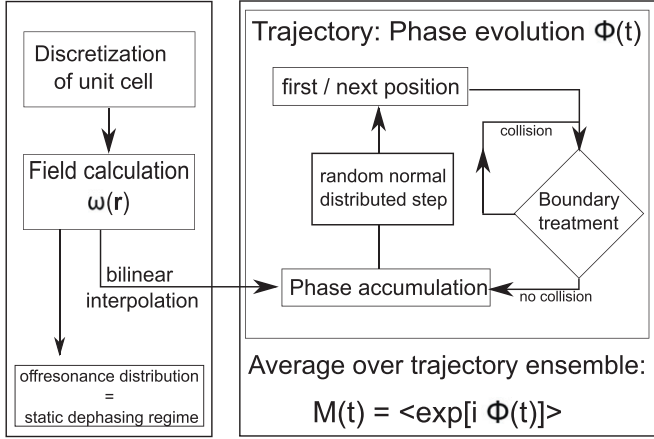
Fig. 17. Flow chart for the numerical simulations. Left box: calculation of the off-resonance field. First, the unit cell with one or more capillaries is chosen and discretized. Then, for all lattice points, the value of $\omega_{lattice}(\mathbf{r})$ is calculated using Eq. (B1) and stored in a lookup table. In the static dephasing regime, the frequency distribution $\rho(\omega)$ was calculated by binning the field values for all lattice points (excluding the points occupied by capillaries) in a histogram with the specified frequency resolution. Right box: random walk simulation: in each time step a new position is calculated. If a collision is detected (see Fig. 19), the model specific boundary conditions are handled with care to correct the new position (see Fig. 20). The field at the new position is interpolated from the lookup table and the phase accumulation is calculated. The program eventually advances to the next time step.

Appendix B. Simulation

In the following we will detail the implementation of our numerical simulation. The first part outlines the calculation of the off-resonance field; the second part treats the incorporation of spin diffusion in the local resonance field of the capillaries through a random walk algorithm (see Fig. 17).

B.1. Off-resonance field calculation

In the multi-capillary approach, the contributions from the surrounding capillaries to the local off-resonance field inside a unit cell are considered. Due to the imposed periodic boundary conditions, the use of rectangular unit cells is reasonable. As the problem is essentially two-dimensional, the unit cell is spanned by the lattice vectors $\mathbf{a}_1$ and $\mathbf{a}_2$. This is visualized in Fig. 18 for the square lattice and the hexagonal lattice. The N capillaries inside each unit cell are located at $\mathbf{L}_i$. The complete off-resonance field, generated by the infinite lattice of unit cells, reads

$$\omega_{lattice}(\mathbf{r}) = \sum_{n_1, n_2} \sum_{i=1}^{N} \omega\left(\mathbf{r} - \mathbf{L}_i + n_1 \mathbf{a}_1 + n_2 \mathbf{a}_2\right), \qquad \text{(B1)}$$

where n_1 and n_2 number the unit cells inside the lattice and $\omega(\mathbf{x})$ is the single-capillary off-resonance field given in Eq. (7). Without loss of generality, $\mathbf{r}$ is restricted to the center unit cell with $n_1 = n_2 = 0$ and excludes the capillary volumes located around $\mathbf{L}_i$. Additionally, $\delta\omega = 1$ was used to allow simple scaling to arbitrary off-resonances.

For the case of the square and the hexagonal lattice, the values of $\mathbf{L}_i$ are known (see e.g. [46]). However, for a specific realization of the plasma model, the positions $\mathbf{L}_i$ have to be calculated according to [24], see also Section 2.2.2.

For practical reasons, i.e. reasons of computational efficiency, it is not possible to cover the whole lattice ($n_1, n_2 \in \{-\infty, +\infty\}$). Thus, a cut-off radius R_{max} was introduced that must be large enough to ensure the periodicity of the field and small enough to allow time-efficient computation. Hence, in Eq. (B1) only addends with $|\mathbf{L}_i + n_1 \mathbf{a}_1 + n_2 \mathbf{a}_2| \le R_{max}$ were considered in the field calculation (see left hand side in Fig. 18). The off-resonance field was calculated on an equidistant Cartesian grid with resolution $\delta a_i = |\mathbf{a}_i|/(G_i - 1)$ in the i-th direction (see middle of Fig. 18), where G_i denotes the number of grid points in this direction.

The generic simulation parameters for the three different geometries are given in Table 3. To obtain a field for a specific volume fraction η, capillary radius R_C and off-resonance frequency $\delta\omega$ the generic field was adapted by defining an exclusion volume around each capillary and rescaling of its amplitude. In our simulations, we used the grid resolution of 0.02μm. This leads to a size of the unit cell of 15.4μm × 15.4μm for the square and 16.5μm × 28.6μm for the hexagonal lattice. To achieve the volume fraction $\eta = 0.15$, one has to choose the corresponding capillary radius $R_C = 3.35$μm. This resolution was considered sufficient, since improving the resolution did not affect simulation results (see also Appendix B.2).

However, the grid resolution δa_i can vary for different scalings: e.g. the variation of the volume fractions η while keeping the capillary radii R_C constant, requires variable values of the lattice vector $\mathbf{a}_i$. For all lattices the calculated off-resonance field was stored for further use.

B.2. Random walk simulation

The starting point of random walk trajectories were distributed within the unit cell with exclusion of the capillaries interiors. For each time step Δt, normal-distributed random numbers with zero mean and standard deviation $\sigma = \sqrt{2D\,\Delta t}$ were calculated to determine the jump to the next position.

Furthermore, at each time step, a collision detection was performed to check if the new position was outside the unit cell or inside a capillary. For the plasma model, the number of capillaries inside the unit cell can become large (see Table 3). Therefore, a recursive search tree was implemented (see Fig. 19). This allowed an efficient way to detect collisions of the trajectory with capillaries, e.g. for a unit

Fig. 18. Scheme of the lattice geometries used for the off-resonance field calculation. Left: visualization of the cut-off radius. Middle: unit cell of the square lattice. Right: unit cell of the hexagonal lattice. The cut-off radius R_{max} defines the circle around the center of a unit cell. Only addends with $\mathbf{L}_i + n_1 \mathbf{a}_1 + n_2 \mathbf{a}_2 \le R_{max}$ are considered.

Table 3
Simulation parameters for the field calculation. For the hexagonal lattice, the number in parentheses for G_1 and G_2 is the number of grid points for the tilt angle $\alpha = 0°$ to achieve a more accurate static frequency distribution.

	$|\mathbf{a}_2|/|\mathbf{a}_1|$	G_1	G_2	R_{max}	m
Square lattice	1	768	768	$108|\mathbf{a}_{1s}|$	1
Hexagonal lattice	$\sqrt{3}$	826 (3304)	1430 (5720)	$100|\mathbf{a}_{1h}|$	2
Plasma model	$\sqrt{3}$	3301	5716	$10|\mathbf{a}_{1p}|$	200

cell with 50 capillaries this resulted in a speed up of approximately a factor of 10. If a collision was detected, the invalid position was corrected according to appropriate boundary conditions: on the capillary surface, the random walk trajectories were reflected (reflecting or homogeneous Neumann boundary conditions, see Fig. 20). On the outer boundary of the dephasing volume we installed either reflecting (Krogh model) or cyclic (i.e. inhomogeneous Neumann) boundary conditions (for square, hexagonal and 2D-OCP simulations).

If the new position at time $t = j\Delta t$ was accepted, the new phase for the k-th trajectory was calculated via

$$\Phi_k(j\Delta t) = \Phi_k([j-1]\Delta t) + \omega_{lattice}(\mathbf{r}_j)\Delta t. \tag{B2}$$

As the off-resonance field was pre-calculated on a pre-defined grid, the off-resonance frequency at the actual positions of the trajectory was interpolated using bilinear interpolation. To obtain the transverse magnetization $M(t = j\Delta t)$, the trajectories were averaged for each time step:

$$M(j\Delta t) = \frac{1}{K}\sum_{k=1}^{K}[\cos(\Phi_k(j\Delta t)) + i\sin(\Phi_k(j\Delta t))] \tag{B3}$$

where K is the number of sampled trajectories. As each trajectory can be calculated independently, parallelization of the algorithm was straight forward.

The accumulated phase error of one trajectory at time-point t is given as $\Delta\Phi(t) \leq \sqrt{m}\Delta t\Delta\omega_{max}$ with $m = \lfloor\frac{t}{\Delta t}\rfloor$ and $\Delta\omega_{max} \approx \delta\omega R_C^2\sqrt{2D\Delta t}/r^3$. Due to the periodicity of the sine and cosine functions in Eq. (B1), small relative off-resonance errors are not sufficient. Since all phase information is already lost at $\Delta\Phi(t) = \pi$, the absolute error $\Delta\omega_{max}$ can be estimated as $\Delta\omega_{max} < \frac{\pi}{\sqrt{m}\Delta t}$. The error in
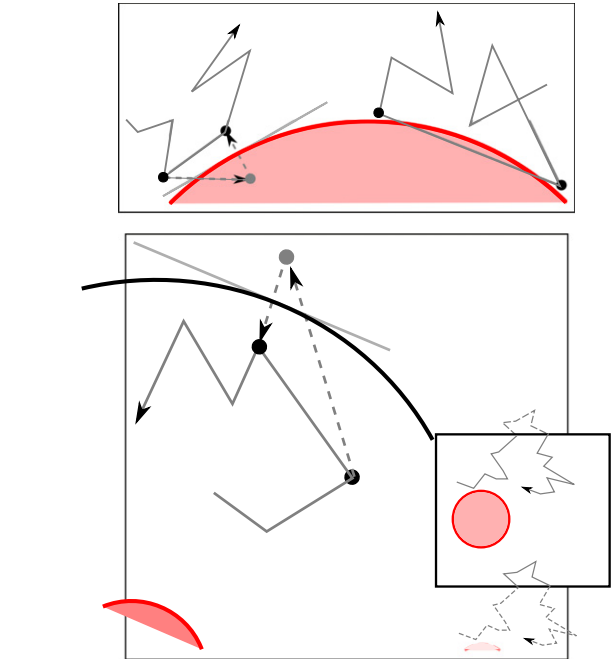
Fig. 20. Scheme of the boundary treatment used in the random walk simulations. Top: capillary surface. The endpoints of forbidden steps into the capillary interior were mirrored along the radial direction (left). For long steps in the capillary vicinity it is possible that the steps jump "through" the capillary wall (right). However, those steps are unlikely for the chosen mean step width and, thus, were allowed for reasons of computational efficiency. Bottom: outer boundary of the unit cell. For the surface of the dephasing volume in the Krogh model, the boundary treatment is analogous to the reflection on the capillary (left). For the multi-capillary model, cyclic boundary condition apply at the surface of the unit cell (right).

magnetization M then follows as

$$|\Delta M(t)|^2 = \sum_{k=0}^{K-1}\left[\frac{\partial M(t)}{\partial\Phi_k(t)}\right]^2[\Delta\Phi(t)]^2 \tag{B4}$$

$$= \frac{[\Delta\Phi(t)]^2}{K}\sum_{k=0}^{K-1}[-\sin(\Phi_k(t)) + i\cos(\Phi_k(t))]^2, \tag{B5}$$
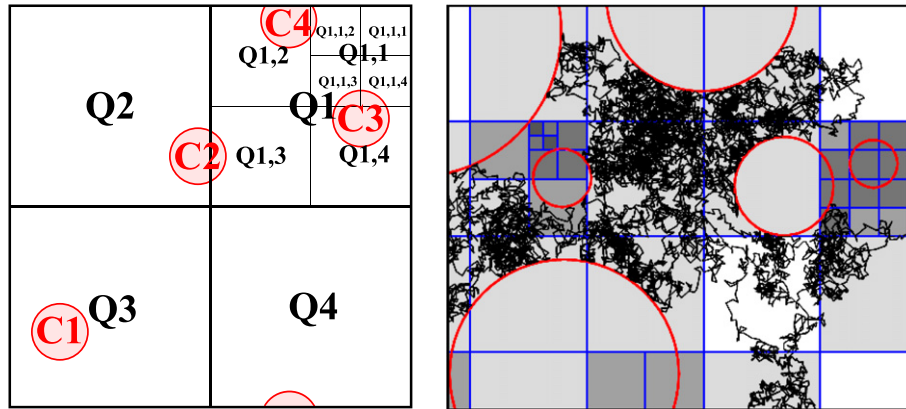

Fig. 19. Scheme of the recursive collision detection in the random walk simulation. Left: to generate the search tree, the unit cell is subdivided into four quadrants. For each quadrant, the number of contained capillaries is checked. If a quadrant contains more than a single capillary, it is again subdivided into four sub-quadrants. This procedure is recursively repeated until each sub-quadrant contains one or no capillary. The advantage of this procedure lies in the fact that each point inside the unit cell can be easily and quickly associated with a sub-quadrant, and only a collision with ≤ 1 capillary has to be checked. This allows the collision detection in $\ln(N)$, where N is the number of capillaries. Right: sample trajectory and refined mesh of the search tree for an exemplary capillary distribution.

therefore, we find

$$|\Delta M(t)| \leq \Delta\omega_{max} \Delta t \frac{\sqrt{m}}{K} \ . \tag{B6}$$

References

[1] Karch R, Neumann F, Ullrich R, Neumüller J, Podesser BK, Neumann M, Schreiner W. The spatial pattern of coronary capillaries in patients with dilated, ischemic, or inflammatory cardiomyopathy. Cardiovasc Pathol 2005;14:135–44.

[2] Ogawa S, Lee TM, Kay AR, Tank DW. Brain magnetic resonance imaging with contrast dependent on blood oxygenation. Proc Natl Acad Sci USA 1990;87:9868–72.

[3] Yablonskiy DA, Sukstanskii AL, He X. Blood oxygenation level-dependent (BOLD)-based techniques for the quantification of brain hemodynamic and metabolic properties - theoretical models and experimental approaches. NMR Biomed 2013;26:963–86.

[4] Davda S, Bezabeh T. Advances in methods for assessing tumor hypoxia in vivo: implications for treatment planning. Cancer Metastasis Rev 2006;25:469–80.

[5] Tatum JL, Kelloff GJ, Gillies RJ, Arbeit JM, Brown JM, Chao KS. et al. Hypoxia: importance in tumor biology, noninvasive measurement by imaging, and value of its measurement in the management of cancer therapy. Int J Radiat Biol 2006;82:699–757.

[6] Torrey HC. Bloch equations with diffusion terms. Phys Rev 1956;104:563–5.

[7] Yablonskiy DA, Haacke EM. Theory of NMR signal behavior in magnetically inhomogeneous tissues: the static dephasing regime. Magn Reson Med 1994;32:749–63.

[8] Sukstanskii AL, Yablonskiy DA. Gaussian approximation in the theory of MR signal formation in the presence of structure-specific magnetic field inhomogeneities. Effects of impermeable susceptibility inclusions. J Magn Reson 2004;167:56–67.

[9] Jensen JH, Chandra R, Ramani A, Lu H, Johnson G, Lee SP. et al. Magnetic field correlation imaging. Magn Reson Med 2006;55:1350–61.

[10] Kiselev VG, Posse S. Analytical model of susceptibility-induced MR signal dephasing: effect of diffusion in a microvascular network. Magn Reson Med 1999;41:499–509.

[11] Tarczon JC, Halperin WP. Interpretation of NMR diffusion measurements in uniform- and nonuniform-field profiles. Phys Rev B 1985;32:2798–807.

[12] Ziener CH, Kampf T, Reents G, Schlemmer HP, Bauer WR. Spin dephasing in a magnetic dipole field. Phys Rev E 2012;85:051908.

[13] Ziener CH, Kurz FT, Kampf T. Free induction decay caused by a dipole field. Phys Rev E 2015;91:032707.

[14] Dickson JD, Ash TWJ, Williams GB, Sukstanskii AL, Ansorge RE, Yablonskiy DA. Quantitative phenomenological model of the BOLD contrast mechanism. J Magn Reson 2011;212:17–25.

[15] Kurz FT, Kampf T, Heiland S, Bendszus M, Schlemmer HP, Ziener CH. Theoretical model of the single spin-echo relaxation time for spherical magnetic perturbers. Magn Reson Med 2014;71:1888–95.

[16] Ziener CH, Kampf T, Jakob PM, Bauer WR. Diffusion effects on the CPMG relaxation rate in a dipolar field. J Magn Reson 2010;202:38–42.

[17] Ziener CH, Kampf T, Melkus G, Herold V, Weber T, Reents G. et al. Local frequency density of states around field inhomogeneities in magnetic resonance imaging: effects of diffusion. Phys Rev E 2007;76:031915.

[18] Krogh A. The supply of oxygen to the tissues and the regulation of the capillary circulation. J Physiol (London) 1919;52:457–74.

[19] Sedlacik J, Rauscher A, Reichenbach JR. Obtaining blood oxygenation levels from MR signal behavior in the presence of single venous vessels. Magn Reson Med 2007;58:1035–44.

[20] Fraser GM, Milkovich S, Goldman D, Ellis CG. Mapping 3-D functional capillary geometry in rat skeletal muscle in vivo. Am J Physiol Heart Circ Physiol 2012;302:H654–64.

[21] Ziener CH, Kampf T, Melkus G, Jakob PM, Schlemmer HP, Bauer WR. Signal evolution in the local magnetic field of a capillary - analogy to the damped driven harmonic oscillator. Magn Reson Imaging 2012;30:540–53.

[22] Kurz FT, Kampf T, Buschle LR, Heiland S, Schlemmer HP, Bendszus M. et al. CPMG relaxation rate dispersion in dipole fields around capillaries. Magn Reson Imaging 2016;34:875–88.

[23] de Groot J, Reardon DA, Batchelor TT. Antiangiogenic therapy for glioblastoma: the challenge of translating response rate into efficacy. Am Soc Clin Oncol Educ Book 2013;71–8.

[24] Karch R, Neumann M, Neumann F, Ullrich R, Neumüller J, Schreiner W. A Gibbs point field model for the spatial pattern of coronary capillaries. Physica A 2006;369:599–611.

[25] Bauer WR, Schulten K. Theory of contrast agents in magnetic resonance imaging: coupling of spin relaxation and transport. Magn Reson Med 1992;26:16–39.

[26] Bauer WR, Nadler W, Bock M, Schad LR, Wacker C, Hartlep A. et al. The relationship between the BOLD-induced T2 and T2*: a theoretical approach for the vasculature of myocardium. Magn Reson Med 1999;42:1004–10.

[27] Ziener CH, Glutsch S, Jakob PM, Bauer WR. Spin dephasing in the dipole field around capillaries and cells: numerical solution. Phys Rev E 2009;80:046701.

[28] Reichenbach JR, Haacke EM. High-resolution BOLD venographic imaging: a window into brain function. NMR Biomed 2001;14:453–67.

[29] Ziener CH, Bauer WR, Jakob PM. Frequency distribution and signal formation around a vessel. Magn Reson Mater Phy 2005;18:225–30.

[30] Ziener CH, Kampf T, Herold V, Jakob PM, Bauer WR, Nadler W. Frequency autocorrelation function of stochastically fluctuating fields caused by specific magnetic field inhomogeneities. J Chem Phys 2008;129:014507.

[31] Grebenkov DS. NMR survey of reflected Brownian motion. Rev Mod Phys 2007;79:1077–137.

[32] Sen PN, Axelrod S. Inhomogeneity in local magnetic field due to susceptibility contrast. J Appl Phys 1999;86:4548–54.

[33] Caillol JM, Levesque D, Weis JJ, Hansen JP. A Monte Carlo study of the classical two-dimensional one-component plasma. Stat Phys 1982;28:325–49.

[34] de Leeuw SW, Perram JW. Statistical mechanics of two-dimensional Coulomb systems: II. The two-dimensional one-component plasma. Physica A 1982;113:546–58.

[35] Metropolis N, Rosenbluth AW, Rosenbluth MN, Teller AH, Teller E. Equation of state calculations by fast computing machines. J Chem Phys 1953;21(6):1087–92.

[36] Kennan RP, Zhong J, Gore JC. Intravascular susceptibility contrast mechanisms in tissues. Magn Reson Med 1994;31:9–21.

[37] Ziener CH, Bauer WR, Melkus G, Weber T, Herold V, Jakob PM. Structure-specific magnetic field inhomogeneities and its effect on the correlation time. Magn Reson Imaging 2006;24:1341–7.

[38] Spees WM, Yablonskiy DA, Oswood MC, Ackerman JJ. Water proton MR properties of human blood at 1.5 Tesla: magnetic susceptibility, T(1), T(2), T*(2), and non-Lorentzian signal behavior. Magn Reson Med 2001;45:533–42.

[39] Ziener CH, Kampf T, Melkus G, Jakob PM, Bauer WR. Scaling laws for transverse relaxation times. J Magn Reson 2007;184:169–75.

[40] Kurz FT, Kampf T, Buschle LR, Schlemmer HP, Heiland S, Bendszus M. et al. Microstructural analysis of peripheral lung tissue through CPMG inter-echo time R2 dispersion. PLoS ONE 2015;10:e0141894.

[41] He X, Yablonskiy DA. Quantitative BOLD: mapping of human cerebral deoxygenated blood volume and oxygen extraction fraction: default state. Magn Reson Med 2007;57:115–26.

[42] Zhang J, Liu T, Gupta A, Spincemaille P, Nguyen TD, Wang Y. Quantitative mapping of cerebral metabolic rate of oxygen (CMRO2) using quantitative susceptibility mapping (QSM). Magn Reson Med 2015;74:945–52.

[43] Ziener CH, Rückl M, Kampf T, Bauer WR, Schlemmer HP. Mathieu functions for purely imaginary parameters. J Comp Appl Math 2012;236:4513–24.

[44] Ziener CH, Kurz FT, Buschle LR, Kampf T. Orthogonality, Lommel integrals and cross product zeros of linear combinations of Bessel functions. SpringerPlus 2015;4:390.

[45] Kurz FT, Buschle LR, Kampf T, Zhang K, Schlemmer HP, Heiland S. et al. Spin dephasing in a magnetic dipole field around large capillaries: approximative and exact results. J Magn Reson 2016;273:83–97.

[46] Bechstedt F, Enderlein R. Semiconductor surfaces and interfaces - their atomic and electronic structures. Berlin: Akademie-Verlag; 1988.

Publication II:
Voxel-wise parametrization
of microvascular regularity

Title: Gibbs point field model quantifies disorder in microvasculature of U87-glioblastoma

Authors: <u>Artur Hahn</u>, Julia Bode, Thomas Krüwel, Lukas R. Buschle, Volker J. F. Sturm, Ke Zhang, Björn Tews, Heinz-Peter Schlemmer, Sabine Heiland, Martin Bendszus, Christian H. Ziener, Michael O. Breckwoldt and Felix T. Kurz

Journal: Journal of Theoretical Biology 494:110230 (2020)

DOI: 10.1016/j.jtbi.2020.110230

Contributions: A.H. performed the data processing and programmed the numerical and analytical tools for processing, visualization, and statistical analysis. J.B., T.K., M.O.B., and B.T. were responsible for animal handling and image data acquisition through tissue clearing and ultramicroscopy. A.H. wrote the numerical simulations to produce idealized plasma distributions with help from L.R.B, V.J.F.S, and K.Z. The study was conceptualized by A.H. and F.T.K., and supervised by F.T.K., C.H.Z., and M.O.B. Statistical analyses were performed by A.H. and F.T.K. and the manuscript was written by A.H. with input from HP.S., S.H., M.B, and all other authors.

Gibbs point field model quantifies disorder in microvasculature of U87-glioblastoma

Artur Hahn [a,b], Julia Bode [c], Thomas Krüwel [c], Thomas Kampf [d,e], Lukas R. Buschle [a,f],
Volker J.F. Sturm [a,f], Ke Zhang [f], Björn Tews [c], Heinz-Peter Schlemmer [f], Sabine Heiland [a],
Martin Bendszus [a], Christian H. Ziener [a,f], Michael O. Breckwoldt [a,g], Felix T. Kurz [a,f,*]

[a] *Department of Neuroradiology, Heidelberg University Hospital, Im Neuenheimer Feld 400, Heidelberg 69120, Germany*
[b] *Department of Physics and Astronomy, University of Heidelberg, Im Neuenheimer Feld 226, Heidelberg 69120, Germany*
[c] *Molecular Mechanisms of Tumor Invasion, Schaller Research Group, University of Heidelberg and German Cancer Research Center (DKFZ), Im Neuenheimer Feld 581, Heidelberg 69120, Germany*
[d] *Department of Experimental Physics 5, University of Würzburg, Am Hubland, Würzburg 97074, Germany*
[e] *Department of Neuroradiology, University Hospital Würzburg, Josef-Schneider-Straße 2, Würzburg 97080, Germany*
[f] *Department of Radiology E010, German Cancer Research Center (DKFZ), Im Neuenheimer Feld 280, Heidelberg 69120, Germany*
[g] *Clinical Cooperation Unit Neuroimmunology and Brain Tumor Immunology, German Cancer Research Center (DKFZ), Im Neuenheimer Feld 280, Heidelberg 69120, Germany*

ARTICLE INFO

ABSTRACT

Microvascular proliferation in glioblastoma multiforme is a biological key mechanism to facilitate tumor growth and infiltration and a main target for treatment interventions. The vascular architecture can be obtained by Single Plane Illumination Microscopy (SPIM) to evaluate vascular heterogeneity in tumorous tissue. We make use of the Gibbs point field model to quantify the order of regularity in capillary distributions found in the U87 glioblastoma model in a murine model and to compare tumorous and healthy brain tissue. A single model parameter Γ was assigned that is linked to tissue-specific vascular topology through Monte-Carlo simulations. Distributions of the model parameter Γ differ significantly between glioblastoma tissue with mean $\langle \Gamma_G \rangle = 2.1 \pm 0.4$, as compared to healthy brain tissue with mean $\langle \Gamma_H \rangle = 4.9 \pm 0.4$, suggesting that the average Γ-value allows for tissue differentiation. These results may be used for diagnostic magnetic resonance imaging, where it has been shown recently that Γ is linked to tissue-inherent relaxation parameters.

1. Introduction

Glioblastoma multiforme, the most common and lethal brain tumor to occur in humans, is highly angiogenic with fast progression (Gatson et al., 2012; Das and Marsden, 2013). Upon developing an angiogenic phenotype (Bergers and Benjamin, 2003), tumor cells regulate the biochemical environment and activate oncogenes to trigger the formation of new capillaries from preexisting vessels by different mechanisms (Aghi and Chiocca, 2005; Ricci-Vitiani et al., 2010; Wang et al., 2010; Soda et al., 2011), *e.g.*, through endothelial cell proliferation and basement membrane degradation (Volpert et al., 1997). The newly formed tumor microvasculature is heterogeneous and increasingly variable in density and structure when compared to healthy brain microvasculature (Gillies et al., 1999; Carmeliet and Jain, 2000), which impacts treatment efficacy

and strategies in irradiation and chemotherapy (McDougall et al., 2002; 2006; Hanahan and Weinberg, 2011; Good and Harrington, 2013; Jain, 2013).

Excellent experimental studies and modeling efforts have paved the way to understand microvasculature as an integral component of any functioning organ (Wiedeman et al., 1981; Pries et al., 1990; Moody et al., 1990; Pries et al., 1995; Pries and Secomb, 2000), also in the context of tumor growth (Carmeliet and Jain, 2000; Chaplain and Anderson, 2004; Döme et al., 2007; Fukumura et al., 2010; Rieger and Welter, 2015), which has enabled the development of sophisticated biophysical models of how vascular networks are formed (Scianna et al., 2013; Cai et al., 2016; Rieger et al., 2016; Spill et al., 2015; Perfahl et al., 2017), maintained, and dynamically adapted throughout the presence of metabolic, hemodynamic, and mechanical influences (Cai et al., 2011; Pries et al., 1996; Pries and Secomb, 2008; Secomb et al., 2013). Decades of experimental, theoretical, and numerical work have revealed a complex coupling between vascular architecture, tissue metabolism, and tumor

growth (Owen et al., 2009; Welter et al., 2009; Vilanova et al., 2018), while different approaches on modeling the capillary bed have increasingly elucidated the nonlinear interplay of vascular geometry, rheology, lumen structure, and extravascular environment in regulating the supply and distribution of oxygen, nutrients, and drugs within tissue (Boujelben et al., 2016; Fang et al., 2008; Goldman, 2008; Macklin et al., 2009; Welter and Rieger, 2013; Wu et al., 2014).

Decades of progress have made it evident that quantitative descriptions and modeling focused on local vessel geometry are not sufficient for a detailed understanding of tissue supply, metabolism, and phenomena like hypoxia (Goldman, 2008). Nonlocal, topological characterizations of vascular networks can usefully augment local analyses and facilitate an understanding of collective phenomena. Recently, large cerebrovascular networks in healthy and tumor-bearing mice were quantified using graph theory, revealing tumor-induced remodeling of connectivity, concealed in geometric vessel properties (Hahn et al., 2019). Several studies have determined space-filling metrics on healthy and pathological vasculature, including measures of self-similarity and fractal properties (Gazit et al., 1995; Smith et al., 1996; Gazit et al., 1997; Baish and Jain, 2000; Gould et al., 2011). However, the utility of such measures has been subject to discussion in the biomedical community, since results can depend on processing, realistic structures are not true fractal objects, and some parameters, such as the lacunarity can vary strongly (errors of up to 50%) within cohorts and studies (Mancardi et al., 2008). Furthermore, it is often difficult to construct a direct link between the determined quantities and the underlying biological concepts or insights.

The complex arrangement and dynamic adaptivity of microvasculature (McDougall et al., 2006; Pries and Secomb, 2008), with a multitude of physiological influences constantly interacting, indicate that statistical methods may be better suited to quantify microvascular architecture, especially in the context of pathological remodeling (Zou and Wu, 1995; Coffey, 1998; Guidolin et al., 2004). It was demonstrated that the statistical distribution of nearest-vessel distances within tissue could grant new insights into vascular remodeling by parametrizing the shapes of tissue regions void of vasculature (Baish et al., 2011), although in this parametrization, the U87 tumor model showed exceptions in the identified trends, rather resembling healthy tissue than other tumor types. Elsewhere, the vessel density distribution has been modeled and compared to random uniform distributions to identify "angiogenic hotspots" in growing tumors (Kather et al., 2015), whereas, in a different study, it was shown that local vascular density does not suffice in assessing radiation effects (Scott et al., 2016). There, a distance-dependent correlation measure, Ripley's L function, was used to quantify vessel distribution inhomogeneity, which yielded more differentiable results after irradiation.

Despite great progress in characterizing anomalies of tumor vasculature, such results have not been linked to any non-invasive imaging modalities, in order to be made useful for diagnostic purposes or treatment monitoring. Statistical methods rely on large histological tissue samples and high-resolution microscopy, providing only retrospective insight. Nevertheless, if successfully linked to a noninvasive imaging method, statistical parametrizations of the microvasculature may be used to develop imaging biomarkers (Deng and Wang, 2017). High resolution fluorescence microscopy enables large-scale studies of the tumor microenvironment to an unprecedented extent, which, in turn, allows for an evaluation of different models for the characterization of tumor microvasculature, as well as correlations with other modalities, such as magnetic resonance imaging (MRI) (Breckwoldt et al., 2016, 2019).

The aim of our study was to assess the value of an entropy point field model taken from statistical physics to characterize cerebral microvasculature, see also (Karch et al., 2006). This model originally describes a system of identical interacting point charges in a canonical ensemble, that are embedded in an oppositely charged, uniformly distributed background (de Leeuw and Perram, 1982). Therefore, hereafter, we refer to the model as one-component plasma (OCP). The OCP model has previously been used in thermodynamic simulations with great reliability (see, *e.g.*, (Alastuey and Jancovici, 1981; Caillol et al., 1982)). An analogy between Poisson's equation, governing a plasma's charge distribution, and the steady-state oxygen diffusion equation through tissue justifies an application of this statistical model to capillary distributions within living tissue (Goldman, 2008). Through the incorporation of a temperature parameter, this model bears the potential to collectively describe perturbing factors and dynamic adaptation of the capillary bed in a simple, statistical manner (Karch et al., 2006). Due to its sensitivity to the disorder and clustering of vessel distributions through a single dimensionless order parameter Γ, the OCP model can be linked to the vascular-induced relaxation rate of a single voxel in an MR experiment (Kurz et al., 2017). It is therefore potentially relevant for the non-invasive evaluation of cerebrovascular pathology, specifically that of glioblastoma multiforme, which thrives on microvascular proliferation (Das and Marsden, 2013).

In this work, we combine advanced imaging technology and numerical methods to test the feasibility of a reliable differentiation between tumorous and healthy brain tissue. We apply the OCP to microvasculature in the murine brain, imaged using high resolution light sheet fluorescence microscopy after optical clearing of the whole brain. Finally, the viability of using MRI to infer on the model parameter Γ in a voxel-wise manner for diagnostic purposes is discussed in light of these and previous results.

2. Methods

2.1. Monte-Carlo simulations of the entropy point field model

A Metropolis-Monte-Carlo simulation (Metropolis et al., 1953) was written in C++ to produce point distributions in "thermal" equilibrium of the entropy point field model with predefined order parameters Γ, in analogy to the methodology in (Karch et al., 2006) (see Appendix A for details on the OCP model). In the simulation, $N = 200$ identically charged point particles were placed randomly into a hexagonal unit box with periodic boundary conditions. A simulation box with width b and height $h = \sqrt{3} \cdot b$, representing a hexagonal unit cell, allows for correct behaviour of the system during "crystallization" with an even particle number N (Caillol et al., 1982).

In analogy to thermodynamics, a Gibbs system was simulated for a given Γ, i.e. fixed temperature $T = q^2/k_B\Gamma$, by "cooling" the initial random point distribution into an energetically appropriate configuration, associated with the chosen temperature. The Metropolis algorithm implements this process by attempting quasi-random moves of the charges and comparing the internal energy before a move, U_{old}, with the energy after the hypothetical move, U_{new} (see Appendix A.1 for details). The internal energy U is determined using Eq. (A.5) in Appendix A, with the convergence parameter set to $\eta = 6/b$, following the conventions of Karch et al., 2006 for the truncation of sums.

In the simulation, a certain position change is accepted with probability $p(\Delta U)$ that scales with the energy difference $\Delta U = U_{old} - U_{new}$:

$$p(\Delta U) = \min\left[\exp\left(\frac{\Delta U}{k_B T}\right), 1\right] = \min\left[\exp\left(\Gamma \cdot \Delta U'\right), 1\right], \quad (1)$$

where $U' = U/q^2$ is the dimensionless free energy (see Eqs. (A.3) and (A.4) in Appendix A). The decision to accept or reject a new charge distribution is made by generating a uniformly

distributed, quasi-random number $x \in [0, 1]$, leading to acceptance if $x \leq p(\Delta U)$. Otherwise, the charge distribution is left in its state before the hypothetical move and the process is repeated with a new attempt.

Each simulation was conducted with 10^5 attempted particle moves in order to reach thermal equilibrium. It was made sure that equilibrium was reached within the simulated time interval for the entire range of considered Γ-values by recording the internal energy U after every accepted move and checking for convergence within the simulation time. 500 respective point distributions were produced for logarithmically incremented values between $\Gamma = 10^{-7}$ and $\Gamma = 10^2$, amounting to 58,000 charge distributions in total, with 500 additional random uniform distributions for reference ($\Gamma \to 0$).

The produced point configurations were characterized using a custom-written script in Matlab R2017a (Mathworks, Natick, MA, USA), to correlate distributive properties with the underlying Γ-values. To omit density effects, the spatial coordinates were rescaled to units of the Wigner–Seitz radius $a = (\pi \rho)^{-1/2}$ with the number density $\rho = N/A$ of N points in an area A (Caillol et al., 1982). The charge positions were taken as the bases for Voronoi (or Dirichlet) tessellations (Okabe et al., 1999), where the box areas were subdivided into so-called Voronoi polygons, one assigned to each reference charge, using the software kit Qhull (Barber et al., 1996). A Voronoi polygon consists of all the points that are closer to that cell's corresponding oxygen source than to any other.

For each charge distribution, nearest neighbor distances d and Voronoi cell attributes, namely the area A_V, perimeter P_V, edge number N_e, and asphericity $\alpha_V = P_V^2/(4\pi A_V)$ were calculated in units of a (excluding boundary cells). The next neighbor distance d is given by the separation of the closest lying oxygen source to a reference source. The asphericity quantifies how strongly a Voronoi cell deviates from circular shape, with an asphericity of $\alpha = 1$ describing a circle and higher values $\alpha > 1$ found for increasingly eccentric polygons (Karch et al., 2006). For each topological property, mean and standard deviation within the plane were calculated. From the 500 configurations produced for each Γ-value, the average of every statistical parameter was determined in order to build a statistical link between the order parameter Γ and the corresponding distribution topology.

2.2. Experimental data acquisition

2.2.1. Animal preparation and imaging

The vessel morphology of undissected, healthy and tumor-bearing mouse brains was imaged with the LaVision Biotec Ultramicroscope II, as described before (Breckwoldt et al., 2016). Briefly, we injected $7.5 \cdot 10^5$ U-87MG cells (ATCC HTB-14), diluted in 5 µl sterile phosphate buffered saline, into the right brain hemisphere, 2 mm lateral and 2 mm ventral of the bregma, in 9 week old, male NOD Scid Gamma mice (NSG, DKFZ, Heidelberg). The cells regularly tested negative for mycoplasma contamination in biweekly examinations before implantation. A total of $n = 6$ animals with glioblastoma were compared against $n = 6$ brain hemispheres from 3 healthy mice (animal approval G223/14 by the regional animal welfare committee in Karlsruhe, Germany).

For the fluorescent staining of vessel lumen, the animals were injected intravenously with 300 µl of 1 mg/ml concentrated lectin-FITC (Sigma-Aldrich, St. Louis, MO, USA). For tumor-bearing mice, this was done 21 days after tumor cell implantation. After 3 min of marker circulation, mice were sacrificed using a ketamine/xylazine overdose and transcardially perfused with 20 ml PBS and 20 ml 4% PFA. The brain was then explanted and optically cleared using the FluoClearBABB protocol (Schwarz et al., 2015). Following a successful tissue clearing, Selective Plane Illumination Microscopy (SPIM) (Ertürk et al., 2012) was used to image the labeled vasculature in the entire brain by fluorescent excitement of the lectin marker with 3.25 µm in-plane resolution and 5 µm between slices in the transverse plane. The following acquisition parameters were used: 5 µm stepsize, dynamic focus on (5-10 steps), camera exposure time of 686 ms, 16-bit low noise gain with combined left and right lightsheet.

2.2.2. Segmentation of vascular architecture

The vessels were segmented from the acquired image stacks using the interactive learning and segmentation software ilastik (Sommer et al., 2011). A 3D-Gaussian filter with an isotropic standard deviation of $\sigma = 1$ (voxel units) was applied to the segmentations using the 3D-smoothing plugin in the ImageJ-distribution Fiji 2.0.0-rc-43/1.51r (Schindelin et al., 2012). The volume was cast back to binary form with a hard intensity threshold at half of the maximum voxel value. A custom Matlab script was used to fill holes in the segmented vessels, followed by an additional noise removal to delete isolated voxel bunches with a volume of less than that of a sphere with a radius of 20 µm. Vessel center lines were extracted using the skeletonization algorithm (Lee et al., 1994) in ImageJ.

Binary masks were manually drawn for each image stack to extract tumor tissue and well-imaged regions in the healthy brain for analysis. In the healthy specimens, this comprised the inner parts of the brain, including the midbrain, hippocampus, thalamus, hypothalamus, septum, striatum, caudate putamen, amygdala, as well as inner sections of the cerebral cortex and cerebellum. The ventricles, exhibiting autofluorescence, were excluded by the masks. Care was taken to incorporate as many brain regions as possible into the healthy controls in order to make a general comparison between tumor and healthy brain vasculature.

2.2.3. Vascular irregularity in the entropy point field model

A custom Matlab routine was written to determine Γ-distributions for glioblastoma and healthy brain vasculature, modeling vessel center lines as one dimensional sources of oxygen (see Appendix A for details). To test the feasibility of extracting the order parameter Γ from magnetic resonance imaging (MRI), the Γ estimations were performed on cubic subvolumes with a side length of 500 µm, dimensions that are representative of an MRI-voxel in clinical routine. The tissue regions validated for analysis by the masks were covered in a tiling box fashion, whereas only cubes entirely inside the masked regions were considered to avoid irregular boundary effects.

For each imaging slice in a subvolume, the capillary centerlines cutting through that slice were interpreted as point-like oxygen sources. Due to the finite thickness of each imaging slice, in which vessel membranes were excited to fluoresce, some vessel segments were conceived as lying partially parallel to the imaging plane. Conceptually approximating the position of such a vessel segment in the infinitesimally thin center slice of the 5 µm thick imaging volume, the centroid of the skeleton piece was considered to assign a single point position to the oxygen source in such cases.

For analysis, the point source coordinates were scaled to units of the Wigner–Seitz radius $a = (\pi \rho)^{-1/2}$ with density $\rho = N/A$ of N oxygen sources in the area A. In analogy to the treatment of simulated point distributions, the vessel positions in each imaging slice were used for Voronoi tessellation (Okabe et al., 1999) and means and standard deviations of polygon area A_V, perimeter P_V, edge number N_e, asphericity α_V, and the nearest neighbor distance d were determined. This approach to quantify the vascular degree of regularity was motivated by work published by Karch et al. in 2005 and 2006 (Karch et al., 2005, 2006), dealing with the perfusion of the human heart with different cardiomyopathies. To avoid statistical undersampling effects, slices containing less than 50 oxygen sources were excluded from the automated analysis. A schematic
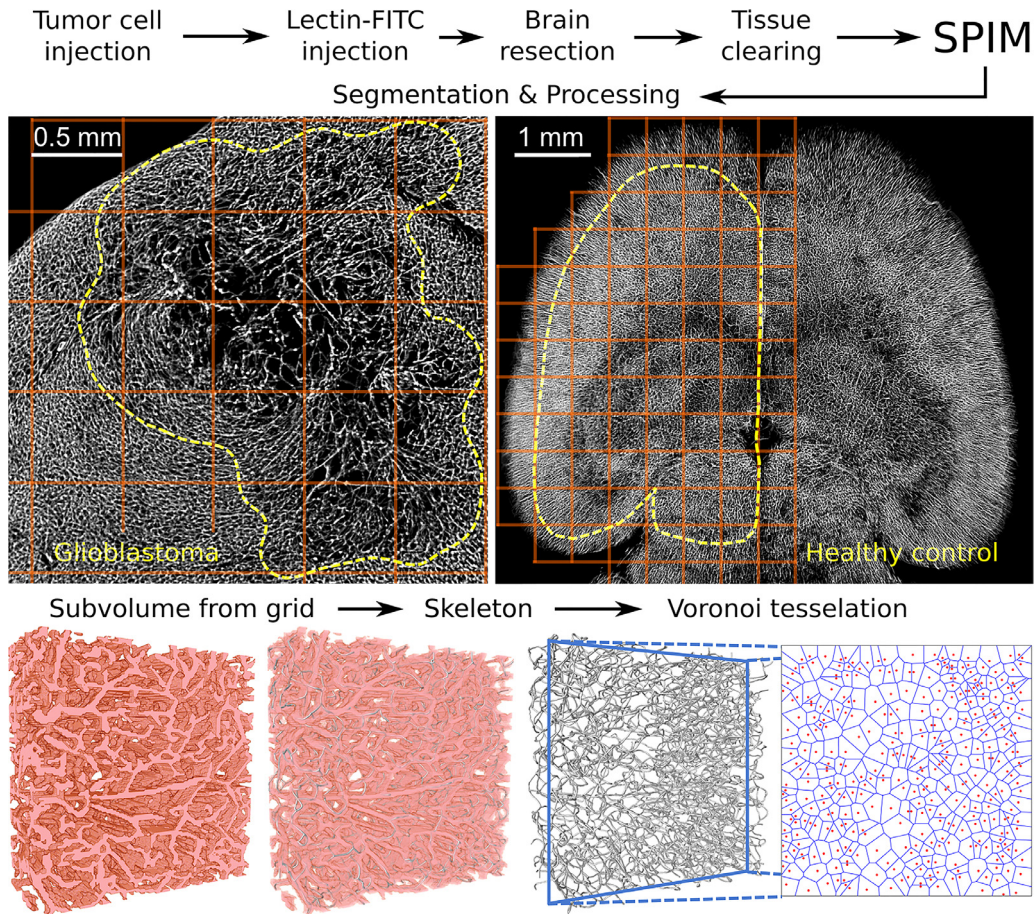
Fig. 1. Schematic representation of data acquisition and processing. Tumor cells were injected into the brains of mice. Once a large tumor had developed, Lectin-FITC was injected to mark the vessel lumen, followed by a brain resection after marker circulation. Tissue clearing made the brain transparent, allowing for plane-wise excitation of the fluorescent marker. Light sheet microscopy (SPIM) was used to image the microvasculature of the entire brain in stacks of planes. Segmentation and artefact processing produced 3D binary vessel representations, as illustrated in the second row through average intensity projections of $200\,\mu$m thick sections (40 slices) of a healthy brain (**right**) and a glioblastoma (**left**). The image data was gridded into cubes of 500 μm side length and cubes lying entirely within the respective regions of interest (encircled by dashed lines) were analyzed as demonstrated in the bottom row. In each qualified imaging slice, the vascular skeleton was used for Voronoi tessellation to provide an estimate for Γ. Ideally, each $(500\,\mu\text{m})^3$ cube would provide 100 Γ-values, from which Γ-distributions could be constructed to characterize the vasculature.

summary of the data acquisition and processing conducted up to the point of analysis is given in Fig. 1.

Each valid image slice in a (500 μm)^3 cropped subvolume was used to attain an estimate for the order parameter Γ. The curves produced from plasma simulations were used to infer on the value of Γ for each examined image section. From the volumes marked by the binary masks, Γ-distributions were determined to statistically characterize the disorder in tissue vascularization for both tissue types.

3. Results

3.1. Plasma simulations

The increasing degree of regularity with Γ is clearly visible in point distributions produced by Metropolis-Monte-Carlo simulations with corresponding Voronoi tessellations (Fig. 2, **a-c**). By averaging means and standard deviations of the considered topological properties within each plane over all simulations for every considered Γ-value, useful relations between the order parameter and a point distribution's expected topology could be revealed (see Fig. 2, **d-e** and Fig. B.1 in Supplementary Material). As a reference, corresponding properties from 500 completely random (uniformly distributed) point distributions are illustrated at $\Gamma = 10^{-\infty}$, representing expected topological properties of point sets without structure. The results indicate that, for $\Gamma < 10^{-2}$, the OCP model, as

simulated in this study, loses its ordering properties and resembles uniform, random point distributions. For $10^{-2} \leq \Gamma \leq 10^2$, polynomial fits to the mean topological properties with the decadic logarithm of Γ yielded continuous interpolations, which could be used to estimate Γ from suitable characteristics through backward inference using the attained curves (with fifth degree polynomials for all properties, except for the mean nearest neighbor distance $\langle d \rangle$, which was better described by a ninth degree polynomial, see Table 1 for details).

All calculated characteristics (with the exception of the mean Voronoi cell perimeter $\langle P_V \rangle$) presented dependences similar to those found in Fig. 2, **d-e** (see Fig. B.1 in Supplementary Material). Of the average topological characteristics considered, particularly the mean nearest neighbor distance $\langle d \rangle$ and Voronoi cell area standard deviation $\sigma(A_V)$ presented dynamic, well defined relations with the Γ-parameter, exhibiting relatively low variance among simulation runs. The characteristic plateau for $\Gamma < 10^{-2}$, suggesting that the influence of the Γ-parameter was lost below this value, was taken into account in subsequent evaluations by assigning $\Gamma = 0$ in this range (corresponding to maximum entropy point distributions).

3.2. Model application to experimental data

The processed ultramicroscopy stacks from $n = 6$ glioblastoma xenografts and $n = 6$ healthy brain hemispheres provided a total of
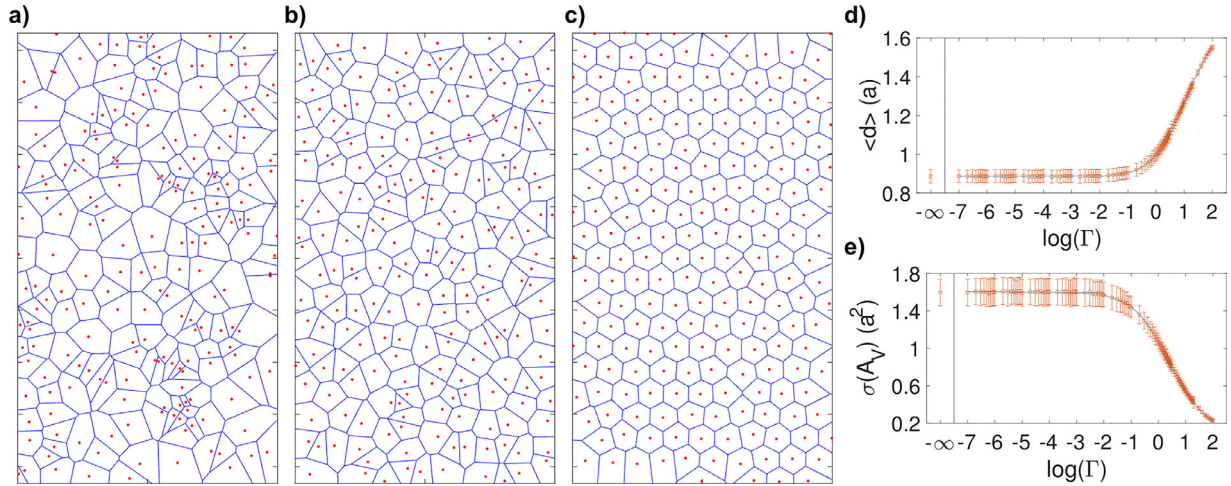
Fig. 2. Results of plasma simulations. Exemplary point distributions (red points) and corresponding Voronoi tesselations (blue lines) with order parameters **a)** $\Gamma = 0.1$, **b)** $\Gamma = 4$, and **c)** $\Gamma = 140$. Average of **d)** the mean nearest neighbor distance $\langle d \rangle$ and **e)** the standard deviation of Voronoi cell areas $\sigma(A_V)$ within, respectively, 500 point distributions simulated at different Γ-values. The mean value for each Γ is marked by a square marker, with error bars indicating the standard deviation among 500 simulation runs. Below the markers, a solid curve shows piecewise polynomial fits to the discrete simulation points.

Table 1
Polynomial coefficients from least-squares fits to the relationships between Γ and the topological characteristics P_t of modeled point distributions. In the dynamic region ($\Gamma > 0.01$), all topological properties P_t (in natural units of the Wigner-Seitz radius a) are described well by a fifth degree polynomial of the form $P_t(\Gamma) = c_5 (\log \Gamma)^5 + c_4 (\log \Gamma)^4 + c_3 (\log \Gamma)^3 + c_2 (\log \Gamma)^2 + c_1 (\log \Gamma) + c_0$, with the exception of the mean nearest neighbor distance $\langle d \rangle$, where a ninth degree polynomial better fits the relationship with $c_6 = 0.0029$, $c_7 = 0.0045$, $c_8 = -0.0002$, and $c_9 = -0.0005$. In the last column, the coefficient of variation R^2, considering the averaged topological properties used for fitting, is given to parametrize the goodness of fit. In the plateau region ($\Gamma \leq 0.01$), the relationships are practically constant and resemble the properties of random point distributions (cf. Figs. 2 and B.1 in Supplementary Material).

Topologic property P_t	$c_0/10^{-2}$	$c_1/10^{-2}$	$c_2/10^{-2}$	$c_3/10^{-2}$	$c_4/10^{-2}$	$c_5/10^{-2}$	R^2
$\langle d \rangle$	99.86	17.63	10.71	1.62	-2.08	-1.45	0.999
$\sigma(d)$	40.55	-8.39	-4.99	-0.53	0.57	0.15	0.999
$\langle A_V \rangle$	309.7	4.72	-0.37	-0.75	0.02	0.08	0.995
$\sigma(A_V)$	106.57	-50.39	-8.17	6.17	1.01	-0.5	0.999
$\langle P_V \rangle$	712.8	2.36	-8.63	-3.22	0.92	0.43	0.999
$\sigma(P_V)$	109.5	-57.14	-7.27	8.17	0.94	-0.74	0.999
$\langle \alpha_V \rangle$	136.94	-7.02	-2.96	0.39	0.34	-0.01	0.999
$\sigma(\alpha_V)$	18.6	-7.57	-2.15	1.22	0.28	-0.13	0.999
$\langle N_e \rangle$	590.39	2.54	0.67	-0.39	-0.07	0.05	0.997
$\sigma(N_e)$	122.63	-14.92	-8.11	-0.37	0.77	0.11	0.999

Table 2
Means μ and standard deviations STD of the topological quantities used to characterize vessel distributions in each plane, found in healthy brain and glioblastoma tissue.

	$d(a)$		$A_V(a^2)$		$P_V(a)$		α_V		N_e	
Tissue type	$\langle d \rangle$	$\sigma(d)$	$\langle A_V \rangle$	$\sigma(A_V)$	$\langle P_V \rangle$	$\sigma(P_V)$	$\langle \alpha_V \rangle$	$\sigma(\alpha_V)$	$\langle N_e \rangle$	$\sigma(N_e)$
Healthy tissue										
μ_H	1.25	0.56	3.0	1.4	6.9	1.5	1.38	0.21	5.90	1.26
STD_H	0.07	0.05	0.1	0.3	0.2	0.3	0.04	0.05	0.04	0.09
Glioblastoma										
μ_G	1.09	0.59	2.8	1.8	6.7	2.0	1.47	0.30	5.82	1.33
STD_G	0.13	0.07	0.3	0.5	0.4	0.4	0.10	0.12	0.12	0.15

27,489 valid image slices from healthy tissue and 18,209 from tumor tissue (each $500\,\mu m \times 500\,\mu m$ in size), after blinding through the masks. The cubic subvolumes for analysis were extracted from imaged tissue volumes of, on average, $14.0 \pm 4.2\,mm^3$ for healthy brain hemispheres and $9.2 \pm 4.7\,mm^3$ per bulk glioblastoma (with standard deviations), after approximately 40% isotropic shrinkage from clearing.

In Table 2, means and standard deviations of each topological quantity are given for healthy and tumor tissue, with corresponding histograms in Fig. 3 and B.2 in the supplements. All topologi-

cal parameters presented differences between tissue types. Based on the plasma simulation results in Fig. 2, **d-e** and supplementary Fig. B.1, as well as the results of Karch et al., 2006, an average over two paramters, namely the mean nearest neighbor distance $\langle d \rangle$ and a Voronoi cell attribute, the standard deviation of the area, $\sigma(A_V)$, were chosen as the most reliable indicators to determine a final estimate of Γ for each slice. Although the variables $\langle d \rangle$ and $\sigma(A_V)$ show some negative correlation (with correlation coefficients $r_H = -0.72$ for healthy datasets and $r_G = -0.39$ for glioblastoma datasets), they contain complementary information, with a
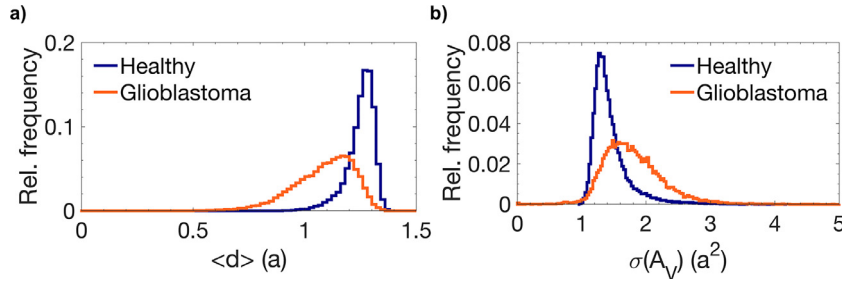
Fig. 3. Relative frequency histograms of topological parameters used to characterize oxygen source distributions in planes through healthy brain tissue and glioblastoma multiforme. **a)** Mean nearest neighbor distance $\langle d \rangle$ and **b)** standard deviation of the Voronoi cell area, in units of the Wigner-Seitz radius a.
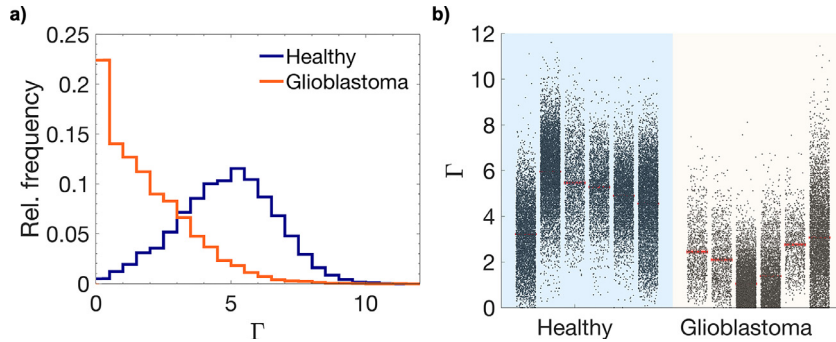

Fig. 4. Distributions of estimated Γ-values in healthy brain tissue and glioblastoma. **a)** Relative frequency histogram for all samples combined with a bin width of $\Delta\Gamma = 0.5$, including 27,489 values from healthy brain tissue and 18,209 values from glioblastoma, and **b)** Γ-estimates for each individual sample, with gray points marking Γ-estimates from individual slices, sample averages as horizontal red lines, and 95% confidence intervals marked by light red shading around the mean values.

stronger sensitivity of $\langle d \rangle$ to local clustering of vessels, while $\sigma(A_V)$ characterizes the cluster distribution throughout the entire plane.

Using the fitted relations established through plasma simulations (Fig. 2, **d-e** and Table 1), the Γ-distributions presented in Fig. 4 were attained from the average of the two values mapped to each $500\,\mu m$ square cross-section through the numerical inversion of the $\langle d \rangle(\Gamma)$ and $\sigma(A_V)(\Gamma)$ relationships. A two-sample t-test of the mean Γ-value from each independent sample rejected the null-hypothesis of distributions with equal means significantly ($p = 0.00027$). Analogous tests with the sample mean distributions of surrogate parameters $\langle d \rangle$ and $\sigma(A_V)$ yielded $p = 0.00093$ and $p = 0.0026$, respectively. The mean Γ-values from sample averages were $\langle \Gamma_H \rangle = 4.9 \pm 0.4$ in the healthy brain and $\langle \Gamma_G \rangle = 2.1 \pm 0.4$ in glioblastoma (with standard errors of mean). The total averages from all samples mixed amounted to $\langle \Gamma_H \rangle' = 4.84 \pm 0.01$ in healthy tissue and $\langle \Gamma_G \rangle' = 1.93 \pm 0.02$ in glioblastoma. The dimensionless order parameter Γ is thus suited for the differentiation of healthy and pathological microvasculature in the case of U87 glioblastoma multiforme.

4. Discussion

In this paper, we have presented a large-scale application of the entropy point field model in form of the OCP on murine brain vasculature, a highly irregular capillary environment, even in the healthy state. We could demonstrate that the OCP parametrization allows for a discrimination of microvasculature in the healthy brain and glioblastoma multiforme on a 500 µm imaging scale. Our results indicate that the dimensionless entropy parameter Γ can differentiate healthy and pathological tissue with greater significance than the individual, intermediate parameters $\langle d \rangle$ and $\sigma(A_V)$, from which Γ was derived. In light of the random sampling of cubic $(500\,\mu m)^3$ sections conducted on entire healthy mouse brains, these are motivating results. The analysis of randomly placed sections throughout the healthy brain incorporated partial volumes from different brain regions within the $500\,\mu m^2$ areas, which

systematically increased microvascular irregularity in the healthy samples. A discrimination of different brain regions and more selective tissue extractions are expected to increase Γ values associated with healthy tissue, leaving potential for further improvements in tumor tissue classification based on Γ, *e.g.*, through the inclusion of brain region priors.

After a rigorous study of the results of Karch et al. (Karch et al., 2006) and the topological attributes included in their original work, we chose only a subset of two properties, the nearest neighbor distance mean $\langle d \rangle$ and Voronoi cell area standard deviation $\sigma(A_V)$, in order to attain an averaged estimate for Γ. This decision was based on several factors. An important prerequisite for the inclusion of a topological parameter was a large dynamic range and definite relationship between Γ and the topological attribute. Some, eventually non-included, parameters presented a high variance and broad plateau in the region $\Gamma < 10^{-2}$, hampering a reliable estimate of Γ (cf. Fig. B.1 in Supplementary Material).

The OCP quantifies the spatial regularity of microvasculature without focusing on local vessel geometry or indirect surrogate parameters, which can be estimated from MRI to quantify tissue perfusion characteristics, *e.g.*, through diffusion weighted intravoxel-incoherent motion (IVIM) imaging (Bihan et al., 1988; Ahlgren et al., 2016), arterial spin labeling (ASL) (Williams et al., 1992; van Osch et al., 2018; Zhang et al., 2019a), or dynamic susceptibility contrast (DSC) measurements, tracking relaxation rate changes during the pass-through of an intravascular contrast agent bolus (Ostergaard et al., 1996; Romano et al., 2012; Emblem et al., 2013; Troprès et al., 2015). While rigorous mathematical derivations exist to predict the exact effects of certain vessel geometries on the transverse relaxation process during free induction decay (Ziener et al., 2012; 2015; Kurz et al., 2016a; 2016c; 2018) and spin echo measurements (Buschle et al., 2018; Kurz et al., 2016; Sukstanskii and Yablonskiy, 2002), their complicated form has hindered prevalent applications in clinical and preclinical settings. Approximations for the extreme cases of negligible and very strong diffu-

sion, which can be made for very large or small vessel geometries, respectively, simplify the solutions slightly at the cost of more idealized presumptions (Kiselev and Posse, 1998; Yablonskiy and Haacke, 1994). In any case, such analytical derivations have always assumed highly simplified cylindrical vessel representations, either in a perfectly regular or completely random (uniformly distributed) arrangement.

We have recently shown that the OCP can be incorporated into the theory of NMR dephasing, successfully relating the Γ-parameter to the field-inhomogeneity induced transverse relaxation rate $R_2' = R_2^* - R_2$ (Kurz et al., 2017). With this model, the existing theory of transverse relaxation in capillary environments could be extended by implementing the degree of disorder through Γ. The OCP framework poses a simple model to continuously bridge the gap between perfect capillary regularity and complete disorder, the only cases for which classical relaxation theory had been developed up to this point. We have now shown that this potentially has high relevance for oncological imaging in the brain.

In our previous study (Kurz et al., 2017), we found that the effects of changes in the intravascular oxygen saturation can outweigh the effects of different order parameters found in the physiological range. Our results, however, showed that the relationship between oxygenation changes and relaxation rate changes depends on Γ, motivating a way to gauge the effects of varying oxygenation through a comparison of transverse relaxation rates at different blood susceptibilities (determined by the blood oxygenation and hematocrit) or through intravascular contrast agents as, e.g., in (Troprès et al., 2004), in order to estimate the order parameter Γ of the underlying microvasculature. By varying the blood susceptibility, the off-resonance magnitude $\delta\omega$ is changed, impacting how the magnetization decays for capillary arrangements with different degrees of disorder (cf. (Kurz et al., 2017), Figs. 11 and 12). This effect may be exploited to infer experimentally on Γ by measuring T_2 and T_2^* to determine $R_2' = (1/T_2^*) - (1/T_2)$ at different blood susceptibilities, varied, e.g., through prolonged inhalation of O_2 or CO_2 enriched gas (Jochimsen and Möller, 2008; Shen et al., 2013). Stronger variations of blood susceptibility can be achieved in analogy to other methods of microvascular quantification relating to vessel density, calibre, and arterio-venous proportions, using MRI during steady-state or dynamic manipulations of T_2 and T_2^*, e.g., by injecting superparamagnetic iron-oxide nanoparticles (SPIONs) or gadolinium-based contrast agents into the bloodstream (see, e.g., vessel size imaging or vessel architectural imaging) (Emblem et al., 2013; Troprès et al., 2001; Farrar et al., 2010; Zhang et al., 2019b).

The development of such specialized methods should be conducted close to real MRI experiments, e.g., through a simultaneous acquisition of 3D T_2 and T_2^* maps and corresponding, highly resolved microvasculature of the same tissue through in vivo multiphoton microscopy (Osswald et al., 2015) or subsequent ex vivo SPIM (Breckwoldt et al., 2019), ideally in combination with a blood oxygenation-sensitive technique such as intrinsic optical signal imaging (Senarathna et al., 2019). Matching such datasets reliably with a precise, well localized, rigid registration bears great challenges and their treatment exceeds the scope of this work. Furthermore, experimental studies of the quantitative influence of contrast agent injections on the blood susceptibility under consideration of arterial input functions and bolus dispersion during flow would aid a refinement of such methodology (Calamante, 2013).

We have shown the theoretical viability of using the OCP to statistically differentiate healthy brain tissue from U87 glioblastoma multiforme, without discriminating gray or white matter, by combining advanced imaging methodology with an automated entropy assessment tool. The OCP serves as a simple model, governed by a single parameter Γ to quantify the degree of disorder in a vessel distribution, which has been successfully incorporated into NMR relaxation theory. Our findings show that the Γ parameter can

serve as a reliable biomarker for tumor diagnostics in such complex vascular environments as the brain. Beyond possible applications in MRI, a continuous parametrization of microvascular disorder, as given by the OCP model, offers a valuable extension to local and periodic approaches of modeling large-scale oxygen supply to tissue (Goldman, 2008).

Funding

Appendix A. Theory

A1. The one-component plasma

In statistical mechanics, Gibbs processes are frequently used to describe many-particle systems in thermal equilibrium with fixed temperature T, particle number N, and volume V. In such a canonical ensemble, the probability density $f(\mathbf{x}_1, ..., \mathbf{x}_N)$ for finding a system of N interacting point charges in the state $\mathbf{x}_1, ..., \mathbf{x}_N$ with coordinates $\mathbf{x}_i$ for particle $i \in \{1, ..., N\}$ is given by:

$$f(\mathbf{x}_1, ..., \mathbf{x}_N) = \frac{1}{Z} \exp\left\{-\frac{U(\mathbf{x}_1, ..., \mathbf{x}_N)}{k_B T}\right\}, \tag{A.1}$$

where $U(\mathbf{x}_1, ..., \mathbf{x}_N)$ is the system's internal energy and k_B is the Boltzmann constant. The canonical partition function Z incorporates all possible configurations of the system and, in the simplifying case of massless point charges without kinetic energy, can be expressed as:

$$Z = \int_\Omega \exp\left\{-\frac{U(\mathbf{x}_1, ..., \mathbf{x}_N)}{k_B T}\right\} d\mathbf{x}_1 ... d\mathbf{x}_N. \tag{A.2}$$

In this idealized setting, the phase space Ω is spanned by all possible particle positions, i.e. the cartesian product V^N.

Since the potential energy of the system only depends on the relative distances of the identical particles, the total energy is conveniently expressed through a sum over pair interaction potentials $\phi(r_{ij})$ for charge pairs $i, j \in \{1, ..., N\}$ with separation $r_{ij} = |\mathbf{x}_j - \mathbf{x}_i|$:

$$U(\mathbf{x}_1, ..., \mathbf{x}_N) = \frac{1}{2} \sum_i \sum_{j \neq i} \phi(r_{ij}). \tag{A.3}$$

The pair interaction potential can be chosen to scale logarithmically with point separation:

$$\phi(r_{ij}) = -q^2 \log\left(\frac{r_{ij}}{L}\right), \tag{A.4}$$

modeling the repulsion of particles with identical charge q. An advantage of considering point particles with vanishing radius is that the particle density does not influence the macroscopic characteristics of the distribution in thermal equilibrium, therefore allowing for an arbitrary choice of the scaling constant L. A convenient gauge is the Wigner–Seitz radius $a = (\pi \rho)^{-1/2}$ with particle density $\rho = N/A$, where the available area A constitutes the volume V in two dimensions. Scaling with the density ρ by setting $L = a$ makes point distributions with different physical densities directly comparable.

Especially in numerical treatments of the OCP, it is common practice to consider relatively small many-particle systems (on the order of 10^2 charges) with periodic boundary conditions, evading boundary effects while keeping computational expense feasible. Particularly useful in such cases, an alternative to Eq. (A.3) can be used to evaluate the total energy (Ewald, 1921). Working with copies of the hexagonal unit cell of area A, containing N charges, each displaced by a translational vector $\boldsymbol{n}$ to periodically tile out an infinite plane, the total internal energy U of the system can be assessed as follows (Karch et al., 2006):

$$U = \frac{q^2}{4} \sum_{\boldsymbol{n}} \sum_{i,j}^{N} {}' \mathrm{E}_1\big[\eta^2(\boldsymbol{r}_{ij} + \boldsymbol{n})^2\big]$$
$$+ \frac{\pi}{A} \sum_{\boldsymbol{k} \neq \boldsymbol{0}} \frac{\exp(-|\boldsymbol{k}|^2/4\eta^2)}{|\boldsymbol{k}|^2} \cdot \left|\sum_{j=1}^{N} q \exp(i\boldsymbol{k} \cdot \boldsymbol{r}_{ij})\right|^2$$
$$- \frac{\pi N^2 q^2}{4\eta^2 A} - \frac{Nq^2}{4}\big(\gamma + \log(\eta^2 a^2)\big). \tag{A.5}$$

The first sum is evaluated in real space, running over all lattice vectors $\boldsymbol{n}$ and charge pairs $i, j \in \{1, ..., N\}$ with separation vector $\boldsymbol{r}_{ij} = \mathbf{x}_j - \mathbf{x}_i$. The prime on the inner sum indicates that the self-interaction term with $i = j$ is left out for $\boldsymbol{n} = \boldsymbol{0}$. The second term is defined in Fourier space with the reciprocal unit vectors $\boldsymbol{k}$, taking into account the long-range interactions of the system. As before, the particle charge is q and the Wigner-Seitz radius is denoted by $a = (\pi \rho)^{-1/2}$. The exponential integral E_1 is given by (Abramowitz and Stegun, 1972):

$$\mathrm{E}_1(z) = \int_z^{\infty} \frac{\mathrm{e}^{-t}}{t} \mathrm{d}t \tag{A.6}$$

and the adjustable parameter η influences the convergence rate of the real and reciprocal space sums. At last, $\gamma = 0.5772...$ is Euler's constant.

A2. A model for the oxygen supply of tissue

In scenarios where the OCP is used to model electrostatics, the logarithmic pair interaction potential in Eq. A.4 emerges from the classical approach of solving the 2D Poisson equation:

$$\varepsilon \Delta \Phi(\mathbf{x}) = -\rho(\mathbf{x}) = -2\pi q \sum_i \delta(\mathbf{x} - \mathbf{x}_i) - C \tag{A.7}$$

with the charge density $\rho(\mathbf{x})$ consisting of point charges q at positions $\mathbf{x}_i$, modeled by Dirac delta functions $\delta(\mathbf{x} - \mathbf{x}_i)$, and a continuous neutralizing background C, serving as source terms for the electrostatic potential $\Phi(\mathbf{x})$ in a medium with permittivity ε (Griffiths, 1999). In the context of this work, however, the logarithmic interaction is additionally motivated by an analogy between the Poisson equation and the steady-state oxygen diffusion equation in two dimensions:

$$D\Delta c(\mathbf{x}) = -I \sum_i \delta(\mathbf{x} - \mathbf{x}_i) + M, \tag{A.8}$$

with pointlike oxygen sources of intensity I at positions $\mathbf{x}_i$. Eq. A.8 governs the steady-state limit ($\partial_t c(\mathbf{x}) = 0\ \forall \mathbf{x}$) of the local oxygen concentration $c(\mathbf{x})$ in tissue with an isotropic oxygen

diffusion coefficient D and homogeneous metabolic oxygen consumption rate M. In the steady-state case, Neumann boundary conditions are suitable, $\nabla c \cdot \boldsymbol{n} = 0$, forbidding flux at the boundaries with normal vector $\boldsymbol{n}$. Neglecting axial diffusion, the 2D problem equivalently models 3D tissue perfused by infinitely long, parallel capillaries (Kurz et al., 2017). Due to the statistical nature of our considerations and the fact that we are not trying to solve the diffusion equation for an actual source configuration, the requirement of long, parallel capillary segments is held loosely and the model is applied to approximate the distribution of vessels in arbitrary cuts through 3D samples.

Assuming that angiogenesis in healthy growing tissue aims for a maximally effective vascularization of the organ, an ideal vessel construct should be quite regularly arranged to avoid long intervascular diffusion distances for oxygen but spare unnecessary energy needed for vessel proliferation and perfusion (Murray, 1926; Sherman et al., 1989). In order to evade a local oversupply of oxygen in certain regions, ideally, sources should be found at locations with local minima of the steady-state concentration distribution $c(\mathbf{x})$, just as electrical charges should arrange themselves in corresponding minima of the electrostatic potential $\Phi(\mathbf{x})$. Consequently, neglecting boundary effects and further drawing on the analogy between $\Phi(\mathbf{x})$ and $c(\mathbf{x})$, the energetically most favorable and effective distribution of oxygen sources in a plane should be arranged in a regular hexagonal crystal lattice (Caillol et al., 1982).

The influence of competing growth processes and external factors that perturb the formation of an optimal vessel architecture can be modeled by employing the canonical ensemble. It can be shown (de Leeuw and Perram, 1982) that the macroscopic characteristics of an OCP with point charges q in thermal equilibrium at temperature T are fully embraced by the dimensionless, scalar coupling constant

$$\Gamma = \frac{q^2}{k_B T}. \tag{A.9}$$

In essence, parametrizing the balance between energy minimization and entropy maximization, Γ can be understood as a measure for the regularity in a point distribution resulting from a Gibbs process. A first-order phase transition has been predicted and observed at $\Gamma \approx 140$, see, e.g., (Choquard and Clerouin, 1983) or (Radloff et al., 1984), above which the plasma acquires a crystalline structure. Below this point, the model exhibits increasingly disordered point configurations for decreasing Γ-values.

In the context of oxygen supply to tissue, we assume that the distribution of sources in an arbitrary plane, i.e. capillaries at positions $\mathbf{x}_i$ in Eq. A.8, can be characterized statistically by the Γ-parameter of the OCP. The scalar coupling constant collectively encompasses the physiological and pathological factors that lead to deviations of vessel structures from a maximally effective form, as well as dynamic variations of the capillary bed due to metabolic and hemodynamic interactions (Vilanova et al., 2018; Zakrzewicz et al., 2002). Large values for Γ suggest a rather regularly arranged capillary bed, spread evenly throughout the tissue, while small values indicate a less homogeneous vascularization. The main focus of this work is to determine and compare typical Γ-values in glioblastoma and healthy brain tissue in mice, in order to assess the potential of the OCP for the development of tumor biomarkers.

Supplementary material

Supplementary material associated with this article can be found, in the online version, at doi:10.1016/j.jtbi.2020.110230.

References

Abramowitz, M., Stegun, I.A., 1972. Handbook of Mathematical Functions with Formulas, Graphs and Mathematical Tables, 9 Dover Publications, New York, USA.

Aghi, M., Chiocca, E.A., 2005. Contribution of bone marrow-derived cells to blood vessels in ischemic tissues and tumors. Mol. Ther. 12, 994–1005. doi:10.1016/j.ymthe.2005.07.693.

Ahlgren, A., Knutsson, L., Wirestam, R., Nilsson, M., Ståhlberg, F., Topgaard, D., Lasič, S., 2016. Quantification of microcirculatory parameters by joint analysis of flowcompensated and nonflowcompensated intravoxel incoherent motion (IVIM) data. NMR Biomed 29 (5), 640–649. doi: 10.1002/nbm.3505.

Alastuey, A., Jancovici, B., 1981. On the classical two-dimensional one-component coulomb plasma. Journal de Physique 42 (1), 1–12. doi:10.1051/jphys:019810042010100.

Baish, J.W., Jain, R.K., 2000. Fractals and cancer. Cancer Res. 60, 3683–3688.

Baish, J.W., Stylianopoulos, T., Lanning, R.M., Kamoun, W.S., Fukumura, D., Munn, L.L., Jain, R.K., 2011. Scaling rules for diffusive drug delivery in tumor and normal tissues. Proc. Natl. Acad. Sci. USA 108 (5), 1799–1803. doi:10.1073/pnas.1018154108.

Barber, C.B., Dobkin, D.P., Huhdanpaa, H., 1996. The quickhull algorithm for convex hulls. In: ACM Transactions on Mathematical Software, 22, pp. 469–483. doi:10.1145/235815.235821.

Bergers, G., Benjamin, L.E., 2003. Tumorigenesis and the angiogenic switch. Nat Rev Cancer 3, 401–410. 10.1038/nrc1093.

Bihan, D.L., Breton, E., Lallemand, D., Aubin, M.L., Vignaud, J., Laval-Jeantet, M., 1988. Separation of diffusion and perfusion in intravoxel incoherent motion MR imaging. Radiology 168 (2), 497–505. doi:10.1148/radiology.168.2.3393671.

Boujelben, A., Watson, M., McDougall, S., Yen, Y.-F., Gerstner, E.R., Catana, C., Deisboeck, T., Batchelor, T.T., Boas, D., Rosen, B., Kalpathy-Cramer, J., Chaplain, M.A.J., 2016. Multimodality imaging and mathematical modelling of drug delivery to glioblastomas. Interface Focus 6, 20160039. 10.1098/rsfs.2016.0039.

Breckwoldt, M.O., Bode, J., Kurz, F.T., Hoffmann, A., Ochs, K., Ott, M., Deumelandt, K., Krüwel, T., Schwarz, D., Fischer, M., Helluy, X., Milford, D., Kirschbaum, K., Solecki, G., Chiblak, S., Abdollahi, A., Winkler, F., Wick, W., Platten, M., Heiland, S., Bendszus, M., Tews, B., 2016. Correlated magnetic resonance imaging and ultramicroscopy (MR-UM) is a tool kit to asses the dynamics of glioma angiogenesis. Elife 5, e11712. doi:10.7554/eLife.11712.

Breckwoldt, M.O., Bode, J., Sahm, F., Krüwel, T., Solecki, G., Hahn, A., Wirthschaft, P., Berghoff, A.S., Haas, M., Venkataramani, V., von Deimling, A., Wick, W., Herold-Mende, C., Heiland, S., Platten, M., Bendszus, M., Kurz, F.T., Winkler, F., Tews, B., 2019. Correlated MRI and ultramicroscopy (MR-UM) of brain tumors reveals vast heterogeneity of tumor infiltration and neoangiogenesis in preclinical models and human disease. Front. Neurosci. 12, 1004. doi:10.3389/fnins.2018.01004.

Buschle, L.R., Ziener, C.H., Zhang, K., Sturm, V.J.F., Kampf, T., Hahn, A., Solecki, G., Winkler, F., Bendszus, M., Heiland, S., Schlemmer, H.-P., Kurz, F.T., 2018. Vessel radius mapping in an extended model of transverse relaxation. MAGMA 31 (4), 531–551. doi:10.1007/s10334-018-0677-9.

Cai, Y., Wu, J., Li, Z., Long, Q., 2016. Mathematical modelling of a brain tumour initiation and early development: a coupled model of glioblastoma growth, pre-existing vessel co-option, angiogenesis and blood perfusion. PLoS One 11 (3), e0150296. doi:10.1371/journal.pone.0150296.

Cai, Y., Xu, S., Wu, J., Long, Q., 2011. Coupled modelling of tumour angiogenesis, tumour growth and blood perfusion. J. Theor. Biol. 279 (1), 90–101. doi:10.1016/j.jtbi.2011.02.017.

Caillol, J.M., Levesque, D., Weis, J.J., Hansen, J.P., 1982. A monte carlo study of the classical two-dimensional one-component plasma. J. Stat. Phys. 28 (2), 325–349. doi:10.1007/BF01012609.

Calamante, F., 2013. Arterial input function in perfusion MRI: A comprehensive review. Prog. Nucl. Magn. Reson. Spectrosc. 74, 1–32. doi:10.1016/j.pnmrs.2013.04.002.

Carmeliet, P., Jain, R.K., 2000. Angiogenesis in cancer and other diseases. Nature 407, 249–257. doi:10.1038/35025220.

Chaplain, M.A., Anderson, A., 2004. Mathematical modelling of tumour-induced angiogenesis: network growth and structure. Cancer Treat. Res. 117, 51–75. doi:10.1007/978-1-4419-8871-3_3.

Choquard, P., Clerouin, J., 1983. Cooperative phenomena below melting of the one-component two-dimensional plasma. Phys. Rev. Lett. 50 (26), 2086. doi:10.1103/PhysRevLett.50.2086.

Coffey, D.S., 1998. Self-organization, complexity and chaos: the new biology for medicine. Nat. Med. 4 (8), 882–885. doi:10.1038/nm0898-882.

Das, S., Marsden, P.A., 2013. Angiogenesis in glioblastoma. N. Engl. J. Med. 369 (16), 1561–1563. doi:10.1056/NEJMcibr1309402.

Deng, J., Wang, Y., 2017. Quantitative magnetic resonance imaging biomarkers in oncological clinical trials: Current techniques and standardization challenges. Chronic Dis. Transl. Med. 3 (1), 8–20. doi:10.1016/j.cdtm.2017.02.002.

Döme, B., Hendrix, M., Paku, S., Tóvarí, J., 2007. Alternative vascularization mechanisms in cancer. Am. J. Pathol. 170, 1–15. doi:10.2353/ajpath.2007.060302.

Emblem, K.E., Mouridsen, K., Bjornerud, A., Farrar, C.T., Jennings, D., Borra, R.J.H., Wen, P.Y., Ivy, P., Batchelor, T.T., Rosen, B.R., Jain, R.K., Sorensen, A.G., 2013. Vessel architectural imaging identifies cancer patient responders to anti-angiogenic therapy. Nat. Med. 19, 1178–1183. doi:10.1038/nm.3289.

Ertürk, A., Becker, K., Jährling, N., Mauch, C.P., Hojer, C.D., Egen, J.G., Hellal, F., Bradke, F., Sheng, M., Dodt, H.U., 2012. Three-dimensional imaging of solvent-cleared organs using 3DISCO. Nat. Protoc. 7 (11), 1983–1995. doi:10.1038/nprot.2012.119.

Ewald, P.P., 1921. Die Berechnung optischer und elektrostatischer Gitterpotentiale. Ann. Phys. 369, 253–287. doi:10.1002/andp.19213690304.

Fang, Q., Sakadžić, S., Ruvinskaya, L., Devor, A., Dale, A.M., Boas, D.A., 2008. Oxygen advection and diffusion in a three dimensional vascular anatomical network. Opt. Express 16 (22), 17530–17541. doi:10.1364/oe.16.17530.

Farrar, C.T., Kamoun, W.S., Ley, C.D., Kim, Y.R., Kwon, S.J., Dai, G., Rosen, B.R., di Tomaso, E., Jain, R.K., Sorensen, A.G., 2010. In vivo validation of MRI vessel caliber index measurement methods with intravital optical microscopy in a U87 mouse brain tumor model. Neuro Oncol. 12 (4), 341–350. doi:10.1093/neuonc/nop032.

Fukumura, D., Duda, D.G., Munn, L.L., Jain, R.K., 2010. Tumor microvasculature and microenvironment: novel insights through intravital imaging in pre-clinical models. Microcirculation 17, 206–225. doi:10.1111/j.1549-8719.2010.00029.x.

Gatson, N., Chiocca, E.A., Kaur, B., 2012. Anti-angiogenic gene therapy in the treatment of malignant gliomas. Neurosci. Lett. 527 (2), 62–70. doi:10.1016/j.neulet.2012.08.001.

Gazit, Y., Baish, J.W., Safabakhsh, N., Leunig, M., Baxter, L.T., Jain, R.K., 1997. Fractal characteristics of tumor vascular architecture during tumor growth and regression. Microcirculation 4 (4), 395–402. doi:10.3109/10739689709146803.

Gazit, Y., Berk, D.A., Leunig, M., Baxter, L.T., Jain, R.K., 1995. Scale-invariant behavior and vascular network formation in normal and tumor tissue. Phys. Rev. Lett. 75, 2428. doi:10.1103/PhysRevLett.75.2428.

Gillies, R.J., Schomack, P.A., Secomb, T.W., Raghunand, N., 1999. Causes and effects of heterogeneous perfusion in tumors. Neoplasia 1 (3), 197–207. doi:10.1038/sj.neo.7900037.

Goldman, D., 2008. Theoretical models of microvascular oxygen transport to tissue. Microcirculation 15 (8), 795–811. doi:10.1080/10739680801938289.

Good, J.S., Harrington, K.J., 2013. The hallmarks of cancer and the radiation oncologist: Updating the 5Rs of radiobiology. Clin. Oncol. (R. Coll. Radiol.) 25 (10), 569–577. doi:10.1016/j.clon.2013.06.009.

Gould, D.J., Vadakkan, T.J., Poché, R.A., Dickinson, M.E., 2011. Multifractal and lacunarity analysis of microvascular morphology and remodeling. Microcirculation 18 (2), 136–151. doi:10.1111/j.1549-8719.2010.00075.x.

Griffiths, D.J., 1999. Introduction to Electrodynamics, 3 Pearson Education Inc, New Jersey, USA.

Guidolin, D., Nico, B., Mazzocchi, G., Vacca, A., Nussdorfer, G.G., Ribatti, D., 2004. Order and disorder in the vascular network. Leukemia 18, 1745–1750. doi:10.1038/sj.leu.2403526.

Hahn, A., Bode, J., Krüwel, T., Solecki, G., Heiland, S., Bendszus, M., Tews, B., Winkler, F., Breckwoldt, M.O., Kurz, F.T., 2019. Glioblastoma multiforme restructures the topological connectivity of cerebrovascular networks. Sci. Rep. 9, 11757. doi:10.1038/s41598-019-47567-w.

Hanahan, D., Weinberg, R.A., 2011. Hallmarks of cancer: the next generation. Cell 144 (5), 646–674. doi:10.1016/j.cell.2011.02.013.

Jain, R.K., 2013. Normalizing tumor microenvironment to treat cancer: bench to bedside to biomarkers. J. Clin. Oncol. 31 (17), 2205–2218. doi:10.1200/JCO.2012.46.3653.

Jochimsen, T.H., Möller, H.E., 2008. Increasing specificity in functional magnetic resonance imaging by estimation of vessel size based on changes in blood oxygenation. Neuroimage 40 (1), 228–236. doi:10.1016/j.neuroimage.2007.10.050.

Karch, R., Neumann, M., Neumann, F., Ullrich, R., Neumüller, J., Schreiner, W., 2006. A Gibbs point field model for the spatial pattern of coronary capillaries. Physica A 369, 599–611. doi:10.1016/j.physa.2006.02.018.

Karch, R., Neumann, F., Ullrich, R., Neumüller, J., Podesser, B.K., Neumann, M., Schreiner, W., 2005. The spatial pattern of coronary capillaries in patients with dilated, ischemic, or inflammatory cardiomyopathy. Cardiovasc. Pathol. 14, 135–144. doi:10.1016/j.carpath.2005.03.003.

Kather, J.N., Marx, A., Reyes-Aldasoro, C.C., Schad, L.R., Zöllner, F.G., Weis, C.-A., 2015. Continuous representation of tumor microvessel density and detection of angiogenic hotspots in histological whole-slide images. Oncotarget 5, 1–14. doi:10.18632/oncotarget.4383.

Kiselev, V.G., Posse, S., 1998. Analytical theory of susceptibility induced NMR signal dephasing in a cerebrovascular network. Phys. Rev. Lett. 81, 5696–5699. doi:10.1103/PhysRevLett.81.5696.

Kurz, F.T., Buschle, L.R., Hahn, A., Jende, J.M.E., Bendszus, M., Heiland, S., Ziener, C.H., 2018. Diffusion effects in myelin sheath free induction decay. J. Magn. Reson. 297, 61–75. doi:10.1016/j.jmr.2018.10.001.

Kurz, F.T., Buschle, L.R., Kampf, T., Zhang, K., Schlemmer, H.-P., Heiland, S., Bendszus, M., Ziener, C.H., 2016. Spin dephasing in a magnetic dipole field around large capillaries: approximative and exact results. J. Magn. Reson. 273, 83–97. doi:10.1016/j.jmr.2016.10.012.

Kurz, F.T., Kampf, T., Buschle, L.R., Heiland, S., Schlemmer, H.-P., Bendszus, M., Ziener, C.H., 2016. CPMG relaxation rate dispersion in dipole fields around capillaries. Magn. Reson. Imaging 34 (7), 875–888. doi:10.1016/j.mri.2016.03.016.

Kurz, F.T., Kampf, T., Buschle, L.R., Schlemmer, H.-P., Bendszus, M., Heiland, S., Ziener, C.H., 2016. Generalized moment analysis of magnetic field correlations for accumulations of spherical and cylindrical magnetic perturbers. Front. Phys. 4, 46. doi:10.3389/fphy.2016.00046.

Kurz, F.T., Ziener, C.H., Rückl, M., Hahn, A., Sturm, V.J.F., Zhang, K., Buschle, L.R., Bendszus, M., Heiland, S., Schlemmer, H.-P., Bauer, W.R., Kampf, T., 2017. The influence of spatial patterns of capillary networks on transverse relaxation. Magn. Reson. Imaging 40, 31–47. doi:10.1016/j.mri.2017.03.012.

de Leeuw, S.W., Perram, J.W., 1982. Statistical mechanics of two-dimensional coulomb systems, II. the two-dimensional one-component plasma. Physica A 113 (3), 546–558. doi:10.1016/0378-4371(82)90156-X.

Lee, T., Kashyap, R.L., Chu, C., 1994. Building skeleton models via 3-D medial surface/axis thinning algorithms. CVGIP: Graphical Models and Image Processing 56, 462–478. doi:10.1006/cgip.1994.1042.

Macklin, P., McDougall, S., Anderson, A.R.A., Chaplain, M.A.J., Cristini, V., Lowengrub, J., 2009. Multiscale modelling and nonlinear simulation of vascular tumour growth. J. Math. Biol. 58 (4–5), 765–798. doi:10.1007/s00285-008-0216-9.

Mancardi, D., Varetto, G., E, B., Maniero, F., Guiot, C., 2008. Fractal parameters and vascular networks: facts & artifacts. Theor. Biol. Med. Model. 5, 12. doi:10.1186/1742-4682-5-12.

McDougall, S.R., Anderson, A.R., Chaplain, M.A., 2006. Mathematical modelling of dynamic adaptive tumour-induced angiogenesis: clinical implications and therapeutic targeting strategies. J. Theor. Biol. 241 (3), 564–589. doi:10.1016/j.jtbi.2005.12.022.

McDougall, S.R., Anderson, A.R., Chaplain, M.A., Sherratt, J.A., 2002. Mathematical modelling of flow through vascular networks: implications for tumour-induced angiogenesis and chemotherapy strategies. Bull. Math. Biol. 64 (4), 673–702. doi:10.1006/bulm.2002.0293.

Metropolis, N., Rosenbluth, A.W., Rosenbluth, M.N., Teller, A.H., Teller, E.J., 1953. Equation of state calculations by fast computing machines. J. Chem. Phys. 21 (6), 1087–1092. doi:10.1063/1.1699114.

Moody, D.M., Bell, M.A., Challa, V.R., 1990. Features of the cerebral vascular pattern that predict vulnerability to perfusion or oxygenation deficiency: an anatomic study. AJNR Am. J. Neuroradiol. 11 (3), 431–439.

Murray, C.D., 1926. The physiological principle of minimum work: I. The vascular system and the cost of blood volume. Proc. Natl. Acad. Sci. USA 12 (3), 207–214. doi:10.1073/pnas.12.3.207.

Okabe, A., Boots, B., Sugihara, K., Chiu, S.N., 1999. Spatial Tessellations: Concepts and applications of Voronoi Diagrams, second Wiley, Chichester.

van Osch, M.J.P., Teeuwisse, W.M., Chen, Z., Suzuki, Y., Helle, M., Schmid, S., 2018. Advances in arterial spin labelling MRI methods for measuring perfusion and collateral flow. J. Cereb. Blood Flow Metab. 38 (9), 1461–1480. doi:10.1177/0271678X17713434.

Osswald, M., Jung, E., Sahm, F., Solecki, G., Venkataramani, V., Blaes, J., Weil, S., Horstmann, H., Wiestler, B., Syed, M., Huang, L., Ratliff, M., Karimian Jazi, K., Kurz, F.T., Schmenger, T., Lemke, D., Gömmel, M., Pauli, M., Liao, Y., Häring, P., Pusch, S., Herl, V., Steinhäuser, C., Krunic, D., Jarahian, M., Miletic, H., Berghoff, A.S., Griesbeck, O., Kalamakis, G., Garaschuk, O., Preusser, M., Weiss, S., Liu, H., Heiland, S., Platten, M., Huber, P.E., Kuner, T., von Deimling, A., Wick, W., Winkler, F., 2015. Brain tumour cells interconnect to a functional and resistant network. Nature 528, 93–98. doi:10.1038/nature16071.

Ostergaard, L., Weisskoff, R.M., Chesler, D.A., Gyldensted, C., Rosen, B.R., 1996. High resolution measurement of cerebral blood flow using intravascular tracer bolus passages. Part I: mathematical approach and statistical analysis. Magn. Reson. Med. 36 (5), 715–725. doi:10.1002/mrm.1910360510.

Owen, M.R., Alarcón, T., Maini, P.K., Byrne, H.M., 2009. Angiogenesis and vascular remodelling in normal and cancerous tissues. J. Math. Biol. 58 (4–5), 689–721. doi:10.1007/s00285-008-0213-z.

Perfahl, H., Hughes, B.D., Alarcón, T., Maini, P.K., Lloyd, M.C., Reuss, M., Byrne, H.M., 2017. 3D hybrid modelling of vascular network formation. J. Theor. Biol. 414, 254–268. doi:10.1016/j.jtbi.2016.11.013.

Pries, A.R., Secomb, T.W., 2000. Microcirculatory network structures and models. Ann. Biomed. Eng. 28 (8), 916–921. doi:10.1114/1.1308495.

Pries, A.R., Secomb, T.W., 2008. Modeling structural adaptation of microcirculation. Microcirculation 15 (8), 753–764. doi:10.1080/10739680802229076.

Pries, A.R., Secomb, T.W., Gaehtgens, P., 1995. Design principles of vascular beds. Circ. Res. 77 (5), 1017–1023. doi:10.1161/01.res.77.5.1017.

Pries, A.R., Secomb, T.W., Gaehtgens, P., 1996. Biophysical aspects of blood flow in the microvasculature. Cardiovasc. Res. 32 (4), 654–667. doi:10.1016/S0008-6363(96)00065-X.

Pries, A.R., Secomb, T.W., Gaehtgens, P., Gross, J.F., 1990. Blood flow in microvascular networks. experiments and simulation. Circ. Res. 67 (4), 826–834. doi:10.1161/01.RES.67.4.826.

Radloff, P.L., Bagchi, B., Cerjan, C., Rise, S.A., 1984. Freezing of the classical two-dimensional, one-component plasma. J. Chem. Phys. 81, 1406. doi:10.1063/1.447775.

Ricci-Vitiani, L., Pallini, R., Biffoni, M., Todaro, M., Invernici, G., Cenci, T., Maira, G., Parati, E.A., Stassi, G., Larocca, L.M., Maria, R.D., 2010. Tumour vascularization via endothelial differentiation of glioblastoma stem-like cells. Nature 468, 824–828. doi:10.1038/nature09557.

Rieger, H., Fredrich, T., Welter, M., 2016. Physics of the tumor vasculature: theory and experiment. Eur. Phys. J. Plus 131, 31. doi:10.1140/epjp/i2016-16031-9.

Rieger, H., Welter, M., 2015. Integrative models of vascular remodeling during tumor growth. Wiley Interdiscip. Rev. Syst. Biol. Med. 7 (3), 113–129. doi:10.1002/wsbm.1295.

Romano, A., Espagnet, M.C.R., Calabria, L.F., Coppola, V., Talamanca, L.F., Cipriani, V., Minniti, G., Pierallini, A., Fantozzi, L.M., Bozzao, A., 2012. Clinical applications of dynamic susceptibility contrast perfusion-weighted MR imaging in brain tumours. Radiol. Med. 117 (3), 445–460. doi:10.1007/s11547-011-0715-4.

Schindelin, J., Arganda-Carreras, I., Frise, E., Kaynig, V., Longair, M., Pietzsch, T., Preibisch, S., Rueden, C., Saalfeld, S., Schmid, B., Tinevez, J.-Y., White, D.J., Hartenstein, V., Eliceiri, K., Tomancak, P., Cardona, A., 2012. Fiji: An open-source platform for biological-image analysis. Nat. Methods 9 (7), 676–682. doi:10.1038/nmeth.2019.

Schwarz, M.K., Scherbarth, A., Sprengel, R., Engelhardt, J., Theer, P., Giese, G., 2015. Fluorescent-protein stabilization and high-resolution imaging of cleared, intact mouse brains. PLoS One 10, e0124650. doi:10.1371/journal.pone.0124650.

Scianna, M., Bell, C.G., Preziosi, L., 2013. A review of mathematical models for the formation of vascular networks. J. Theor. Biol. 333, 174. doi:10.1016/j.jtbi.2013.04.037.

Scott, J.G., Fletcher, A.G., Anderson, A.R.A., Maini, P.K., 2016. Spatial metrics of tumour vascular organisation predict radiation efficacy in a computational model. PLoS Comput. Biol. 12 (1), e1004712. doi:10.1371/journal.pcbi.1004712.

Secomb, T.W., Alberding, J.P., Hsu, R., Dewhirst, M.W., Pries, A.R., 2013. Angiogenesis: An adaptive dynamic biological patterning problem. PLoS Comput. Biol. 9 (3), e1002983. doi:10.1371/journal.pcbi.1002983.

Senarathna, J., Yu, H., Deng, C., Zou, A.L., Issa, J.B., Hadjiabadi, D.H., Gil, S., Wang, Q., Tyler, B.M., Thakor, N.V., Pathak, A.P., 2019. A miniature multi-contrast microscope for functional imaging in freely behaving animals. Nat. Commun. 10 (99). doi:10.1038/s41467-018-07926-z.

Shen, Y., Pu, I.M., Ahearn, T., Clemence, M., Schwarzbauer, C., 2013. Quantification of venous vessel size in human brain in response to hypercapnia and hyperoxia using magnetic resonance imaging. Magn. Reson. Med. 69, 1541–1552. doi:10.1002/mrm.24258.

Sherman, T.F., Popel, A.S., Koller, A., Johnson, P.C., 1989. The cost of departure from optimal radii in microvascular networks. J. Theor. Biol. 136, 245–265. doi:10.1016/S0022-5193(89)80162-6.

Smith, T.G., Lange, G.D., Marks, W.B., 1996. Fractal methods and results in cellular morphology - dimensions, lacunarity and multifractals. J. Neurosci. Methods 69, 123–136. doi:10.1016/S0165-0270(96)00080-5.

Soda, Y., Marumoto, T., Friedmann-Morvinski, D., Soda, M., Liu, F., Michiue, H., Pastorino, S., Yang, M., Hoffman, R.M., Kesari, S., Verma, I.M., 2011. Transdifferentiation of glioblastoma cells into vascular endothelial cells. Proc. Natl. Acad. Sci. USA 108 (11), 4274–4280. doi:10.1073/pnas.1016030108.

Sommer, C., Straehle, C., Koethe, U., Hamprecht, F.A., 2011. ilastik: interactive learning and segmentation toolkit. In: Proc IEEE Int Symp Biomed Imaging, pp. 230–233. doi:10.1109/ISBI.2011.5872394.

Spill, F., Guerrero, P., Alarcón, T., Maini, P.K., Byrne, H.M., 2015. Mesoscopic and continuum modelling of angiogenesis. J. Math. Biol. 70 (3), 485–532. doi:10.1007/s00285-014-0771-1.

Sukstanskii, A.L., Yablonskiy, D.A., 2002. Effects of restricted diffusion on MR signal formation. J. Magn. Reson. 157 (1), 92–105. doi:10.1006/jmre.2002.2582.

Troprès, I., Farion, L.L.R., Segebarth, C., Rèmy, C., 2004. Vessel size imaging using low intravascular contrast agent concentrations. MAGMA 17, 313–316. doi:10.1007/s10334-004-0067-3.

Troprès, I., Grimault, S., Vaeth, A., Grillon, E., Julien, C., Payen, J.F., Lamalle, L., Décorps, M., 2001. Vessel size imaging. Magn. Reson. Med. 45 (3), 397–408. doi:10.1002/1522-2594(200103)45:3<397::aid-mrm1052>3.0.co;2-3.

Troprès, I., Pannetier, N., Grand, S., Lemasson, B., Moisan, A., Péoc'h, M., Rémy, C., Barbier, E.L., 2015. Imaging the microvessel caliber and density: Principles and applications of microvascular MRI. Magn. Reson. Med. 73, 325–341. doi:10.1002/mrm.25396.

Vilanova, G., Burés, M., Colominas, I., Gomez, H., 2018. Computational modelling suggests complex interactions between interstitial flow and tumour angiogenesis. J. R. Soc. Interface 15 (146), 20180415. doi:10.1098/rsif.2018.0415.

Volpert, O.V., Dameron, K.M., Bouck, N., 1997. Sequential development of an angiogenic phenotype by human fibroblasts progressing to tumorigenicity. Oncogene 14, 1495–1502. doi:10.1038/sj.onc.1200977.

Wang, R., Chadalavada, K., Wilshire, J., Kowalik, U., Hovinga, K.E., Geber, A., Fligelman, B., Leversha, M., Brennan, C., Tabar, V., 2010. Glioblastoma stem-like cells give rise to tumour endothelium. Nature 468, 829–833. doi:10.1038/nature09624.

Welter, M., Bartha, K., Rieger, H., 2009. Vascular remodelling of an arterio-venous blood vessel network during solid tumour growth. J. Theor. Biol. 259 (3), 405–422. doi:10.1016/j.jtbi.2009.04.005.

Welter, M., Rieger, H., 2013. Interstitial fluid flow and drug delivery in vascularized tumors: A computational model PLoS One 8, e70395 doi:10.1371/journal.pone.0070395.

Wiedeman, M.P., Tuma, R.F., Mayrovitz, H.N., 1981. An Introduction to Microcirculation. Elsevier Academic Press, New York doi:10.1016/B978-0-12-749350-3.X5001-8.

Williams, D.S., Detre, J.A., Leigh, J.S., Koretsky, A.P., 1992. Magnetic resonance imaging of perfusion using spin inversion of arterial water. Proc. Natl. Acad. Sci. USA 89 (1), 212–216. doi:10.1073/pnas.89.1.212.

Wu, M., Frieboes, H.B., Chaplain, M.A., McDougall, S.R., Cristini, V., Lowengrub, J.S., 2014. The effect of interstitial pressure on therapeutic agent transport: coupling with the tumor blood and lymphatic vascular systems. J. Theor. Biol. 355, 194–207. doi:10.1016/j.jtbi.2014.04.012.

Yablonskiy, D.A., Haacke, E.M., 1994. Theory of NMR signal behaviour in magnetically inhomogeneous tissues: The static dephasing regime. J. Magn. Reson. 32, 749–763. doi:10.1002/mrm.1910320610.

Zakrzewicz, A., Secomb, T.W., Pries, A.R., 2002. Angioadaptation: Keeping the vascular system in shape. News Physiol. Sci. 17, 197–201. doi:10.1152/nips.01395.2001.

Zhang, K., Sturm, V.J., Buschle, L.R., Hahn, A., Yun, S.D., Shah, N.J., Bendszus, M., Heiland, S., Schlemmer, H.-P., Ziener, C.H., Kurz, F.T., 2019. Dual-contrast pCASL using simultaneous gradient-echo/spin-echo multiband EPI. Magn. Reson. Imaging 57, 359–367. doi:10.1016/j.mri.2018.11.018.

Zhang, K., Yun, S.D., Triphan, S.M.F., Sturm, V.J., Buschle, L.R., Hahn, A., Heiland, S., Bendszus, M., Schlemmer, H.-P., Shah, N.J., Ziener, C.H., Kurz, F.T., 2019. Vessel architecture imaging using multiband gradient-echo/spin-echo EPI. PLoS One 14 (8), e0220939. doi:10.1371/journal.pone.0220939.

Ziener, C.H., Kampf, T., Kurz, F.T., 2015. Diffusion propagators for hindered diffusion in open geometries. Concepts Magn. Reson. 44, 150–159. doi:10.1002/cmr.a.21346.

Ziener, C.H., Kampf, T., Reents, G., Schlemmer, H.-P., Bauer, W.R., 2012. Spin dephasing in a magnetic dipole field. Phys. Rev. E 85 (5), 51908. doi:10.1103/PhysRevE.85.051908.

Zou, G., Wu, H., 1995. Nearest-neighbor distribution of interacting biological entities. J. Theor. Biol. 172 (4), 347–353. doi:10.1006/jtbi.1995.0032.

Supplementary Material

Hahn et al., *J Theor Biol* 494:110230 (2020)
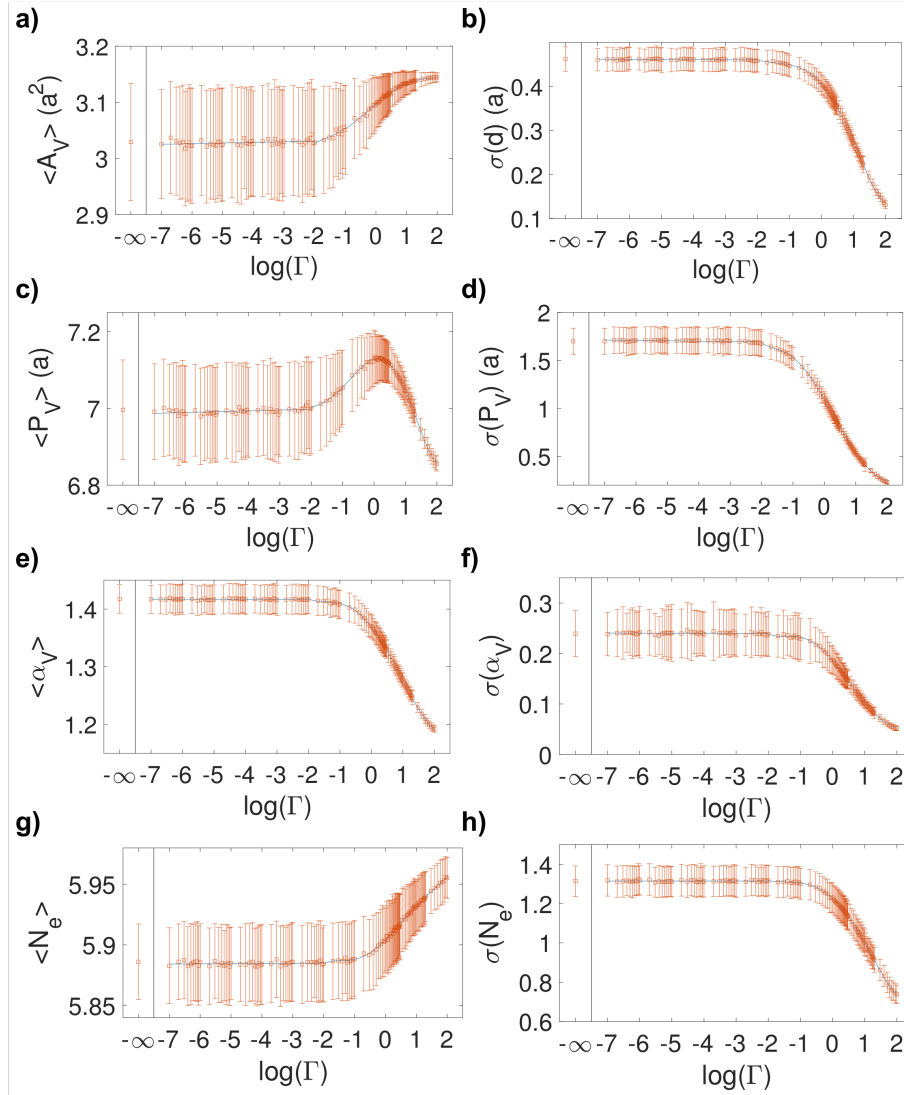
Appendix B. Supplementary figures

Figure B.1: **Numerically attained topological parameter dependences on Γ.** The mean of topological quantity x within a point distribution is marked by $\langle x \rangle$ and its standard deviation by $\sigma(x)$, with x taking the following measures: **a)** Voronoi cell area A_V, **b)** nearest neighbor distance d, **c-d)** Voronoi cell perimeter P_V, **e-f)** asphericity $\alpha_V = P_V^2/(4\pi A_V)$, and **g-h)** number of edges N_e. Mean values for each simulation setting are marked by squares with error bars representing the standard deviation among 500 simulation runs for each Γ value. Distances are given in units of the Wigner-Seitz radius a. Simulated datapoints are connected by polynomial fits (degree 5 for $\Gamma > 0.1$, linear below) to clarify continuous relationships with Γ.
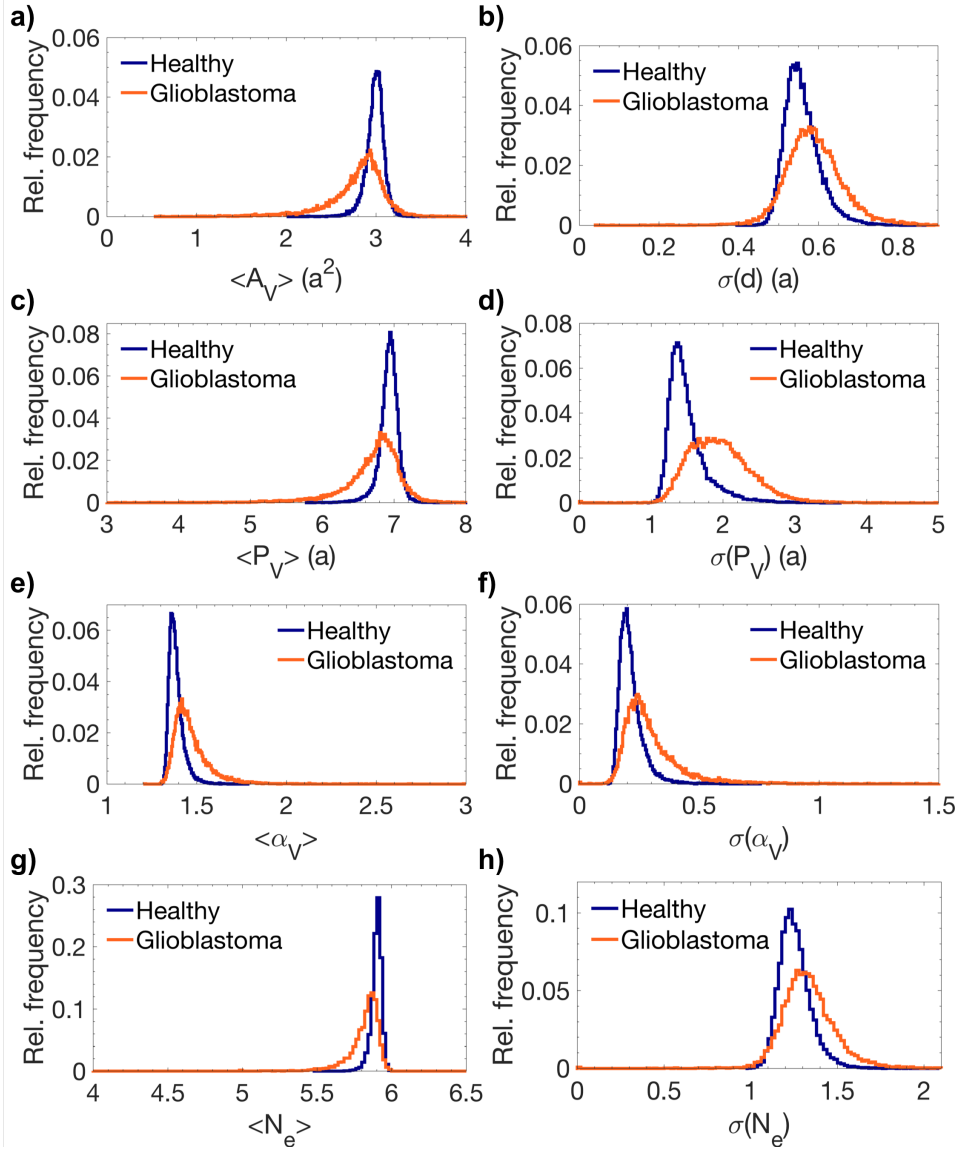
Figure B.2: **Relative frequency histograms of topological parameter distributions obtained from Voronoi tesselations of imaged vessel distributions.** Specifically, means $\langle x \rangle$ and standard deviations $\sigma(x)$ with x as the **a)** Voronoi cell area A_V, **b)** nearest neighbor distance d, **c-d)** Voronoi cell perimeter P_V, **e-f)** asphericity α_V, and **g-h)** number of edges N_e. Length units were scaled by the Wigner-Seitz radius a.

Publication III:
Partitioned quantification of vessel geometry by cuboids

Title: Large-scale characterization of the microvascular geometry in development and disease by tissue clearing and quantitative ultramicroscopy

Authors: <u>Artur Hahn</u>, Julia Bode, Allen Alexander, Kianush Karimian-Jazi, Katharina Schregel, Daniel Schwarz, Alexander C. Sommerkamp, Thomas Krüwel, Amir Abdollahi, Wolfgang Wick, Michael Platten, Martin Bendszus, Björn Tews, Felix T. Kurz and Michael O. Breckwoldt

Journal: Journal of Cerebral Blood Flow & Metabolism 271678X20961854 (2020)

DOI: 10.1177/0271678X20961854

Contributions: J.B., T.K., and B.T. established ultramicroscopy and tissue clearing. Acquisition of ultramicroscopy datasets was performed by J.B. and T.K. Programming of Matlab code and analysis was done by A.H. and F.T.K. Image segmentation and training of the sample images was performed by A.H. and A.A., A.C.S. and T.K. helped with tissue clearing. T.K. performed tumor cell implantations. F.T.K. provided analytical tools. B.T., F.T.K., and M.O.B. conceptualized and supervised the study and performed analyses. A.H, B.T., F.T.K., and M.O.B. wrote the article with input from J.B., A. A., K.KJ., K.S., D.S., A.C.S., A.Ab., W.W., M.P., and M.B.

Original Article

Large-scale characterization of the microvascular geometry in development and disease by tissue clearing and quantitative ultramicroscopy

Artur Hahn[1,2,*], Julia Bode[3,*], Allen Alexander[1,4],
Kianush Karimian-Jazi[1], Katharina Schregel[1],
Daniel Schwarz[1] (iD), Alexander C Sommerkamp[3,5],
Thomas Krüwel[3], Amir Abdollahi[6,7,8], Wolfgang Wick[9,10],
Michael Platten[4,11], Martin Bendszus[1], Björn Tews[3],
Felix T Kurz[1] and Michael O Breckwoldt[1,4] (iD)

Abstract

Three-dimensional assessment of optically cleared, entire organs and organisms has recently become possible by tissue clearing and selective plane illumination microscopy ("ultramicroscopy"). Resulting datasets can be highly complex, encompass over a thousand images with millions of objects and data of several gigabytes per acquisition. This constitutes a major challenge for quantitative analysis. We have developed post-processing tools to quantify millions of microvessels and their distribution in three-dimensional datasets from ultramicroscopy and demonstrate the capabilities of our pipeline within entire mouse brains and embryos. Using our developed acquisition, segmentation, and analysis platform, we quantify physiological vascular networks in development and the healthy brain. We compare various geometric vessel parameters (e.g. vessel density, radius, tortuosity) in the embryonic spinal cord and brain as well as in different brain regions (basal ganglia, corpus callosum, cortex). White matter tract structures (corpus callosum, spinal cord) showed lower microvascular branch densities and longer vessel branch length compared to grey matter (cortex, basal ganglia). Furthermore, we assess tumor neoangiogenesis in a mouse glioma model to compare tumor core and tumor border. The developed methodology allows rapid quantification of three-dimensional datasets by semi-automated segmentation of fluorescently labeled objects with conventional computer hardware. Our approach can aid preclinical investigations and paves the way towards "quantitative ultramicroscopy".

[1]Neuroradiology Department, University Hospital Heidelberg, Heidelberg, Germany
[2]Department of Physics and Astronomy, University of Heidelberg, Heidelberg, Germany
[3]Schaller Research Group at the University of Heidelberg and the German Cancer Research Center (DKFZ), Molecular Mechanisms of Tumor Invasion, Heidelberg, Germany
[4]Clinical Cooperation Unit Neuroimmunology and Brain Tumor Immunology, German Cancer Research Center (DKFZ), Heidelberg, Germany
[5]Faculty of Biosciences, Heidelberg University, Heidelberg, Germany
[6]German Cancer Consortium and Heidelberg Institute of Radiation Oncology, National Center for Radiation Research in Oncology, Heidelberg, Germany
[7]Heidelberg University School of Medicine, Heidelberg University, Heidelberg, Germany

[8]Translational Radiation Oncology, German Cancer Research Center (DKFZ), Heidelberg, Germany
[9]Neurology Clinic and National Center for Tumor Diseases, University Hospital Heidelberg, Heidelberg, Germany
[10]Clinical Cooperation Unit Neurooncology, German Cancer Consortium (DKTK), German Cancer Research Center (DKFZ), Heidelberg, Germany
[11]Department of Neurology, University Medical Center Mannheim, Heidelberg University, Heidelberg, Germany

*These authors contributed equally to this work.

Corresponding author:
Michael Breckwoldt, Department of Neuroradiology, University of Heidelberg, Im Neuenheimer Feld 400, Heidelberg 69120, Germany.
Email: michael.breckwoldt@med.uni-heidelberg.de

Introduction

Vascular remodeling is a key feature of development and disease.[1,2] Neoangiogenesis is a hallmark of cancer and its investigation, both qualitatively and quantitatively is crucial for preclinical and clinical cancer studies. Tumor neoangiogenesis is also closely linked to tumor progression and metastasis formation.[3] Histological (two-dimensional (2D)) analysis of serially segmented sections and 3D image reconstruction is currently the gold standard to quantify vascular networks. However, this is both time consuming and labor intensive. Moreover, reconstructed volumes are generally small.[4] Current 3D-imaging techniques such as magnetic resonance imaging (MRI) and positron emission tomography (PET) do not possess enough spatial resolution to visualize the small capillaries of the microvasculature, though perfusion techniques enable functional probing of vascular parameters and tumor vascularization.[5–9] Micro-computed tomography (μCT) has high resolution and can be combined with capillary filling to investigate the microvasculature.[9,10] Intravital laser scanning microscopy and multiphoton microscopy also offer high spatial resolution ($\sim$200 nm) but are limited by a penetration depth of $\sim$500 μm and small field of view.[10]

Recently, selective plane illumination microscopy ("ultramicroscopy") in conjunction with tissue clearing has gained significant interest. Several techniques have been developed that use fluids and colloids with the refractive index of proteins to render tissue fully transparent.[11–15] Tissue clearing of entire organs or even organisms has recently been demonstrated and is becoming an essential tool in the life sciences and especially neuroscience community for circuit reconstruction and the study of 3D cellular distributions.[16,17] Light sheet microscopy speeds up the acquisition of large datasets compared to confocal techniques and resulting datasets can encompass several gigabytes that can be recorded in a reasonable time. We have previously described an approach for assessing glioma microvessels in a mouse glioma model[18,19] and have shown that this approach is also feasible in human glioma specimen.[20] These approaches were, however, limited to quantifications of small tissue blocks and did not encompass the entire dataset due to lack of segmentation and post-processing tools.

In the present work, we present a numerical pipeline developed for the automated processing and analysis of large bio-imaging datasets with a software implementation usable with conventional hardware. We developed a Matlab program for the quantification of vascular networks in arbitrary 3D imaging volumes upon segmentation with specially trained classifiers in ilastik[21,22] and automated macro-implementations for Fiji[23] for pre-processing steps. The presented imaging pipeline enables large-scale, in-depth studies of vascular architecture in entire organs without the need for histological sectioning or advanced computer hardware.

Methods

Animal models

To assess the vessel architecture in a tumor context we injected 7.5×10^4 U87-MG cells in nine weeks old, male NOD Scid Gamma (NSG; Jackson Laboratories, Bar Harbor, USA; $n = 6$ mice). Cells were injected into the right basal ganglia as described previously.[24] Mice were sacrificed for imaging 21 days post tumor cell implantation. We compared intratumoral vessel morphology with nontumor bearing healthy control mice (nine-weeks old, male NSG; $n = 3$ mice with six analyzed brain hemispheres).

For intravital dye labeling of the vasculature, mice were anaesthetized with ketamine 10% (90 μg/g body-weight) and xylazinhydrochloride 2% (7.5 μg/g body-weight) and injected intravenously with 100 μL of Texas red lycopersicon esculentum (Tomato) lectin (12 mg/kg, Vector laboratories TL-11,761 mg/mL). After 5 min of circulation, mice were transcardially perfused in deep anesthesia using 20 mL PBS followed by 20 mL 4% PFA. Embryos and whole brains were harvested and fixed overnight in 4% PFA, followed by PBS.

To study vessel morphology in development, we used three months old, female, pregnant C57BL6/6N mice (in house breeding at DKFZ) and extracted the embryos at E13.5 after injection with lectin of the mother animal in deep ketamine and xylazine hydrochloride anesthesia ($n = 4$ embryos) using the protocol described above. All experiments were approved by the

regional animal welfare authority (Regierungspräsidium Karlsruhe, animal protocols: G127/16; DKFZ383) and were in accordance with the Federation for Laboratory Animal Science Associations (FELASA, category B) and Society for Laboratory Animal Science (GV-Solas, standard guidelines) and with the Guide for the Care and Use of Laboratory Animals published by the U.S. National Institutes of Health. Reporting complies with the ARRIVE guidelines (Animal Research: Reporting in Vivo Experiments).

Clearing and imaging

Embryos and brains were cleared using the FluoClearBABB protocol over several days.[25] In brief, samples were dehydrated using an ascending buthanol series from 30 to 100% (pH adjusted) for 24 h each. Embryos were transferred into BABB (pH-adjusted) and incubated for 48 h. After setting the refractive index (RI) of tissue to the RI of the clearing solution, samples became transparent. For imaging, a selective plane illumination microscope was used (Ultramicroscope II, LaVision Biotec, Bielefeld, Germany). Overview images of embryos were performed using 1x magnification (3.25 μm in-plane resolution). For magnifications of the vessel architecture of the embryo brain we used up to 4× magnification (800 nm in-plane resolution). For adult brains, a magnification of 1× was used (in-plane resolution of 3.25 μm) in order to acquire the entire brain, avoiding the necessity of stitching. For all experiments, the step size between image acquisitions in the transverse plane was 5 μm.

Image analysis

Masks were manually drawn over the raw image data to delineate different regions to be analyzed individually and saved in equal-sized TIFF-stacks. The imaged vasculature was segmented from the raw images using the interactive learning and segmentation toolkit "ilastik".[22] Random forest classifiers in ilastik were trained simultaneously on all datasets from each cohort using a standard desktop PC. The trained classifiers were used on the datasets in an automated fashion using batch-processing in ilastik to export the binary vessel segmentations. The resulting vessel structures were smoothed with a 3D-Gaussian filter with isotropic $\sigma = 1$ (voxel units) using the 3D-smoothing plugin in the ImageJ distribution Fiji 2.0.0-rc-43/ 1.51r.[26] Subsequently, the smoothed data were binarized with threshold at half of the voxel value range. A custom-written Matlab script was used to fill hollow vessels and holes in the binary vessel representations (Matlab version R2016b, Mathworks, Natick, MA,

USA). Vessel centerlines were extracted with a custom-written macro using the skeletonization plugin in ImageJ.[27] Branching points, vessel endpoints, and intermediate vessel skeleton voxels were automatically identified using the AnalyzeSkeleton plugin in ImageJ.[4]

Automated quantification

Custom codes were written in Matlab to automatically quantify vascular parameters contained within an imaged volume of arbitrary shape, size, and resolution. To accelerate the quantification of large datasets and enable incremental analyses of large datasets, the developed program can dissect a given volume into cuboids of chosen dimensions. This allows for asymptotic studies of arbitrarily large acquisition volumes. Using different masks, independent regions of a segmented dataset can be analyzed individually.

Each subvolume from the 3D tiling box layout of chosen dimensions, imposed on the masked image data, is quantified with basic geometric measures in physical units. This includes the fraction of blood vessel volume in tissue, fVV, the microvascular density MVD (branch segments per mm^3 tissue volume), and the vessel surface and length densities, ρ_A (mm^2 lumen area per mm^3 tissue volume) and ρ_L (mm vessel length per mm^3 tissue volume), for a basic assessment of tissue perfusion density in each subvolume. The vessel segments between branching and/or endpoints are separately quantified as tubular objects; mean radius $\bar{r}$, segment length l, Euclidean vessel endpoint separation d, lumen surface area A, and tortuosity $\tau = l/d$.[28] Through an a priori labeling of each vessel branch in the original, undissected dataset, the vessel properties determined from different partitioning subvolumes are matched and combined to deliver estimates of the geometric properties of actual vessel branches without artificial divisions. The quantification algorithm is tailored to treat vascular networks with many small, interwoven structures sized close to the pixel resolution and has been validated with well-defined ground truth models for precision (see Supplemental methods and Supplemental Figure 1 for further details).

Parameter distributions characterizing the geometric vessel properties of given datasets are saved for the vasculature in the individual subvolumes and automatically combined to deliver a global quantification of the tissue regions marked by the masks. The geometric characteristics of individual vessel segments are saved in lists with matched entries of $\bar{r}$, l, A, and τ. These lists can be processed further for statistical analyses. The processing order of the partitions from the 3D grid can be chosen sequentially or randomly and already analyzed subvolumes can be merged for combined

statistics while the basic analysis of individual subvolumes is still running in parallel. This offers the possibility to analyze parameter distributions statistically before an image was entirely processed. This can be useful with large datasets and limited computational power. Analyses can be restarted and will continue in case of a system failure or limited computational time slots, making our pipeline useful for processing large datasets. The developed numerical pipeline including validation scripts and a user documentation are available from the authors upon reasonable request.

Statistical analysis

Separate Matlab codes were developed to process the extracted results, conduct statistical testing and provide data visualizations. Vessel property distributions and parameters extracted from the sampled subvolumes were compared between different tissue groups. Statistical hypothesis testing between groups was performed with the nonparametric Kruskal–Wallis test in Matlab, using mean parameter values from each specimen. We used nonparametric tests because sample size of $n = 3$ to 6 animals was too small to test for normal distribution. Histograms and 2D-distribution representations can automatically be created with optional discrimination of vessel segments in certain radius-, length-, or tortuosity-ranges. Data are presented as

mean $\pm$ standard deviation (S.D.) and $p < 0.05$ was considered significant ($*p < 0.05$; $**p < 0.01$; $***p < 0.001$).

Results

For dissecting the microvascular anatomy in its entirety, we employed an intravital dye labeling approach using intravenously injected fluorescent lectins.[29] Lectins were injected, animals sacrificed and cleared using the FluoClearBABB protocol (Figure 1(a)). After clearing, imaging was performed by selective plane illumination microscopy. Labeled vessels were segmented semi-automatically in the entire dataset based on edge and texture features and fluorescence intensity. We analyzed various vessel parameters including vessel density, segment length, radius, tortuosity, surface area, and ratio of vessel volume within the tissue. The analysis generated data points for 5×10^4 to 3×10^6 vessel segments per sample. To demonstrate the utility of the approach, we probed microvascular features in development, physiological, and pathological conditions.

Uncovering divergent microvascular architectures in different brain regions

Healthy mice were injected with lectin-FITC, sacrificed and cleared. After clearing of the whole brain, both
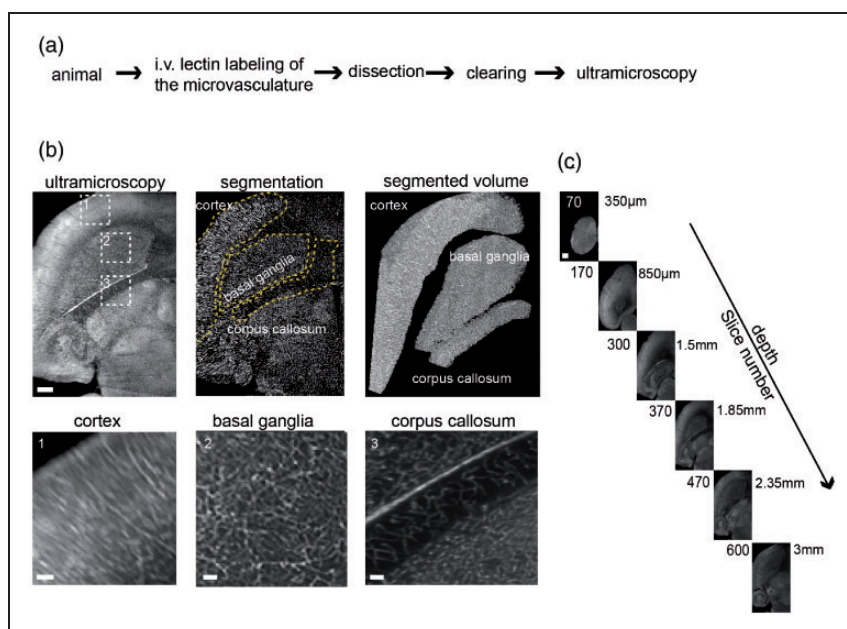

Figure 1. Ultramicroscopy of the microvasculature in healthy mice. (a) Experimental outline for tissue preparation and SPIM. Healthy, female black six wild-type mice were injected intravenously with fluorescent lectins to label the microvasculature before perfusion. (b) Ultramicroscopic image processing and three-dimensional view of the analyzed regions of interest in the healthy mouse brain, magnified images (dashed boxes) of cortex, basal ganglia, and corpus callosum. Yellow dashed lines indicate the segmented subregions. (c) Images of the acquired z-stack. Step size is 5 μm. The entire stacks consisted of ∼600–1000 single-plane images. Scale bar = 500 μm and 100 μm in magnified images in B.

hemispheres were recorded by ultramicroscopy ($n = 6$ hemispheres from $n = 3$ mice). In order to investigate microvascular parameters in different regions of the healthy brain, we extracted vascular parameters in the cortex (grey matter), corpus callosum (white matter), and basal ganglia using masks and counter masks (Figure 1(b) and (c), Supplemental movie 1, 2). Each brain region contained distinct vascular properties: The cortex yielded highest variance in microvascular density (MVD) (Figure 2(a)). Overall, the mean MVD in the corpus callosum was markedly lower ($3.5 \pm 0.9 \times 10^4$ branch vessels/mm^3) compared to the cortex ($5.1 \pm 1.6 \times 10^4$ mm^{-3}, $p < 0.05$) and basal ganglia ($4.8 \pm 0.5 \times 10^4$ mm^{-3}, $p < 0.05$, Figure 2(a) and (b)). Also, the corpus callosum showed lower mean partial vessel volumes fVV (corpus callosum; 0.18 ± 0.05 vs. cortex; 0.25 ± 0.04, $p = 0.01$) and longer vessel segments (corpus callosum; $26.2 \pm 3.5\,\mu m$ vs. cortex; $21.43 \pm 4.5\,\mu m$, $p = 0.02$). Vessel segments in the corpus

callosum also showed a trend towards higher tortuosity compared to the other regions (corpus callosum; 1.16 ± 0.03 vs. cortex; 1.13 ± 0.02 and basal ganglia; 1.14 ± 0.01, $p > 0.05$). Similarly, while the mean vessel surface density ρ_A did not differ significantly (corpus callosum; 36 ± 23 mm^{-1} vs. basal ganglia; 41 ± 10 mm^{-1} and cortex; 38 ± 11 mm^{-1}, $p > 0.05$), the vessel length density ρ_L underlined the reduced vascular proliferation in the corpus callosum (corpus callosum; 534 ± 95 mm^{-2} vs. basal ganglia; 793 ± 75 mm^{-2}, $p = 0.004$ and cortex; 737 ± 96 mm^{-2}, $p = 0.01$). Mean vessel radius and surface area did not differ significantly between the examined brain regions ($p > 0.05$, Figure 2(a) and (b)).

Quantitative assessment of tumor angiogenesis

To investigate microvascular dynamics in a pathological paradigm, we employed the U87-MG glioma
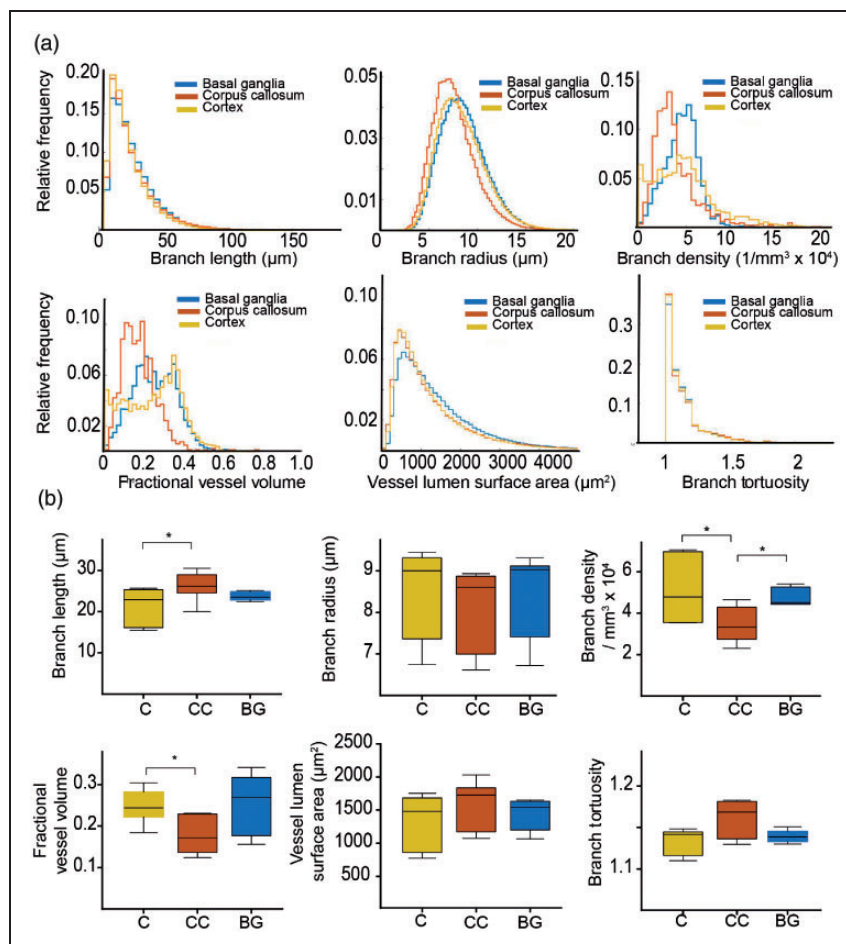

Figure 2. Microvascular parameters in the healthy mouse brain. (a) Histograms show quantification results from ultramicroscopic images and demonstrate significant differences between the indicated vessel parameters in different regions of the healthy brain. (b) Whisker plots demonstrate vessel parameters of different regions in the healthy brain (median with 50% quantile and extremal values (whiskers) from $n = 3$ mice for six analyzed brain hemispheres. * $= p < 0.05$.
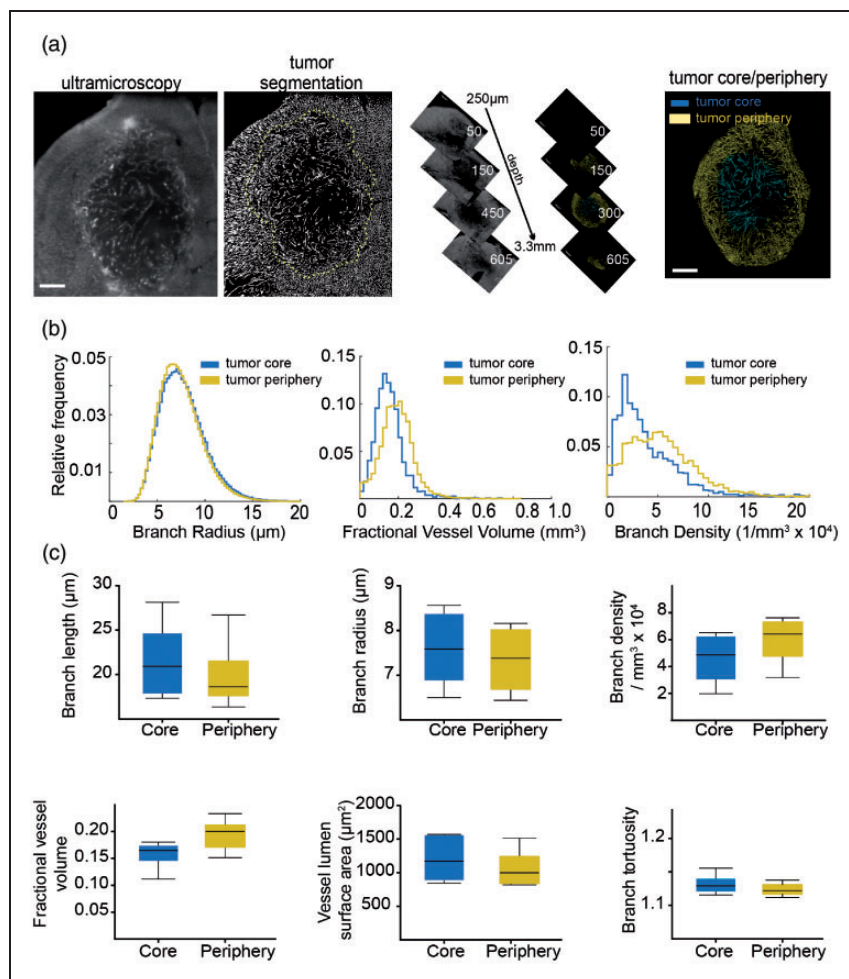C: cortex; Cc: corpus callosum; BG: basal ganglia.

Figure 3. Microvasculature remodeling in the U87 glioma model. (a) Ultramicroscopic image processing and three-dimensional view of region of interest in mouse U87 glioma tumors. Yellow dashed line indicates the segmented tumor area. (b) Histogram representation of quantified vessel parameters showing tumor core and tumor periphery. (c) Whisker plots are shown for the obtained parameters of U87 mouse tumors ($n = 6$ mice). Scale bar $= 500$ μm.

model ($n = 6$ mice). After lectin labeling of the microvasculature and clearing, tumors were divided into two separate tumor compartments: the tumor periphery, representing the infiltrative zone (outer 50% of the tumor, as measured from the centroid of the mask in the radial direction) and the tumor core (inner 50%). We hypothesized that the tumor core might show major microvascular differences compared to the tumor periphery (Figure 3(a), Supplemental movie 3). However, contrary to our hypothesis, most vessel parameters did not differ significantly between the tumor core and tumor periphery (Figure 3(b) and (c)), except the fractional vessel volume fVV (tumor core; 0.16 ± 0.03 vs. tumor periphery; 0.20 ± 0.03, $p = 0.05$). The mean vessel length density ρ_L (tumor core; 511 ± 143 mm^{-2} vs. periphery; 633 ± 164 mm^{-2}, $p = 0.2$) and surface density ρ_A (tumor core; $30 \pm$

15 mm^{-1} vs. periphery; 34 ± 17 mm^{-1}, $p > 0.05$) did also not differ significantly.

Probing the microvasculature in development

To further extend our approach and show the applicability to developmental studies, we assessed the microvasculature in embryonic mice (e13.5, $n = 4$ embryos). Intravenous lectin injection of the mother animal resulted in excellent labeling of the entire embryonic microvasculature, including microvessels in the nervous system, parenchymal organs (e.g. heart, liver, kidney), and cardiovascular system with high signal-to-noise ratio (Figure 4(a), Supplemental movie 4, 5). We focused our analysis on the central nervous system and compared microvascular properties of the brain and spinal cord (Figure 4(a) to (c)). Analysis of vessel
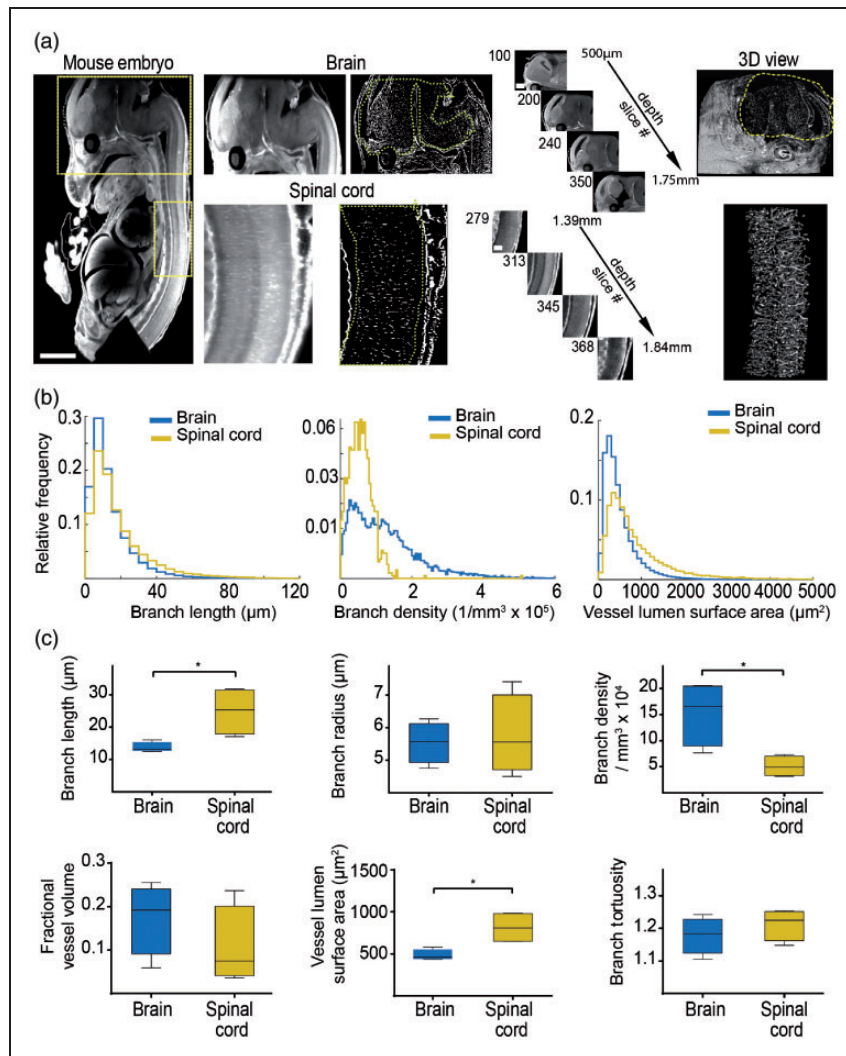
Figure 4. Assessing microvascular parameters in development. (a) Ultramicroscopic image processing and three-dimensional view of the brain and spinal cord in the mouse embryo (e13.5). Yellow boxes indicate magnified regions (brain and spinal cord). (b) Histogram representations of the quantified ultramicroscopic images demonstrate significant differences in vessel parameters between brain and spinal cord. (c) Whisker plots show parameter statistics for the spinal cord and brain microvasculature ($n = 4$ embryos). Scale bar is 500 μm in embryo images, 250 μm in magnified brain images, and 100 μm in magnified spinal cord images. $* = p < 0.05$.

parameters demonstrated that the spinal cord exhibits significantly longer vessel segments with less branches compared to the developing brain (mean vessel segment length, spinal cord; 24.6 ± 7.8 μm vs. embryonic brain; 13.8 ± 1.6 μm, $p < 0.05$, Figure 4(c)). This resulted in a larger vessel surface area in the spinal cord compared to the brain (spinal cord: 775.6 ± 150.6 μm^2 vs. embryonic brain; 483.6 ± 66.5 μm^2, $p = 0.02$). Furthermore, the mean vessel density was significantly lower in the embryonic spinal cord compared to the embryonic brain (spinal cord; $5.4 \pm 2.3 \times 10^4$ vs. brain; $15.3 \pm 6.3 \times 10^4$, $p = 0.02$). While the vessel length density ρ_L exhibited a wide distribution (spinal cord; 313 ± 246 mm^{-2} vs. brain; 475 ± 306 mm^{-2}, $p > 0.05$), the

mean vessel surface density ρ_A showed significant differences (spinal cord; 28 ± 6 mm^{-1} vs. brain; 47 ± 8 mm^{-1}, $p = 0.02$). The mean vessel radius, tortuosity, and fractional vessel volume showed no significant differences between the embryonic brain and spinal cord (Figure 4(c)).

Discussion

Vascular patterning is crucial for understanding embryonic development, growth, and pathology. Cancer is one of the most notable examples, in which vessel parameters influence the prognosis and treatment outcome.[30] Neo-angiogenesis has been attributed

as a main denominator for tumor progression and metastasis. This has led to an increased interest in employing inhibitors of angiogenesis to curb cancer and antiangiogenic agents have become standard of care for, e.g. ovarian cancer or renal cell carcinoma.[31] In addition, there is also ample evidence to suggest a crucial role of vasculature parameters for the success of chemotherapeutic and immunotherapeutic treatment regimens.[32] Paradoxically, in other tumor contexts, antiangiogenic treatments have been linked to earlier progression, increased invasion, and metastasis formation.[33] Impaired microvascular function may lead to tumor hypoxia, a crucial factor associated with the development of resistant cell populations.[34] Therefore, further investigations into mechanisms of angiogenesis and possible druggable targets in preclinical models are warranted.[35]

Ultramicroscopy and tissue clearing using light sheet microscopy have gained a lot of traction in recent years, especially in the field of neuroscience.[17] However, despite the unprecedented 3D resolution, the utility of the technology has been mainly limited to qualitative studies.[36,37] The quantitative analysis of ultramicroscopy datasets was significantly hindered by the lack of analyses protocols and tools to segment all objects of interest in the complex and large 3D datasets that can easily encompass several gigabytes from a single acquisition. In our study, the analysis of each sample generated, on average, 5×10^4 (in embryonic spinal cord) to 3×10^6 single data points (in healthy brain samples). The technique employed by us can analyze vessel radii as small as $3 \, \mu m$, limited by the image resolution, and robustly generates the main morphological microvascular parameters without the need for high-performance computational hardware or expensive proprietary licenses for image processing software (with the exception MATLAB).

To demonstrate the utility of our platform, we analyzed whole embryos as well as healthy and tumor containing brain samples. The technique is also amenable to other organs with good labeling efficacy (Supplemental Figure 2). After clearing, microscopic image acquisition of a tissue sample took $\sim 4 \, h$. We employed ilastik[22] to segment the entire vasculature contained in the image stacks, which took 30–90 min for classifier training and ~ 4–6 h for automated pixel classification and TIFF-export of an image stack of 1 GB in an 8-bit format ($1766 \times 1284 \times 446$ ($\sim 10^9$) pixels). The segmented "angiome" was quantified using custom-written MATLAB code designed to analyze and calculate the length of vessels between branches, radius, tortuosity, surface area, and various vessel density parameters. The automated quantification of a 1 GB dataset containing 200,766 vessel branches took $\sim 1 \, h$ with a standard, quad-core

computer and 16 GB of random access memory (RAM). The entire processing pipeline can be executed on a standard personal computer, with the feasible image size being limited only by the RAM addressable by ilastik and MATLAB.

Our developed processing algorithm enables incremental analyses of large datasets, processing 3D data in a partitioned manner and saving partial results. If the MATLAB quantification is interrupted, the code can be restarted with identical settings to continue where it left off, sparing already quantified subvolumes. This makes "asymptotic analyses" possible. If appropriate for a given investigation, long analyses can be terminated once the parameter distributions reach an asymptotic state, where further processing of more randomly sampled subvolumes is not expected to change relative parameter distributions. Such methods may become relevant for future investigations such as, e.g. large-tissue µCT or high-resolution, large field-of-view imaging modalities.

Our analysis of different areas of the healthy brain demonstrated a significant difference in several microvascular parameters, such as vessel density, tortuosity and partial vessel volume between cortex, basal ganglia, and corpus callosum. Our analysis demonstrated that white matter regions like the corpus callosum have longer vessel segments with less branches and lower vessel density, consistent with lower energy demands of long-range axonal projections compared to grey matter regions of the cortex and basal ganglia.[38] This finding was mirrored in the embryonic spinal cord when compared to the embryonic brain where branch length and branch density in the spinal cord was also lower compared to the brain.

The analysis of U87 tumors was performed on the tumor core versus tumor periphery. In contrast to our hypothesis that the infiltrative tumor border might have increased vascular densities and more aberrant vessel morphologies compared to the tumor core, there were only minor differences between the two tumor regions, except for the mean fractional vessel volume, which was higher in the tumor periphery. The absence of significant differences between the other vessel parameters might be explained by the lack of necrosis and rather uniform vascular patterning in U87 tumors at the stage of analysis (day 21 after tumor cell implantation). It is well conceivable that pathological angiogenesis kicks in only at later tumor stages (e.g. day 35 after tumor cell implantation) or is more prominent in other, more invasive brain tumor models.[39]

We further demonstrate the value of our approach for developmental studies in mice embryos. We found significant differences between microvasculature patterns of different organs in the embryo. Our analysis

of the microvasculature of brain and spinal cord revealed differences in vessel branch densities consistent with the idea that the higher neuronal density in the brain requires higher vascular supply. The spinal cord consisted of longer vessel segments with fewer branches compared to the brain, presumably because of the long fiber tracts and lower neuronal densities in the spinal cord compared to the brain.

The quantitative analysis presented here constitutes a proof-of-principle study to showcase the developed pipeline. The data processing and analysis can be easily adapted to different experimental setups. Limitations of our study include the necessity to obtain high-quality optical recordings with high signal-to-noise ratio in order to achieve robust segmentations. We found that the trainable toolkit "ilastik" provided the best segmentation of our data, offering flexibility and customization to suit different image types, and did not demand excessive processing power, but the segmentation step can be substituted with a method of choice. Our technique includes semi-automatic segmentation, data post-processing, and comprehensive quantitative analyses. By using a partitioning approach, the analysis of an arbitrarily formed and sized 3D image segmentation can be conducted on standard desktop and laptop computers without the need for advanced computing resources, such as computing clusters or graphics cards.

While there are different image post processing tools available, such as Imaris or Amira to visualize, analyze, and quantify microscopy data, our processing pipeline was optimized to quantify complex vascular structures with microvessels sizes at the scale of the image resolution. With a vessel radius estimation tailored to the microvascular scale and connectivity, as well as the entirely automated quantification of an extensive set of basic geometric parameters, our pipeline is able to efficiently analyze vascular datasets. While Imaris and Amira offer powerful capabilities for data visualization, animation, and interactive exploration, their generality and ability to deal with large input images is a disadvantage in comparison to our pipeline. Such powerful image processing tools allow manual data exploration but could in our hands not characterize thousands to millions of vessels in a given dataset.

The vessel radii found in this study and consequently also fractional vessel volumes are most likely overestimated by the imaging procedure and limited resolution inherent to our experimental setup. Since most capillaries are on the order of one to two pixels, the overlaying point spread function leads to an "over-estimation" of the segmentation, manual, and automated alike. At an axial resolution of 3–5 µm, this can amplify capillary radii and vessel volumes, leading to artificially large values. This constitutes a systematic error throughout the experiment.

Additional post-processing steps, e.g. morphological thinning of the segmented images can be applied for correction.[18] Statistical analysis of the presented data is difficult to perform due to the wealth of data: we compared the mean of each parameter per mouse, thus averaging thousands of data points per animal in order to not overestimate effect sizes in our statistical analysis. Our approach could further be extended to radiomics and atlas-based registration as previously highlighted[40] and different other quantitative measures can be implemented in the piecewise analysis, such as local connectivity and regularity parametrizations.[18]

In summary, ultramicroscopy is a fast and straight-forward technique that generates large datasets of entire organs or organisms. Our described "toolbox" can be used to investigate physiological and pathological states as well as treatment regimens in disease models. Imaging of the microvasculature using SPIM served as a proof of principle; our processing pipeline can be applied to 3D data from any imaging modality, e.g. µCT, magnetic resonance angiography, laser-scanning, or electron microscopy. Our approach can obtain robust and quantitative microvascular parameters, which could be easily expanded to other fluorescent objects of interest that can be quantified in a partitioned manner, e.g. immune cell distributions, neuronal projections, or migratory patterns of fluorescently labeled stem or tumor cells to quantitatively map cellular 3D distributions in entire organs and intact organisms.

Funding

Declaration of conflicting interests

The author(s) declared no potential conflicts of interest with respect to the research, authorship, and/or publication of this article.

Authors' contributions

J.B., T.K., and B.T. established ultramicroscopy and tissue clearing. Acquisition of ultramicroscopy datasets was performed by J.B. and T.K. Programming of Matlab code and analysis was done by A.H. and F.T.K. Image segmentation and training of the sample images was performed by A.H. and A.A., A.C.S. and T.K. helped with tissue clearing. T.K. performed tumor cell implantations. F.T.K. provided analytical tools. B.T., F.T.K., and M.O.B. conceptualized and supervised the study and performed analyses. A.H, B.T. F. T.K., and M.O.B. wrote the article with input from J.B., A. A., K.KJ., K.S., D.S., A.C.S., A.Ab., W.W., M.P., and M.B.

Supplemental material

Supplemental material for this article is available online.

ORCID iDs

Daniel Schwarz 🆔 https://orcid.org/0000-0002-9017-8245
Michael O Breckwoldt 🆔 https://orcid.org/0000-0002-9980-2390

References

1. Augustin HG and Koh GY. Organotypic vasculature: from descriptive heterogeneity to functional pathophysiology. *Science* 2017; 357: eaal2379.
2. Udan RS, Culver JC and Dickinson ME. Understanding vascular development. *Wiley Interdiscip Rev Dev Biol* 2013; 2: 327–346.
3. Huang J, Frischer JS, Serur A, et al. Regression of established tumors and metastases by potent vascular endothelial growth factor blockade. *Proc Natl Acad Sci USA* 2003; 100: 7785–7790.
4. Carreras IA, González RF, Barrutia AM, et al. 3D reconstruction of histological sections: application to mammary gland tissue. *Microsc Res Technol* 2010; 73: 1019–1029.
5. Weiskopf N, Mohammadi S, Lutti A, et al. Advances in MRI-based computational neuroanatomy: from morphometry to in-vivo histology. *Curr Opin Neurol* 2015; 28: 313–322.
6. Kickingereder P, Radbruch A, Burth S, et al. MR perfusion–derived hemodynamic parametric response mapping of bevacizumab efficacy in recurrent glioblastoma. *Radiology* 2016; 279: 542–552.

7. Federau C, Meuli R, O'Brien K, et al. Perfusion measurement in brain gliomas with intravoxel incoherent motion MRI. *AJNR* 2014; 35: 256–262.
8. Liang J, Cheng Q, Huang J, et al. Monitoring tumour microenvironment changes during anti-angiogenesis therapy using functional MRI. *Angiogenesis* 2019; 22: 457–470.
9. Belderbos S, González-Gómez MA, Cleeren F, et al. Simultaneous in vivo PET/MRI using fluorine-18 labeled Fe3O4@Al(OH)3 nanoparticles: comparison of nanoparticle and nanoparticle-labeled stem cell distribution. *EJNMMI Res* 2020; 10: 73.
10. Helmchen F and Denk W. Deep tissue two-photon microscopy. *Nat Methods* 2005; 2: 932–940.
11. Chung K, Wallace J, Kim S-Y, et al. Structural and molecular interrogation of intact biological systems. *Nature* 2013; 497: 332–337.
12. Dodt H-U, Leischner U, Schierloh A, et al. Ultramicroscopy: three-dimensional visualization of neuronal networks in the whole mouse brain. *Nat Methods* 2007; 4: 331–336.
13. Renier N, Wu Z, Simon DJ, et al. iDISCO: a simple, rapid method to immunolabel large tissue samples for volume imaging. *Cell* 2014; 159: 896–910.
14. Hama H, Kurokawa H, Kawano H, et al. Scale: a chemical approach for fluorescence imaging and reconstruction of transparent mouse brain. *Nat Neurosci* 2011; 14: 1481–1488.
15. Ertürk A, Mauch CP, Hellal F, et al. Three-dimensional imaging of the unsectioned adult spinal cord to assess axon regeneration and glial responses after injury. *Nat Med* 2011; 18: 166–171.
16. Pan C, Schoppe O, Parra-Damas A, et al. Deep learning reveals cancer metastasis and therapeutic antibody targeting in the entire body. *Cell* 2019; 179: 1661–1676.
17. Ueda HR, Ertürk A, Chung K, et al. Tissue clearing and its applications in neuroscience. *Nat Rev Neurosci* 2020 ; 21: 61–79.
18. Hahn A, Bode J, Krüwel T, et al. Glioblastoma multiforme restructures the topological connectivity of cerebrovascular networks. *Sci Rep* 2019; 9: 11757–11717.
19. Breckwoldt MO, Bode J, Kurz FT, et al. Correlated magnetic resonance imaging and ultramicroscopy (MR-UM) is a tool kit to assess the dynamics of glioma angiogenesis. *eLife* 2016; 5: 3212.
20. Breckwoldt MO, Bode J, Sahm F, et al. Correlated MRI and ultramicroscopy (MR-UM) of brain tumors reveals vast heterogeneity of tumor infiltration and neoangiogenesis in preclinical models and human disease. *Front Neurosci* 2019; 12: 28272–28210.
21. Sommer C, Straehle C, Köthe U, et al. ilastik: interactive learning and segmentation toolkit. In: *Eighth IEEE international symposium on biomedical imaging (ISBI)*, 2011, pp. 230–233. New York: IEEE.
22. Berg S, Kutra D, Kroeger T, et al. ilastik: interactive machine learning for (bio)image analysis. *Nat Methods* 2019; 16: 1226–1232.
23. Schindelin J, Arganda-Carreras I, Frise E, et al. Fiji: an open-source platform for biological-image analysis. *Nat Methods* 2012; 9: 676–682.

24. Wirthschaft P, Bode J, Simon AEM, et al. A PRDX1-p38α heterodimer amplifies MET-driven invasion of IDH-wildtype and IDH-mutant gliomas. *Int J Cancer* 2018; 143: 1176–1187.

25. Schwarz MK, Scherbarth A, Sprengel R, et al. Fluorescent-protein stabilization and high-resolution imaging of cleared, intact mouse brains. *PLoS ONE* 2015; 10: e0124650–26.

26. Di Ieva A, Grizzi F, Sherif C, et al. Angioarchitectural heterogeneity in human glioblastoma multiforme: a fractal-based histopathological assessment. *Microvasc Res* 2011; 81: 222–230.

27. Lee TC, Kashyap RL and Chu CN. Building skeleton models via 3-D medial surface axis thinning algorithms. *CVGIP: Graphical Models and Image Processing* 1994; 56: 462–478.

28. Bullitt E, Gerig G, Pizer SM, et al. Measuring tortuosity of the intracerebral vasculature from MRA images. *IEEE Trans Med Imaging* 2003; 22: 1163–1171.

29. Wälchli T, Mateos JM, Weinman O, et al. Quantitative assessment of angiogenesis, perfused blood vessels and endothelial tip cells in the postnatal mouse brain. *Nat Protoc* 2015; 10: 53–74.

30. Folkman J. Role of angiogenesis in tumor growth and metastasis. *Semin Oncol* 2002; 29: 15–18.

31. Weis SM and Cheresh DA. Tumor angiogenesis: molecular pathways and therapeutic targets. *Nat Med* 2011; 17: 1359–1370.

32. Fukumura D, Kloepper J, Amoozgar Z, et al. Enhancing cancer immunotherapy using antiangiogenics: opportunities and challenges. *Nat Rev Clin Oncol* 2018; 15: 325–340.

33. Chen C-T and Hung M-C. Beyond anti-VEGF: dual-targeting antiangiogenic and antiproliferative therapy. *Am J Trans Res* 2013; 5: 393–403.

34. Lathia JD, Mack SC, Mulkearns-Hubert EE, et al. Cancer stem cells in glioblastoma. *Genes Dev* 2015; 29: 1203–1217.

35. Kloepper J, Riedemann L, Amoozgar Z, et al. Ang-2/VEGF bispecific antibody reprograms macrophages and resident microglia to anti-tumor phenotype and prolongs glioblastoma survival. *Proc Natl Acad Sci USA* 2016; 113: 4476–4481.

36. Lugo-Hernandez E, Squire A, Hagemann N, et al. 3D visualization and quantification of microvessels in the whole ischemic mouse brain using solvent-based clearing and light sheet microscopy. *J Cereb Blood Flow Metab* 2017; 37: 3355–3367.

37. Jährling N, Becker K and Dodt H-U. 3D-reconstruction of blood vessels by ultramicroscopy. *Organogenesis* 2009; 5: 227–230.

38. Schmid F, Barrett MJP, Jenny P, et al. Vascular density and distribution in neocortex. *NeuroImage* 2019; 197: 792–805.

39. Lagerweij T, Dusoswa SA, Negrean A, et al. Optical clearing and fluorescence deep-tissue imaging for 3D quantitative analysis of the brain tumor microenvironment. *Angiogenesis* 2017; 20: 533–546.

40. Todorov MI, Paetzold JC, Schoppe O, et al. Machine learning analysis of whole mouse brain vasculature. *Nat Methods* 2020; 17: 442–449.

Supplementary Material

Hahn et al., *J Cereb Blood Flow Metab* 271678X20961854 (2020)

Supplemental methods

Automated partitioning analysis

After the automated dissection of a segmented and post-processed input dataset, each subvolume of desired dimensions (in 3D) is analyzed individually. Different regions of interest (ROIs), marked by manually drawn masks on the original image data beforehand, are considered exclusively within the cuboid subvolumes, also with partial volume coverage. The subvolumes are analyzed consecutively, either sequentially following the linear index of the partitions, or in random order to allow for asymptotic analyses of very large datasets. The partitioned analysis can be terminated and picked up again where left off, by restarting the program with identical settings. Quantifications are conducted using the post-processed image stacks, containing the binary vessel architecture, as well as the tagged skeleton data with differentiated centerline voxels. The voxel size (resolution) along each imaging dimension needs to be specified and is used to provide results with physical units (in our study, on the scale of micrometers).

Before partitioning the masked image volume for quantitative processing, the original vessel segments in the undissected image are labeled. When the analysis of the individual partitions is finished (or while it is still running, with some partitions finished), a separate script can be executed in a second Matlab instance to merge the results present thus far. The vessel properties determined in the individual partitions are combined to deliver estimates of true vessel segment properties without artificial cuts through processing. This is done by comparing the branch labels within each partition with the original, globally labeled data. Vessel lengths and surfaces are added, while tortuosity and mean segment radii are calculated by a weighted average using the partitioned segment lengths as weights. The finally determined vessel properties are written to lists in text files in matching order, with an additional text file showing the labels of the corresponding branches in the original dataset. Thus, the vessels corresponding to different labels can be located in the original dataset for visual analysis.

Perfusion density quantifications

Vascular density measures are determined for each subvolume of predefined dimensions. The fractional vessel volume fVV is given by the ratio of voxels identified as blood vessels to the total number of voxels within a region of interest in the cuboid, marked by the respective mask. The MVD is calculated as the number of individual vessel segments per mm³ tissue volume within a masked region. Vessel segments are defined by the skeleton's branch voxels between two branching/end points.

The microvascular surface density ρ_A is quantified for each subvolume to give a measure of lumen surface area with respect to tissue volume under supply. The vessel surface area is determined in physical units of mm^2 using the discrete voxel intensity gradients along each imaging dimension. The discrete gradient is calculated by subtracting intensities of voxels with an offset of one voxel length along each dimension. Taking the absolute value, the resulting image stacks show vessel edges along each dimension in binary form. The edge information along each dimension is combined and linearly interpolated between voxels to attain the vessel surface as a tessellation of voxel surface elements with known physical area (see next subsection for details). The sum of all surface elements in a volume is normalized by the physical tissue volume in mm^3 to provide the vessel surface density ρ_A in mm^{-1}. The total Euclidean skeleton length is normalized with the tissue volume to provide the averaged vessel length density ρ_L for the region of interest in mm/mm^3.

Individual vessel quantifications

Individual vessel segments between branching points are labeled and analyzed geometrically within each processing partition. The segment length l is obtained as the sum of Euclidean inter-voxel distances along the vessel centerline between branching points and/or end points, considering physical voxel dimensions. The segment tortuosity τ is simply characterized by the ratio $\tau = l/d$, with the geodesic endpoint separation d [1]. This dimensionless quantity is often called the distance metric and gives a simple quantification of the degree of curvature of a vessel segment [2].

The mean radius $\bar{r}$ of a vessel segment is determined as the average over all radius values r along its skeleton line. For each voxel on the centerline of a branch, the radius $\bar{r}$ at that point is estimated using two methods. The first method is a simple implementation using Euclidean distance maps, generated with the Matlab-function 'bwdist' [3]. For each skeleton point, the nearest background voxel in the binary vessel dataset is identified to determine the corresponding physical distance using the voxel resolution. This works best for isotropic resolutions, since the distance map does not consider physical pixel sizes. This method can be deactivated with a Boolean flag in the script if the image resolution is too anisotropic. In this case, only the following method is used to estimate the mean segment caliber.

A second radius value for each skeleton point is estimated using the lumen surface of the vessels. Along each dimension, 2D-slices of the imaged volume are consecutively scanned and vessel boundary voxels, surrounding each skeleton segment, are probed to average their physical distance from the centerline. The distances in the standard scanning slices (x-y-, x-z, and y-z plane) are projected onto the plane perpendicular to the 3D orientation of the skeleton segment at the respective point of intersection

with the scanning plane using a trigonometric correction with $\sin(\alpha)$, where α is the angle between the local 3D vessel skeleton orientation and the scanning plane at the point of intersection P (see **supplemental Fig. 1, A,B**). This correction provides an estimate of the radius values perpendicular to the vessel centerline. In each scanning slice, the cut vessels with at least one skeleton pixel inside are processed to attain a radius estimate from every pixel of the respective vessel cross section's perimeter (see **supplemental Fig. 1, A,B** for details). From all three scanning directions, the values accumulated for each vessel segment are averaged to attain an estimate of the segment's mean radius.

The mean radius values from the second method are averaged with the radii from the distance map method with equal weighting, unless deactivated due to strong resolution anisotropy. The mean segment radius $\bar{r}$ is quantified as the average of all values determined for the respective vessel segment. During the second radius estimation method, the area of each vessel surface element is added up to quantify the lumen surface area A in μm^2. Each geometric property is associated with the respective segment label in a subvolume under analysis and saved in lists.

Vessel branches in the original input data were labeled before dissection. The properties of vessel instances divided by artificial dissection are determined by combining the corresponding vessel piece characteristics. The mean branch radius $\bar{r}$ and tortuosity τ are averaged, using the respective segment lengths in different partitions as weights; the length l and surface area A are summed for each vessel labeled in the original, masked image volume.

Evaluation of quantification accuracy

Most quantitative measures determined by the custom algorithm in Matlab are well-defined and straight-forward to calculate numerically (see previous subsections), given a valid segmentation of the imaged vasculature. For realistic vessel networks with tortuous segments and complex connectivity, the mean radius is an ill-defined property, which is nontrivial to determine. Initially, we tried implementing a radius quantification using virtual planes, oriented perpendicular to the 3D skeleton at each pixel of the skeleton with different interpolation techniques and corrections to project and discern individual vessel parts in arbitrarily placed planes through the discrete image volume. This turned out to be problematic due to the interpolation of structures sized near the resolution limit, thus we restarted with an entirely new approach avoiding interpolation, specifically tailored to data with many relevant structures around the image resolution (see previous subsection for details).

The radius quantification we present in this work was validated using synthetic TIFF-stacks created with a custom Matlab script, holding "segmented" cylinders with

well-defined radii at different 3D orientations and pixel dimensions of 3.25 x 3.25 x $5\,\mu$m. Each synthesized volume contained 10 straight cylinders with identical 3D orientation and different positions, but no intersections in order to avoid variable radii at crossings (see **supplemental Fig. 1, E,G** for examples and relevant orientation angles). The "polar" angle θ between the original imaging plane ($3.25\,\mu$m resolution) and the orthogonal z-axis in stack direction ($5\,\mu$m steps) was varied in steps of 10° between 0° and 90°, covering the non-periodic range. The in-plane angle φ between the x- and y-axes was set to 0° and 45° to cover the two in-plane orientations that yield the highest difference in effective pixel lengths of the in-plane axis perpendicular to the cylinder orientation ($3.25\,\mu$m and $\sqrt{2 \cdot 3.25^2} \approx 4.6\,\mu$m). Synthetic volumes were produced with cylinder radii of 3, 6, 8, 10, 12, and $15\,\mu$m, inspired by the radius distributions found in the results of our study (see main **Figs. 2-4**).

Our assessment of the radius quantification accuracy is summarized in **supplemental Fig. 1, C**, presenting the mean bias and its standard deviation for different 3D orientations and radius values. Since the accuracy of the quantified radii strongly depends on the segment's orientation, more differentiated validation results are presented in **supplemental Fig. 1, D,F**. For each modeled cylinder radius, the mean quantified radii (from respectively 10 cylinders) are plotted with standard deviations for each θ and φ angle individually. The validation shows that, under most circumstances, the quantified radii agree very well with the ground truth. Since the algorithm was optimized for structures near the resolution limit, the accuracy is best for small vessels with mean radii $r \lesssim 10\,\mu$m, where most orientations yield deviations below $1\,\mu$m, with an exception for large cylinders at very small angles $\theta \approx 10°$. Averaging over all angle orientations, the mean quantification bias and variance are well within the limits of one pixel size, as summarized in **supplemental Fig. 1, C**.

Supplemental references

1. E. Bullitt, G. Gerig, S. M. Pizer, W. Lin, and S. R. Aylward. Measuring tortuosity of the intracerebral vasculature from MRA images. *IEEE Transactions on Medical Imaging* 22(9):1163-71, 2003.

2. S. Lorthois, F. Lauwers, and F. Cassot. Tortuosity and other vessel attributes for arterioles and venules of the human cerebral cortex. *Microvascular Research* 91:99-109, 2014.

3. C. R. Maurer, R. Qi, and V. Raghavan. A linear time algorithm for computing exact Euclidean distance transforms of binary images in arbitrary dimensions, *IEEE Transactions on Pattern Analysis and Machine Intelligence* 25(2):265-270, 2003.

Supplemental figures
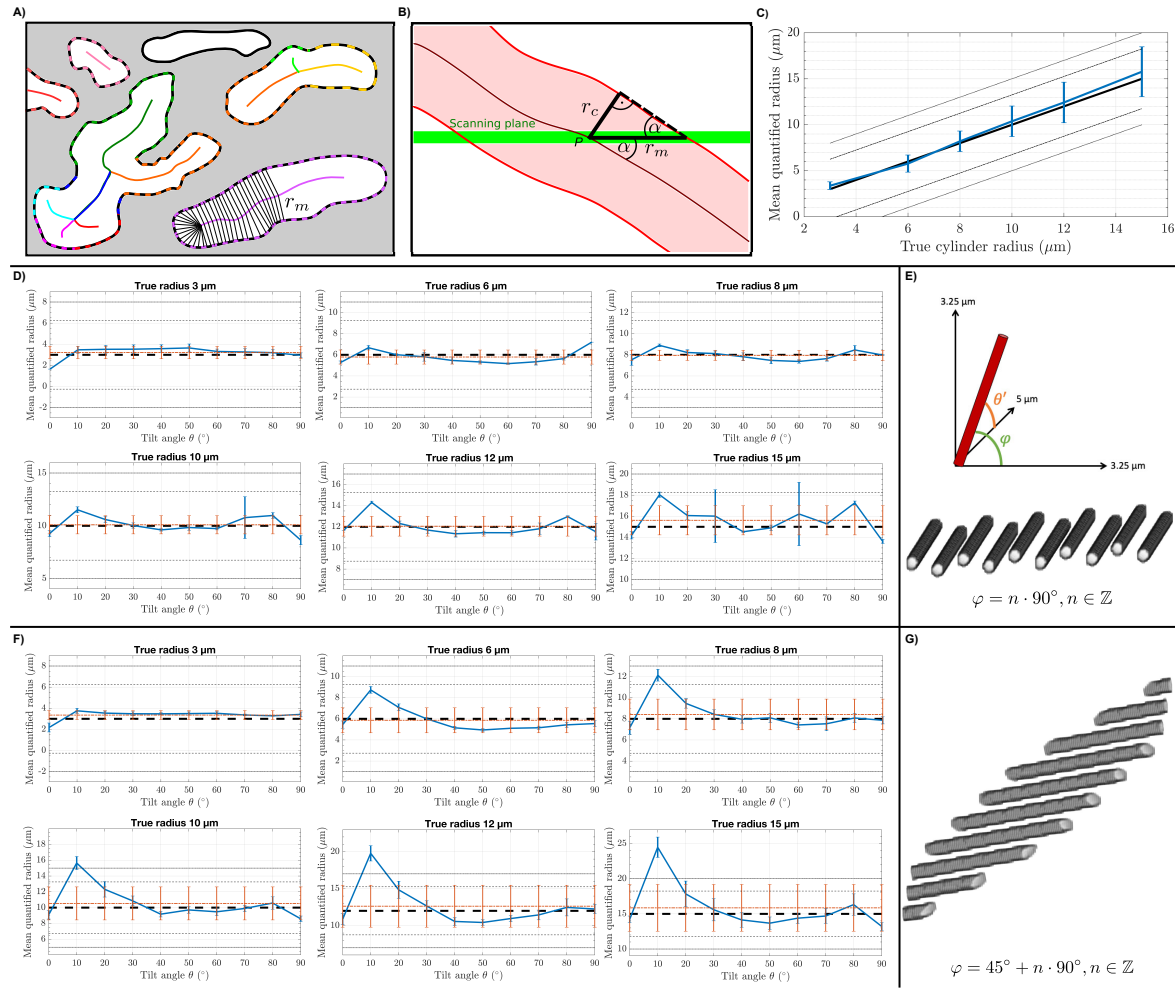
Supplemental Fig. 1: Quantification details and validation of determined vessel radii. A) Sketch of a schematic 2D scanning plane with several vessels cutting the plane (the tissue background is colored in gray). The central top vessel area (with black outline) does not contain a skeleton segment in the depicted slice and is therefore ignored in this slice. The vessel cuts containing labeled skeleton pixels are processed by iterating over the perimeters of each area, marked by dashed black-colored lines, matching the label color of the nearest contained skeleton branch. As demonstrated in half of the bottom right vessel (purple), for each pixel on the perimeter of the cross section, the distance to the nearest skeleton pixel is determined (considering the real physical pixel resolution, making this approach stable even for very anisotropic pixel dimensions). In cases where differently labeled skeleton branches lie within one vessel cross section, the perimeter is processed piecewise with pixel distances assigned to their closest branch (see top right and bottom left cross sections). Each radius value determined within a scanning plane (x-y, x-z, and y-z plane), called r_m, is projected onto the plane orthogonal to the local 3D skeleton orientation. **B)** Sketch of a scanning plane cutting a vessel as seen from above, with angle α between the skeleton and the

95

scanning plane at skeleton pixel P. If a segment is not parallel to the imaging plane, the measured radius r_m is multiplied with $\sin(\alpha)$ for a corrected radius r_c, approximating the true radius orthogonal to the vessel orientation. The r_c values attained from all perimeter pixels along each scanning direction are averaged for each branch label, which yields mean segment radii based on the lumen shape. **C)** Accuracy validation summary of the implemented radius quantification from analyzing model volumes with differently oriented cylinders with pre-defined radius. The true cylinder radius is on the x-axis and the radii quantified by the algorithm are shown as mean and standard deviation over all tested vessel orientations (see panels **D** and **F** for details). The true radius is plotted in black beneath the blue error bar lines and a deviation of the in-plane resolution ($3.25\,\mu$m) is marked by thin dashed lines, with the z-resolution range ($5\,\mu$m) as thin dotted lines. Panels **D** and **F** present the mean quantified radii of cylinders with different orientations between the x and y axis (defined by the angle φ) and the z-axis (parametrized by θ, see panel **E**) and predefined radii of $r = \{3, 6, 8, 10, 12, 15\}\,\mu$m. The true radius is plotted as a bold dashed, horizontal line, while the quantified radii of ten identically oriented but differently positioned cylinders are presented for each angle θ between 0° and 90° through the mean and standard deviation among those ten cylinders with blue connected error bars. For each model radius, the mean determined radius and its standard deviation over the θ orientations is shown as orange error bars across the entire range. The pixel resolutions are shown, added to and subtracted from the true cylinder radius, by thin, dashed and dotted lines. **D)** The results for different θ orientations with $\varphi = 0°$, *i.e.*, the cylindrical axis running parallel to the x-direction with $3.25\,\mu$m pixel size. **F)** The same analysis with cylinders oriented diagonally in the x-y-plane with $\varphi = 45°$. **E)** Visualization of the angles θ and φ with a 3D rendering of synthesized cylinders (generated by the Volume Viewer plugin in Fiji) with a radius of $8\,\mu$m at a resolution of 3.25 x 3.25 x $5\,\mu$m and $\theta = 10°$. **G)** Volume rendering of $8\,\mu$m validation cylinders with $\theta = 10°$ and $\varphi = 45°$ at our imaging resolution.

A

Mouse embryo

brain

heart

lung

spinal cord

kidney

B

3D-rendering

MIP
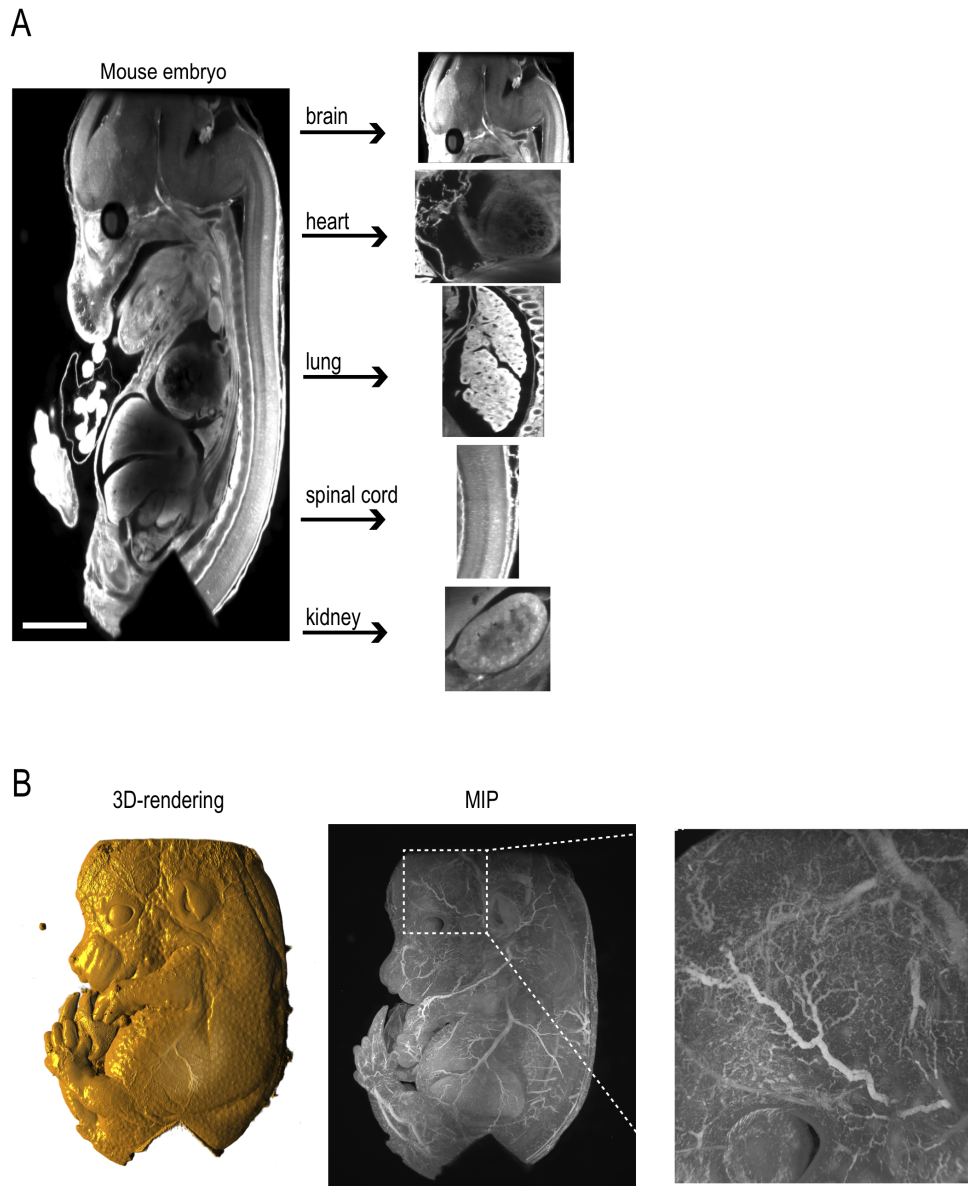
Suppl. Fig. 2, Quantitative ultramicroscopy, Hahn et al.,

Supplemental Fig. 2: Different organs of the mouse embryo in ultramicroscopy that can be used for analysis and quantification (**A**). 3D rendering and maximum intensity projection of a mouse embryo after lectin FITC labeling of the mother animal (**B**).

Supplemental movie captions

Supplemental movies available online under https://doi.org/10.1177/0271678X20961854.

Supplemental movie 1: Ultramicroscopy of the healthy mouse brain. Raw images (left column) and segmented images (right column) are shown.

Supplemental movie 2: Healthy mouse brain regions (basal ganglia, corpus callosum, and cortex) that were used for quantification.

Supplemental movie 3: Ultramicroscopy of U87 tumor bearing mice with segmented SPIM images after clearing (left column) and segmented images after application of the mask (right column). Tumor periphery (pseudocoloured in yellow) and tumor core (pseudocoloured in blue) are shown.

Supplemental movie 4: Ultramicroscopy of the mouse embryo. Raw SPIM images after clearing (left column) and segmented images before (middle column) and after application of the mask (right column) are shown.

Supplemental movie 5: Ultramicroscopy of the mouse embryo spinal cord. Raw SPIM images after clearing (left column) and segmented images before (middle column) and after application of the mask (right column) are shown.

Publication IV:
Quantification of entire vascular networks of brain tumors

Title: Glioblastoma multiforme restructures the topological connectivity of cerebrovascular networks

Authors: <u>Artur Hahn</u>, Julia Bode, Thomas Krüwel, Gergely Solecki, Sabine Heiland, Martin Bendszus, Björn Tews, Frank Winkler, Michael O. Breckwoldt and Felix T. Kurz

Contributions: A.H. and F.T.K. conceived the study. J.B., T.K., and B.T. performed microscopy experiments. A.H. provided analytical and numerical tools. A.H. and F.T.K. analyzed the data and interpreted the experiments. A.H., J.B., G.S., F.K., S.H., M.B., M.O.B., and F.T.K. wrote the paper. All authors read and approved the final manuscript.

SCIENTIFIC REPORTS
natureresearch

OPEN

Glioblastoma multiforme restructures the topological connectivity of cerebrovascular networks

Artur Hahn[1,2], Julia Bode[3], Thomas Krüwel[3], Gergely Solecki[4,5], Sabine Heiland[1], Martin Bendszus[1], Björn Tews[3], Frank Winkler[4,5], Michael O. Breckwoldt[1,6] & Felix T. Kurz[1]

Glioblastoma multiforme alters healthy tissue vasculature by inducing angiogenesis and vascular remodeling. To fully comprehend the structural and functional properties of the resulting vascular network, it needs to be studied collectively by considering both geometric and topological properties. Utilizing Single Plane Illumination Microscopy (SPIM), the detailed capillary structure in entire healthy and tumor-bearing mouse brains could be resolved in three dimensions. At the scale of the smallest capillaries, the entire vascular systems of bulk U87- and GL261-glioblastoma xenografts, their respective cores, and healthy brain hemispheres were modeled as complex networks and quantified with fundamental topological measures. All individual vessel segments were further quantified geometrically and modular clusters were uncovered and characterized as meta-networks, facilitating an analysis of large-scale connectivity. An inclusive comparison of large tissue sections revealed that geometric properties of individual vessels were altered in glioblastoma in a relatively subtle way, with high intra- and inter-tumor heterogeneity, compared to the impact on the vessel connectivity. A network topology analysis revealed a clear decomposition of large modular structures and hierarchical network organization, while preserving most fundamental topological classifications, in both tumor models with distinct growth patterns. These results augment our understanding of cerebrovascular networks and offer a topological assessment of glioma-induced vascular remodeling. The findings may help understand the emergence of hypoxia and necrosis, and prove valuable for therapeutic interventions such as radiation or antiangiogenic therapy.

Vascular networks are transport networks that provide vital substances such as oxygen and nutrients to living tissue and remove biological waste products. Their characteristic morphology allows regulation of the surrounding biological environment, including thermoregulation and physiological ion balance to maintain tissue homeostasis[1]. Motivated by energy cost minimization (Murray's law[2,3]), healthy vasculature typically follows a hierarchical arterio-venous branching scheme, with blood flowing through thick arteries, successively branching into thinner arterioles, followed by capillaries and a similarly organized venous system, draining the tissue in vice-versa[4]. Forming efficient transport networks, healthy vessel constructs are inherent to tree-structured arterial and venous parts, interwoven by dense, regular capillary beds[5–7].

Malignant tumors disrupt the local biochemical environment and regulation of pro- and antiangiogenic factors, such as vascular endothelial growth factor, angiopoietins and Ang-2[8,9]. As a solid tumor grows, the pre-existing vasculature is adapted and constantly modified by several mechanisms including angiogenesis[10],

[1]Heidelberg University Hospital, Department of Neuroradiology, Heidelberg, 69120, Germany. [2]University of Heidelberg, Department of Physics and Astronomy, Heidelberg, 69120, Germany. [3]University of Heidelberg and German Cancer Research Center (DKFZ), Schaller Research Group, Molecular Mechanisms of Tumor Invasion, Heidelberg, 69120, Germany. [4]Heidelberg University Hospital, Neurology Clinic and National Center for Tumor Diseases, Heidelberg, 69120, Germany. [5]German Cancer Consortium (DKTK), Clinical Cooperation Unit Neurooncology, Heidelberg, 69120, Germany. [6]German Cancer Research Center (DKFZ), Clinical Cooperation Unit Neuroimmunology and Brain Tumor Immunology, Heidelberg, 69120, Germany. Correspondence and requests for materials should be addressed to F.T.K. (email: felix.kurz@med.uni-heidelberg.de)

vessel dilation[11], regression, constriction, and occlusion[12,13]. The complex interplay of these processes, dynamically regulated during tumor progression by biochemical, metabolic, mechanical, and hydrodynamic influences[14,15], leads to highly heterogeneous vessel architectures throughout the tumor volume[8,16], that may impact response to radiotherapy[17].

Extensive research has been conducted to investigate the structure of tumor vasculature and how it sets itself apart from healthy vessel constructs. Most studies of this nature have focused on local vessel properties, such as microvascular density (*MVD*), vessel segment geometry and space-filling properties (see, *e.g.*[18–21] and references therein). Although sophisticated models have been developed to analyze global properties of large-scale vessel architectures in theory[22,23], topological analyses of vascular networks that consider properties such as local clustering of vascular nodes or inter-node connectedness remain scarce and either focus on two-dimensional vascular networks[24], smaller three-dimensional networks, *e.g.*, of lymph nodes[25], or subnetworks, including only certain vessel types[26–30].

In general, experimentally extracted vessel networks are usually constrained to either small imaging volumes or limited resolution; full vascular networks in brain tissue, including small capillaries, could only be obtained histologically or by laborious combinations of multi-scale imaging modalities, as, *e.g.*, in[31,32]. A recent approach using fluorescence ultramicroscopy, however, made it possible to image detailed micro- and mesoscopic vascular structures of entire organs[33,34] and was successfully applied to mice brain[35,36]. A detailed structural and functional quantification of such entire vascular networks may unveil previously unknown consequences of vascular remodeling and aid the development of targeted antiangiogenic therapies.

In this study, we present numerical quantifications of blood vessel networks from entire GL261 and U87 glioblastoma xenografts in mice, as well as comparable healthy brain regions in a mouse model, including capillaries with diameters down to approximately 3 μm. Geometric properties of the vasculature, extracted from tumors and healthy brain hemispheres, were quantified using custom-written, highly scalable codes in Matlab (Mathworks, Natick, MA, USA). As in other quantitative studies of multi-scale vessel data, *e.g.*[37], the fractional blood Vessel Volume (*fVV*), vessel length density ρ_L, and vascular surface density ρ_A were determined and the individual vessel segments were characterized by their mean radius $\bar{r}$, length *l*, tortuosity τ and surface area *A*. Augmenting the geometric analysis with graph theoretical analysis tools, the vessel architectures are modeled as undirected networks to reveal local and nonlocal topological properties. The connectivity characteristics are studied on multiple length scales with the help of a network theoretical community paradigm[38].

High local heterogeneity within and among tumors makes a global geometric characterization of tumor vasculature difficult. Nevertheless, one would expect the mechanisms of vascular remodeling during tumor growth to reflect in the global network topology of the emerging vessel constructs. The graph theoretical framework offers powerful tools for the assessment of global network characteristics of large vascular systems, encompassing 10^5–10^6 constituent segments. We present network theoretical quantifications on the largest cerebrovascular networks studied so far, resolve basic topological characteristics of healthy brain vasculature, and show how the vascular connectivity changes in U87 and GL261 glioblastoma.

Methods

Data acquisition. *Tissue preparation and imaging.* 3D vessel morphology was imaged *ex vivo* using fluorescence light sheet microscopy as described before[35]. In brief, we injected 7.5 · 10^4 U-87MG (ATCC HTB-14) cells in 9 week old, male NOD Scid Gamma mice (NSG, DKFZ, Heidelberg) and 10^5 GL261 glioma cells (National Cancer Institute NCI, Bethesda, MD, USA) in 6–8 week old, female C57Bl/6J mice (Charles River Laboratories, Sulzfeld, Germany; n = 6 mice). The cells were tested biweekly for mycoplasma contamination with negative outcome. Cells were diluted in 5 μl sterile phosphate and buffered saline (PBS, Sigma-Aldrich Chemie GmbH, Taufkirchen, Germany) and injected in the striatum of the right hemisphere, 2 mm lateral and 2 mm ventral of the bregma. Respectively, *n* = 6 animals with glioblastoma were compared against *n* = 6 brain hemispheres from n_m = 3 healthy mice as controls. All animal experiments were conducted in accordance with appropriate guidelines and approved by the regional ethics committee in Karlsruhe, Germany (permit numbers G223/14, G187/10, G188/12, G145/10, and G287/15).

21 days post tumor cell implantation for U87 specimens and 28 days post injection for GL261 mice, the animals were injected intravenously with 300 μl of lectin-FITC (Sigma-Aldrich, St. Louis, MO, USA) at a concentration of 1 mg/ml. After 3 minutes of incubation, mice were sacrificed by a ketamine/xylazine overdose. Mice were transcardially perfused with 20 ml PBS and 20 ml 4% PFA. The brain was explanted and optically cleared using the FluoClearBABB protocol[34]. Upon successful tissue clearing, Selective Plane Illumination Microscropy (SPIM) was employed to image the microvasculature in the entire brain by fluorescent excitement of the lectin marker (3.25 × 3.25 μm in-plane resolution and 5 μm between slices in the transverse plane) with the following acquisition parameters on an Ultramicroscope II (LaVision Biotec, Bielefeld, Germany): 100% laser power, 5 μm stepsize, dynamic focus on (5–10 steps), Andor camera exposure time of 686.345 ms, 16-bit low noise gain, left and right light sheet together.

Post-processing. The acquired image stacks were segmented using the interactive learning and segmentation toolkit ilastik[39]. To reduce noise, the binary vessel representations attained this way were smoothed with a 3D-Gaussian filter with isotropic standard deviation $\sigma = 1$ (voxel units), using the 3D-smoothing plugin in the ImageJ-distribution Fiji 2.0.0-rc-43/1.51r[40]. The volume was again binarized with intensity threshold at half of the maximum voxel value. A self-written script in Matlab was used to fill holes in the binary structures (i.e. "hollow" vessels) to correct for segmentation artefacts. A self-written Matlab script further reduced noise by removing isolated voxel bunches with a volume of less than a sphere with a 6 μm radius (based on 6-connectivity[41]).

The skeletonization algorithm[42] in ImageJ was used to extract the vessels' center lines. The plugin AnalyzeSkeleton[43] assigned a tag to each skeleton voxel, identifying end-points (with less than two neighboring skeleton voxels), junctions (with more than two neighbors), and so-called slab voxels (with exactly two neighbors). The tagged skeletons were later used for vessel/node labeling and connectivity list construction.

Binary masks were manually drawn over each image stack to select the tumor volume and corresponding regions in the healthy brain hemispheres for analysis. Care was taken that only well-resolved regions with minimal blurring were incorporated in the control datasets. This comprised the inner parts of the brain, including the midbrain, hippocampus, thalamus, hypothalamus, septum, striatum, caudate, putamen, amygdala, and inner sections of the cerebral cortex and cerebellum. The ventricular system, exhibiting false fluorescence, was blinded by the masks. Tumor boundaries were assessed visually by two neuroradiologist physicians based on microvascular anomalies (increased irregularity and overall tortuosity) in the tumor region. Tumor cores were masked separately based on a transition within the tumor vasculature from a more dense outer shell to a less vascularized center, presumed to exhibit hypoxia.

As detailed in[41], segmentations are often ambiguous at structure boundaries, which can have great effects on vessel geometry at the given resolution. We suspect the images to be subject to "fluorescent overexposure", which would cause background voxels to be illuminated and registered in the segmentation, causing vessels to appear thicker. To compensate for this over-fluorescence and over-segmentation, we implemented a circumferential thinning in Matlab, which eliminates the boundary layer voxels from the segmented structures, with the exception of voxels constituting the skeleton. All processing steps conducted leave the network topology unchanged by definition.

Geometric and topological analysis.   *Vessel geometry.*   The masked, binary image stacks were processed in Matlab R2016b (Mathworks, Natick, MA, USA) using custom written codes. The fraction of blood-filled tissue volume marked by perfused vessels was determined in a tiling box approach, quantifying the fractional vessel volume, fVV, with an isotropic resolution of 500 μm on the shrunken tissue. The same cubic subvolumes were used to determine the microvascular density, MVD, here defined as the number of individual vessel segments per mm³ tissue volume (after shrinkage due to tissue clearing). The vessel length density, ρ_L, and vascular surface density ρ_A, were defined as the total vessel length per shrunken tissue volume in each sample (mm/mm³), and as lumen surface area per tissue volume (mm²/mm³), respectively.

Geometric properties of the individual vessel segments, including mean radius $\bar{r}$, segment length l and surface area A, were determined using custom Matlab codes on the binary and skeletonized image stacks. A detailed mean radius calculation was implemented along branch lines. The tortuosity τ of each vessel segment was quantified by the ratio of true vessel length l and Euclidean endpoint separation d as $\tau = l/d$, often referred to as the distance metric[44,45].

Network topology.   To quantify the topology of the vasculature, the branching point connections were modelled as an undirected network by interpreting vessel branching and end points as nodes, interconnected by vessel segments as edges. Utilizing graph theory, the entire systems' connectivity properties could be quantified, which enables an assessment of topological characteristics on different scales and allows for comparisons with random graph models and other types of complex networks. The topological properties under consideration are described in the following.

Scale-free characteristic.   In each vascular network, the degree k of every node, i.e. the number of attached vessel branches, was determined, delivering the degree distribution $P(k)$. The relative frequency distributions $P(k)$ were modelled with a power law: $P(k) \sim k^{-\gamma}$, introducing the degree exponent γ. It has been found that many real networks exhibit such degree distributions, often with $2 \leq \gamma \leq 3$, identifying them as "scale-free networks[46–48]".

Small-world characteristic.   The "small-world" properties[49,50] can be assessed with three topological measures: the characteristic path length L, the network diameter D, and the average clustering coefficient C. While, along with the total number of nodes N, L and D mirror global network traits, C offers insight into the nature of local node connectivity and the tendency towards forming graph theoretical cliques[51].

The mean clustering coefficient C of a network is determined as the average of the clustering coefficients C_i of the individual nodes $i \in \{1, …, N_n\}$. The clustering coefficient C_i can be defined as the ratio of the number of edges between the direct topological neighbors of vertex i and the maximum number of edges connecting all of its neighbors[51]. For a node i with k_i neighbors and E_i connections between these neighbors, the clustering coefficient of the vertex is given by $C_i = 2E_i/k_i(k_i - 1)$.

The characteristic path length L, also called the average shortest path length, describes the mean number of edges on a geodesic to link any two nodes connected by a path on the graph. An implementation of Johnson's algorithm for the shortest paths problem was used from the MatlabBGL library version 4.0[52]. The small-world property is associated with an exceptionally slow rise in L as the network size N_n grows[53]. The network diameter D is given by the maximum of all shortest paths, i.e. the greatest node pair separation in the topological sense. The diameter D can reflect the degree to which the small-world property is globally persistent.

Community unfolding.   Expecting a hierarchical branching scheme[2,3,6,7,54] with a tolerance for locally clustered, lattice-like capillary structures[55–57], a modularity-based clustering approach was taken in this study. Using the

Louvain community unfolding algorithm[58,59], the networks were partitioned recursively with the aim of maximizing the intracommunity connectivity while keeping intercommunity connections sparse.

The relative dominance of intracommunity edges in a partitioned network can be quantified by the modularity Q, defined as[58]:

$$Q = \frac{1}{2m} \sum_{i,j} \left[A_{ij} - \frac{k_i k_j}{2m} \right] \delta(c_i, c_j),$$

(1)

with $-1 \leq Q \leq 1$. For a weighted network, the adjacency matrix element A_{ij} holds the weight of the edge connecting nodes i and j, $k_i = \sum_j A_{ij}$ is the weighted degree of node i, c_i is the community that node i is assigned to, $m = \frac{1}{2} \sum_{ij} A_{ij}$ is a normalization factor (the sum over all edge weights) and $\delta(u, v)$ is the Kronecker-Delta with $\delta(u, v) = 1$ for $u = v$ and $\delta(u, v) = 0$ otherwise.

Briefly, the Louvain method starts with every vertex assigned to its own community and then iteratively moves nodes to neighboring communities, always seeking an increase in modularity Q. Once a local maximum in Q is reached, the algorithm delivers a level of clustering with each node assigned to a community. In the next step, these communities are taken as meta-nodes with the intercommunity connections as edges. The clustering process is repeated recursively on the resulting meta-networks until no more reassignments can increase the modularity and a global maximum in Q is reached. Each local maximum in Q is expected to reflect the modular structure of the network at a different scale[58].

Community structure. In order to get a more comprehensible view of the giant networks concerning large-scale structures, the spatial distribution and structure of the uncovered communities were studied. We consider a community j, comprised of a subset $Q_j \subseteq \{1, \ldots, N_n\}$ of $n_j = |Q_j|$ nodes from the total of N_n vertices. With the spatial coordinates $\vec{x_q}, q \in Q_j$, of each node assigned to community j, the cluster's node centroid $\vec{r_j}$ could be determined: $\vec{r_j} = \sum_{q \in Q_j} \vec{x_q}/n_j$.

The spatial extent R_j of community j can be parametrized by the mean Euclidean distance of its constituent nodes $q \in Q_j$ from the community centroid $\vec{r_j}$: $R_j = \frac{1}{n_j} \sum_{q \in Q_j} |\vec{x_q} - \vec{r_j}|$. In the topological sense, the size of a community is usually determined by its number of nodes n_j[53]. In the context of vascular networks, another sensible cluster size parametrization is the number of vessel segments (edges) e_j included in cluster j.

A community's topological perimeter is typically understood as the number of nodes in the community which are involved in connections to other communities[53]. A closely related quantity in the vascular context is the number of connecting edges of cluster j to other communities, reflecting the cluster's supply situation. This measure is regarded as the perimeter P in this study.

Community connectivity. Each community was treated as a meta-node with weighted intercommunity edges, inherited from connected basic nodes in different clusters. The location of meta-node j was interpreted as the community centroid $\vec{r_j}$, while its size is reflected by the parameters n_j, e_j and R_j. The community degree, defined as $k_{c,j} = 2e_j + P_j$, is a measure for the importance of cluster j as a supply entity in the network, summarizing size and connectivity in analogy to unclustered networks with allowed self-connectivity.

Graph theoretical quantifications of the clustered meta-networks include the assessment of degree distributions $P(k_c)$ and degree relations of neighboring communities, clustering coefficients C_c, as well as characteristic path lengths L_c and network diameters D_c. With the spatial location of every cluster, $\vec{r_j}$, the shortest paths between communities were studied depending on their physical separation Δ ($\Delta_{ij} = |\vec{r_j} - \vec{r_i}|$ for communities i and j).

All statistical testing was conducted using the Kruskal-Wallis-Test, available with Matlab. This is a nonparametric one-way ANOVA, which does not assume a Gaussian distribution of samples.

Results

Glioblastoma can mimic the large scale vessel geometry in healthy brain tissue. The data acquisition process for the results presented is illustrated in Fig. 1a. In healthy controls, we found a mean fractional vessel volume of $\langle fVV_h \rangle = 9.8 \pm 3.3\%$ (with standard error of mean), which is in reasonable agreement with documented values of an intracranial mean $\langle fVV_{ic} \rangle = 5.8 \pm 0.4\%$ and maximum $\langle fVV_{max} \rangle \approx 7.9\%$ in the medulla and cerebral cortex, determined from micro-CT measurements at $20\,\mu$m isotropic resolution[60]. The incorporated 3D volume tiling with $500\,\mu$m cubes comprised a total of 1265 boxes in healthy tissue, 871 in U87 tumors (101 in the core), and 364 in GL261 tumors (76 in the core). In total, approximately 4.4 million healthy vessel segments were compared to 1.8 million vessels in U87 glioblastoma (21 400 in the core region) and 380 000 vessels in GL261 tumor tissue (22 200 in the core). Table 1 summarizes the mean geometric properties of the tissue samples under consideration.

Distributions of the fractional vessel volume fVV and microvascular density MVD, determined over $500\,\mu$m cubes, were positively skewed in all tissue types (Fig. 1b,c). Values were significantly lower in full GL261 tumors (fVV: $p = 0.007$; MVD: $p = 0.004$ from testing with 6 vs. 6 sample means), while U87 glioblastoma showed density distributions similar to the healthy controls, when including the periphery (Table 1). The U87 tumor cores exhibited more heterogeneity than the GL261 models. On the $500\,\mu$m scale, the U87 tumors featured regions with considerably decreased branching density MVD, while the fVV did not show matching voids (Fig. 1b,c). While vessel calibres and lengths were virtually unchanged in the full U87 specimens, the core vessels showed considerably larger radii and branching lengths, which can account for heightened fVV at relatively low MVD. The GL261 model showed opposite trends in the core, with shorter, thinner vessels, resulting in lower fVV despite higher
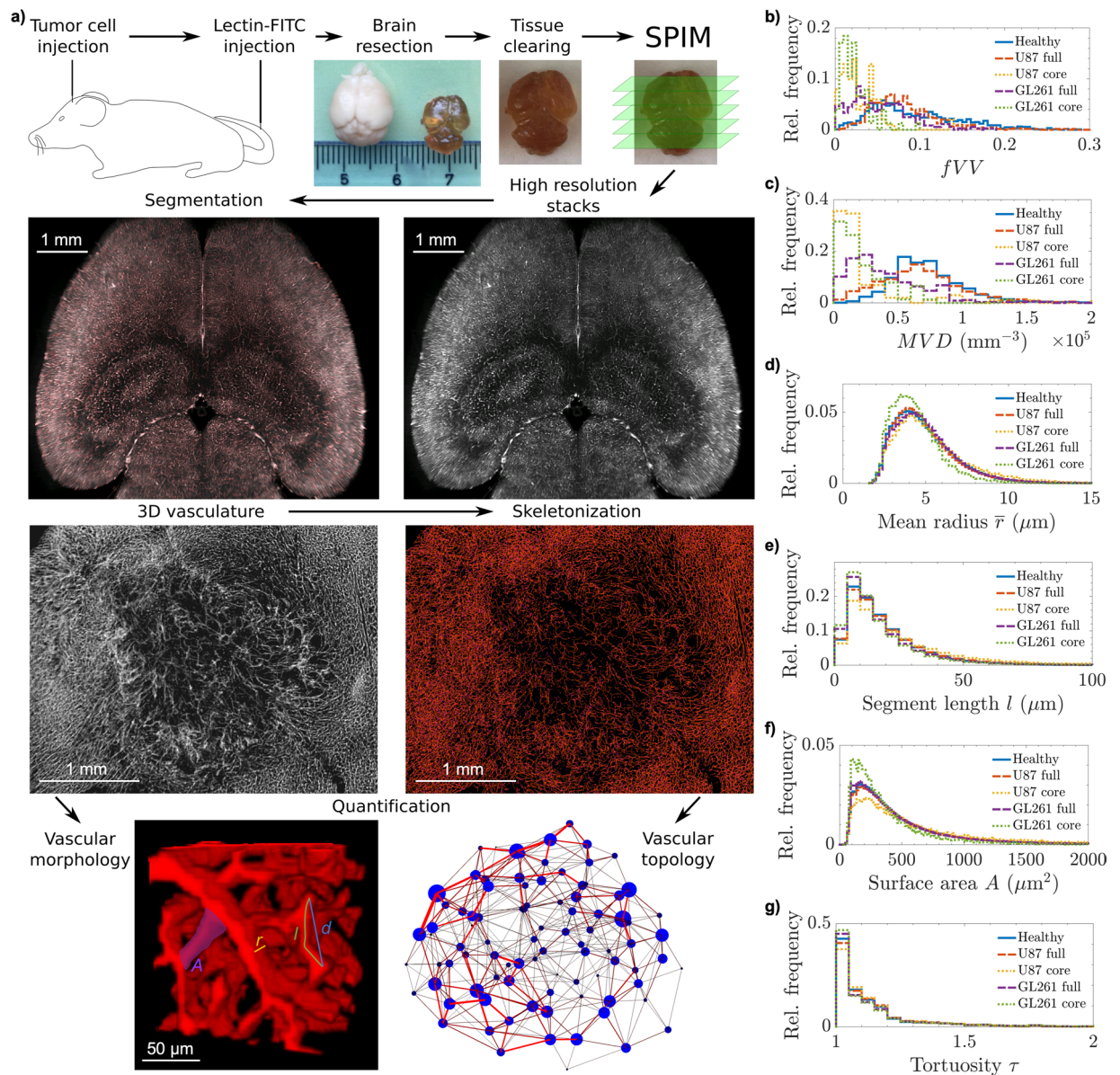
103

Figure 1. Data acquisition and processing with geometric quantifications. (**a**) Schematic illustration of experimental procedures, including tumor cell and fluorescent marker injections, brain resection and clearing, with photographs of uncleared and cleared brains with cm scale, and Selective Plane Illumination Microscopy (SPIM). In the second row, an original image from a stack of a healthy mouse brain is presented on the right, with the binary segmentation overlay in red to the left (see Supplementary Movies 1, 2 and 3 for segmentation results in more detail). Below the brain segmentation image, an average intensity projection from a 200 μm thick section of a segmented, noise-filtered, and hole-filled image stack of a U87 glioblastoma is shown. To the right, the skeletonized version of the same dataset is presented, with branch voxels in orange and branching points in magenta. The vascular network quantifications on this post-processed data are illustrated in the last row. The vascular morphology assessment is clarified in a cube of 130 μm side length, marking a radius value r, length l and endpoint-separation d, as well as a segment's surface area A. Using the vascular skeleton, the network topology is studied, which is illustrated by a clustered graph, presenting the spatial distribution of vessel communities in a U87 glioblastoma. From the geometric quantifications, relative frequency distributions of (**b**) fractional vessel volume fVV and (**c**) microvascular density MVD in cubes with 500 μm side length, and distributions of geometric characteristics of all individual vessel segments are presented: (**d**) mean vessel radius $\bar{r}$, (**e**) segment length l, (**f**) surface area A, and (**g**) segment tortuosity τ.

MVD. The vessel length density ρ_L was significantly lower in all tumor samples compared with healthy controls (U87 full: $p = 0.01$; GL261 and cores: $p = 0.004$ from testing with, respectively, 6 sample means, Table 1).

The increased vessel length in U87 glioblastoma, and especially its core, suggests suppressed branching and vessel occlusion, while the shift towards shorter segment lengths and smaller radii suggest more active

	$\langle V \rangle\, \mathbf{mm^3}$	$\langle fVV \rangle\, \%$	$\langle MVD \rangle \cdot 10^3\, \mathbf{mm^{-3}}$	$\langle \rho_L \rangle\, \mathbf{mm^{-2}}$	$\langle \rho_A \rangle\, \mathbf{mm^{-1}}$	$\langle \overline{R} \rangle\, \mu m$	$\langle l \rangle\, \mu m$	$\langle A \rangle\, \mu m^2$	$\widetilde{\tau}$	τ_{95}
Healthy networks	14.7 ± 4.1	10.3 ± 3.7	53 ± 10	980 ± 99	25.4 ± 10.0	$4.9^{+1.7}_{-1.2}$	19^{+15}_{-9}	505^{+472}_{-240}	1.071	1.453
U87 full networks	8.3 ± 4.3	7.2 ± 1.6	38 ± 12	734 ± 145	16.8 ± 4.4	$4.9^{+1.7}_{-1.2}$	20^{+16}_{-10}	547^{+566}_{-267}	1.079	1.463
U87 core networks	0.3 ± 0.3	3.0 ± 1.4	11 ± 8	268 ± 146	6.1 ± 3.9	$5.4^{+2.2}_{-1.5}$	25^{+24}_{-13}	806^{+1089}_{-446}	1.080	1.481
GL261 full networks	2.8 ± 1.0	4.8 ± 0.9	23 ± 7	413 ± 74	13.8 ± 8.4	$5.0^{+1.7}_{-1.3}$	18^{+16}_{-9}	491^{+466}_{-235}	1.070	1.553
GL261 core networks	0.3 ± 0.2	1.9 ± 0.1	13 ± 9	214 ± 103	7.5 ± 5.7	$4.4^{+1.3}_{-1.0}$	17^{+16}_{-8}	386^{+361}_{-177}	1.066	1.557

Table 1. Global tissue properties from $n = 6$ healthy brain hemispheres (healthy networks) and tumor specimens (full networks and exclusively tumor cores). Means with standard deviation (SD) are given for the tissue volume of each specimen V (after shrinkage from clearing), fractional vessel volume fVV, microvascular density MVD, total vessel length density ρ_L (in mm/mm^3), and vascular surface density ρ_A (in mm^2/mm^3). Arithmetic means and average directed deviations of geometric vessel properties with log-normal distributions, namely mean radius $\overline{r}$, segment length l and surface area A. The exponentially distributed segment tortuosity τ is characterized by the median $\widetilde{\tau}$ and 95%-quantile τ_{95}.

	$\langle \rho_n \rangle \cdot 10^3\, \mathbf{mm^{-3}}$	$\langle N_n \rangle \cdot 10^3$	$\langle N_e \rangle \cdot 10^3$	$\langle \overline{k} \rangle$	$\langle k_{max} \rangle$	$\langle \gamma \rangle$	$\langle C \rangle$	$\langle \beta \rangle$
Healthy networks	35.7 ± 13.7	505 ± 207	817 ± 330	3.24 ± 0.11	20.7 ± 4.1	8.72 ± 1.18	0.049 ± 0.012	2.36 ± 0.01
U87 full networks	27.4 ± 13.0	196 ± 99	286 ± 150	2.89 ± 0.15	17.3 ± 3.4	8.53 ± 1.38	0.056 ± 0.010	2.36 ± 0.01
U87 core networks	9.3 ± 6.4	3 ± 3	4 ± 4	2.29 ± 0.26	8.5 ± 2.6	2.79 ± 4.52	0.078 ± 0.021	2.2 ± 0.4
GL261 full networks	19.1 ± 5.1	52 ± 21	80 ± 36	3.06 ± 0.16	31.5 ± 9.2	5.35 ± 0.87	0.123 ± 0.019	1.4 ± 0.2
GL261 core networks	10.5 ± 7.0	3 ± 3	5 ± 5	2.67 ± 0.36	15.7 ± 8.6	4.18 ± 2.20	0.144 ± 0.004	1.6 ± 0.3
Random networks	31.6 ± 13.4	358 ± 216	561 ± 359	3.22 ± 0.19	14.3 ± 0.9	n.a.	$(1 \pm 1) \cdot 10^{-5}$	n.a.

Table 2. Mean basic network properties with SD among, $n = 6$ healthy and tumor-bearing specimens, respectively. Node density in (shrunken) tissue volume ρ_n, as well as the total number of branching nodes N_n and edges N_e per specimen. Mean local connectivity measures from all healthy and tumor specimens, including mean node degree $\overline{k}$, maximum degree per specimen k_{max}, and clustering coefficient C; the scaling exponent β from fitting $C_i(k_i) \sim k_i^{-\beta}$ is given with SD among samples. For comparison, corresponding quantities are also given for $n_r = 12$ Erdös-Rényi graphs[66] with node and edge numbers equal to the healthy and full U87 networks. n.a.: not applicable.

angiogenesis in the GL261 tumor core (Fig. 1d–f). The more sharply peaked radius distribution suggests a flattened branching hierarchy in glioblastoma with respect to healthy vasculature[3]. The lumen surface area A per vessel segment is correlated with the length l and radius $\overline{r}$, showing more clearly the opposing trends in U87 and GL261 vessel remodeling. The vessel tortuosity τ approximately followed shifted exponential distributions (with $\tau \geq 1$ by definition) in all tissue types (Fig. 1g) and is characterized by the median $\widetilde{\tau}$ and 95%-quantile τ_{95} in Table 1.

The vessel tortuosity τ again showed distinct alterations in each tumor model. In U87 glioblastoma and its core, both the median $\widetilde{\tau}$ and upper quantile τ_{95} increased moderately from healthy controls to tumor cores ($p < 0.01$ for core vs. control). In contrast, in GL261 models, the median $\widetilde{\tau}$ decreased towards the core, while τ_{95} strongly increased ($p < 0.01$ for full networks and cores vs. controls); the GL261 tumors upheld a large number of relatively straight segments with several very tortuous ones. Such heterogeneity with a tendency towards increased tortuosity is consistent with the findings of previous studies[37]. Analogous tests against healthy tissue on the remaining geometric vessel properties did not indicate statistical significance ($\langle \overline{r} \rangle$: $p > 0.4$; $\langle l \rangle$: $p > 0.1$; $\langle A \rangle$: $p > 0.1$ for all tumor sets, including cores). Extended sample sizes could show that the mean vessel tortuosity, if accessible, may serve as a biomarker for tumor vasculature, supporting previous findings in humans[61,62].

Altered network topology in glioblastoma multiforme.
We present the first topological quantifications on cerebrovascular networks of such size and resolution. The custom-written codes were validated on functional human brain networks previously quantified[63] to assure correct numerical implementations.

Heterogeneous effects on local vessel connectivity in different glioblastoma types. By modeling branching and vessel end points as the nodes of a network, interconnected by vessel segments as edges, the connectivity in such large systems can be characterized using graph theory[41,64]. In accordance with an elevated MVD (edge density), the larger healthy tissue samples also featured higher node densities ρ_n, leading to healthy networks of larger size N_n and N_e compared with tumor networks (Table 2).

The degree k of a node corresponds to the number of vessels meeting at that vertex. The vascular skeletons exhibited high degree nodes, presumably at the intersection between arterial and venous tree branches with the
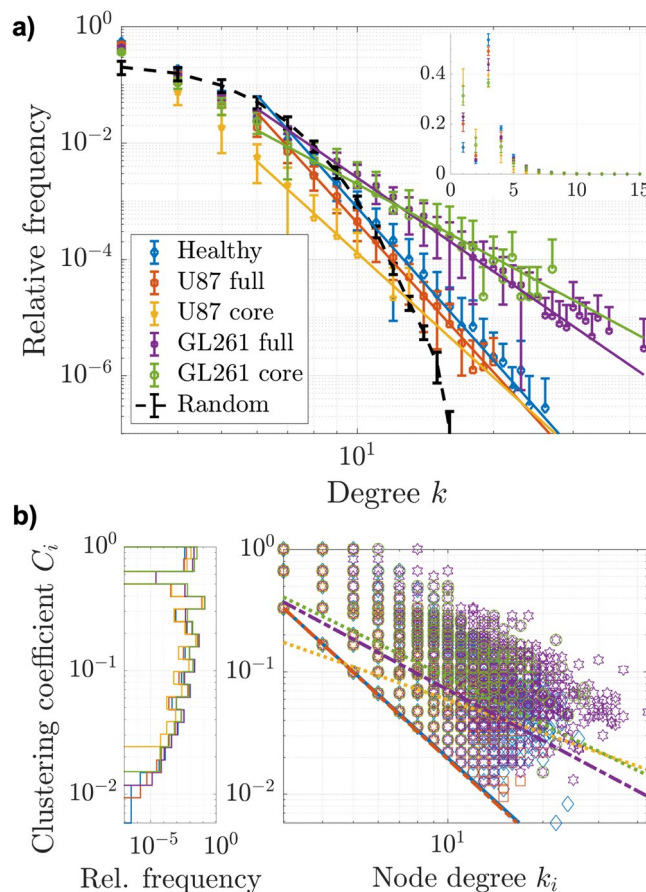
105

Figure 2. Vascular network topology. (**a**) Degree distributions (mean with SD among samples) from $n = 6$ healthy brain hemispheres, full U87 and GL261 tumors, and tumor cores, respectively. For comparison, the mean degree distribution from $n_r = 12$ random Erdös-Rényi graphs[66] with the corresponding node and edge numbers, is displayed as well, following a Poisson distribution. The large plot presents the distributions for $k \geq 3$ on logarithmic axes, while the inlayed plot shows the full distributions on linear scales. The logarithmic plot includes straight lines in corresponding colors, representing power law fits to the vascular data. (**b**) Bivariate distributions of node clustering coefficients C_i with corresponding node degrees k_i, including all nodes with $k \geq 3$ from all datasets and power law fits in corresponding colors. The marginal distributions of clustering coefficients C_i are displayed with a logarithmic ordinate axis to better illustrate differences along the entire range.

dense capillary mesh[5,20] or in angiogenic hotspots[65], especially in the tumor periphery. In Supplementary Movies 4 and 5, we show vascular nodes with degree $k = 24$ from a healthy network, and $k = 14$ from the U87 tumor periphery. The healthy microvascular networks consistently featured higher degree vertices than the U87 vessel networks, while the GL261 periphery yielded the highest k_{max} (Table 2 and Fig. 2a). The increased abundance of terminal branches with degree $k = 1$ in both tumor models is a strong indicator for angiogenesis (see inlay in Fig. 2a). Vessel endpoints constituted $20 \pm 3\%$ of all nodes in full U87 networks ($36 \pm 7\%$ in the core) and $23 \pm 2\%$ of nodes in the GL261 networks ($32 \pm 4\%$ in core), in contrast to $11 \pm 2\%$ in healthy networks (with SD among samples). In consequence, the mean node degree $\langle \overline{k} \rangle$ was decreased in both tumor models (Table 2). Nodes with degree $k = 2$ are an artefact of skeletonization and dealt with in the discussion.

In Table 2, mean local connectivity measures are given for the vascular networks, as well as comparable random graphs[66]. Since the random networks were constructed from the same number of constituents as the healthy and U87 tumor networks, the node density ρ_n, the size parameters N_n and N_e, and the mean node degree $\langle \overline{k} \rangle$ are identical to the weighted means over the reference networks. Yet, as expected, the vascular networks are subject to greater organization and heterogeneity, which reflects in the considerably higher maximum degree k_{max} at unchanged mean degree $\overline{k}$.

The degree distributions of the vascular networks approximately obey a power law $P(k) \sim k^{-\gamma}$ for higher degrees, with least squares fits for $k \geq 5$ showing good approximations of the vascular data (Fig. 2a). Despite unusually large exponents, this classifies the healthy and pathological vasculature as scale-free networks[53], placing them in line with many complex networks in nature, including the human brain[63], metabolic[67], and protein networks[68]. While both tumor models decreased the exponent γ with respect to healthy networks, the change was much stronger in GL261 tumors when comparing full networks, whereas U87 cores showed the highest heterogeneity, followed by GL261 cores (see mean $\langle \gamma \rangle$ in Table 2).

106

The clustering coefficient C quantifies the degree to which a node's neighboring nodes are well interconnected. Real, scale-free networks often have much higher clustering coefficients than comparable random networks, even with quasi-identical degree distributions[53,69]. Generally, the studied vascular networks presented much higher clustering than corresponding random graphs with mean $\langle C_r \rangle = (1 \pm 1) \cdot 10^{-5} \approx \langle \bar{k}/N_e \rangle$[53]. The tumor vasculature exhibited an increased mean clustering coefficient $\langle C \rangle$ compared to healthy networks, which, by definition, indicates a higher abundance of local vessel loops. Both pathological models showed stronger clustering in the tumor core, but the effects were much more amplified in GL261 tumors (Table 2).

Distributions of individual node clustering coefficients C_i with corresponding degrees k_i are presented in Fig. 2b. U87 tumor networks had a slightly higher relative number of cliques around low degree branching points ($k \leq 5$), increasing the abundance of $C_i = 1$ nodes. Although in rare occurrence, the healthy vessel networks featured nodes with slightly elevated clustering for most degree values above $k = 5$, as compared to the U87 tumors, while GL261 tumors showed significantly increased clustering, also for high degree nodes ($p < 0.004$ for GL261 cores and full tumors; $p = 0.025$ for U87 cores and $p > 0.1$ for full U87 networks compared to controls, tested with mean C per tissue specimen).

The approximate scaling of node clustering coefficients with $C_i(k_i) \sim k_i^{-\beta}$ has been identified as a hallmark of networks with hierarchical structure[70]. Robust power-law fits on the individual node values yielded the scaling exponents β given in Table 2. Despite the large spread of clustering coefficients C_i (Fig. 2b), the healthy and pathological networks studied here can be classified as hierarchical networks.

Reshaped nonlocal connectivity.   In order to quantify the vascular networks' nonlocal topology, the branching nodes were clustered based on modularity, using the Louvain community unfolding algorithm[58]. An exemplary consecutive community unfolding process on a full U87 glioblastoma and healthy brain hemisphere is presented graphically in Fig. 3a. For the topological quantifications reported in the following, the partitioning schemes corresponding to global maximum modularity Q were used for each network (in Fig. 3a, the rightmost community networks). To suppress boundary effects, isolated communities (disconnected vessel clusters) including less than twenty edges were removed from our analysis.

Tumor-induced decomposition of large-scale community structures.   The Louvain algorithm unveiled considerably larger clusters in healthy vessel networks than it did in glioblastoma vasculature, with dramatic differences in tumor cores and amplified effects in the GL261 model. This reflects in the communities' number of nodes n, number of vessel edges e, and the mean physical extent R, as well as the community perimeter P, i.e. the number of vessels to neighboring communities, with broader distributions in healthy networks and much smaller modular communities in all tumors (Table 3 and Fig. 3b–d).

At the highest partitioning level, determined by Eq. (1), the mean maximum modularity in healthy control networks was approximately 0.5. This modularity was maintained in tumors, but with much smaller vessel clusters (see modularities $\langle Q \rangle$ and node numbers $\langle \bar{n} \rangle$ in Table 3). While the modularity was slightly lower in tumor cores, it was even increased in GL261 tumors, compared to healthy controls, following a drastic breakdown of large vessel communities. Corresponding Erdös-Rényi networks, clustered with the same procedure, yielded maximum modularity close to zero, with mean value $\hat{Q}_r = (6 \pm 32) \cdot 10^{-7}$ from $n_r = 12$ random networks. Practically, the same modularity was maintained in healthy and pathological vessel networks, but on substantially different community size scales.

The clustering sequence in Fig. 3a demonstrates that the healthy brain exhibits a more uniform distribution of differently sized clusters throughout the tissue, while the glioblastoma upholds large vessel communities asymmetrically at its boundaries. The rightmost images show that modular clusters are disrupted and separated in the glioblastoma, and vessel communities are not as dense or large as they are in the healthy brain. This indicates that tumor-induced vessel remodeling leads to a breakdown of pre-existing topological clusters in order to form smaller supply entities, which could be regulated more independently.

The correlation between community size e and perimeter P can be associated with the isolation of modular vessel communities. Robust power-law fits to the roughly linear relationship on logarithmic axes (Fig. 3e), assuming $P(e) \sim e^{\xi}$, yielded the exponents ξ in Table 4 (corresponding to the slopes plotted in Fig. 3e). An analogous quantification on large parts of the cortical vasculature in a mouse model documented an exponent of 0.83 ± 0.04[30], where values between 2/3 and 1 were interpreted as a manifestation of weak community structure, while lower scaling exponents ξ would indicate the persistence of strongly isolated communities. Our results show that community interconnectivity differs in tumor core and periphery, but both tumor models showed consistent changes from healthy vasculature. Full tumor networks showed an increased exponent ξ with relatively little deviation from the assumed relationship. In contrast, tumor cores had lowered exponents with large uncertainty and stronger variance, with more pronounced differences to healthy tissue in the GL261 models.

For each vessel segment connecting a cluster to another, on average, a vessel community incorporated $\langle e/P \rangle$ internal edges (sample mean with SD from all communities given in Table 4). All types of vascular networks exhibited pronounced modular structures. Tumor vasculature exhibited higher heterogeneity in community isolation with a tendency towards reduced cluster connectivity (Fig. 3e). Whereas communities were most modular in full GL261 networks including the periphery, the U87 model showed stronger community isolation in its core, with higher heterogeneity in tumor peripheries for both models.

Furthermore, the vessel communities in tumor tissue presented higher heterogeneity in vessel segment densities, especially towards lower values (Fig. 3f; tumor networks featured communities with relatively large spatial extent R and low edge number e). The glioblastoma upheld vessel clusters with a low number of intercommunity segments P in a wide range of edge numbers e (Fig. 3e) and mean cluster radii R (Fig. 3g). The tumor networks
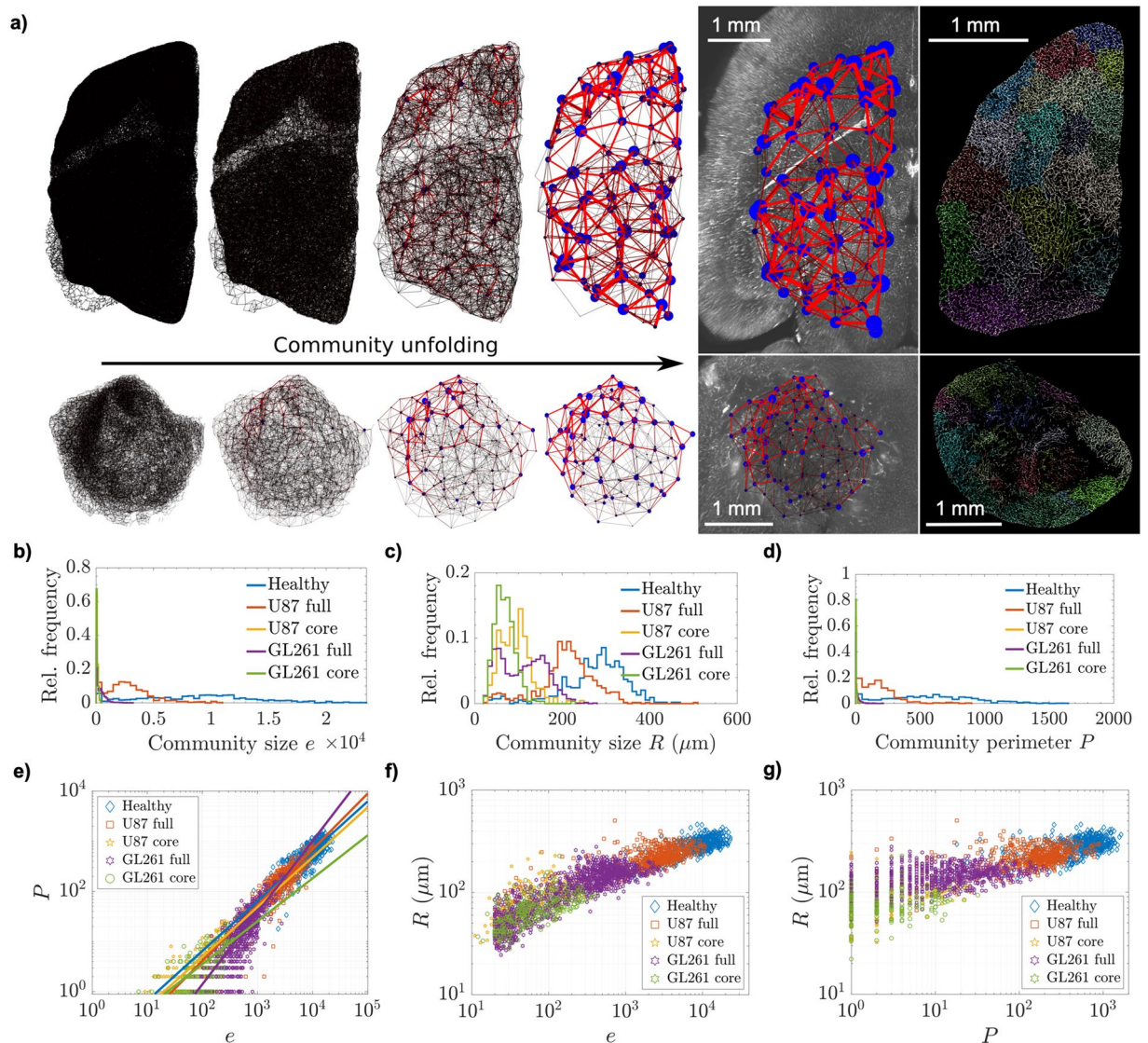
107

Figure 3. Modular network structure. (**a**) Schematic graphs of the community unfolding process on an entire vascular network in a healthy brain hemisphere (top) and full U87 glioblastoma (bottom). Each level of partitioning represents a local maximum in modularity Q, attained with increasing community sizes. The rightmost graph shows the clustering scheme with global maximum modularity over a central slice of the original SPIM-image. Communities are depicted by circles with diameter and brightness (blue) proportional to cluster size e_j, while the weight of a connection (the number of intercommunity vessel segments) is encoded in the edge thickness and brightness (red). Cluster positions are given by their centroid $\vec{r_j}$. The specimens encompass comparable (shrunken) tissue volumes of $V_h = 12.11$ mm^3 and $V_g = 12.87$ mm^3 in healthy control and tumor tissue, respectively (excluding ventricular space in the healthy brain, blinded for analysis). To the right of the partitioning chains, projections of 100 μm thick sections of the skeletonized vessel data show community affiliation (at global maximum Q) through the color of each branch segment. Relative distributions of community size properties from all specimens follow, namely (**b**) internal number of edges e, (**c**) mean physical extent R, and (**d**) community perimeter P. Panel (**e**) presents the relationship between a community's number of internal edges e and its perimeter P. Linear fits to the log-log-representation are plotted in lighter colors over the datapoints, presenting slopes ξ. The following plots illustrate the relationships between (**f**) community edges e and mean physical extent R, as well as (**g**) perimeter P and R.

not only presented a significant breakdown of vascular community size, but also decomposed connectivity among existing communities.

The identified vessel communities form meta-networks on larger length-scales of several hundred micrometers. The connections between communities can be interpreted as weighted edges between community nodes (see graph illustration in Fig. 3a). Standard graph theoretical measures, derived from the undirected meta-networks of healthy and pathological vascular communities, revealed profound characteristics in the organization of

108

	$\langle Q \rangle$	$\langle N_c \rangle$	$\langle N_{ice} \rangle \cdot 10^3$	$\langle \rho_c \rangle$ mm^{-3}	$\langle \rho_{ice} \rangle \cdot 10^3$ mm^{-3}	$\langle \bar{n} \rangle \cdot 10^3$	$\langle \bar{e} \rangle \cdot 10^3$	$\langle \bar{R} \rangle \mu$m	$\langle \bar{P} \rangle$
Healthy networks	0.51 ± 0.01	88 ± 21	25.18 ± 9.35	6 ± 2	1.8 ± 0.8	5.6 ± 3.1	8.8 ± 5.1	275 ± 74	573 ± 344
U87 full networks	0.50 ± 0.02	112 ± 30	8.17 ± 4.35	14 ± 7	1.2 ± 0.7	1.9 ± 1.3	2.8 ± 2.1	211 ± 65	173 ± 143
U87 core networks	0.43 ± 0.06	36 ± 24	0.08 ± 0.12	179 ± 147	0.3 ± 0.4	0.07 ± 0.06	0.09 ± 0.08	94 ± 35	5 ± 6
GL261 full networks	0.57 ± 0.03	204 ± 50	1.38 ± 0.89	77 ± 18	0.5 ± 0.3	0.3 ± 0.3	0.4 ± 0.5	110 ± 51	14 ± 26
GL261 core networks	0.48 ± 0.12	45 ± 30	0.06 ± 0.08	176 ± 58	0.2 ± 0.3	0.06 ± 0.05	0.09 ± 0.08	70 ± 25	3 ± 5

Table 3. Structural properties of communities uncovered in the vascular networks. Mean values with SD among samples are given for the final partitioning modularity Q, the number of communities per specimen N_c, the number of intercommunity edges N_{ice}, the mean number of communities and intercommunity edges per mm^3 (shrunken) tissue volume, ρ_c and ρ_{ice}, respectively, the mean number of nodes $\bar{n}$ and edges $\bar{e}$ per community, as well as mean physical extent $\bar{R}$ and perimeter $\bar{P}$ of the communities within each sample.

	ξ	$\langle e/P \rangle$	$\langle \bar{k}_c \rangle$	κ	$\langle \bar{k}_{c,u} \rangle$	$\langle C_c \rangle$	$\langle L_c \rangle$	$\langle D_c \rangle$
Healthy networks	0.99 ± 0.01	18 ± 11	17780 ± 5930	0.18 ± 0.01	8.8 ± 1.7	0.51 ± 0.02	3.1 ± 0.4	7.3 ± 1.1
U87 full networks	1.11 ± 0.01	22 ± 35	5360 ± 2760	0.37 ± 0.01	9.2 ± 0.9	0.50 ± 0.04	3.1 ± 0.4	7.5 ± 1.4
U87 core networks	0.99 ± 0.12	27 ± 23	140 ± 130	0.88 ± 0.03	2.3 ± 1.1	0.28 ± 0.22	2.6 ± 1.0	5.7 ± 2.2
GL261 full networks	1.43 ± 0.01	58 ± 71	780 ± 370	0.87 ± 0.02	5.5 ± 0.9	0.40 ± 0.05	4.4 ± 0.4	11.0 ± 1.8
GL261 core networks	0.86 ± 0.15	39 ± 33	140 ± 100	0.87 ± 0.03	2.0 ± 0.8	0.17 ± 0.21	2.4 ± 1.3	6.0 ± 4.2

Table 4. Connectivity between communities. Isolation scaling exponents ξ from robust fits assuming $P(e) \sim e^{\xi}$, mean number of internal vessel segments per intercommunity edge e/P, mean community degree $k_c = 2e + P$ and assortativity exponent κ from fits approximating the neighboring degree relationship with $\langle k_{c1} \rangle (k_c) \sim k_c^{\kappa}$, mean number of unique topological neighbor-communities $\bar{k}_{c,u}$, community clustering coefficient C_c, characteristic path length L_c and diameter D_c of the meta-networks, averaged from all specimens, and given with SD.

tumor-specific vessel clusters. Effects were again more pronounced in GL261 tumors, but from both models studied here, general trends may be extracted from our results.

The importance of a community as a supply entity is reflected by the community degree $k_c = 2e + P$, adapting the classical notion of the degree of a node with P connections to other nodes and e connections to itself (internal vessel edges). The clustered meta-networks did not show scale-free properties and degree distributions mainly reflected the breakdown of large vessel communities in healthy tissue. This effect was more pronounced in full GL261 networks, but produced similar degree distributions in the cores of both tumor models (Table 4 and Fig. 4a). In contrast to the basic vessel networks analyzed before, the meta-networks presented reduced clustering coefficients C_c between communities in glioblastoma, with higher heterogeneity and lower interconnectivity in tumor cores (Table 4 and Fig. 4b). The community clustering coefficients C_c did not present a distinct dependence on the degree k_c, advocating a loss of the basic networks' hierarchical organization in the large-scale meta-networks (Fig. 4b).

We observed a positive correlation between the degrees of directly connected communities in all vascular networks (Fig. 4c), which indicates that vessel communities are subject to assortative mixing[71,72]. Such mixing is based on large, well-connected communities that are preferentially attached to other communities of similar importance; an unexpected finding, as spatial networks typically yield flat $\langle k_{c1} \rangle$ distributions[73]. As robust power law fits assuming $\langle k_{c1} \rangle (k_c) \sim k_c^{\kappa}$ emphasized, the assortativity was more pronounced in glioblastoma vasculature (exponents κ in Table 4 shown as slopes of straight lines in Fig. 4c). Both tumor models presented very similar community sorting in the core, with little difference in entire GL261 networks, but more similarity of full U87 networks with healthy cerebrovasculature. A significant increase of assortative mixing in tumor vasculature is clear in both models.

The communities in GL261 tumor tissue and all tumor cores tended to be connected to a smaller number of distinct neighboring clusters, while in the full U87 networks, communities had slightly more topological neighbors than healthy networks. This indicates abnormally high community interconnectivity in the U87 periphery (Fig. 4d). A comparison of the mean number of unique neighboring clusters $\langle \bar{k}_{c,u} \rangle$ (Table 4) with the mean community perimeter $\langle \bar{P} \rangle$ (Table 3) shows that intercommunity connections in a healthy network are often enforced by many more individual vessel segments. With much larger healthy communities (Table 3), this observation makes sense when considering the supply and drainage functions of the intercommunity connections to the clusters, and it supports the notion of reduced community interconnectivity in tumor tissue.

In nonlocal connectivity, U87 and GL261 tumor-derived community networks presented diverse properties. Considerably higher densities ρ_c of much smaller vessel communities in tumor tissue can be associated with a rise in mean topological diameter D_c, i.e. the longest path through the network over communities, and mean path length L_c between any pair of connected communities, in relativity to reduced tumor network sizes in comparison to healthy controls (Table 4). Nevertheless, the vascular networks in tumor tissue exhibited relatively small
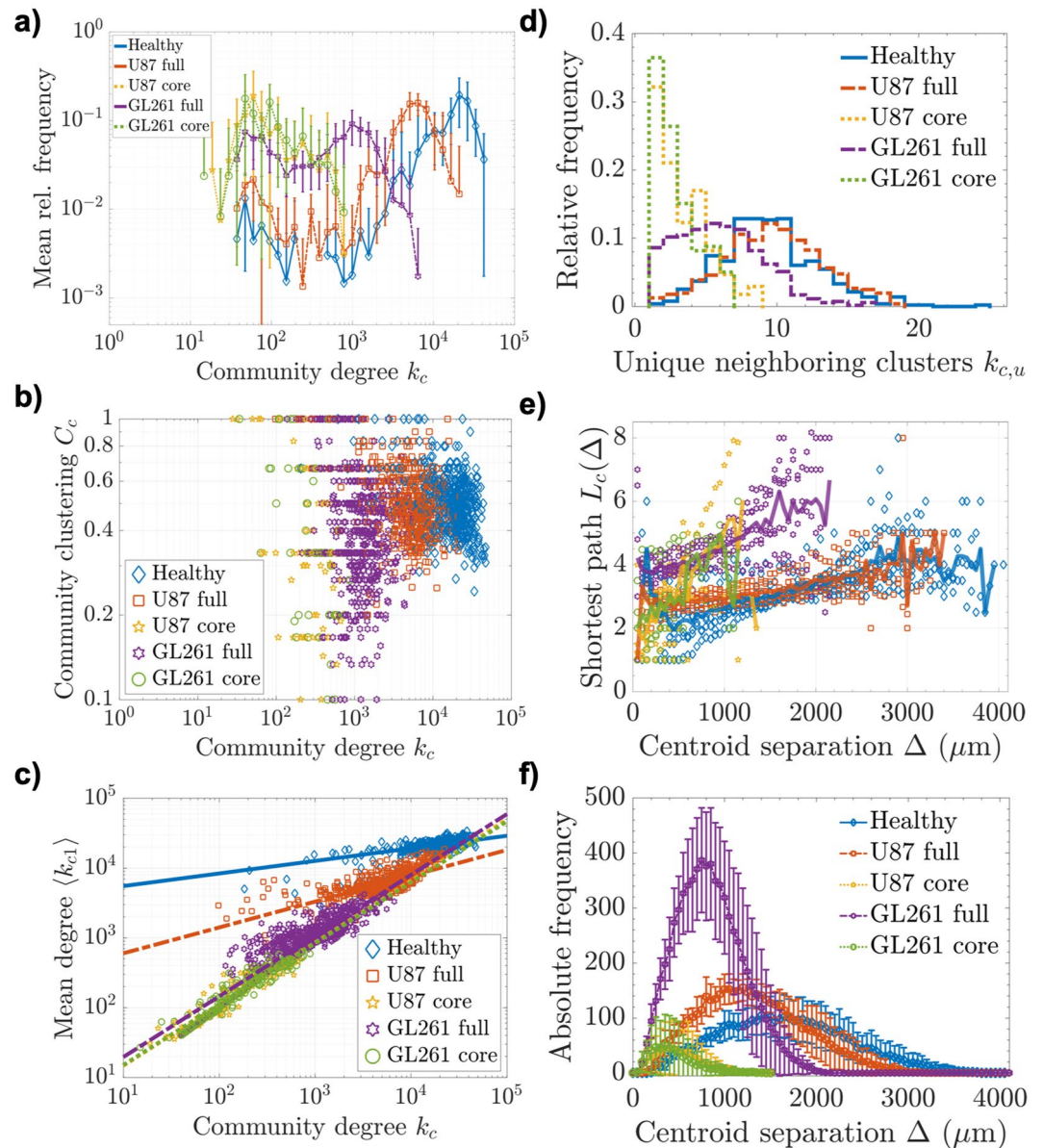
109

Figure 4. Community interconnectivity. (**a**) Mean log-binned frequency distributions of community degree $k_c = 2e + P$ (with SD among samples), (**b**) community clustering coefficients C_c vs. k_c, and (**c**) mean degree of neighboring communities $\langle k_{c1} \rangle$ vs. k_c with fits $\langle k_{c1} \rangle (k_c) \sim k_c^{\kappa}$. (**d**) Relative frequency distributions of the number of unique topological neighbor communities $k_{c,u}$, (**e**) separation-dependent shortest path length L_c between two connected communities, separated by the Euclidean distance $\Delta \pm \delta/2$ with increments of $\delta = 50\,\mu m$. The datapoints represent individual community-pair instances and the brighter lines connect the mean values over all datasets for each distance bin in Δ. (**f**) The number of community pairs with centroid separation $\Delta \pm \delta/2$ (with SD among samples).

topological path length increases, which becomes more apparent in dependence of the physical separation Δ between the community centroids (Fig. 4e; the number of occurrences for each pair separation bin is presented in Fig. 4f).

The mean path length $L_c(\Delta)$ in full U87 tumor networks was not appreciably higher than in healthy tissue, even for large distances between community centroids in the millimeter range (Fig. 4e). U87 tumor cores and GL261 specimens were subject to more heterogeneity, with mean path lengths exhibiting a steeper rise with physical separation, but also over considerably smaller communities (see n, e, R in Table 3). Our results show that the well-connected U87 tumor periphery facilitates short path lengths between virtually all communities in the tumor. Despite a decreased intercommunity edge density ρ_{ice} and communities with considerably smaller physical extent R and vessel numbers n (Table 3 and Fig. 3b,c), tumors maintained relatively short topological separations between communitites, even over large distances through the tissue.

110

Discussion

We characterized entire, perfused vascular systems in healthy mice brain, U87- and GL261-glioblastoma xenografts using basic geometric and network theoretical measures. The U87 cell line is known to have undergone genetic drift over recent years, growing in a solid, bulky manner instead of promoting diffuse infiltration of the brain parenchyma, like most human gliomas[74]. Furthermore, this tumor model has been found to have anomalous microvascular properties, with vessel distributions rather resembling healthy vasculature than other tumors in some aspects[75]. The solid growth pattern of the U87-glioma aided in delineating the tumor tissue from healthy tissue to attain first quantifications of entire tumor-immanent vascular networks, with the highly angiogenic GL261 model serving for further comparison. The methods presented here can be applied to arbitrary 3D-image data, independent of the imaging technique, and therefore, they are transferable to humans and other pathologies.

Our results render the tumor tissue to be irregularly perfused with a high variation in local vessel densities and characteristic differences in core and periphery, consistent with general knowledge[76,77]. We did not observe any significant increase in blood volume fraction fVV or mean vessel radii $\bar{r}$, as has been documented with different experimental methods and brain tumors, including the U87 cell line[78–82]. This is expected to be attributed to the tumor stage examined and the collective character of the geometric comparisons, which stand in contrast to local, selective analyses of angiogenic regions[83].

In our integrative study of the full vascular network, we found U87 tumor tissue to feature very low vessel densities MVD, but relatively unchanged blood volume fractions fVV in some regions on the 500 μm scale. Increased vessel calibre in the U87 tumor core indicates hypoxic vasodilation, which can compensate the tissue's fractional blood volume with very little perfused vessels[84]. While the main hallmarks of tumor angiogenesis are believed to be an elevated vessel density MVD and fractional blood volume fVV, dilated vessel radii $\bar{r}$, higher tortuosity τ, and decreased branching lengths l[85], our comparisons with vasculature from different regions of the healthy brain did not reveal elevated vessel densities significant on a global scale. The MVD and fVV were overall decreased in glioblastoma, while branching lengths l and vessel radii $\bar{r}$ changed distinctly in both tumor models. Previous studies have shown that the above-mentioned properties, relating to vascular density, can change and decrease with tumor progression[83], shifting angiogenic activity to the tumor periphery, while reducing the perfusion density in the core[77,86].

Our quantifications of healthy cerebrovascular networks included many brain regions with heterogeneous perfusion densities, without a differentiation of vessel types. The healthy networks featured high calibre arteries and veins that increased the average vessel radius. The tumor networks were in deficit of such large vessels, but presented a shift of small capillaries towards higher calibres, with the exception of GL261 tumor cores, which possibly included necrotic tissue. From our results, the dilation of small capillaries, related to tumor angiogenesis[85,87], could be inferred in the GL261 periphery. In support of previous studies, we found that an elevated vessel tortuosity, even in singular, extreme cases, has the potential of serving as a geometric biomarker for tumor vasculature[61,85,88].

Despite the disruptive effects of tumor growth on the local vasculature, the pathological vessel networks maintained basic classifications from graph theory that were also identified in healthy cerebrovascular networks, namely scale-free degree scaling with high exponents and the hierarchical clustering structure. This suggests that healthy and tumor-nurturing vascular networks both belong to the same class of transport networks with characteristic properties and topological scaling in size. Nonetheless, the uncovered network topology provides hints as to how vascular networks in the glioblastoma form. The dramatically increased relative abundance of terminal branches with degree $k = 1$ (vessel endpoints) in the tumor networks is a strong indicator for neovascularization[89], pointing to sprouting angiogenesis, vascular mimicry, or vasculogenesis as likely mechanisms[90,91]. Elevated vessel tortuosities τ and local clustering coefficients C in the glioblastoma support the impression of angiogenesis playing an important role in the network formation, while promoting an increased abundance of vessel loops[86]. Not all signs point to angiogenesis, though; the decreased branching density MVD and longer vessel segments in tumor tissue are atypical for brain tumor angiogenesis[85].

The breakdown in node diversity towards lower degree intersections, observed in tumor cores, indicates a degeneration of the preexisting vasculature during tumor development. This is supported by the significant decomposition of modular community sizes and general decrease in vascular density. Vessel occlusions on a large scale must have broken down the original, healthy network, eliminating high degree nodes and splitting existing vessel clusters. While tumor cores were supplied by sparse, very small and scarcely interconnected vessel communities, the periphery was found to maintain larger communities with more diversity and higher community clustering.

In glioblastoma networks, practically the same modularity was maintained by smaller community structures with stronger assortative mixing. Large supply entities were abandoned during tumor growth with focus on local metabolic needs and the effective transport of nutrients and oxygen. With small, light vessel clusters, nutrient rich blood can be transported long distances without being deprived along the way through large, dense community structures. The prospective gain in long-range transport efficiency leaves regions along the way undersupplied. The topological remodeling observed here may play an important role in the formation of hypoxic and necrotic regions and should be further investigated over a time course during tumor progression.

Albeit a decreased volume density of intercommunity vessel edges ρ_{ice} at considerably higher density, ρ_c, of smaller communities, the clustered glioblastoma networks presented relatively short characteristic path lengths L_c. The assortative mixing may be related to this aspect, which is, in effect, again geared towards the transport efficiency of the network. The small-world property has been investigated briefly on relatively large sections of the vibrissa primary sensory cortex of mice[30]. There, the absence of strict graph theoretical cliques was interpreted as an indicator that the studied microvasculature did not form small-world networks (cf.[30], Online Methods). A reliable assessment of the small-world property should evaluate the scaling of the characteristic path length L_c

111

with the number of meta-nodes N_c[53]. This is not possible with, respectively, 6 samples in similar size ranges, but one should note the short mean path length of $\langle L_c \rangle \approx 3$–5, that separates most of the roughly 10^2 communities in each network.

Vasculature as a complex network. From a graph theoretical standpoint, the vascular networks quantified in this study present very unusual topological properties. Many factors can be involved in forming these networks, but a consensus in most theoretical models, treating the formation of scale-free networks, is that the dynamic growth process plays a central role in the emergence of a power law degree distribution. This is an important aspect in the original Barabási-Albert model[46], as well as most methods thereafter, incorporating, *e.g.*, preferential attachment, fitness models, and edge dynamics (for review, see, *e.g.*[53,69]).

Although recent years saw numerous publications on scale-free networks with degree exponents $\gamma \leq 3$, scientific literature lacks the documentation and treatment of large, complex networks with high degree exponents, as encountered here. The similarity of γ-exponents in both types of networks suggests that the scale-free property with high degree exponents is immanent to large intracranial vessel networks, healthy and pathological, at the capillary scale. A previous study, modeling the Havers and Volkmann channels in cat humeri, revealed scale-free characteristics with degree exponents $\gamma \approx 3.7$–3.8[92]. Although arguably in a different system, these vascular networks also present unusually high scaling exponents.

It has been shown that scale-free networks can be very resilient against random failures, since, if a fraction of nodes chosen randomly is lost, a majority of them is expected to have low degree. In random networks, highly connected vertices, often called hubs, are usually responsible for the global connectedness in the graph[53]. Thus, for random networks, a certain abundance of hubs is important for a system's stability and some models have shown that exponents $\gamma < 3$ result in increased robustness against random failures, while higher exponents lead to a quicker loss of global connectivity[53,93]. In the context of blood vessel networks, a node with high degree is not necessarily a node of central importance for nonlocal connectivity. Adapting the earlier argument, an increased exponent γ should result in a decreased likelihood of losing locally important high degree nodes from random failures. In this case, this speaks for a strong sustainability of the system's diversity against stochastic damaging events.

The vascular networks exhibit relatively high clustering coefficients compared to random graphs. In the vascular context, high clustering coefficients manifest in local vessel loops consisting of only three edges, which guarantees high network stability, but, in abundance, is inefficient for nutrient and waste transport. The predominance of closed paths in intracranial vasculature, though mostly formed by a larger number of edges, has been shown to serve in flow rebalancing upon vessel occlusion[28,94]. Large vessel loops were not investigated in this study, but increased clustering coefficients in the pathological networks indicate that glioblastoma promotes good conditions for flow rebalancing and ensures local supply somewhat redundantly.

The vessel networks' clustering with $C_i(k_i) \sim k_i^{-\beta}$ is reminiscent of hierarchical networks. Such scaling has been found in some real networks and can be reproduced by several models, incorporating different network evolution mechanisms[70,95]. Although it has been reported that the scaling exponent in true hierarchical networks often takes on values $\beta \approx 1$, and this has been proven analytically for two hierarchical network models[96,97], deviating values still present the power-law scaling with degree. To our knowledge, hierarchical clustering has not been observed in real networks embedded in Euclidean space. It has been assumed, so far, that the spatial constraints, linked to cost factors in connectivity, suppress the formation of such hierarchical structures in spatial networks[70,73].

The basic vascular networks combined scale-free degree distributions with hierarchical scaling of clustering coefficients, while strictly embedded in Euclidian space. The scale-free property supports the stability of the network over long time periods[93], while the hierarchical organization can be expected to be related to the optimization of transport efficiency[7]. To our knowledge, no comparable real network with such high degree and clustering exponents, γ and β, has been quantified before. The findings suggest that tissue vasculature, when modeled as an undirected network, may form a distinct class of networks with unprecedented properties. Such a conclusion demands further investigations, including more statistics and different vascular networks, but the motivation for such studies should hereby be established.

Methodological challenges. Intracranial vascular networks are composed of a myriad of individual vessel branches with different geometries. An attempt to study the full range of blood vessel instances pervading any animal tissue bears great experimental and computational challenges. The trade-off between high resolution and large acquisition volumes, that most imaging modalities are bound to, limits the capabilities to attain detailed and extensive anatomical information about full vascular systems. Regarding this compromise, the data acquisition enabling this study pushes the current frontiers of easily reproducible, large-scale biological imaging without need for co-registration or stitching.

The segmentation process plays a critical role in data treatment. Due to differently expressed imaging artefacts, each dataset was segmented individually with great care to reproduce the visual perception of vessels in the original image stacks. It may be argued that this produces subjective segmentations with no clear thresholds or fixed parameters between datasets, but, on the available data, the results are superior to alternative, threshold-based methods. Furthermore, any masking procedure used to differentiate healthy and tumor tissue suffers a certain ambiguity in tissue boundaries, which can influence statistical results.

It should be noted that the SPIM imaging procedure only incorporates perfused vessels. This is a positive feature in our context, since occluded vessels do not contribute to the network's function, and are, a fortiori, not of interest in this study. However, a caveat regarding the presented geometric quantifications arises from the tissue clearing, where dehydration leads to an isotropic volume shrinkage of up to 40%[35], which translates to vessel

112

lengths and radii with a factor of $0.6^{1/3} \approx 0.84$. Since the smallest capillaries typically present *in vivo* diameters of around $4\,\mu$m[98,99], a shrinkage of 40% would correspond to a reduced vessel diameter of 3.37 μm. In such extreme cases, with a resultion of 3.25–5 μm in our study, more than 90% of the enclosing voxel will still be illuminated by vascular contrast, thus still safely registering the voxel as containing vasculature in accordance with Risser *et al.*, who validated that a resolution in our range is just high enough to register the entire microvasculature[100].

A highly accurate quantification for small capillaries was not possible in this study, as vessels with radii below approximately 3 μm appear with single-voxel thickness. This pitfall was acceptable, as the aim of this paper was not to advance the large body of literature dealing with absolute geometric vessel properties, but to provide a detailed topological analysis of the entire microvasculature. The vascular network topology is not affected by tissue shrinkage or vascular radius distortion, since it only considers connections between vessels. One exception are distance-dependent measures, in which case physical separations are expected to scale linearly with a factor close to $0.6^{-1/3} \approx 1.186$ in the original tissue before clearing[35]. The vessel connectivity, however, is robust under the imaging and post-processing and the geometric properties are comparable within the scope of an experiment. The inclusion of the smallest vessels in our analysis was crucial to uncover the true network topology, as the capillary bed has been shown to have dense, mesh-like properties[5,18].

A general issue with topological studies of biological data is the skeletonization process. Irregular surfaces and boundary perturbations cause single voxel stubs in the skeleton, which are by definition nodes with degree $k = 2$[41]. Even though such nodes do not contribute to the vessel network in any sensible way, they were not removed from our analysis. Although pruning can help eliminate such nodes[41], we refrained from such manipulations with arbitrary parameter choice in pruning length and method to avoid unnecessary data manipulation.

Another systematic effect of discrete image data is the emergence of high degree nodes. With high local node densities, neighboring branching points in the skeleton, *e.g.*, consecutive bifurcations, can combine to vertices of high degree[41]. Examples are shown in Supplementary Movies 4 and 5. This effect produces long tails in the degree distributions, which, at first glance, may seem unphysiological. While higher resolution acquisitions are expected to break the high-degree nodes up into multiple low-degree branching points, the emerging power law in degree distributions is nonetheless meaningful at the treated length scale. From a large-scale perspective, branching points, which are separated by less than the diameter of the network's smallest vessels, can sensibly be modeled as single meeting points of multiple vessels. When considered during the interpretation of the results, the implications of this caveat on our understanding of such large transport networks are rather constructive.

General topological properties of the cerebral vasculature have barely been quantified in the past. Although graph theoretical modeling has been applied to more and more anatomical systems in recent years[22,64], our work provides the first multi-scale topological quantifications of the cerebral vasculature in a mammal to this detail. Furthermore, over the past decades, many studies have elucidated geometric and structural abnormalities of tumor vasculature in diverse settings and contexts[14,15,23], but none have investigated the topological consequences of tumor growth on an entire vascular network.

The topological quantifications presented here only utilize a small subset of tools available in network theory to delineate the nature of complex networks. As the amount of data describing large systems and the availability of computational power have increased, a multitude of methods has been developed in the field of graph theory (see[59] for a recent overview). Our quantifications of such large samples of the cerebral angiome are, to our knowledge, the first of this scale and detail. The undirected graph framework was employed in order to deliver first basic network characteristics. On such large systems made up of many similar constituents, this approach has proven to be successful in uncovering previously veiled system properties. Future studies should build on these results and extend our understanding of large vascular systems as complex networks, how tumor development alters these networks, and how we can use this in treatment.

Conclusions

In conclusion, we found that tumor growth can alter the vascular topology without substantial reflections in geometric features of individual vessels in large-scale considerations. Tools from network theory are capable of grasping collective changes to the vascular network that are concealed in local analyses. This could better facilitate the delineation and grading of different forms of vascular remodeling, as demonstrated with the glioblastoma models U87 and GL261. The fundamental graph properties characterizing the cerebrovascular network were maintained in the glioblastoma, but local and nonlocal clustering, as well as long-range connectivity were characteristically rearranged, with more assortative mixing of strongly decomposed vessel communities. This may have profound implications on oxygenation and nutrient distribution to the tissue, which could be used for the development of tailored treatment strategies.

References

1. González-Alonso, J. Human thermoregulation and the cardiovascular system. *Exp Physiol* **97**, 340–346, https://doi.org/10.1113/expphysiol.2011.058701 (2012).
2. Murray, C. D. The physiological principle of minimum work: I. the vascular system and the cost of blood volume. *Proc Natl Acad Sci USA* **12**, 207–214 (1926).
3. Murray, C. D. The physiological principle of minimum work: Ii. oxygen exchange in capillaries. *Proc Natl Acad Sci USA* **12**, 299–304 (1926).
4. Wiedeman, M. P., Tuma, R. F. & Mayrovitz, H. N. *An Introduction to Microcirculation*. (Elsevier Academic Press, New York, 1981).
5. Lorthois, S. & Cassot, F. Fractal analysis of vascular networks: Insights from morphogenesis. *J Theor Biol* **262**, 614–633, https://doi.org/10.1016/j.jtbi.2009.10.037 (2010).
6. Corson, F. Fluctuations and redundancy in optimal transport networks. *Phys Rev Lett* **104**, 048703, https://doi.org/10.1103/PhysRevLett.104.048703 (2010).
7. Ronellenfitsch, H. & Katifori, E. Global optimization, local adaptation, and the role of growth in distribution networks. *Phys Rev Lett* **117**, 138301, https://doi.org/10.1103/PhysRevLett.117.138301 (2016).

8. Carmeliet, P. & Jain, R. K. Angiogenesis in cancer and other diseases. *Nature* **407**, 249–257, https://doi.org/10.1038/35025220 (2000).

9. Holash, J. *et al.* Vessel cooption, regression, and growth in tumors mediated by angiopoietins and vegf. *Science* **284**, 1994–1998, https://doi.org/10.1126/science.284.5422.1994 (1999).

10. Carmeliet, P. & Jain, R. K. Molecular mechanisms and clinical applications of angiogenesis. *Nature* **473**, 298–307, https://doi.org/10.1038/nature10144 (2011).

11. Erber, R. *et al.* Ephb4 controls blood vascular morphogenesis during postnatal angiogenesis. *EMBO J* **25**, 628–641, https://doi.org/10.1038/sj.emboj.7600949 (2006).

12. Holash, J., Wiegand, S. J. & Yancopoulos, G. D. New model of tumor angiogenesis: dynamic balance between vessel regression and growth mediated by angiopoietins and vegf. *Oncogene* **18**, 5356–5362, https://doi.org/10.1038/sj.onc.1203035 (1999).

13. Rieger, H. & Welter, M. Integrative models of vascular remodeling during tumor growth. *Wiley Interdiscip Rev Syst Biol Med* **7**, 113–129, https://doi.org/10.1002/wsbm.1295 (2015).

14. Scianna, M., Bell, C. G. & Preziosi, L. A review of mathematical models for the formation of vascular networks. *J Theor Biol* **333**, 174, https://doi.org/10.1016/j.jtbi.2013.04.037 (2013).

15. Logsdon, E. A., Finley, S. D., Popel, A. S. & Gabhann, F. M. A systems biology view of blood vessel growth and remodelling. *J Cell Mol Med* **18**, 1491–1508, https://doi.org/10.1111/jcmm.12164 (2014).

16. Döme, B., Hendrix, M., Paku, S. & Tóvarí, J. Alternative vascularization mechanisms in cancer. *Am J Pathol* **170**, 1–15, https://doi.org/10.2353/ajpath.2007.060302 (2007).

17. Winkler, F. *et al.* Kinetics of vascular normalization by vegfr2 blockade governs brain tumor response to radiation: Role of oxygenation, angiopoietin-1, and matrix metalloproteinases. *Cancer Cell* **6**, 553–563, https://doi.org/10.1016/j.ccr.2004.10.011 (2004).

18. Gazit, Y., Berk, D. A., Leunig, M., Baxter, L. T. & Jain, R. K. Scale-invariant behavior and vascular network formation in normal and tumor tissue. *Phys Rev Lett* **75**, 2428, https://doi.org/10.1103/PhysRevLett.75.2428 (1995).

19. Jain, R. K. Normalization of tumor vasculature: an emerging concept in antiangiogenic therapy. *Science* **307**, 58–62, https://doi.org/10.1126/science.1104819 (2005).

20. Cassot, F., Lauwers, F., Fouard, C., Prohaska, S. & Lauwers-Cances, V. A novel three-dimensional computer-assisted method for a quantitative study of microvascular networks of the human cerebral cortex. *Microcirculation* **13**, 1–18, https://doi.org/10.1080/10739680500383407 (2006).

21. Perfahl, H. *et al.* 3d hybrid modelling of vascular network formation. *J Theor Biol* **414**, 254–268, https://doi.org/10.1016/j.jtbi.2016.11.013 (2017).

22. Reichold, J. *et al.* Vascular graph model to simulate the cerebral blood flow in realistic vascular networks. *J Cereb Blood Flow Metab* **29**, 1429–1443, https://doi.org/10.1038/jcbfm.2009.58 (2009).

23. Rieger, H., Fredrich, T. & Welter, M. Physics of the tumor vasculature: Theory and experiment. *Eur Phys J Plus* **131**, 31, https://doi.org/10.1140/epjp/i2016-16031-9 (2016).

24. Alves, A. P., Mesquita, O. N., Gómez-Gardeñes, J. & Agero, U. Graph analysis of cell clusters forming vascular networks. *R Soc Open Sci* **5**, 171592, https://doi.org/10.1098/rsos.171592 (2018).

25. Kelch, I. D. *et al.* Organ-wide 3d-imaging and topological analysis of the continuous microvascular network in a murine lymph node. *Sci Rep* **5**, 16534, https://doi.org/10.1038/srep16534 (2015).

26. Wahl, E. M., Daniels, F. H., Leonard, E. F., Levinthal, C. & Cortell, S. A graph theory model of the glomerular capillary network and its development. *Microvasc Res* **27**, 96–109, https://doi.org/10.1016/0026-2862(84)90044-X (1984).

27. Wahl, E. M., Quintas, L. V., Lurie, L. L. & Gargano, M. L. A graph theory analysis of renal glomerular microvascular networks. *Microvasc Res* **67**, 223–230, https://doi.org/10.1016/j.mvr.2003.11.005 (2004).

28. Blinder, P., Shih, A. Y., Rafie, C. A. & Kleinfeld, D. Topological basis for the robust distribution of blood to rodent neocortex. *Proc Natl Acad Sci USA* **107**, 12670–12675, https://doi.org/10.1073/pnas.1007239107 (2010).

29. Espinoza-Valdez, A., Femat, R. & Ordaz-Salazar, F. C. A model for renal arterial branching based on graph theory. *Math Biosci* **225**, 36–43, https://doi.org/10.1016/j.mbs.2010.01.007 (2010).

30. Blinder, P. *et al.* The cortical angiome: an interconnected vascular network with noncolumnar patterns of blood flow. *Nat Neurosci* **16**, 889–897, https://doi.org/10.1038/nn.3426 (2013).

31. Heinzer, S. *et al.* Hierarchical microimaging for multiscale analysis of large vascular networks. *Neuroimage* **32**, 626–636, https://doi.org/10.1016/j.neuroimage.2006.03.043 (2006).

32. Kim, E. *et al.* Multiscale imaging and computational modeling of blood flow in the tumor vasculature. *Ann Biomed Eng* **40**, 2425–2441, https://doi.org/10.1007/s10439-012-0585-5 (2012).

33. Ertürk, A. *et al.* Three-dimensional imaging of solvent-cleared organs using 3disco. *Nat Protoc* **7**, 1983–1995, https://doi.org/10.1038/nprot.2012.119 (2012).

34. Schwarz, M. K. *et al.* Fluorescent-protein stabilization and high-resolution imaging of cleared, intact mouse brains. *PLoS One* **10**, e0124650, https://doi.org/10.1371/journal.pone.0124650 (2015).

35. Breckwoldt, M. O. *et al.* Correlated magnetic resonance imaging and ultramicroscopy (mr-um) is a tool kit to asses the dynamics of glioma angiogenesis. *Elife* **5**, e11712, https://doi.org/10.7554/eLife.11712 (2016).

36. Breckwoldt, M. O. *et al.* Correlated mri and ultramicroscopy (mr-um) of brain tumors reveals vast heterogeneity of tumor infiltration and neoangiogenesis in preclinical models and human disease. *Front Neurosci* **12**, 1004, https://doi.org/10.3389/fnins.2018.01004 (2019).

37. Stamatelos, S. K., Kim, E., Pathak, A. P. & Popel, A. S. A bioimage informatics based reconstruction of breast tumor microvasculature with computational blood flow predictions. *Microvasc Res* **91**, 8–21, https://doi.org/10.1016/j.mvr.2013.12.003 (2014).

38. Newman, M. E. J. Modularity and community structure in networks. *Proc Natl Acad Sci USA* **103**, 8577–8582, https://doi.org/10.1073/pnas.0601602103 (2006).

39. Sommer, C., Straehle, C., Koethe, U. & Hamprecht, F. A. ilastik: Interactive learning and segmentation toolkit. In *Proc IEEE Int Symp Biomed Imaging*, 230–233, https://doi.org/10.1109/ISBI.2011.5872394 (2011).

40. Schindelin, J. *et al.* Fiji: an open-source platform for biological-image analysis. *Nat Methods* **9**, 676–682, https://doi.org/10.1038/nmeth.2019 (2012).

41. Hirsch, S., Reichold, J., Schneider, M., Székely, G. & Weber, B. Topology and hemodynamics of the cortical cerebrovascular system. *J Cereb Blood Flow Metab* **32**, 952–967, https://doi.org/10.1038/jcbfm.2012.39 (2012).

42. Lee, T., Kashyap, R. L. & Chu, C. Building skeleton models via 3-d medial surface/axis thinning algorithms. *CVGIP: Graphical Models and Image Processing* **56**, 462–478, https://doi.org/10.1006/cgip.1994.1042 (1994).

43. Arganda-Carreras, I., Fernandez-Gonzalez, R., Munoz-Barrutia, A. & Ortiz-De-Solorzano, C. 3d reconstruction of histological sections: Application to mammary gland tissue. *Microsc Res Tech* **73**, 1019–1029, https://doi.org/10.1002/jemt.20829 (2010).

44. Bullitt, E., Gerig, G., Pize, S. M., Lin, W. & Aylward, S. R. Measuring tortuosity of the intracerebral vasculature from mra images. *IEEE Trans Med Imaging* **22**, 1163–1171, https://doi.org/10.1109/TMI.2003.816964 (2003).

45. Lorthois, S., Lauwers, F. & Cassot, F. Tortuosity and other vessel attributes for arterioles and venules of the human cerebral cortex. *Microvasc Res* **91**, 99–109, https://doi.org/10.1016/j.mvr.2013.11.003 (2014).

114

46. Barabási, A.-L. & Albert, R. Emergence of scaling in random networks. *Science* **286**, 509–512, https://doi.org/10.1126/science.286.5439.509 (1999).
47. Barabási, A.-L., Albert, R. & Jeong, H. Mean-field theory for scale-free random networks. *Physica A* **272**, 173–187, https://doi.org/10.1016/S0378-4371(99)00291-5 (1999).
48. Albert, R., Jeong, H. & Barabási, A.-L. Error and attack tolerance of complex networks. *Nature* **406**, 378–382, https://doi.org/10.1038/35019019 (2000).
49. Milgram, S. The small world problem. *Psychol Today* **2**, 60–67 (1967).
50. de Sola Pool, I., Kochen, M., Milgram, S. & Newcomb, T. *The Small World*. (Ablex, Norwood, NJ, 1989).
51. Watts, D. J. & Strogatz, S. H. Collective dynamics of 'small-world' networks. *Nature* **393**, 440, https://doi.org/10.1038/30918 (1998).
52. Gleich, D. F. *Models and Algorithms for PageRank Sensitivity*. Ph.D. thesis, Stanford University, Chapter 7 on MatlabBGL, (accessed 20.05.2019) (2009).
53. Albert, R. & Barabási, A.-L. Statistical mechanics of complex networks. *Rev Mod Phys* **74**, 47–97, https://doi.org/10.1103/RevModPhys.74.47 (2002).
54. Katifori, E., Szöllősi, G. J. & Magnasco, M. O. Damage and fluctuations induce loops in optimal transport networks. *Phys Rev Lett* **104**, 048704, https://doi.org/10.1103/PhysRevLett.104.048704 (2010).
55. Fleury, V. & Schwartz, L. Diffusion limited aggregation from shear stress as a simple model of vasculogenesis. *Fractals* **7**, 33–39, https://doi.org/10.1142/S0218348X99000050 (1999).
56. Fleury, V. & Schwartz, L. Modelisation of 3-d microvasculature by interlaced diffusion limited aggregation. *Fractals* **8**, 255–259, https://doi.org/10.1142/S0218348X00000317 (2000).
57. Nguyen, T. H., Eichmann, A., le Noble, F. & Fleury, V. Dynamics of vascular branching morphogenesis: the effect of blood and tissue flow. *Phys Rev E* **73**, 061907–1–14, https://doi.org/10.1103/PhysRevE.73.061907 (2006).
58. Blondel, V. D., Guillaume, J.-L., Lambiotte, R. & Lefebvre, E. Fast unfolding of communities in large networks. *J Stat Mech* **8**, https://doi.org/10.1088/1742-5468/2008/10/P10008 (2008).
59. Barabási, A.-L. *Network Science*. (Cambridge University Press, United Kingdom, 2016).
60. Chugh, B. P. *et al.* Measurement of cerebral blood volume in mouse brain regions using micro-computed tomography. *Neuroimage* **47**, 1312–1318, https://doi.org/10.1016/j.neuroimage.2009.03.083 (2009).
61. Bullitt, E. *et al*. Vessel tortuosity and brain tumor malignancy: a blinded study. *Acad Radiol* **12**, 1232–1240, https://doi.org/10.1016/j.acra.2005.05.027 (2005).
62. Bullitt, E. *et al*. Blood vessel morphological changes as visualized by mra during treatment of brain metastases: A feasibility study. *Radiology* **245**, 824–830, https://doi.org/10.1148/radiol.2453061889 (2007).
63. Eguíluz, V. M., Chialvo, D. R., Cecchi, G. A., Baliki, M. & Apkarian, A. V. Scale-free brain functional networks. *Phys Rev Lett* **94**, 018102, https://doi.org/10.1103/PhysRevLett.94.018102 (2005).
64. Estrada, E. *The Structure of Complex Networks - Theory and Applications*. (Oxford University Press, New York, 2012).
65. Kather, J. N. *et al*. Continuous representation of tumor microvessel density and detection of angiogenic hotspots in histological whole-slide images. *Oncotarget* **5**, 1–14, https://doi.org/10.18632/oncotarget.4383 (2015).
66. Erdös, P. & Rényi, A. On the evolution of random graphs. *Publ Math Inst Hung Acad Sci* **5**, 17–61 (1960).
67. Jeong, H., Tombor, B., Albert, R., Oltvai, Z. N. & Barabási, A.-L. The large-scale organization of metabolic networks. *Nature* **407**, 651–654, https://doi.org/10.1038/35036627 (2000).
68. Jeong, H., Mason, S. P., Barabási, A.-L. & Oltvai, Z. N. Lethality and centrality in protein networks. *Nature* **411**, 41–42, https://doi.org/10.1038/35075138 (2001).
69. Boccaletti, S., Latora, V., Moreno, Y., Chavez, M. & Hwang, D.-U. Complex networks: Structure and dynamics. *Phys Rep* **424**, 175–308, https://doi.org/10.1016/j.physrep.2005.10.009 (2006).
70. Ravasz, E. & Barabási, A.-L. Hierarchical organization in complex networks. *Phys Rev E* **67**, 026112, https://doi.org/10.1103/PhysRevE.67.026112 (2003).
71. Newman, M. E. J. Assortative mixing in networks. *Phys Rev Lett* **89**, 208701, https://doi.org/10.1103/PhysRevLett.89.208701 (2002).
72. Newman, M. E. J. Mixing patterns in networks. *Phys Rev E* **67**, 026126, https://doi.org/10.1103/PhysRevE.67.026126 (2003).
73. Barthélemy, M. Spatial networks. *Phys Rep* **499**, 1–101, https://doi.org/10.1016/j.physrep.2010.11.002 (2011).
74. Lenting, K., Verhaak, R., ter Laan, M., Wesseling, P. & Leenders, W. Glioma: Experimental models and reality. *Acta Neuropathol* **133**, 263–282, https://doi.org/10.1007/s00401-017-1671-4 (2017).
75. Baish, J. W. *et al*. Scaling rules for diffusive drug delivery in tumor and normal tissues. *Proc Natl Acad Sci USA* **108**, 1799–1803, https://doi.org/10.1073/pnas.1018154108 (2011).
76. Nagy, J. A., Chang, S.-H., Shih, S.-C., Dvorak, A. M. & Dvorak, H. F. Heterogeneity of the tumor vasculature. *Semin Thromb Hemost* **36**, 321–331, https://doi.org/10.1055/s-0030-1253454 (2010).
77. Vajkoczy, P., Schilling, L., Ullrich, A., Schmiedek, P. & Menger, M. D. Characterization of angiogenesis and microcirculation of high-grade glioma: An intravital multifluorescence microscopic approach in the athymic nude mouse. *J Cereb Blood Flow Metab* **18**, 510–520, https://doi.org/10.1097/00004647-199805000-00006 (1998).
78. Deane, B. & Lantos, P. The vasculature of experimental brain tumours: Part 1. A sequential light and electron microscope study of angiogenesis. *J Neurolog Sci* **49**, 55–66, https://doi.org/10.1016/0022-510X(81)90188-X (1981).
79. Dennie, J. *et al*. NMR imaging of changes in vascular morphology due to tumor angiogenesis. *Magn Reson Med* **40**, 793–799, https://doi.org/10.1002/mrm.1910400602 (1998).
80. Packard, S. D. *et al*. Functional response of tumor vasculature to P_aCO_2: Determination of total and microvascular blood volume by MRI. *Neoplasia* **5**, 330–338, https://doi.org/10.1016/S1476-5586(03)80026-X (2003).
81. Farrar, C. T. *et al*. *In vivo* validation of mri vessel caliber index measurement methods with intravital optical microscopy in a u87 mouse brain tumor model. *Neuro Oncol* **12**, 341–350, https://doi.org/10.1093/neuonc/nop032 (2010).
82. Lemasson, B. *et al*. Assessment of multiparametric mri in a human glioma model to monitor cytotoxic and anti-angiogenic drug effects. *NMR Biomed* **24**, 473–482, https://doi.org/10.1002/nbm.1611 (2011).
83. Mathivet, T. *et al*. Dynamic stroma reorganization drives blood vessel dysmorphia during glioma growth. *EMBO Mol Med* **9**, 1629–1645, https://doi.org/10.15252/emmm.201607445 (2017).
84. Michiels, C. Physiological and pathological responses to hypoxia. *Am J Pathol* **164**, 1875–1882, https://doi.org/10.1016/S0002-9440(10)63747-9 (2004).
85. Jain, R. K. *et al*. Angiogenesis in brain tumours. *Nat Rev Neurosci* **8**, 610–622, https://doi.org/10.1038/nrn2175 (2007).
86. Kim, E., Zhang, J., Hong, K., Benoit, N. E. & Pathak, A. P. Vascular phenotyping of brain tumors using magnetic resonance microscopy (μMRI). *J Cereb Blood Flow Metab* **31**, 1623–1636, https://doi.org/10.1038/jcbfm.2011.17 (2011).
87. Less, J. R., Skalak, T. C., Sevick, E. M. & Jain, R. K. Microvascular architecture in a mammary carcinoma: Branching patterns and vessel dimensions. *Cancer Res* **51**, 265–273 (1991).
88. Warren, B. The vascular morphology of tumors. In Peterson, H.-I. (ed.) *Tumor blood circulation: Angiogenesis, vascular morphology and blood flow of experimental and human tumors.*, 1–47 (CRC Press, Boca Raton, FL, 1979).
89. Rege, A., Thakor, N. V., Rhie, K. & Pathak, A. P. *In vivo* laser speckle imaging reveals microvascular remodeling and hemodynamic changes during wound healing angiogenesis. *Angiogenesis* **15**, 87–98, https://doi.org/10.1007/s10456-011-9245-x (2012).

90. Das, S. & Marsden, P. A. Angiogenesis in glioblastoma. *N Engl J Med* **369**, 1561–1563, https://doi.org/10.1056/NEJMcibr1309402 (2013).
91. Patan, S. Vasculogenesis and angiogenesis as mechanisms of vascular network formation, growth and remodeling. *J Neurooncol* **50**, 1–15, https://doi.org/10.1023/A:1006493130855 (2000).
92. da Fontoura Costa, L. & Viana, M. P. Complex channel networks of bone structure. *Appl Phys Lett* **88**, 033903, https://doi.org/10.1063/1.2166473 (2006).
93. Cohen, R., Erez, K., ben Avraham, D. & Havlin, S. Resilience of the internet to random breakdowns. *Phys Rev Lett* **85**, 4626, https://doi.org/10.1103/PhysRevLett.85.4626 (2000).
94. Schaffer, C. B. *et al.* Two-photon imaging of cortical surface microvessels reveals a robust redistribution in blood flow after vascular occlusion. *PLoS Biol* **4**, 22, https://doi.org/10.1371/journal.pbio.0040022 (2006).
95. Baiesi, M. & Manna, S. S. Scale-free networks from a hamiltonian dynamics. *Phys Rev E* **68**, 047103, https://doi.org/10.1103/PhysRevE.68.047103 (2003).
96. Dorogovtsev, S. N., Goltsev, A. V. & Mendes, J. F. F. Pseudofractal scale-free web. *Phys Rev E* **65**, 066122, https://doi.org/10.1103/PhysRevE.65.066122 (2002).
97. Noh, J. D. Exact scaling properties of a hierarchical network model. *Phys Rev E* **67**, 045103, https://doi.org/10.1103/PhysRevE.67.045103 (2003).
98. Tsai, P. S. *et al.* Correlations of neuronal and microvascular densities in murine cortex revealed by direct counting and colocalization of nuclei and vessels. *J Neurosci* **29**, 14553–14570, https://doi.org/10.1523/JNEUROSCI.3287-09.2009 (2009).
99. Santisakultarm, T. P. *et al. In vivo* two-photon excited fluorescence microscopy reveals cardiac- and respiration-dependent pulsatile blood flow in cortical blood vessels in mice. *Am J Physiol Heart Circ Physiol* **302**, H1367–H1377, https://doi.org/10.1152/ajpheart.00417.2011 (2012).
100. Risser, L. *et al.* From homogeneous to fractal normal and tumorous microvascular networks in the brain. *J Cereb Blood Flow Metab* **27**, 293–303, https://doi.org/10.1038/sj.jcbfm.9600332 (2007).

Acknowledgements

Author Contributions

A.H. and F.T.K. conceived the study. J.B., T.K., and B.T. performed microscopy experiments. A.H. provided analytical and numerical tools. A.H. and F.T.K. analyzed the data and interpreted the experiments. A.H., J.B., G.S., F.K., S.H., M.B., M.O.B., and F.T.K. wrote the paper. All authors read and approved the final manuscript.

Additional Information

Supplementary information accompanies this paper at https://doi.org/10.1038/s41598-019-47567-w.

Competing Interests: The authors declare no competing interests.

Publisher's note: Springer Nature remains neutral with regard to jurisdictional claims in published maps and institutional affiliations.

116

Glioblastoma multiforme restructures the topological connectivity of cerebrovascular networks

Artur Hahn, Julia Bode, Thomas Krüwel, Gergely Solecki, Sabine Heiland, Martin Bendszus, Björn Tews, Frank Winkler, Michael O. Breckwoldt, and Felix T. Kurz

Supplementary Video Legends

Supplementary Movie 1: Segmentation of a healthy brain hemisphere. Segmentation results from a healthy mouse brain hemisphere, presenting raw imaging data from SPIM, overlaid with the binary vessel segmentation from ilastik in semitransparent red. The AVI-movie (.avi) shows 300 consecutive image slices, each 5 µm apart, at 25 frames per second (fps).

Supplementary Movie 2: Segmentation of a U87 glioblastoma. Segmentation results from a U87 glioblastoma specimen in a mouse brain, presenting raw SPIM data, overlaid with the binary vessel segmentation from ilastik in semitransparent red. The AVI-movie shows 500 consecutive image slices, each 5 µm apart, at 25 fps.

Supplementary Movie 3: Segmentation of a GL261 glioblastoma. Segmentation results from a GL261 glioblastoma xenograft, with raw SPIM data, overlaid with the ilastik segmentation in semitransparent red. The AVI-movie shows 400 consecutive image slices, each 5 µm apart, at 25 fps.

Supplementary Movie 4: High degree node in healthy tissue. AVI-movie, showing a volume rendering of a vascular subvolume from healthy grey matter, comprising a volume of 130 x 130 x 100 µm, depicting a node with degree k=24 (extended node voxels marked in glowing orange). The first 360° rotation shows the segmented and post-processed vasculature in semitransparent red, followed by the additional appearance of the vascular skeleton voxels, as used for analysis, in blue for another 360° rotation. For the last rotation, the discrete skeleton representation is replaced by tube structures, determined in the image processing software Amira 5.4.1 (Thermo Fisher Scientific, Waltham, MA, USA) for better visualization. The movie frames were created using Amira ResolveRT FEI 5.4.

Supplementary Movie 5: High degree node in U87 glioblastoma. AVI-movie showing a volume rendering of a vascular subvolume from a U87 glioblastoma's peripheral region, comprising a volume of 188 x 188 x 110 µm, depicting a node with degree k=14 (extended node voxels marked in glowing orange). The first 360° rotation shows the segmented and post-processed vasculature in semitransparent red, followed by the additional appearance of the vascular skeleton voxels, as used for analysis, in blue for another 360° rotation. For the last rotation, the discrete skeleton representation is replaced by tube structures, determined in the image processing software Amira for better visualization. The movie frames were created using Amira.

Publication V:
Tumor voxel classification
based on transverse relaxation

Authors: <u>Artur Hahn</u>, Julia Bode, Sarah Schuhegger, Thomas Krüwel, Volker J. F. Sturm, Ke Zhang, Johann M. E. Jende, Björn Tews, Sabine Heiland, Martin Bendszus, Michael O. Breckwoldt, Christian H. Ziener and Felix T. Kurz

Contributions: A.H. and F.T.K. conceptualized this study. J.B., T.K., B.T., and M.O.B. handled animals and conducted tissue clearing and fluorescence microscopy. A.H. and S.S. segmented the raw image data and conducted quality assurance. Image post-processing, NMR simulations, and automated large-scale processing were implemented by A.H. with assistance with post-processing tools by V.J.F.S. and K.Z. Analyses were performed by A.H. and F.T.K. and the manuscript was written by A.H. and F.T.K. with contributions from J.B., J.M.E.J., S.H., M.B., M.O.B., and C.H.Z.

SPECIAL ISSUE RESEARCH ARTICLE

NMR IN BIOMEDICINE WILEY

Brain tumor classification of virtual NMR voxels based on realistic blood vessel-induced spin dephasing using support vector machines

Artur Hahn[1,2] 🄳 | Julia Bode[3] | Sarah Schuhegger[1,2] | Thomas Krüwel[3] | Volker J.F. Sturm[1,4] | Ke Zhang[1,4] | Johann M.E. Jende[1] | Björn Tews[3] | Sabine Heiland[1] | Martin Bendszus[1] | Michael O. Breckwoldt[1,5] | Christian H. Ziener[1,4] | Felix T. Kurz[1,4]

[1]Department of Neuroradiology, Heidelberg University Hospital, Heidelberg, Germany

[2]Department of Physics and Astronomy, University of Heidelberg, Heidelberg, Germany

[3]Schaller Research Group at the University of Heidelberg and the German Cancer Research Center (DKFZ), Molecular Mechanisms of Tumor Invasion, Heidelberg, Germany

[4]Department of Radiology E010, German Cancer Research Center (DKFZ), Heidelberg, Germany

[5]Clinical Cooperation Unit Neuroimmunology and Brain Tumor Immunology, German Cancer Research Center (DKFZ), Heidelberg, Germany

Correspondence
Felix T. Kurz, Department of Neuroradiology, Heidelberg University Hospital, Im Neuenheimer Feld 400, 69120. Heidelberg, Germany.
Email: felix.kurz@med.uni-heidelberg.de

Funding information
The Chica and Heinz Schaller Stiftung; Deutsche Forschungsgemeinschaft, Grant/Award Numbers: DFG KU 3555/1-1, ZI 1295/2-1, SFB 1389; Else Kröner-Fresenius Stiftung, Grant/Award Numbers: 2017 - A25, 2019_EKM.23; Novartis Foundation for Sustainable Development

Remodeling of tissue microvasculature commonly promotes neoplastic growth; however, there is no imaging modality in oncology yet that noninvasively quantifies microvascular changes in clinical routine. Although blood capillaries cannot be resolved in typical magnetic resonance imaging (MRI) measurements, their geometry and distribution influence the integral nuclear magnetic resonance (NMR) signal from each macroscopic MRI voxel. We have numerically simulated the expected transverse relaxation in NMR voxels with different dimensions based on the realistic microvasculature in healthy and tumor-bearing mouse brains (U87 and GL261 glioblastoma). The 3D capillary structure in entire, undissected brains was acquired using light sheet fluorescence microscopy to produce large datasets of the highly resolved cerebrovasculature. Using this data, we trained support vector machines to classify virtual NMR voxels with different dimensions based on the simulated spin dephasing accountable to field inhomogeneities caused by the underlying vasculature. In prediction tests with previously blinded virtual voxels from healthy brain tissue and GL261 tumors, stable classification accuracies above 95% were reached. Our results indicate that high classification accuracies can be stably attained with achievable training set sizes and that larger MRI voxels facilitated increasingly successful classifications, even with small training datasets. We were able to prove that, theoretically, the transverse relaxation process can be harnessed to learn endogenous contrasts for single voxel tissue type classifications on tailored MRI acquisitions. If translatable to experimental MRI, this may augment diagnostic imaging in oncology with automated voxel-by-voxel signal interpretation to detect vascular pathologies.

KEYWORDS
angiogenesis, glioblastoma multiforme, machine learning, microvasculature, signal classification, spin dephasing, support vector machines, vascular pathology

1 | INTRODUCTION

A hallmark of most tumor types is a characteristic remodeling of the existing microvasculature towards a more favorable environment for tumor growth and cell proliferation throughout all stages of development.[1-4] Specifically, the most malignant brain tumor, glioblastoma multiforme, thrives on microvascular proliferation, with strong variations in vessel density and shape from tumor core to periphery.[5-7] As of today, there exists no radiological imaging modality directly sensitive to such pathological changes in capillary geometry that has made it to routine clinical translation. The gold standard for neuro-oncological imaging remains to be T_1-weighted MRI with dynamic contrast enhancement using paramagnetic agents based on gadolinium.[8]

Currently used medical imaging tools in clinical MRI typically examine pathological tissue alterations on a macroscopic scale through educated comparisons of proximal voxel intensities by a radiological specialist. However, voxel-intrinsic relaxation characteristics of single imaging points can encode useful information about the underlying tissue microenvironment. Of the assessable NMR decay curves from each voxel, which can be sampled by varying acquisition schemes with different echo times and combinations of spin echo and gradient echo measurements, only a single "snapshot" or small set of echo times are typically used to produce gray-scale images for radiological evaluation or quantitative maps with simple exponential decay rates $R_2 = 1/T_2$ and $R_2^* = T_2^*$.

The development of an in vivo, noninvasive imaging technique sensitive to microvascular reshaping on a sub-voxel level would tremendously extend current possibilities of MRI instrumentation in medical imaging. It is conceivable that "abstract contrasts" could be defined to classify or characterize individual voxel signals from custom MRI acquisitions based on sampling the nonlinear transverse relaxation process at different echo times. Such abstract contrasts could be defined by tailored combinations of multiparametric signal features, which can be uncovered and optimized in a data-driven manner, using numerical simulations to cost-efficiently explore a broad spectrum of MRI sequences to optimize a classification or regression problem, like mapping the probability of an underlying tumor pathology to each MRI voxel. In this example, the abstract contrast would be the probability of a voxel signal originating from tumor tissue or the associated tissue type classification.

Numerical developments of such abstract contrast mappings based on standard, physical NMR contrasts must be guided by a known ground-truth; in our case, using the microvascular tissue structure, which can be imaged in animal experiments at high resolution, eg, using fluorescence microscopy techniques such as selective plane illumination microscopy (SPIM).[6] The ground-truth tissue microstructure can be combined with numerical modeling of relevant biophysical aspects and NMR physics to simulate MRI acquisitions in such tissue. Numerically, a vast range of standard contrasts and weightings can be explored with relatively little expense, to develop custom MRI protocols which incorporate pulse sequences to probe the relevant physical contrasts needed to define the abstract contrast.

Due to effectively paramagnetic deoxygenated hemoglobin, blood vessels embody omnipresent magnetic susceptibility inclusions in biological tissue. Motivated by the blood oxygenation level-dependent (BOLD) effect,[9,10] first attempts at defining abstract contrasts could be made with endogenous means, abstaining from external contrast agents. A successful implementation of such abstract contrasts could offer invaluable assistance in tumor diagnosis and monitoring, and aid in the planning of therapy regimes based on tumor microstructure. Furthermore, the in vivo vessel susceptibility can be controlled experimentally in a dynamic or steady-state fashion by O_2- or CO_2-enriched gas inhalation[11,12] or intravascular contrast agents.[7,13,14] This makes tissue vasculature an attractive ground-truth starting point for an exploration of abstract contrasts to identify pathological anomalies affecting vascular geometry or function.

Theoretical work, especially during the past 3 decades, has pioneered the realm of microscopic tissue characterizations based on NMR measurements.[15-19] Such studies have analytically demonstrated that geometric properties of magnetically susceptible inclusions in tissue (like blood vessels) far below the length scale of MRI resolutions can be quantified through sophisticated signal modeling techniques. It has been shown that properties of simple geometric vessel or nerve models can be linked to the transverse relaxation induced by spin dephasing across an imaging voxel in MRI.[20-23]

Although a simplified cylindrical vessel array can model some microvascular geometries quite well (as, eg, in the myocardium[24]), capillary structures in such complex tissue environments as the brain can deviate strongly from a regular arrangement of long, straight cylinders. Recent advances in high-resolution fluorescence microscopy with biological organisms have made it possible to attain full three-dimensional (3D) reconstructions of the microvascular system in entire organs[25] and small animals[26] through postmortem imaging of undissected specimens in single, semi-automated acquisitions. With the SPIM imaging employed here,[6] upon an ex vivo tissue clearing procedure, the previously marked vessel lumen in the semitransparent organ of interest can be excited to fluoresce within thin sheets in the transverse imaging plane. The volume of interest is scanned in consecutive planes, producing image stacks of the entire specimen's tissue microstructure.

Tortuous and interwoven capillary networks cannot be modeled adequately with a small set of geometric signature parameters, as in the theoretical models referenced before. Nonetheless, the microvascular architecture induces transverse relaxation patterns during NMR measurements, which may be characteristic of certain tissue types and pathologies. Motivated by theory, the collective geometric properties of the microvasculature in an NMR voxel are expected to impact the transverse relaxation and its detailed form in a convoluted but systematic way. Although they cannot be predicted analytically for complex, realistic vessel arrangements, we conjecture that such relaxation patterns could be distinguishable using machine learning.

In this work, we conduct an in silico investigation of whether the characteristic remodeling of local vessel geometries, induced during tumor growth, can be sensed through the endogenous transverse relaxation process during a free induction decay (FID)-type experiment (with T_2^* relaxation). In this initial proof-of-concept, all biological tissue properties apart from the vessel architecture were set to be constant and equal in all samples to refrain from introducing a bias, which could systematically amplify differences between healthy and pathological tissue. While the assumption of constant blood oxygenation exaggerates the susceptibility impact of arterial vessels with respect to venous parts, we used this simplification as a lowest order approximation for the realistic tissue environment. We refrained from conducting computationally highly demanding blood flow simulations, which require suited boundary conditions and should ideally be coupled with metabolic demand and extravascular oxygen diffusion models. Further, we avoid making simple ad hoc assumptions concerning the hemodynamics and intravascular oxygen distribution to keep the systematic bias and error introduced minimal.

Our motivation was to challenge the idea of conducting independent tissue type classifications on each voxel of an MRI scan with statistical machine learning methods based on extended sampling and parametrizations of the spin dephasing process. We used realistic 3D vessel structures from large, undissected mouse brains to numerically simulate the transverse relaxation accountable to spin dephasing due to magnetic field inhomogeneities brought upon by the microvasculature. Support vector machine (SVM) classifiers for a dephasing-based tumor voxel identification tool were trained and tested in several scenarios with two different glioma cell lines for a proof of principle. We included two different glioma types with distinct growth patterns and angiogenic phenotypes: the U87 glioma model was derived from a human brain tumor with nondiffusely infiltrative growth patterns and relatively homogeneous, leaky vessels, while GL261 is a syngeneic mouse model of glioblastoma multiforme with diffusely infiltrative characteristics, stronger angiogenesis and hypoxia.[27]

We have combined state-of-the-art ultramicroscopy with a highly parallelized data-processing pipeline to investigate the dephasing attenuation during hypothetical T_2^*-weighted MRI acquisitions with virtual NMR voxels at different length scales. We simulated the extravascular signal contribution from diffusing water protons in virtual NMR voxels sampled from high-resolution 3D light sheet fluorescence microscopy datasets, acquired from the brains of healthy and tumor-bearing mice (U87 and GL261 glioblastoma cell lines). The signal attenuation due to vessel-induced field inhomogeneities in single NMR voxels was parametrized in a sparse manner (with standard exponential fit parameters and custom fit functions for the short- and long-time signal regimes) to deliver NMR relaxation features, which could be linked to the originating tissue type through SVM classification. This endeavor should evaluate the theoretical feasibility of constructing single MRI voxel classifiers, which are sensitive to brain tumor vasculature through a learned endogenous contrast using support vector machines.

2 | METHODS

2.1 | Animal models, clearing and imaging

All experiments were conducted in line with standard guidelines of animal care and approved by the regional animal welfare committee (permit numbers: G187/10, G188/12, G145/10, G287/15 and G223/14, Regierungspräsidium Karlsruhe, Karlsruhe, Germany). Details concerning animal handling, preparation, and imaging have been elaborated in previous publications.[28,29] In brief, we injected 7.5 x 10^4 U87 MG cells in 9-12 week-old male NOD Scid Gamma mice (NSG; Jackson Laboratories, Bar Harbor, ME; n = 6 mice) and 10^5 GL261 glioma cells (National Cancer Institute, Bethesda, MD), diluted in 2 µl sterile phosphate buffered saline (PBS, Sigma-Aldrich Chemie GmbH, Taufkirchen, Germany) in 6-8 week-old female C57Bl/6 J mice (Charles River Laboratories, Sulzfeld, Germany; n = 6 mice), implanting in the right brain hemisphere, 2 mm lateral and 2 mm ventral of the bregma using a Hamilton syringe, driven by a fine step motor.

Mice with a U87 tumor were sacrificed for imaging 21 days posttumor cell implantation and mice with a GL261 tumor after ~ 4 weeks (once a large intracranial tumor could be seen in the monitoring scan, which was conducted with the GL261 animals beginning 1 week after cell injection, using T1-weighted Gd-contrast-enhanced MRI scans on a 9.4 T BioSpec 94/20 USR [Bruker BioSpin GmbH, Ettlingen, Germany] with isotropic 80 µm resolution). In addition to the tumor-bearing animals, n = 3 healthy, male, NOD Scid Gamma mice were sacrificed at 12 weeks of age for healthy controls.

Before sacrificing, mice were anesthetized with ketamin 10% (90 µg/g bodyweight) and xylazinhydrochloride 2% (7.5 µg/g bodyweight) and injected intravenously with 12 mg/kg Texas red *Lycopersicon esculentum* (Tomato) lectin (Vector laboratories TL-1176, 1 mg/ml) for intravital dye labeling of the vasculature. After 5 minutes of circulation, mice were transcardially perfused in deep anesthesia using 20 ml of PBS followed by 20 ml of 4% PFA. The entire brain was explanted and fixed overnight in 4% PFA, followed by PBS. The undissected organs were cleared using the FluoClearBABB protocol.[30]

Upon successful tissue clearing, a selective plane illumination microscope (Ultramicroscope II, LaVision Biotec, Bielefeld, Germany) was used to image the microvasculature in the entire brain by fluorescent excitement of the lectin marker plane by plane. Imaging was performed using 2x magnification (3.25 µm in-plane resolution) and the step size between slices in the transverse plane was set to 5 µm. Images were acquired using two light sheets with 100% laser power, 686 ms of camera exposure, and 16-bit low noise gain.

2.2 | Data processing

2.2.1 | Image postprocessing

The raw, TIFF-formatted image stacks, exported from the Ultramicroscope, were first segmented manually using the trainable segmentation toolkit ilastik.[31] The binary vessel architecture attained from ilastik in TIFF-stacks was treated with a simple hole-filling algorithm in Matlab to fill hollow vessel segmentations (eg, some large vessels where the fluorescing lumen interior was not filled during segmentation). Finally, all isolated blood voxel bunches which did not exceed a total (six-connected) volume of a sphere with a radius of 20 μm (33 510 μm^3 volume) were eliminated. This step served the purpose of reducing noise and segmentation artifacts in the tissue representation and the 20 μm sphere was an ad hoc parameter based on empirical comparison with different values, starting at 6 μm, which would only eliminate singular or two connected but isolated microscopy voxels at the dataset resolution.

Masks were manually drawn over the image stacks, blinding regions around the respective tissue of interest in each dataset. Tumors were outlined based on our visual perception of abnormal vessel density and heightened tortuosity of the vasculature around the tumor site, indicating vessel recruitment and angiogenesis.[1] From the healthy brain acquisitions, well-imaged regions were outlined by the masks (excluding only the outer cortex due to blurring) and the ventricular system was blinded due to autofluorescence. Each brain hemisphere of the healthy mice was masked and treated independently, providing six tissue sources for healthy virtual voxels. In the following analyses, tissue subvolumes only entirely within the masked regions were considered.

2.2.2 | Data partitioning and automation algorithms

We developed a custom processing pipeline for the segmented ultramicroscopy datasets using Python 3.6 (Python Software Foundation, https://www.python.org/) with MPI parallelization,[32] C++11 with OpenMP multithreading version 3.1 (OpenMP Architecture Review Board, https://www.openmp.org/), Matlab R2017b (Mathworks, Natick, MA), and automation scripts written for the bash shell on unix systems to interact with a cluster workload management system. To accelerate the production of training data for machine learning, a partitioning algorithm was written in Python 3 to overlay the large, arbitrarily masked input stack with a regular grid of chosen 3D dimensions [s_1, s_2, s_3]. From this grid, the algorithm sampled image subvolumes in a parallel manner using multiple compute nodes with distributed memory, conducting off-resonance field calculations based on the contained microvasculature and starting NMR simulations with further parallelization through OpenMP (Figure 1).

To harness the full numerical power of high-performance computing (HPC) clusters, we implemented a hierarchical, three-level parallelization algorithm (Figure 1B) to run on the BwForCluster MLS&WISO Production (see details in the Acknowledgements). A top-level script, the "job distributor", takes a chosen set of segmented microscopy stacks and distributes them across the computational cluster for processing. This is done by invoking the Moab Cluster Suite (Adaptive Computing, Naples, FL) workload scheduling system to employ computational resources as specified by the user, with a variable number of computational nodes and cores for parallel execution on each image stack. If the resources requested exceeded current availability, the job assignments remained in queue until the requested resources per dataset were free.

The Python scripts initialized on each dataset by the workload manager were parallelized through the Message Passing Interface MPI,[32] using Intel MPI with mpi4py[33] on Intel Python 3.6.2 (Intel Corporation, Santa Clara, CA) with GCC 4.8.2 (Red Hat 4.8.2–15) for Linux. The parallel program partitioned each masked microscopy dataset into subvolumes of size [s_1, s_2, s_3]. Upon a successful test for mask coverage, a Matlab script was executed by each worker node on its subvolume to calculate the magnetic field perturbations induced throughout the tissue subvolume by deoxygenated hemoglobin assumed throughout the vasculature. From each side of a subvolume, 50 μm were removed from analysis to eliminate edge effects, while the remaining virtual NMR voxel was used to simulate spin dephasing. The padding with 50 μm of tissue in each direction offered a good trade-off between image data exploitation and local off-resonance integrity, since far-field effects beyond 50 μm were of the order of 1% or less of the influence close to the vessels.

2.2.3 | Numerical simulations of spin dephasing

The procedure used to simulate spin dephasing within a given virtual voxel containing highly resolved vessel structures in 3D, dubbed the Finite Perturber Method (FPM), has been described in detail elsewhere.[34] Briefly, the local Larmor frequency shift Δ (r) caused by a distribution of a magnetically susceptible material in a homogeneous external magnetic field B_0 can be determined by a mathematical convolution of the paramagnetic structure with the dipole field kernel $d(r)$ in 3D:

$$\Delta\ (r) =\ B_0 \cdot \Delta\ (r) * d(r), \quad d(r) = \frac{3\cos^2\ -1}{4\ r^3}$$
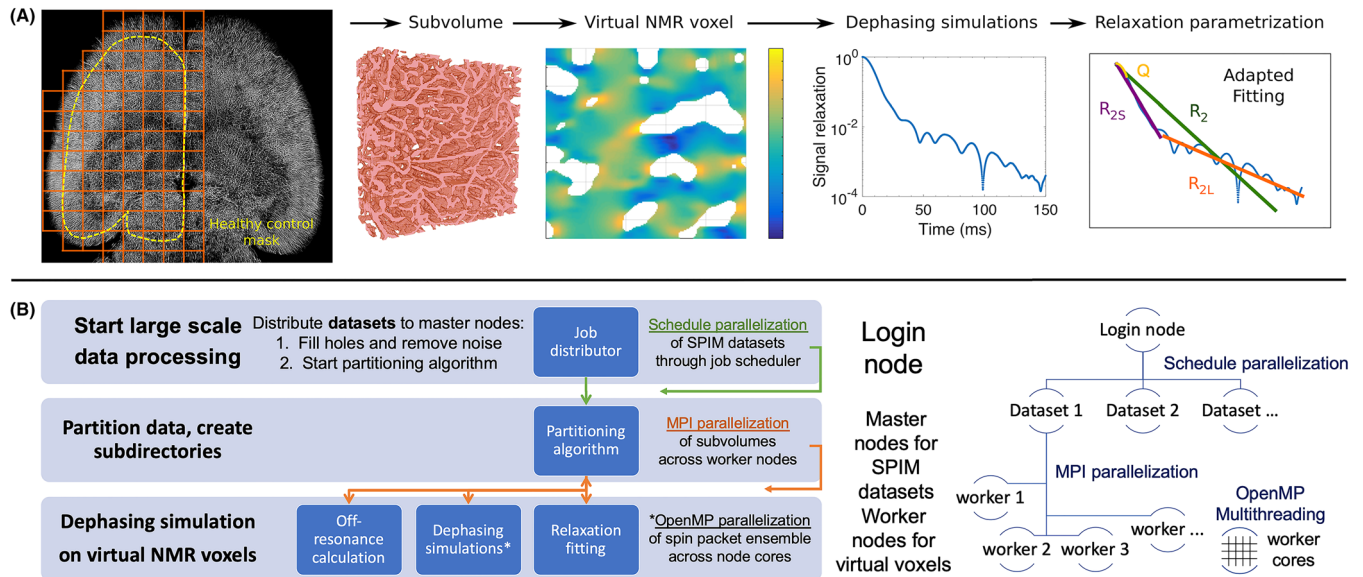
123

(A)

(B)

FIGURE 1 Data partitioning and processing. (A) Schematic flowchart of the numerical processing conducted on masked, segmented ultramicroscopy datasets of 3D vascular structure (left image). Each volume partition of the grid that lies within the mask was modeled as a virtual NMR voxel, containing the known microvasculature. Following a determination of the blood vessel induced off-resonance frequency distribution within the virtual voxel (color-coded in a 2D cut through a cubic voxel with 100 μm side length; third image), the extravascular water proton signal was numerically simulated in FID conditions. The magnetization decay accountable to spin dephasing was parametrized using different fit functions and a differentiation between short- and long-time decay. (B) Schematic presentation of the implemented processing hierarchy. The diagram should be read in rows across the full width of the image from top to bottom. The top level consists of postprocessing the image segmentation and starting the partitioning algorithm on each microscopy dataset. On the computational cluster used, the top-level python script was written to interact with the Moab scheduling system to distribute datasets to be processed across the cluster according to the availability of requested resources (here, referred to as "schedule parallelization"). Using the message passing interface MPI, each dataset was simultaneously treated by independent computational nodes of the network (dubbed "workers"), with over 100 parallel processes per dataset, depending on the cluster exhaustion. On the BwForCluster used here, each worker node controls 16-40 computational cores, which are used through OpenMP multithreading to simulate the magnetization precession during spin packet diffusion

with polar angle of position vector $\boldsymbol{r}$ to the external field orientation. In this relation, which can be derived using classical magnetostatics,[35] the perturber is described by the spatial distribution of the magnetic susceptibility difference $\Delta\chi = \Delta\chi_0(1 - Y)$Hct to the extravascular tissue, with blood oxygen saturation Y [0 : 1], hematocrit Hct, and susceptibility difference $\Delta\chi_0$ between fully oxygenated and deoxygenated blood.

The discrete 3D convolution was implemented in a computationally efficient way, making use of the Fourier convolution theorem.[36] Accordingly, the above computation can be carried out as an entry-wise 3D matrix product in the spatial frequency domain, followed by an inverse Fourier transformation:

$$\Delta\omega(\boldsymbol{r}) = \gamma B_0 \cdot F^{-1}\{F\{\Delta\chi(\boldsymbol{r})\} \cdot F\{d(\boldsymbol{r})\}\}.$$

This was implemented with discrete Fast Fourier Transformations in Matlab, taking into account the anisotropic imaging resolution from ultramicroscopy. The characteristic off-resonance frequency $\delta\omega_0 = \gamma B_0\Delta\chi$ was set to $\delta\omega_0 = 500$ rad/s^{-1}, corresponding to an average blood oxygenation of $Y \approx 0.6$ with Hct ≈ 0.4 and field strength $B_0 = 7$ T. The blood composition was simplified with constant values and the external magnetic field B_0 was simulated longitudinal to the forward-facing mouse, as would be the case in a standard animal scanner. Virtual voxels for simulation were sampled from all over the brain, except for the outer cortex due to image blurring at the boundaries. Under inclusion of the capillary bed, which generally does not exhibit orientation anisotropy in brain tissue, vessel orientations are assumed to be uniformly distributed within the virtual voxels.

The magnetization evolution in the extravascular tissue compartment was simulated following an ideal excitation pulse, producing fully in-phase transverse magnetization across the NMR voxel at $t = 0$. The phase evolution of virtual spin packets placed randomly throughout the tissue was simulated in the rotating frame of $\omega_0 = \gamma B_0$, based on the local off-resonance frequencies $\Delta\omega(\boldsymbol{r})$ encountered during a 3D discrete-time, continuous-space random walk with tunable time steps and Gaussian distributed step size to model water diffusion. This random-walk implementation was motivated by the Bloch–Torrey equation, which governs the NMR signal evolution with proton diffusion effects.[37] In our simulations, the vessels acted as impermeable diffusion barriers toward the virtual spin packets and we omitted longitudinal relaxation with T_1, as well as intrinsic spin–spin relaxation in order to focus on dephasing effects from the Larmor frequency distribution

(*r*) and avoid introducing possibly biasing ad hoc relaxation rates for the different tissue types. It has been shown that the intravascular signal decays relatively fast,[38,39] and cerebral blood volume ratios below 10%[25] yield accordingly low signal contributions even in the short-time regime, thus an exclusion of its contribution was considered acceptable in this proof-of-concept. Our numerical implementation was realized in C++ with OpenMP multithreading to simulate multiple spin packets in parallel, using an arbitrary number of processes which is adjustable to hardware capabilities.

The simulation results were validated on a cylindrical vessel model with known closed-form solution for the signal decay $M(t)$ including diffusion effects.[19] Our simulations reproduced the theoretically expected dephasing effects from different model geometries with very high accuracy (see Figure S1). The simulation parameters set in this study were as follows: virtual voxel sizes in {100 μm, 200 μm, 300 μm, 400 μm} with 50 μm excess tissue to each cubic side to avoid voxel boundary effects (with no overlap between neighboring subvolumes) were sampled from a grid over the imaged, masked tissue in random order; mean extravascular spin packet density of 4 μm^{-3}; water proton diffusion coefficient $D = 1$ μm^2/ms; diffusion time step $t = 0.1$ ms; simulation time $t = 1$ second; resolution of grid with calculated field distortion: 3.25 x 3.25 x 5 μm^3, with trilinear interpolation between grid points; independent pseudo-random diffusion steps generated using the C++11 Mersenne-Twister random number engine mt19937_64 with system time seed and thread-dependent offset. The random numbers generated for different spin packet subsets during OpenMP parallelization were tested successfully to be independent.

2.2.4 | Parametrization of dephasing relaxation

The two transverse components of the integral magnetization from each virtual voxel were saved in text files for the time series simulated. Different levels of Rician noise[40] were imposed on the signal $M(t)$, defined with respect to the maximum signal magnitude $M(t = 0) = M_0 = 1$, by adding independent Gaussian noise to the real and imaginary magnetization components with signal-to-noise ratios SNR = {2, 4, 10, 50, 100, 300, 500} prior to calculating the signal magnitude. The noisy magnetization decays were parametrized using scalar fit variables, attained through linear least squares fits to the natural logarithm of the simulated signal magnitude. The different fit functions and their corresponding variables are summarized in Table 1. The biexponential fit, which assumes the form $M(t) = A_1\exp(-B_1t)+A_2\exp(-B_2t)$, was conducted through mixed linear and nonlinear optimization, using a Matlab implementation of the Nelder–Mead simplex[41] to minimize the sum of squared logarithmic errors for the decay rates (with initial values $B_1 = 1$ ms^{-1}, $B_2 = 0$) and linear least squares fitting for the amplitudes A_1 and A_2. For each fit parameter, a goodness of fit variable was saved as a feature as well to consider the conformity of each decay with certain functional types, including piecewise fits with different short- and long-time signal forms.

The number of spin packets composing the signal evolution in each simulation was of the order of 10^6-10^8 per virtual voxel, depending on its dimensions. While dephasing was simulated over the duration of 1 second, a numerical noise regime was reached at some point, where the residual signal, typically with a magnitude of below 10^{-3}·M_0, would exhibit brief drops to below 10^{-5}·M_0 with fast rephasing back to around 10^{-3}·M_0 and strong volatility with values in between (see Figure S2). Prior to adding Rician noise and fitting, the beginning of this numerical noise regime was automatically determined for each simulated decay using a custom-written routine in Matlab. Specifically, a numerical finite difference differentiation of $\log_{10}(-\ln M(t))$ vs. $\log_{10}(t)$ with signal magnitude $M(t)$ and time t was conducted on consecutive time steps (see Figure S2 for details):

$$b(t) = \frac{\log_{10}[-\ln[M(t+t)]] - \log_{10}[-\ln[M(t)]]}{\log_{10}[t+t] - \log_{10}[t]},$$

TABLE 1 Dephasing relaxation parametrizations. Different fit models and associated dephasing relaxation parameters serving as scalar features for SVM classification . For each fit function, the time ranges it was applied to are specified in the third column, where "full time range" refers to the dephasing signal up to the beginning of the numerical noise regime, "short time" denotes the short-time signal, and "long time" the signal range between the short-time limit and the numerical noise regime. Multiple time range specifications mean that a fit model was applied to different ranges individually. The sum of squared errors (SSE) was determined over the respective time range and the fit error (FE) quantifies the half width of the 95% confidence interval on the respective fit parameters.

Fit model	Dephasing parameters	Time regime
$M(t) = \exp(-R_2t)$	$R_2, T_2 = 1/R_2$, SSE, FE	Full-time range
$M(t) = \exp(-Qt^2)$	Q, SSE, FE	Short time, full range
$M(t) = \exp(-R_{2L}t - P_L)$	R_{2L}, P_L, SSE	Long time
$M(t) = \exp(-at^b)$	a, b, SSE	Short time, long time
$M(t) = A_1\exp(-B_1t) + A_2\exp(-B_2t)$	A_1, B_1, A_2, B_2	Long time

and with respect to the first signal time point M(t) = t = 0.1 ms:

$$b'(t) = \frac{\log_{10}[-\ln[M(t)]] - \log_{10}[-\ln[M(\ t)]]}{\log_{10}[t] - \log_{10}[\ t]}.$$

This yielded the time-dependent exponents $b(t)$ and $b'(t)$ for t in milliseconds, under the assumption of $M(t) = \exp(-at^b)$. The exponent $b(t)$ was averaged over a symmetric sliding window with a width of 20.1 ms for the sliding mean $\bar{b}(t)$. The variance of $b(t)$ with respect to the sliding average was calculated with $\mathrm{var}(b) = (b(t) - \bar{b}(t))^2$ and again smoothed with a 20.1 ms sliding window mean for $\overline{\mathrm{var}}(b)$. Empirically, it was found that the first incidence of $\overline{\mathrm{var}}(b) \geq 50$ reliably determined the beginning of the noise regime, while higher thresholds would result in later signal truncation (see Figure S2). This ad hoc method was developed to avoid truncating signals too early, eg, when such noise may be superimposed on a signal which is still decaying with meaningful information. In experimental MRI, this procedure is typically replaced by considering SNR thresholds.

In prior theoretical studies,[15,42,43] where the dephasing influence of spheroidal and cylindrical, paramagnetic inclusions was treated analytically, it was shown that the dephasing attenuation in such systems can generally be divided into a short-time regime with Gaussian decay form, $M(t) = \exp(-Qt^2)$, and a long-time regime with approximately Lorentzian behavior; $M(t) = \exp(-R_{2L}t)$. By parametrizing the signal with $M(t) = \exp(-at^b)$, the exponent $b(t)$ was thus used to determine the end of the short-time regime for each signal. Indeed, the finite difference quotients initially yielded $b = 2$ for all simulated signals, with different rates and forms of decrease (see Figure S2b,f). For $b(t)$ from numerical differentiation on consecutive time steps, the threshold marking the end of the short-time regime was empirically chosen at $b_t = 1.7$. An analogous exponent $b'(t)$ was calculated through finite difference quotients of the signal with respect to the first time step $t = 0.1$ ms, with a threshold at $b'_t = 1.9$. The two threshold-passing time points were averaged to result in a robust assessment of the transition from short- to long-time regime, which was tested empirically on a large set of randomly sampled signals from all tissue types (see Figure S3).

2.3 | Machine learning using support vector machines

We used the LibSVM library[44] with Python 3.6.1 to train SVM classifiers on the numerical NMR data. The spin-dephasing features of each virtual voxel (see Table 1) were scaled for SVM training using svm-scale. A C-support vector classifier was used to divide the input data into two classes through a hyperplane in the higher dimensional kernel image space. In an a priori test using linear and radial basis function (RBF) kernels, the RBF was determined to be the better performing transformation for the problem at hand. The grid search function, included with LibSVM, was implemented into the custom training algorithm using Python 3 to identify optimal SVM parameters on each training set prior to training on the entire set. We used 3-fold cross-validation on the training data during the grid search to optimize C $\{2^x\}$ with x between -5 and 15 in steps of 2 and $\{2^y\}$ with y between -15 and 3 in steps of 2. Signals for subsequent prediction testing were excluded from the parameter optimization.

SVM training and testing were conducted on different, independent subsets of virtual NMR voxels to produce so-called learning curves, which portray the prediction accuracy (percentage of correct NMR decay classifications) of a classifier on previously blinded signals, depending on the number of training voxels used (see Table 2 for training set sizes). In any case, all training was performed on balanced datasets with equal

TABLE 2 Simulated signal contributions from imaged datasets. For every virtual voxel size (VVS, cubic voxels with side lengths of 100-400 μm), the number of virtual voxels extracted from each tumor-bearing mouse is presented. The first value in the second column is the number of U87 tumor signals per mouse and the second value is the analogous quantity from mice with a GL261 tumor. The numbers are relatively small because balanced sets were ensured, such that each mouse contributed equally to training. In any case, the number of contributed tumor signals per mouse was matched with equal contributions from each healthy brain hemisphere. Since GL261 tumors were small compared with the U87 specimens, for large virtual voxels (300 and 400 μm side length), all simulated signals from GL261 tumors were included (a total of 13 signals from 400 μm voxels and 53 signals from 300 μm voxels) and matched with an equal number of healthy tissue signals for training. In these cases, predictions were tested on unbalanced datasets, mainly consisting of healthy tissue signals. The third column details the number of training signals used to generate learning curves. Different stages of the learning curves are divided by vertical lines; and, for each stage, the first training set size s_b, the increment s_d, and the last training set size s_e, are given in the form s_b:s_d:s_e. In any case, the training sets consisted of an equal number of signals from tumors and healthy tissue.

VVS (μm)	Virtual voxels per mouse (U87/GL261)	Balanced training set sizes for learning curve generation (U87/GL261)
100	300/90	2:4:98|100:8:260|280:20:600|650:50:1000|1100:100:3000/
		2:4:98|100:8:260|280:20:600|650:50:900
200	60/17	2:4:98|100:8:260|280:20:600|2:4:98|106:8:170
300	15/all (53 total)	2:4:98|100:8:260/2:4:106
400	5/all (13 total)	2:4:50/2:2:26

contributions from each tissue group (healthy brain tissue and tumors). In the U87 tumor study, all training and prediction sets also consisted of equal contributions from each mouse. For the smaller GL261 tumors, all available signals were used in the cases of 300 and 400 μm virtual voxel side length (VVS), while training sets were still ensured to be group-balanced (see Table 2 for details).

2.4 | Statistical analysis

For U87 tumor classifications, training was conducted on different subsets of signals from, respectively, five animals with prediction testing exclusively on the signals from the sixth, previously blinded, mouse. This was done, respectively, six times with different pairs of healthy and tumor-bearing mice for prediction, such that each imaged mouse would be isolated for prediction once. For each of these learning curves, different random permutations of the training signals were used to produce individual learning curve instances, which were averaged to yield results unbiased of the training signal order. To keep computational expense feasible, the number of random training set permutations was varied for different virtual voxel sizes: 100 permutations for VVS = 400 μm, 10 permutations for VVS = 300 μm, three permutations for VVS = 200 μm, and one permutation for VVS = 100 μm.

For GL261 tumor signal classifications, the procedure was analogous to the U87 tumor model for VVS = 100 and 200 μm. Due to smaller tumor sizes, for VVS = 300 and 400 μm, all available virtual voxels were used from GL261 tumors, matched with an equal number of healthy training signals for each training epoch, and predictions were conducted on the residual signals not used for training. While training sets were always balanced, prediction sets were dominated by healthy signals during GL261 tumor classification with VVS of 300 and 400 μm. In the other cases, where prediction sets were also balanced with equal signal contributions from tumors and healthy tissue, learning curves were also produced exclusively from classification testing on these individual groups. In these cases, training was conducted using five mice from each group with prediction tests on signals exclusively from the remaining healthy or tumor-bearing mouse, separately. As before, the prediction specimens were permuted so that each imaged mouse was subject to exclusive prediction testing once.

3 | RESULTS

3.1 | Classification of dephasing in U87 tumor tissue using all FID parametrizations

SVM classifiers were trained on randomly sampled signals from five U87 tumors and five healthy brain hemispheres, using the full set of FID features listed in Table 1. Classifiers were tested on the simulated signals of the remaining mouse, with six permutations such that each mouse was excluded once for prediction testing (see Figures S4-S7). The permutation-averaged results from training and prediction testing with different SNR levels on the simulated dephasing signals are presented in Figure 2, with predictions on balanced sets, as well as signals exclusively from U87 glioblastoma or healthy brain tissue. The learning processes, results and accuracies presented in the following are fully reproducible.

The learning curves in Figure 2 indicate that robust classifiers can be trained for the tumor classification problem based on the dephasing features. Especially with higher training data availability, the learning curves presented continuously rising prediction accuracies with little volatility for minor training set changes. With sufficient amounts of training data, classification accuracies were also relatively stable under random permutations of the training signal order (see Figures S4-S7). When permuting the imaged animals exclusively used for prediction testing, stronger variability was observed, which is certainly influenced by imaging and segmentation differences between mice, as well as the origin and placement of the virtual NMR voxels used for training (more details in the Discussion).

Using all dephasing parametrizations from Table 1, stable prediction accuracies of 70%-80% could be maintained in predictions on separately imaged and segmented datasets of mice which were completely excluded from any training. The classifiers were very robust against noisy NMR data, performing well even with high levels of noise superimposed on the dephasing signal. At the lowest signal-to-noise ratio of SNR = 2, the average prediction accuracy in the stable regime suffered only by around 5%-10% compared with the noise-free signal (Figure 2).

With balanced prediction sets from healthy and pathological tissue, classification accuracies of 70%-75% were reached as of ~ 300-800 training signals from virtual voxels with side length VVS = 100 μm, depending on the noise level in the NMR data. For VVS = 200 μm, a minimum of 600 training signals sufficed. Despite much more limited training sets, larger voxels with VVS = 300 μm granted prediction accuracies of 75% above ~ 100 training signals and similar values were attained from VVS = 400 μm above 40 training instances (20 signals from healthy brains and 20 from glioblastoma tissue, ie, four simulated dephasing processes from each training mouse). Our results suggest that, for this tissue classification problem and the range of voxel sizes probed, larger NMR voxels grant higher classification success with less training data.

Prediction tests conducted exclusively on healthy or tumor-born signals, individually, show that the classification accuracy on healthy test signals is higher than on tumor signals for all voxel sizes (Figure 2, second and third columns). With increasing training set sizes, tumor tissue
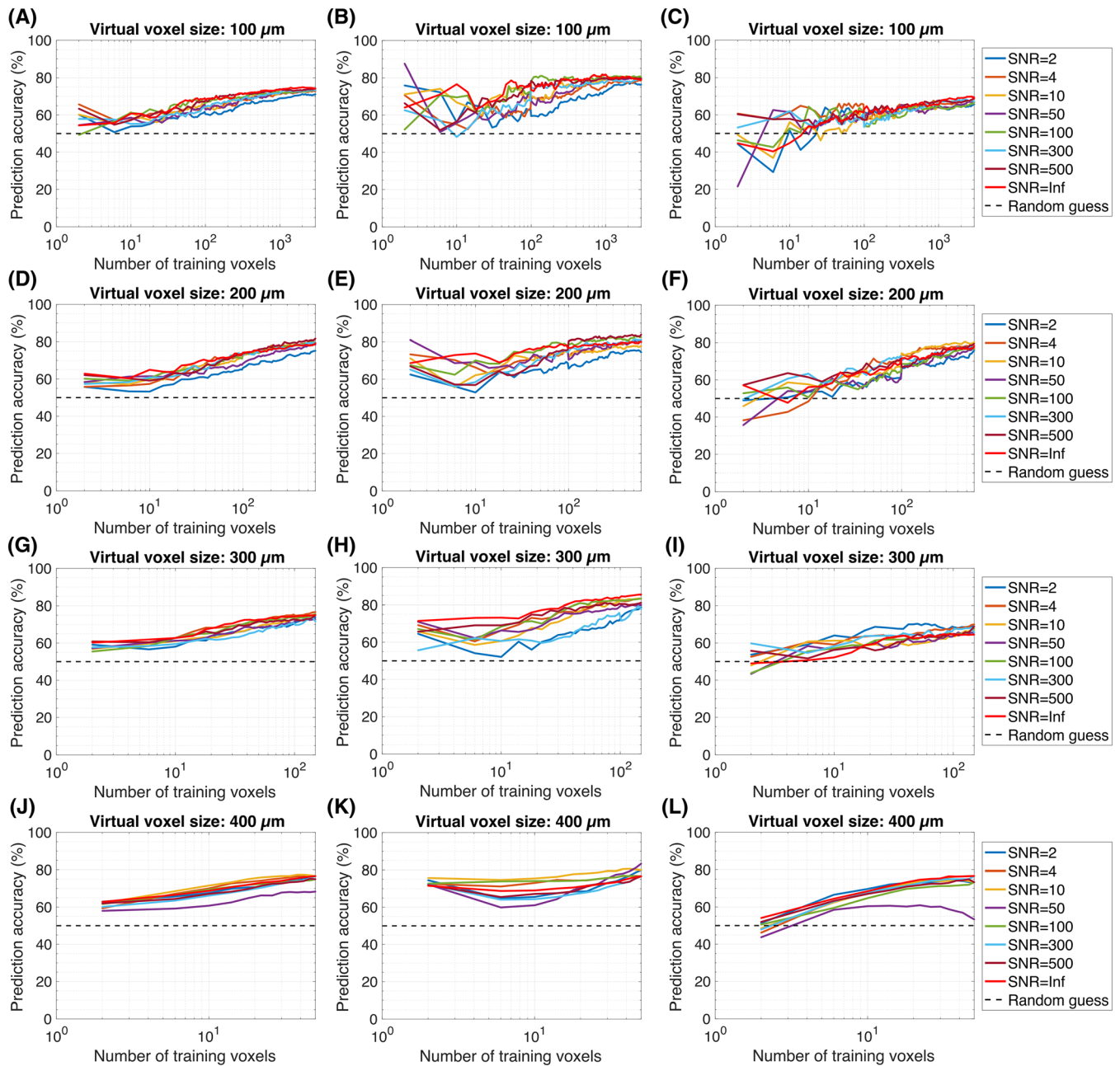
FIGURE 2 Learning curves with different virtual voxel sizes and noise levels from classifications of healthy tissue vs. U87 glioblastoma using the entire set of dephasing parametrizations. Plots presenting the mean prediction accuracy of grid-search optimized classifiers, achieved by training with virtual voxel subsets from, respectively, n = 5 healthy brain hemispheres and U87 tumors at virtual voxel sizes of 100 (A-C), 200 (D-F), 300 (G-I) and 400 μm (J-L), using all fit parameters listed in Table 1 as signal features. The prediction accuracy was plotted on the y-axis against the number of training voxels on logarithmic x-axes. All plotted learning curves are averages from different permutations of prediction testing animals and training subsets (see Figures S4-S7). All learning curve points, including the individual permutation cases, were created from balanced training and prediction sets with equal contributions from glioblastoma and healthy brain voxels. The left column presents the mean prediction accuracy on such balanced datasets. The center column depicts the prediction accuracies of classifiers tested exclusively on healthy voxel signals, while the right column shows the analogy for virtual voxels extracted exclusively from U87 tumor tissue. In all scenarios, training sets were balanced. For comparison, the classification accuracy of random guessing was plotted at 50%

prediction accuracies caught up to the healthy tissue rates and partly surpassed the latter, depending on the noise level included in the signals. With sufficient training signals, the classification accuracies became approximately equal. The virtual voxel signals with VVS = 300 μm preserved considerably lower classification specificity on tumor voxels throughout the entire training range, indicating that a stable classification regime was not reached with the limited training set of at most 150 simulated signals.

3.2 | Classification of dephasing in U87 tumors with a sparse FID parametrization

The above training and prediction scenarios were repeated with a subset of FID features, which were found to fit the simulated signals well with a small set of parameters; the Gaussian decay rate Q in the short-time limit and the biexponential fit parameters A_1, A_2, B_1, and B_2 in the long-time regime (see Table 1 and Figure S3). Posing a set of fit variables which can be determined when the dephasing process is superimposed with intrinsic spin–spin relaxation (a mono-exponential decay), these variables offer an efficient parametrization which could be applied to experimentally sampled T_2^* decay (FID-like NMR measurements).

Compared with the above results from training with the full set of parameters in Table 1, classification accuracies were much more sensitive to Rician NMR noise in this case (see Figure 3). For good signal-to-noise ratios of SNR ≥ 100, defined with respect to the maximum signal intensity $M(t = 0)$, prediction accuracies generally behaved more favorably than before, reaching higher values with less training data and more similar specificity for both tissue groups. For all virtual voxel dimensions, mean prediction accuracies around 80% were reached with the small animal cohort included in this study. Higher noise levels with SNR ≤ 50 resulted in dramatically lowered classification accuracies and more volatility in the learning curves. High noise levels paired with too little training data tended to result in a classification bias towards healthy signals, leading to increased prediction accuracies on healthy brain voxels and high rates of misclassification on tumor signals, whereas this bias was sometimes opposite for extreme noise levels (cf. Figure 3, central and right columns), yielding generally unreliable predictions.

3.3 | Classification of dephasing in GL261 tumors

The microscopy data from mice with GL261 glioblastoma yielded smaller tumor samples, so the predictions on 300 and 400 μm voxels were made on unbalanced datasets with more virtual voxels from healthy tissue for prediction testing. For smaller virtual voxels, prediction sets also contained equal group contributions from animals excluded from training. For 300 and 400 μm NMR voxels, all available NMR decays were used from each mouse (varying between animals), but care was taken to use only balanced training sets from GL261 tumors and healthy brain tissue. In these cases, at each stage, classifiers were tested on the remaining signals not used for training. The classification performance on datasets including at least one virtual voxel from each tissue group is presented in Figure 4.

The learning curves attained in the tumor classification problem with GL261 gliomas resembled their analogies from U87 tumors for small virtual voxels with VVS of 100 and 200 μm. Again, the classification using all relaxation parametrizations in Table 1 was more robust against low SNR (see Figure 4). Training classifiers with only the short-time Gaussian decay rate Q and biexponential fit parameters was also much more prone to noise in this case, whereas the prediction accuracy on tumor signals was affected more dramatically (cf. Figure 5). Noise levels with SNR = 4-10 introduced a bias in the classification towards healthy signals, enhancing the true positive rate on healthy virtual voxels to over 95%, while tumor-intrinsic signals were correctly classified at a mean rate of around 30% with SNR = 4 and accuracies around or above 50% for SNR = 2. For sufficient training set sizes, the bias towards healthy classifications decreases for SNR ≥ 10, yielding similar specificity on healthy and pathological signals.

Classifier performance exceeded the previous study case with signals from U87 glioblastoma, reaching 80%-90% on GL261 data using all FID features. Similar performance was achieved using the sparse parametrization with Gaussian and biexponential fits for sufficient SNR ≥ 100 (see Figures 4 and 5). With very limited training data availability for large NMR voxels with VVS of 300 and 400 μm, the classification bias in favor of healthy signals dominated most of the tested range (see Figures 4 and 5, G-L). Again, the full set of dephasing parameters facilitated faster convergence of learning curves with different SNR, but a stable prediction regime could not be reached with the available data. Overall, the results of the GL261 tumor classification study support the previously motivated hypothesis that larger NMR voxels emphasize the dephasing differences induced by angiogenesis and vascular remodeling in the brain, enabling more reliable signal classifications on individual NMR voxels.

4 | DISCUSSION

The successful proof-of-principle presented in this study indicates that it is possible to achieve a learning of abstract endogenous contrast tied to a tissue type classification for brain tumors. The developed processing pipeline can be used to classify arbitrary tissue types, including vessel structures from different organs and pathologies. As this decade represents the true advent of ultramicroscopy, the availability of high-resolution vessel acquisitions is expected to become more relevant in coming years. The toolbox introduced in this work can be applied to a range of biological systems to test the theoretical feasibility of achieving a signal classification based on tailored MRI sequences, and further to optimize such sequences for certain classification tasks.

Our results provide strong evidence that the NMR voxel size has a considerable impact on the capabilities of a classifier, since different vessel remodeling effects can be more pronounced on characteristic length scales. The voxel size influenced the behavior of our classifiers for small training sets, as well as the slope of the learning curves, their speed of convergence, and presumably the maximum possible
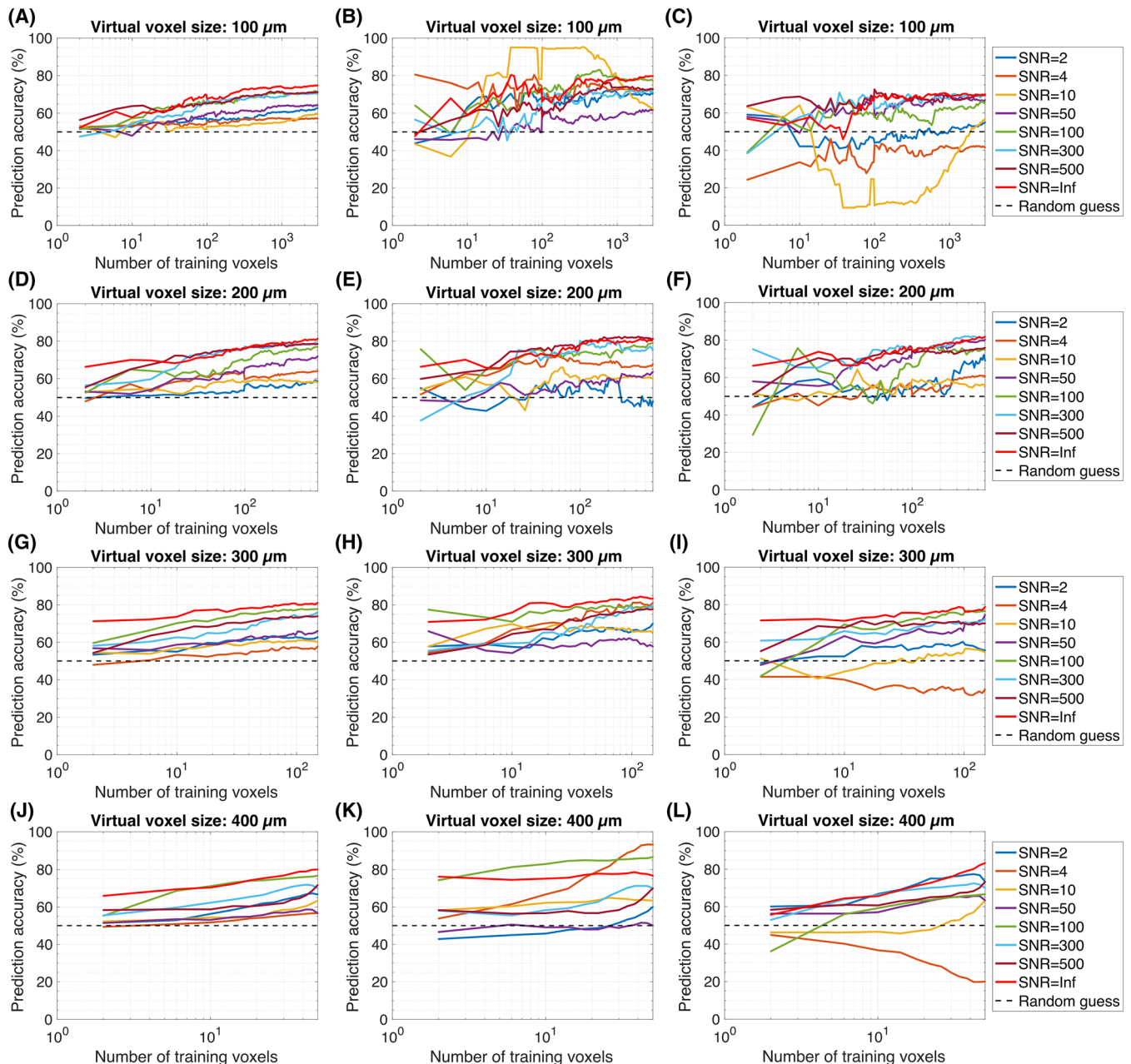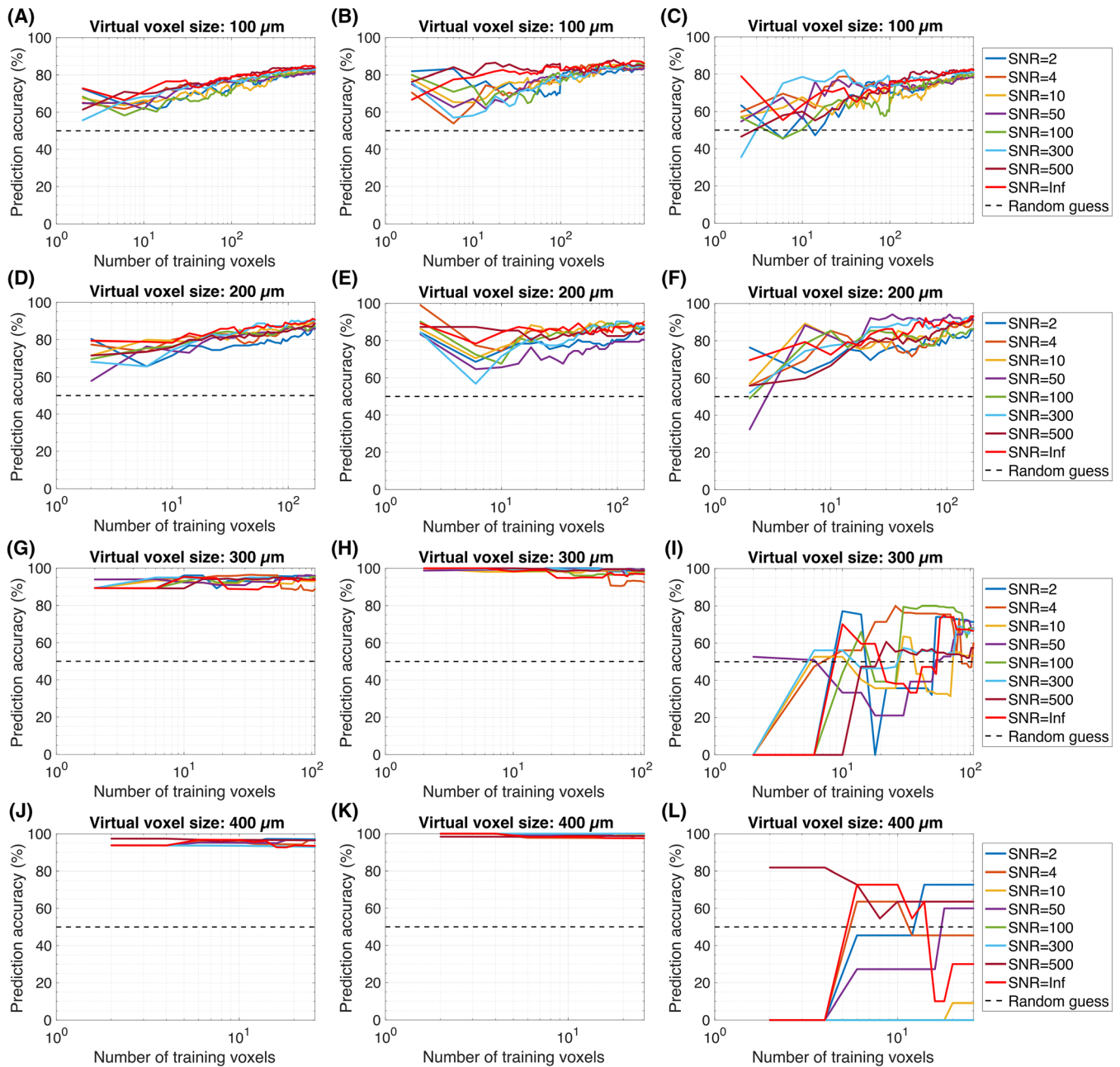
FIGURE 3 Learning curves with different virtual voxel sizes and noise levels from classification of healthy tissue vs. U87 glioblastoma using a sparse set of five dephasing parameters. Plots depicting the mean prediction accuracy of grid-search optimized classifiers, achieved by training with virtual voxel subsets from, respectively, $n = 5$ healthy brain hemispheres and U87 tumors at virtual voxel sizes of 100 (A-C), 200 (D-F), 300 (G-I) and 400 μm (J-L), using only the short-time Gaussian decay rate and the parameters from long-time biexponential fits as signal features. The mean prediction accuracy was plotted on the y-axis against the number of training voxels on logarithmic x-axes. All curves represent averages from different permutations of prediction testing animals and training subsets (Figures S4-S7). Every individual learning curve point was attained from balanced training and prediction sets with equal contributions from glioblastoma and healthy brain voxels. The left column presents the mean prediction accuracy on mixed testing datasets. The center column depicts the prediction accuracies of classifiers tested exclusively on healthy voxel signals and the right column shows the prediction accuracy on virtual voxels extracted exclusively from U87 tumor tissue. In all scenarios, training sets were balanced. For comparison, the classification accuracy of a random classifier was plotted at 50% prediction accuracy. Our initial results suggest that high resolutions may be counterproductive for tumor signal classifications of this kind. In proceeding studies, the generalizability of trained classifiers will be tested, eg, by training and testing with different virtual voxel dimensions. With a growing amount of data for training, as well as further tuning of the voxel dimensions and relaxation parametrization, the capabilities of support vector machines for voxel-by-voxel MRI classifications yet remain to be discovered. This numerical study with a small cohort of 15 mice strongly motivates further microscopic acquisitions to increase the amount of available training data, include further tumor models, and conduct more powerful statistical analyses.
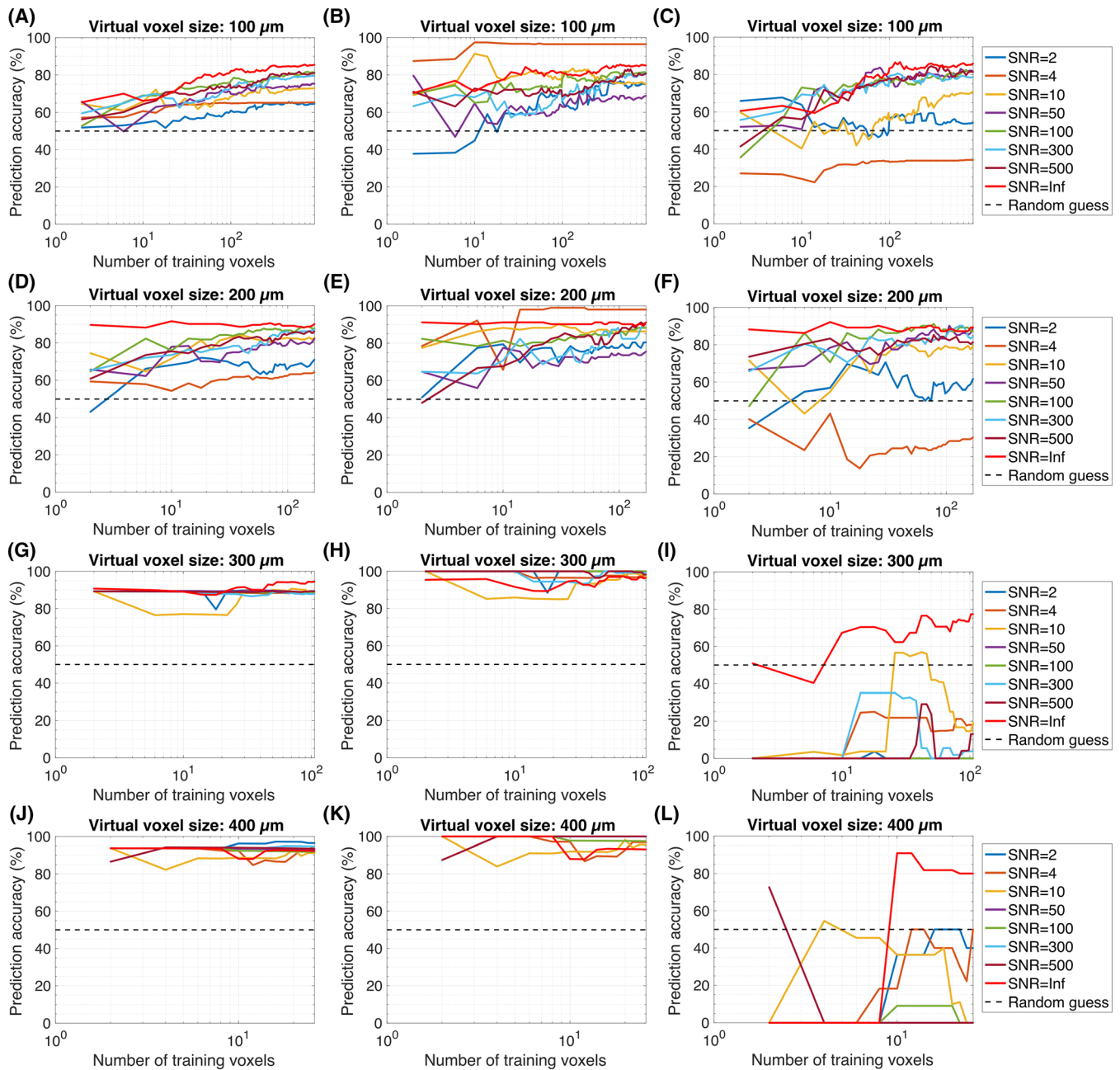
FIGURE 4 Learning curves with different virtual voxel sizes and noise levels for the classification of healthy tissue vs. GL261 glioblastoma using the entire set of dephasing parametrizations. Plots presenting the mean prediction accuracy of grid-search optimized classifiers at virtual voxel sizes of 100 (A-C), 200 (D-F), 300 (G-I) and 400 μm (J-L), using all fit parameters listed in Table 1 as relaxation features. The prediction accuracy was plotted on the y-axis against the number of training voxels on logarithmic x-axes. For virtual voxel side lengths VVS = 100 and 200 μm, training was conducted with virtual voxel subsets from, respectively, n = 5 healthy brain hemispheres and GL261 tumors with balanced training and testing datasets. Larger virtual voxels yielded too little data for balanced prediction sets, therefore training was always conducted with an equal number of healthy and pathological signals, while predictions were tested on predominantly healthy voxels. The left column shows mean prediction accuracies on mixed sets of virtual voxels from tumors and healthy tissue. The center column presents prediction accuracies of classifiers tested exclusively on healthy voxel signals and the right column shows the analogy for virtual voxels extracted exclusively from GL261 tumors. For orientation, the classification accuracy from random guessing was plotted at 50%

The classification accuracies in our study show potential for further improvement through higher training set sizes, signaled by the continuous rising trends, observed in learning curves with sufficient signal SNR. Our results from training and testing classifiers on noisy dephasing data revealed that distinct relaxation parametrizations exhibit different stability against noise. Favorable goodness of fit does not guarantee robust classification in this case. An extensive statistical study of sensible dephasing parametrizations and combinations thereof go beyond the scope of this introductory proof-of-principle, but will be the subject of future considerations aiming at conducting automated dimensionality reductions on

FIGURE 5 Learning curves with different virtual voxel sizes and noise levels for the classification of healthy tissue vs. GL261 glioblastoma using the sparse set of relaxation parametrizations. Plots presenting the mean prediction accuracy of grid-search optimized classifiers at virtual voxel sizes of 100 (A-C), 200 (D-F), 300 (G-I) and 400 μm (J-L), using the short-time Gaussian decay rate and long-time biexponential fit parameters as relaxation features. The prediction accuracy was plotted on the y-axis against the number of training voxels on logarithmic x-axes. For virtual voxel sizes VVS = 100 and 200 μm, training was conducted with virtual voxel subsets from, respectively, n = 5 healthy brain hemispheres and GL261 tumors with balanced training and testing sets. Larger virtual voxels delivered too little data for balanced prediction sets, therefore training was always conducted with an equal number of healthy and pathological signals, while predictions were tested on predominantly healthy voxels. The left column shows mean prediction accuracies on mixed sets of simulated signals from tumors and healthy tissue. The center column presents prediction accuracies on exclusively healthy voxel signals and the right column shows the analogy for virtual voxels from GL261 tumor tissue. The classification accuracy of random guessing was plotted at 50%

NMR feature sets for such classification tasks to ultimately optimize experimental sequence designs for analogous real-life measurements. With dephasing during FID-like measurements as a starting point, MRI acquisition techniques, sampling densities, and relevant echo time regimes are design parameters which can be optimized to facilitate reliable signal fits for the relaxation parameters deemed most relevant for a classification task. The developed software framework allows for effortless extensions to different sequence types, incorporating, eg, spin echoes, steady-state free precession, diffusion weighting, or dynamic susceptibility measurements.

The simulation framework can be extended for biophysical aspects of physiological processes and the in vivo tissue microenvironment. This includes, eg, blood flow and hemodynamics, oxygen transport and diffusion, vessel permeability, metabolic demands and interactions, and other physiological aspects affecting blood susceptibility and extravascular water diffusion.[5,45–47] In this initial study, we simplified the blood oxygenation to be constant throughout the vasculature; a common practice in MR-focused biophysical modeling of microvascular networks.[21,48,49] To keep the systematic bias between healthy and tumor-intrinsic tissue voxels minimal and avoid introducing errors from false biological assumptions or inadequate modeling, the oxygenation and other blood properties were set equal for both tissue types. In reality, not only the vascular geometry and topological connectivity in these tumor models are distinct in comparison with healthy cerebrovasculature,[25] but so are the associated hemorheology, vessel lumen characteristics, and blood oxygen saturations, exhibiting local hypoxia and necrosis.[50–53] Such differences are expected to translate to spin dephasing and amplify classification accuracies further, since comparable conditions are not present in the healthy brain.

In this proof-of-concept study, we aimed at making minimal ad hoc assumptions about the physiology and, instead, focused on the ubiquitous differences in local vessel geometry, which are temporally constant throughout an MRI acquisition. We therefore used equal blood composition and oxygen saturations throughout all simulations. In experimental MRI acquisitions, the vessel susceptibility can be controlled through gas inhalation or the injection of (super-) paramagnetic contrast agents, such as SPIONs or gadolinium chelates.[13,14] Such intravascular contrast agents dramatically increase the vessel susceptibility, by far outweighing blood oxygenation-dependent effects, which in turn negates the impact of local oxygenation variations. Upon the initial bolus wash-in, the vessel susceptibility can be considered approximately constant over the dimensions of an MRI voxel on the timescale of an acquisition. Thus, if desired, the constant vessel susceptibility can be approximated in experimental settings. A change of diffusion regime through higher blood susceptibility should be considered in the numerical simulation settings, possibly justifying a static dephasing approximation,[15] which is computationally far more efficient.

We have modeled a simplified biological environment that includes vessel-specific magnetic susceptibility and diffusion effects in the extravascular space. Intravascular blood water signal was omitted in this study due to weak signal contributions, low blood volume ratio, and flow effects of excited spins through each virtual voxel, which cannot be modeled in our framework with missing hemodynamics. In realistic MRI, the entire biological system is present, there are hardware imperfections, and the signal decay is overlaid with longitudinal T_1 and intrinsic spin–spin relaxation. Nonetheless, a study isolating the vessel-specific effects, which can be substantial in realistic NMR experiments, was necessary to challenge the sheer possibility of such a signal classification in an optimal environment. The developed framework can also be used to model exogenous, intravascular susceptibility contrast agents, which can be used to amplify the vessel-induced dephasing effects.

To improve the depiction of realistic biological and experimental settings, the simulation algorithms can be augmented with further features, eg, by considering longitudinal relaxation and more realistic, locally varying blood compositions, as well as the intravascular blood water signal. The intravascular blood oxygenation can be approximated numerically using blood flow simulations with suitable boundary conditions,[54,55] or determined experimentally within smaller tissue sections, eg, through spectral contrast optical coherence tomography angiography[56] or by using custom experimental setups.[57] Generally, different microscopic imaging modalities offering higher resolutions and/or spatial isotropy should prove beneficial for the classification quality.

Healthy brain tissue is known to present higher microvascular regularity compared with the highly heterogeneous tumor microenvironment.[6,58] In this study, virtual NMR voxels were sampled randomly from all over the healthy brain, including transition zones between brain regions, white and gray matter. Large cubic subvolumes extracted from the healthy brain included different regions with distinct vasculatures, which are expected to have increased heterogeneity in the healthy signal simulations. The classification accuracy can most likely be improved by training with healthy tissue samples from specific brain regions, with a separate tissue class for voxels overlaying different tissues in boundary regions. This could hypothetically be combined in practice with a class probability type prediction from an independent segmentation algorithm, identifying brain regions based on macroscopic voxel locations a priori. Tissue-specific vascular characteristics, which vary throughout the brain, can be learned in the training process to increase the sensitivity of the classifier to possibly pathological abnormalities.

For each classifier, the misclassification rate of healthy signals can be determined on known tissue samples a priori and modeled as statistical noise in true classification tests. Since every voxel of an MRI acquisition is classified independently, but the misclassification noise should either be randomly spread out or accumulated (eg, at brain region boundaries), an abnormal spatial clustering of pathological classifications could pose a quite reliable tumor identifier if the classification capabilities demonstrated here can be translated to experimental MRI scenarios.

This work served the purpose of conducting proof-of-principle type classification tests without major efforts to explore the vast field of statistical machine learning models possibly suitable for this problem. We used established SVM implementations and settings with a simple, easy-to-manage grid-search optimization of the SVM hyperparameters. Two proven kernel functions, responsible for transforming the input features to a higher-dimensional vector space, were tested here: the RBF and the linear kernel function. Furthermore, only FID-type dephasing was simulated and parametrized with an ad hoc set of 24 scalar features from signal fits. Optimizing and ultimately reducing the feature catalogue to the most relevant and robust parameters has the potential of improving classifiers immensely. Simulations involving advanced MRI sequences, such as spin echo and diffusion-weighted MRI, may also extend the capabilities of this method.

We observed effects of intra- and inter-tumoral heterogeneity when running the learning curve generation with different test animal pairs, as well as random permutations of the balanced training data. High variances of prediction accuracy between training runs with different permutations of training data for small training set sizes are a hallmark of intra-tumor heterogeneity, including hypoxic and well-vascularized regions with angiogenesis. A strong variance of learning curve accuracies when permuting the prediction test animals indicates inter-tumoral differences, but is also affected by imaging and segmentation differences among animals, which could exhibit different artefacts, clearing and imaging quality.

The GL261 glioma could be identified more accurately despite smaller training set sizes. The GL261 model is known to be more angiogenic than U87 representatives,[27] and, although visual evaluations of the U87 capillary network in the image datasets facilitate untroublesome tumor spotting, the automated classification of U87 signals proved to be more difficult. This may be explained by previous results, where it has been shown that the early stage U87 glioma microvasculature resembles healthy brain tissue in some aspects, such as the statistical distribution of distances of extravascular tissue voxels to their nearest blood vessel,[59] which is closely related to the microscopic distribution of off-resonant Larmor frequencies probed in this study.

Our results, from a relatively small animal cohort, affirm the feasibility of constructing reliable NMR voxel classifiers for angiogenic tumors. This motivates analogous test cases in other organs with distinctive vascular pathologies, eg, the heart muscle with cardiomyopathy.[60] Regardless of the application, future studies should focus on ranking the NMR features and investigating their statistical power, robustness against noise, and the role of different relaxation parametrizations for classification problems. Based on their prediction stability for different NMR voxel sizes and noise levels, optimal dephasing parametrizations should be sought for different experimental conditions concerning SNR and resolution. A reliable treatment of this problem demands larger animal cohorts for more statistical power, but in this proof-of-principle, it could be shown that such efforts are worth investing.

In conclusion, we have demonstrated the theoretical feasibility of a voxel-by-voxel type detection of brain tumors based on dephasing-induced transverse relaxation patterns in FID-type NMR experiments. Using numerically simulated signal evolutions on virtual NMR voxels, inter-sample classification accuracies beyond 90% could be achieved with surprisingly small training datasets, with characteristic improvements towards larger voxels. Our results from a cohort of six tissue samples of each type, including two distinct tumor models, strongly motivate further studies in this direction with expanded high-resolution vascular imaging. We have developed a highly scalable numerical toolkit to explore different experimental conditions and MRI sequences in an idealized setting, focused around mesoscopic magnetic susceptibility inclusions within tissue, most prominently embodied by blood vessels. This toolbox can be employed to design optimized MRI sequences with endogenous or exogenous contrast to exclusively sample the information-sensitive imaging parameter space in subsequent experimental acquisitions. If successfully translatable, such tailored acquisitions could be used to train SVM classifiers to detect vascular pathologies and anomalies in real, in vivo MRI measurements based on independent voxel classifications.

ORCID

Artur Hahn https://orcid.org/0000-0002-4493-3887

REFERENCES

1. Carmeliet P, Jain RK. Angiogenesis in cancer and other diseases. *Nature*. 2000;407(6801):249-257.
2. Holash J, Maisonpierre PC, Compton D, et al. Vessel cooption, regression, and growth in tumors mediated by angiopoietins and VEGF. *Science*. 1999;284(80):1994-1998.
3. Carmeliet P, Jain RK. Molecular mechanisms and clinical applications of angiogenesis. *Nature*. 2011;473(7347):298-307.
4. Rieger H, Welter M. Integrative models of vascular remodeling during tumor growth. *Wiley Interdiscip Rev Syst Biol Med*. 2015;7(3):113-129.
5. Rieger H, Fredrich T, Welter M. Physics of the tumor vasculature: Theory and experiment. *Eur Phys J Plus*. 2016;131(2):31.
6. Breckwoldt MO, Bode J, Sahm F, et al. Correlated MRI and ultramicroscopy (MR-UM) of brain tumors reveals vast heterogeneity of tumor infiltration and neoangiogenesis in preclinical models and human disease. *Front Neurosci*. 2019;12:1004.
7. Zhang K, Yun SD, Triphan SMF, et al. Vessel architecture imaging using multiband gradient-echo/spin-echo EPI. *PLoS One*. 2019;14(8):e0220939.

8. Gordon Y, Partovi S, Müller-Eschner M, et al. Dynamic contrast-enhanced magnetic resonance imaging: fundamentals and application to the evaluation of the peripheral perfusion. *Cardiovasc Diagn Ther*. 2014;4(2):147-164.

9. Ogawa S, Lee TM, Kay AR, Tank DW. Brain magnetic resonance imaging with contrast dependent on blood oxygenation. *Proc Natl Acad Sci U S A*. 1990;87(24):9868-9872.

10. Yablonskiy DA, Sukstanskii AL, He X. Blood oxygenation level-dependent (BOLD)-based techniques for the quantification of brain hemodynamic and metabolic properties - theoretical models and experimental approaches. *NMR Biomed*. 2013;26(8):963-986.

11. Jochimsen TH, Möller HE. Increasing specificity in functional magnetic resonance imaging by estimation of vessel size based on changes in blood oxygenation. *Neuroimage*. 2008;40(1):228-236.

12. Shen Y, Pu IM, Ahearn T, Clemence M, Schwarzbauer C. Quantification of venous vessel size in human brain in response to hypercapnia and hyperoxia using magnetic resonance imaging. *Magn Reson Med*. 2013;69(6):1541-1552.

13. Farrar CT, Kamoun WS, Ley CD, et al. In vivo validation of MRI vessel caliber index measurement methods with intravital optical microscopy in a U87 mouse brain tumor model. *Neuro Oncol*. 2010;12(4):341-350.

14. Emblem KE, Mouridsen K, Bjornerud A, et al. Vessel architectural imaging identifies cancer patient responders to anti-angiogenic therapy. *Nat Med*. 2013;19(9):1178-1183.

15. Yablonskiy DA, Haacke EM. Theory of NMR signal behavior in magnetically inhomogeneous tissues: the static dephasing regime. *Magn Reson Med*. 1994;32(6):749-763.

16. Kiselev VG, Posse S. Analytical model of susceptibility-induced MR signal dephasing: effect of diffusion in a microvascular network. *Magn Reson Med*. 1999;41(3):499-509.

17. Bauer WR, Nadler W. Spin dephasing in the extended strong collision approximation. *Phys Rev E*. 2002;65:066123.

18. Kurz FT, Kampf T, Heiland S, Bendszus M, Schlemmer H-P, Ziener CH. Theoretical model of the single spin-echo relaxation time for spherical magnetic perturbers. *Magn Reson Med*. 2014;71(5):1888-1895.

19. Ziener CH, Kurz FT, Kampf T. Free induction decay caused by a dipole field. *Phys Rev E*. 2015;91:032707.

20. Ziener CH, Kampf T, Reents G, Schlemmer H-P, Bauer WR. Spin dephasing in a magnetic dipole field. *Phys Rev E*. 2012;85(5):051908.

21. Buschle LR, Ziener CH, Zhang K, et al. Vessel radius mapping in an extended model of transverse relaxation. *Magn Reson Mater Physics, Biol Med*. 2018;31(4):531-551.

22. Kurz FT, Buschle LR, Kampf T, et al. Spin dephasing in a magnetic dipole field around large capillaries: Approximative and exact results. *J Magn Reson*. 2016;273:83-97.

23. Kurz FT, Buschle LR, Hahn A, et al. Diffusion effects in myelin sheath free induction decay. *J Magn Reson*. 2018;297:61-75.

24. Bauer WR, Nadler W, Bock M, et al. Theory of coherent and incoherent nuclear spin dephasing in the heart. *Phys Rev Lett*. 1999;83(20):4215-4218.

25. Hahn A, Bode J, Krüwel T, et al. Glioblastoma multiforme restructures the topological connectivity of cerebrovascular networks. *Sci Rep*. 2019;9(1):11757.

26. Pan C, Schoppe O, Parra-Damas A, et al. Deep learning reveals cancer metastasis and therapeutic antibody targeting in the entire body. *Cell*. 2019;179(7):1661-1676.

27. Jacobs VL, Valdes PA, Hickey WF, De Leo JA. Current review of in vivo GBM rodent models: emphasis on the CNS-1 tumour Model. *ASN Neuro*. 2011;3(3):AN20110014.

28. Breckwoldt MO, Bode J, Kurz FT, et al. Correlated magnetic resonance imaging and ultramicroscopy (MR-UM) is a tool kit to asses the dynamics of glioma angiogenesis. *Elife*. 2016;5:e11712.

29. Wirthschaft P, Bode J, Simon AEM, et al. A PRDX1-p38 heterodimer amplifies MET-driven invasion of *IDH* -wildtype and *IDH* -mutant gliomas. *Int J Cancer*. 2018;143(5):1176-1187.

30. Schwarz MK, Scherbarth A, Sprengel R, Engelhardt J, Theer P, Giese G. Fluorescent-protein stabilization and high-resolution imaging of cleared intact mouse brains. *PLoS One*. 2015;10(5):e0124650.

31. Berg S, Kutra D, Kroeger T, et al. ilastik: interactive machine learning for (bio)image analysis. *Nat Methods*. 2019;16(12):1226-1232.

32. Clarke L, Glendinning I, Hempel R. The MPI Message Passing Interface Standard. In: *Programming Environments for Massively Parallel Distributed Systems*. Basel: Birkhäuser Basel; 1994:213-218.

33. Dalcín L, Paz R, Storti M. MPI for Python. *J Parallel Distrib Comput*. 2005;65(9):1108-1115.

34. Pathak AP, Ward BD, Schmainda KM. A novel technique for modeling susceptibility-based contrast mechanisms for arbitrary microvascular geometries: The finite perturber method. *Neuroimage*. 2008;40(3):1130-1143.

35. de Rochefort L, Nguyen T, Brown R, et al. *In vivo* quantification of contrast agent concentration using the induced magnetic field for time-resolved arterial input function measurement with MRI. *Med Phys*. 2008;35(12):5328-5339.

36. Arfken GB. *Mathematical Methods for Physicists*. 3rd ed. Orlando, Florida, USA: Academic Press; 1985.

37. Torrey HC. Bloch equations with diffusion terms. *Phys Rev*. 1956;104(3):563-565.

38. Spees WM, Yablonskiy DA, Oswood MC, Ackerman JJ. Water proton MR properties of human blood at 1.5 Tesla: magnetic susceptibility, T1, T2, T2*, and non-Lorentzian signal behavior. *Magn Reson Med*. 2001;45(4):533-542.

39. Lin A-L, Qin Q, Zhao X, Duong TQ. Blood longitudinal (T1) and transverse (T2) relaxation time constants at 11.7 Tesla. *Magma*. 2012;25(3):245-249.

40. Gudbjartsson H, Patz S. The Rician distribution of noisy MRI data. *Magn Reson Med*. 1995;34(6):910-914.

41. Lagarias JC, Reeds JA, Wright MH, Wright PE. Convergence properties of the Nelder-Mead simplex method in low dimensions. *SIAM J Optim*. 1998;9(1):112-147.

42. Sukstanskii AL, Yablonskiy DA. Theory of FID NMR signal dephasing induced by mesoscopic magnetic field inhomogeneities in biological systems. *J Magn Reson*. 2001;151(1):107-117.

43. Sukstanskii AL, Yablonskiy DA. Gaussian approximation in the theory of MR signal formation in the presence of structure-specific magnetic field inhomogeneities. Effects of impermeable susceptibility inclusions. *J Magn Reson*. 2004;167(1):56-67.

44. Chang C-C, Lin C-J. LIBSVM: A library for support vector machines. *ACM Trans Intell Syst Technol*. 2011;2(3):27:1-27:27.

45. Pries AR, Secomb TW. Microcirculatory network structures and models. *Ann Biomed Eng*. 2000;28(8):916-921.

46. Sweeney PW, D'Esposito A, Walker-Samuel S, Shipley RJ. Modelling the transport of fluid through heterogeneous, whole tumours in silico. *PLoS Comput Biol*. 2019;15(6):e1006751.

47. Kurz FT, Kampf T, Buschle LR, et al. CPMG relaxation rate dispersion in dipole fields around capillaries. *Magn Reson Imaging*. 2016;34(7):875-888.

48. Kurz FT, Ziener CH, Rückl M, et al. The influence of spatial patterns of capillary networks on transverse relaxation. *Magn Reson Imaging*. 2017;40: 31-47.

49. Buschle LR, Kampf T, Kurz FT, et al. Voxel-size dependent quantitative susceptibility mapping of blood vessel networks: A simulation study. *Z Med Phys*. 2019;29(3):282-291.

50. Clarke RH, Moosa S, Anzivino M, et al. Sustained radiosensitization of hypoxic glioma cells after oxygen pretreatment in an animal model of glioblastoma and in vitro models of tumor hypoxia. *PLoS One*. 2014;9(10):e111199.

51. Boujelben A, Watson M, Mcdougall S, et al. Multimodality imaging and mathematical modelling of drug delivery to glioblastomas. *Interface Focus*. 2016;6(5):20160039.

52. Wang P, Wan W, Xiong S, et al. HIF1 regulates glioma chemosensitivity through the transformation between differentiation and dedifferentiation in various oxygen levels. *Sci Rep*. 2017;7(1):1-16.

53. Forster JC, Harriss-Phillips WM, Douglass MJJ, Bezak E. A review of the development of tumor vasculature and its effects on the tumor microenvironment. *Hypoxia*. 2017;5:21-32.

54. Stamatelos SK, Kim E, Pathak AP, Popel AS. A bioimage informatics based reconstruction of breast tumor microvasculature with computational blood flow predictions. *Microvasc Res*. 2014;91:8-21.

55. d'Esposito A, Sweeney PW, Ali M, et al. Computational fluid dynamics with imaging of cleared tissue and of in vivo perfusion predicts drug uptake and treatment responses in tumours. *Nat Biomed Eng*. 2018;2(10):773-787.

56. Winkelmann JA, Eid A, Spicer G, Almassalha LM, Nguyen T-Q, Backman V. Spectral contrast optical coherence tomography angiography enables single-scan vessel imaging. *Light Sci Appl*. 2019;8(1):7-9.

57. Senarathna J, Yu H, Deng C, et al. A miniature multi-contrast microscope for functional imaging in freely behaving animals. *Nat Commun*. 2019; 10(1):99.

58. Jain RK, di Tomaso E, Duda DG, Loeffler JS, Sorensen AG, Batchelor TT. Angiogenesis in brain tumours. *Nat Rev Neurosci*. 2007;8(8):610-622.

59. Baish JW, Stylianopoulos T, Lanning RM, et al. Scaling rules for diffusive drug delivery in tumor and normal tissues. *Proc Natl Acad Sci U S A*. 2011; 108(5):1799-1803.

60. Karch R, Neumann F, Ullrich R, et al. The spatial pattern of coronary capillaries in patients with dilated, ischemic, or inflammatory cardiomyopathy. *Cardiovasc Pathol*. 2005;14(3):135-144.
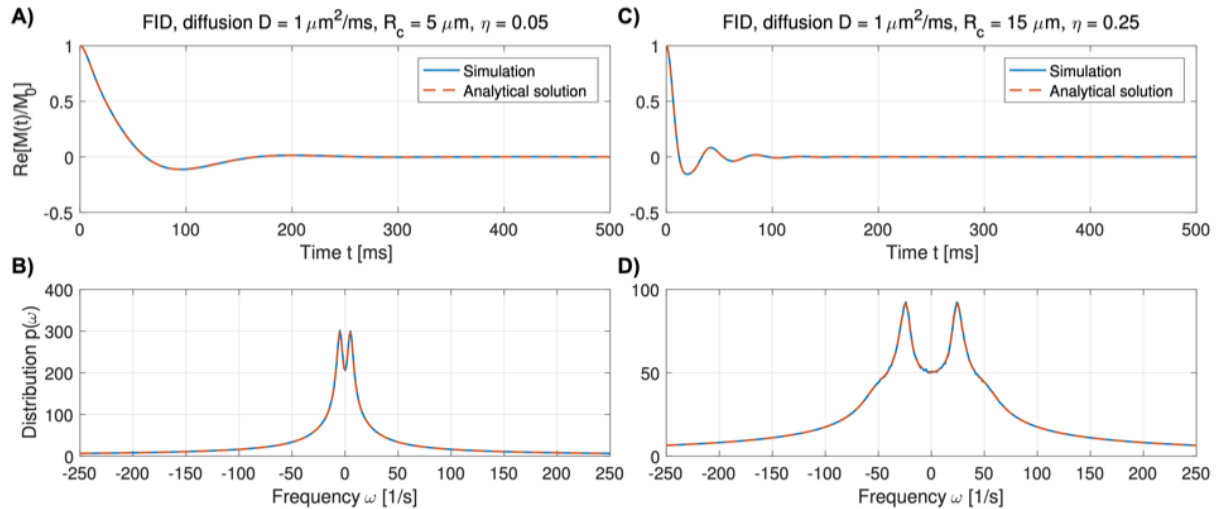
SUPPORTING INFORMATION

Additional supporting information may be found online in the Supporting Information section at the end of this article.
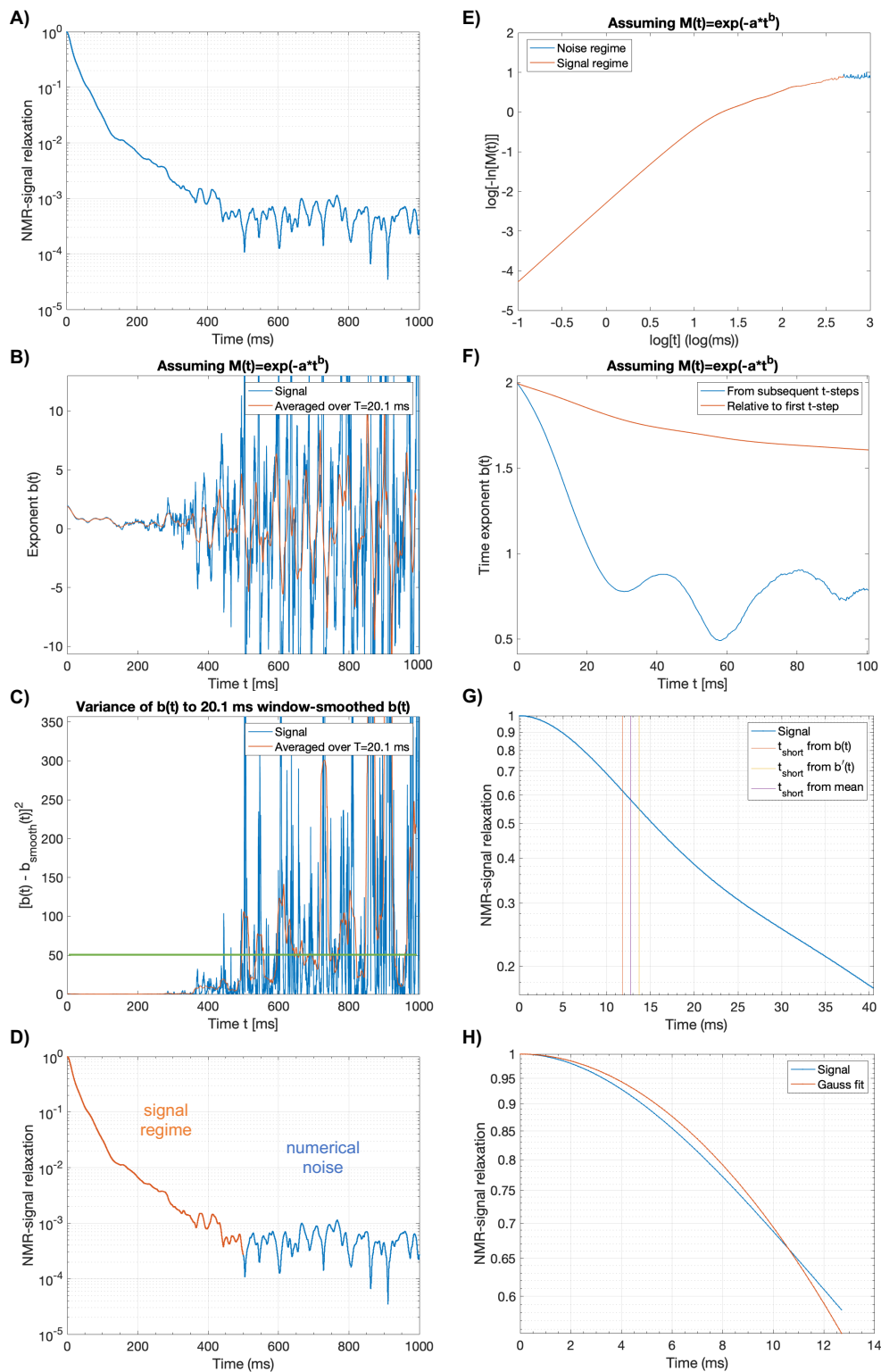
Supplemental Fig. S1. **Validation of the numerical dephasing simulations by comparison with closed-form solutions of the Bloch-Torrey equation.** For the infinite cylindrical vessel model, a closed-form analytical solution of the Bloch-Torrey equation[1] could be derived in previous studies[2]. Magnetization evolutions simulated on model geometries of a single cylindrical blood vessel with 5 μm radius (**A)** and **B)**) and 15 μm radius (**C)** and **D)**), occupying, respectively, 5% and 25% tissue volume were plotted along with the corresponding analytical solutions of the magnetization evolution expected from these geometries. The top row shows the evolution of the real part of the total magnetization $M(t)$, normalized to its starting value M_0. The bottom row presents the frequency density of states $p(\omega)$, attained through a Fourier transformation of the complex magnetization decay. The results presented precisely coinciding curves, validating our numerical implementations, which, in contrast to the analytical solution, cannot only be applied to the cylindrical vessel model, but to arbitrary paramagnetic susceptibility distributions in 3D space. This validation proves the correct implementation of the underlying NMR physics in the simulations used to calculate spin dephasing based on the imaged microvasculature in real biological tissue.

Supplemental Fig. S2. **Demonstration of automated noise regime and short-time limit assessment.** Panels **A-D** demonstrate the automated detection of the numerical noise regime onset on a virtual voxel from healthy brain tissue: the full simulated dephasing relaxation process (**A**) is parametrized assuming $M(t) = \exp(-at^b)$ to determine the time exponent $b(t)$ through consecutive-step numerical differentiation,

presented in panel **B** along with the sliding-window average of *b(t)* over a 20.1 ms symmetric time window. The squared deviation of *b(t)* from its windowed mean is calculated and again averaged over the same sliding window (**C**). An empirically optimized threshold of 50 was chosen for the window-smoothed variance (green line in panel **C**), which, when first exceeded, marked the beginning of the time regime dominated by numerical noise, to be excluded from further analysis (**D**). Panels **E-F** present the automated determination of the transition from the short-time to the long-time signal regime, based on the above parametrization of dephasing with variable time exponent *b(t)*. Panel **E** shows the dephasing relaxation plotted as $\log_{10}(-\ln(M(t)))$ vs. $\log_{10}(t)$, which renders the time exponent *b* as the slope of the curve. All simulated decays exhibited a characteristic decrease in slope, in this example, discernible around *t* = 10 ms. The exponent *b(t)*, determined previously (**B**) was augmented with an analogy, *b'(t)*, calculated through finite difference quotients at every time point with respect to *t*=0.1 ms (**F**). Thresholds of 1.7 and 1.9 for *b(t)* and *b'(t)*, respectively, contributed estimates of the end of the short-time regime with Gaussian signal decay[3], which were averaged to yield the sought transition point (**G**). In panel **H**, a Gaussian fit with $M(t) = \exp(-Qt^2)$ to the short time dephasing signal from this example is presented (s. **Supplemental Fig.** S3 for more examples).
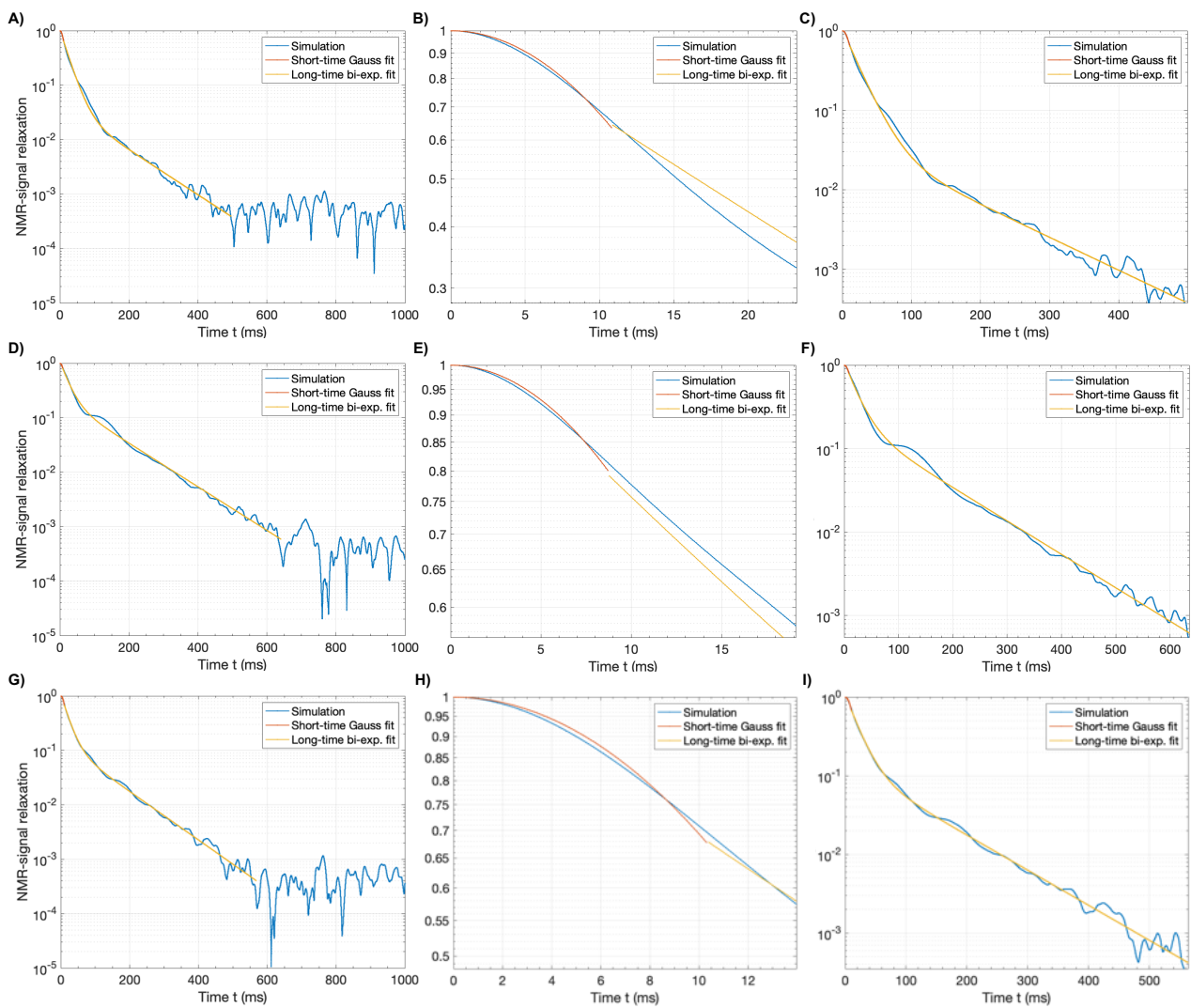
Supplemental Fig. S3. **Examples of short-time Gaussian fits with long-time bi-exponential fits to simulated dephasing relaxation.** The reduced set of relaxation parameters tested for classification tasks is presented here, with an example from healthy brain tissue (**A-C**), U87 glioblastoma (GBM) (**D-F**), and GL261 GBM (**G-I**). The first column of panels depicts the entire simulated time frame with short-time Gaussian fits, assuming $M(t) = \exp(-Qt^2)$ and long-time bi-exponential fits, modeling the signal as $M(t) = A_1\exp(-B_1t) + A_2\exp(-B_2t)$. The second column zooms in on the short-time signal regime and the third column presents the signal regime before the dominance of numerical noise. The time points of signal regime transitions were determined automatically with the ad-hoc algorithm described in **Supplemental Fig.** S2.
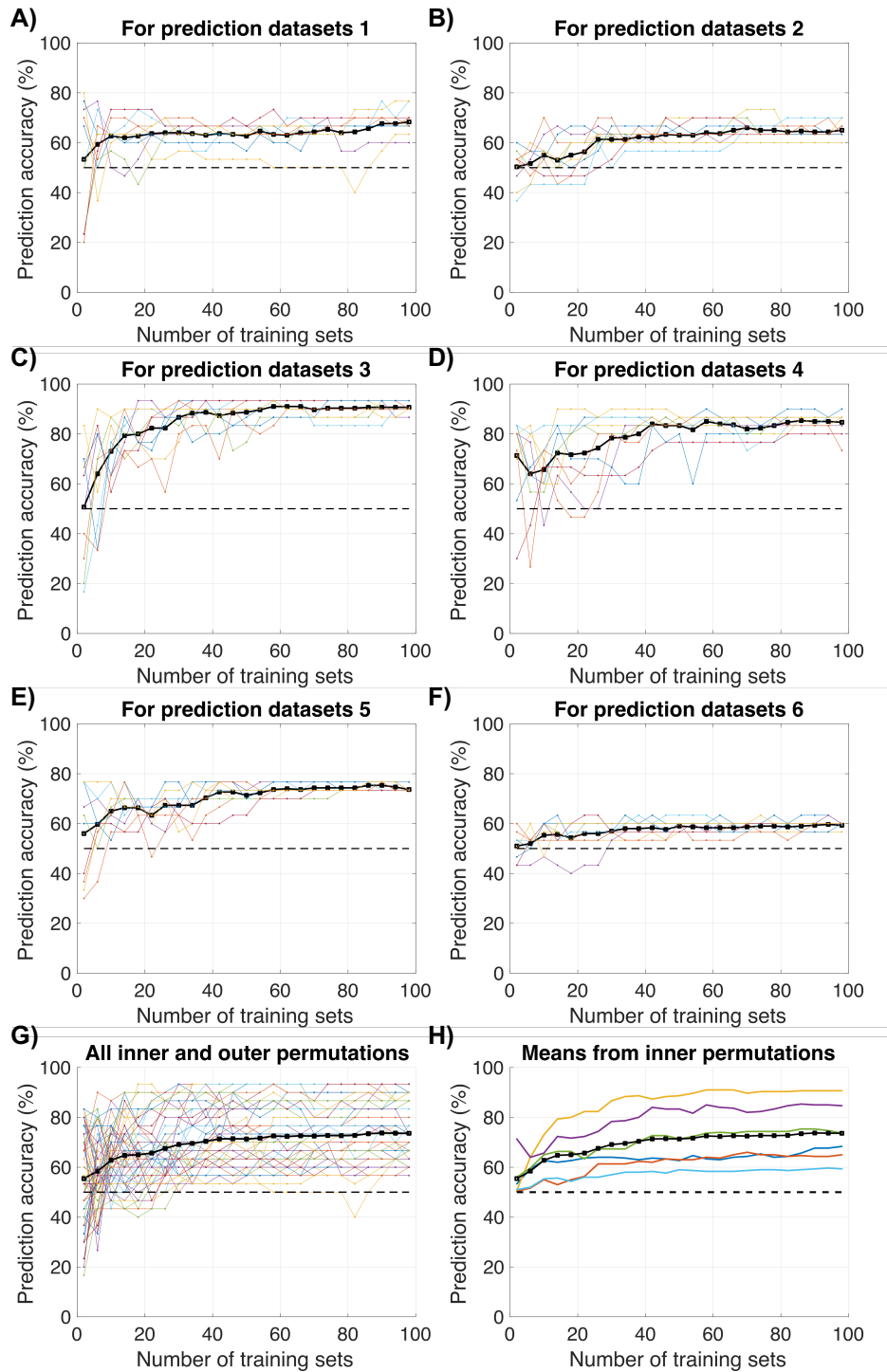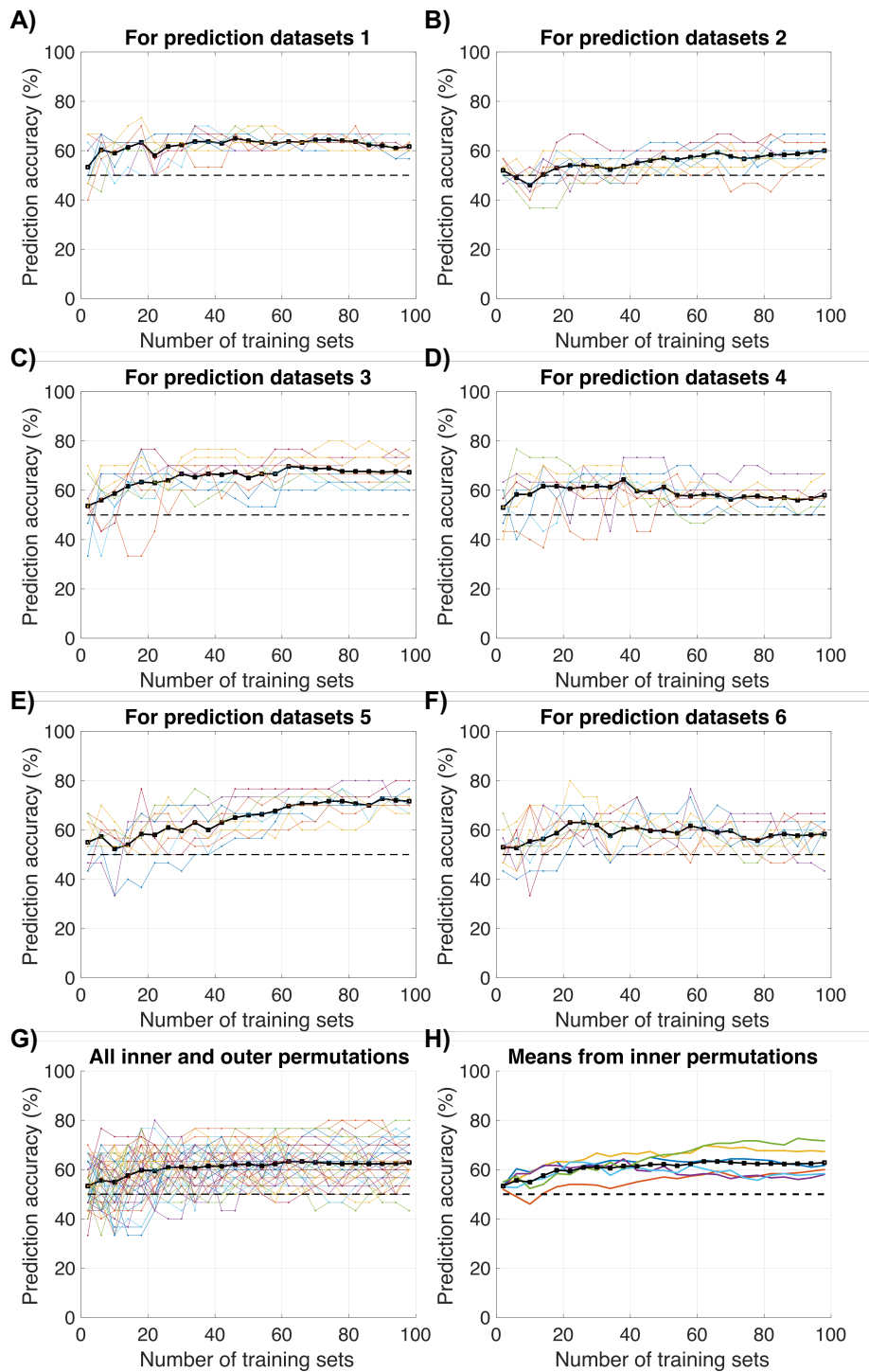
Supplemental Fig. S4. **Individual learning curves from different permutations of training and prediction testing subsets of virtual voxel signals, using the full set of relaxation parametrizations with weak NMR noise at SNR = 100.** Panels **A-F** present training scenarios with predictions on different healthy and tumor-bearing mice, depicting individual learning curves from, respectively, 10 random permutations of the

training data from n=5 mice of each group. The learning curves from different training signal permutations are colored, with the mean prediction accuracy from 10 runs plotted in a bold black line. Panel **G** includes all learning curves from the different training and prediction data permutations, i.e., summarizing the results in **A-F**, with the total mean prediction accuracies for each training run in bold black, overlaying the colored curves from individual runs. Panel **H** shows the same mean learning curve in bold black as panel **G**, but with averaged prediction accuracies from the random training set permutations shown in distinct colors for each prediction animal pair (the bold black curves in panels **A-F**).
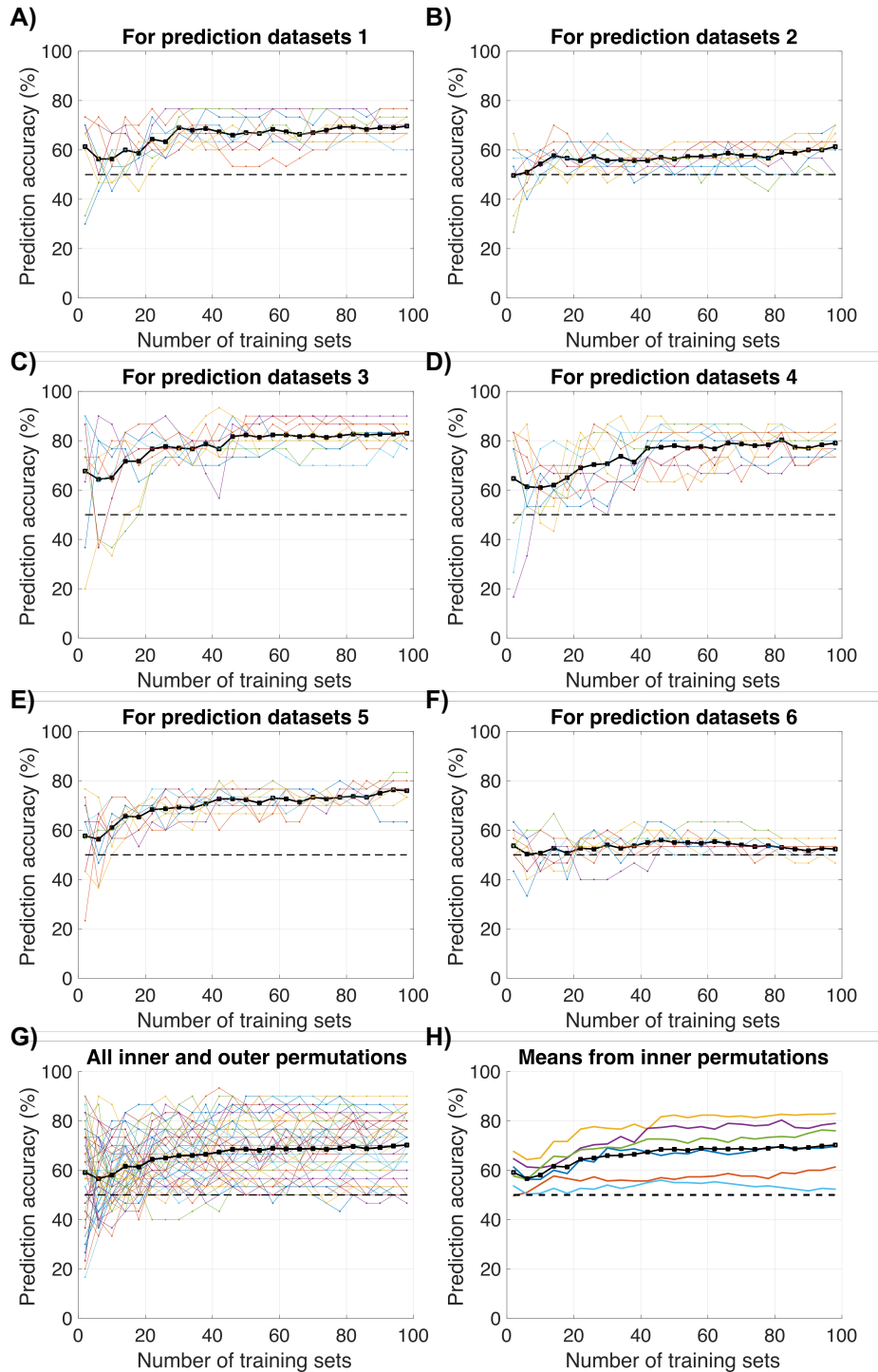
Supplemental Fig. S5. **Individual learning curves from different permutations of training and testing subsets of virtual voxel signals, using the full set of relaxation parametrizations with strong noise at SNR = 2.** Panels **A-F** present training scenarios with predictions on different healthy and tumor-bearing mice, depicting individual learning curves from, respectively, 10 random permutations of the training data from n=5 mice of each group. The learning curves from different training signal permutations are

colored, with the mean prediction accuracy from 10 runs plotted in a bold black line. Panel **G** includes all learning curves from the different training and prediction data permutations, i.e., summarizing the results in **A-F**, with the total mean prediction accuracies for each training run in bold black, overlaying the colored curves from individual runs. Panel **H** shows the same mean learning curve in bold black as panel **G**, but with averaged prediction accuracies from the random training set permutations shown in distinct colors for each prediction animal pair (bold black curves in panels **A-F**).

Supplemental Fig. S6. **Individual learning curves from different permutations of training and testing signals, using the sparse set of relaxation parameters from Gaussian short-time and bi-exponential long-time fits and low noise at SNR = 100.** Panels **A-F** present training scenarios with predictions on different healthy and tumor-bearing mice, depicting individual learning curves from, respectively, 10 random permutations of the training data from n=5 mice of each group. The learning curves from

different training signal permutations are colored, with the mean prediction accuracy from 10 runs plotted in a bold black line. Panel **G** includes all learning curves from the different training and prediction data permutations, i.e., summarizing the results in **A-F**, with the total mean prediction accuracies for each training run in bold black, overlaying the colored curves from individual runs. Panel **H** shows the same mean learning curve in bold black as panel **G**, but with averaged prediction accuracies from the random training set permutations shown in distinct colors for each prediction animal pair (bold black curves in panels **A-F**).

Supplemental Fig. S7. **Individual learning curves from permutations of training and testing signal sets, using the sparse relaxation parametrization with Gaussian short-time and bi-exponential long-time decay and strong noise at SNR = 2.** Panels **A-F** present training scenarios with predictions on different healthy and tumor-bearing mice, depicting individual learning curves from, respectively, 10 random permutations of the training data from n=5 mice of each group. The learning curves from different

training signal permutations are colored, with the mean prediction accuracy from 10 runs plotted in a bold black line. Panel **G** includes all learning curves from the different training and prediction data permutations, i.e., summarizing the results in **A-F**, with the total mean prediction accuracies for each training run in bold black, overlaying the colored curves from individual runs. Panel **H** shows the same mean learning curve in bold black as panel **G**, but with averaged prediction accuracies from the random training set permutations shown in distinct colors for each prediction animal pair (bold black curves in panels **A-F**).

References

1. Torrey HC. Bloch Equations with Diffusion Terms. Phys Rev. 1956;104(3):563-565. doi:10.1103/PhysRev.104.563

2. Ziener CH, Kurz FT, Kampf T. Free induction decay caused by a dipole field. Phys Rev E. 2015;91:032707. doi:10.1103/PhysRevE.91.032707

3. Sukstanskii AL, Yablonskiy DA. Gaussian approximation in the theory of MR signal formation in the presence of structure-specific magnetic field inhomogeneities. Effects of impermeable susceptibility inclusions. J Magn Reson. 2004;167(1):56-67. doi:10.1016/j.jmr.2003.11.006

4 Discussion

Many pathologies, especially chronic illnesses have characteristic effects on tissue microstructure. Infamous examples are glioblastoma multiforme and other cancer types, which alter the cellular tissue composition, metabolism, function, and nutritional supply of affected organs. Neurodegenerative diseases such as Alzheimer's, Parkinson's, dementia, and schizophrenia have also been suspected to be tied to microstructural changes within the brain, suggested by an altered axon myelination [173, 174] and microscopic iron accumulations in certain cells [175].

As a chronic disease progresses, it often increasingly deforms the tissue architecture on a cellular level. This makes microstructure-sensitive medical imaging a field worthwhile advancing, anticipated to become increasingly relevant to clinical practice. It can provide useful information about sub-resolution structures for diagnostics and treatment monitoring [36]. As shown in the introduction to this thesis, MRI represents a promising candidate for such developments due to its inherent sensitivity to microscopic and mesoscopic tissue structure and dynamics, as well as the wealth of possible contrasts to highlight different aspects. This is supported by the exponential increase of research publications pertaining to microstructural MRI in recent years [176].

During the first half century since its invention in the 1970's, MRI has evolved tremendously in diversity and refinement. On the one hand, increasing technical precision and sophisticated engineering have boosted the quality of imaging with more powerful and homogeneous magnets, gradient coils, and RF transmission and reception systems. On the other hand, continuous developments of new spin system preparation and manipulation techniques with creative pulse sequence designs have conceived a myriad of contrast types and signal weightings.

In medical imaging, sophisticated sequence designs have increasingly been combined with external manipulations to not only produce new contrasts, but also probe the responses of tissue to different conditions. Examples include the use of intravascular contrast agents, *e.g.*, for DCE or DSC [30, 34], and MRE, where tissue stiffness is probed by imaging shear wave propagation from an external application of mechanical, sonic or ultrasound compressions using MRI [107, 108]. Clinical and preclinical research regularly finds promising use cases for different MRI techniques to image specific pathologies for diagnostic aid, *e.g.*, MRE for liver fibrosis and tumor imaging [109, 110].

Arguably, up to this point, most such applications of MRI in clinical imaging to uncover or grade specific conditions have been discovered mainly through experiment and experience. While the microscopic origins of disease-characteristic hypo- and hyper-intensities of different contrasts can often be explained, at least on a phenomenological or

qualitative level, clinically established gold-standards in diagnostics are often based on experience and empirical findings built throughout years. For instance, malignant brain tumors are often characterized with contrast-enhanced T_1-weighted MRI, differentiating enhancing and non-enhancing tumors, which reveals the intactness of the blood-brain barrier and some tumor properties relating to the prognosis [177]. With some exceptions, *e.g.*, diffusion weighted MRI (DWI and DTI) [178], MRE [108, 179], MR-spectroscopic imaging (MRSI) [180], and magnetic resonance thermometry [181] (see section 1.2.5 for more details), MRI techniques rarely permit a direct quantitative interpretability of measurements on a single voxel level for real, physical information about the underlying tissue in gauged units. Most methods only allow for an assessment of relative changes of the MRI signal, usually in comparison with other imaging voxels within the same acquisition, to indicate tissue anomalies on a sub-voxel level.

With the rise of artificial intelligence (AI) and machine learning, this may change in the future. While the past fifty years have mainly brought forth new MRI contrasts based on physical manipulation of the sample magnetization and direct imaging of its responses, data-driven methods can be expected to augment basic contrasts achievable with MRI in the future. After all, letting a computer interpret a signal based on many examples it has seen of healthy cases and how a measurement "should" look, in order to detect deviations thereof, is not so much different from what has been done in the past decades utilizing MRI in clinical imaging, just that the interpretation of new images and comparison with known controls has been the responsibility of human radiologists, relying on their training and experience. For one, trained physician specialists know how a healthy anatomy should look with certain MRI contrasts and can recognize tissue anomalies on a macroscopic level. Further, their experience, established textbook knowledge, and ability to access and compare a wealth of data for all kinds of pathologies acquired from around the world, grants them the possibility to interpret deviations from the norm. A diagnosis is typically made based on combinations of the findings from imaging with other conditions a patient has, *e.g.*, from an anamnesis or laboratory examinations.

Considering the status quo, it becomes apparent that AI could assist radiologists in many of the tasks they implicitly carry out on their way to arriving at a diagnosis. Based on images acquired with certain contrasts, a comparison with a database of healthy and pathological signals by a computer could yield a healthy classification or a set of possible conditions which have been seen causing the observed types of signal anomalies. Hypothetical advantages of handing this task over to machines are manyfold. For one, the amount of data that can be compared quantitatively by a computer in a short time is horrendous. A computer would base its recommendations on quantitative measures, which need to be transparent and explainable (an important requirement for

machine learning in many real-life applications). This is a large research topic in the field of AI, often referred to as explainable machine learning [182, 183], which has gained tremendous attention in recent years. Naturally, explainability will play a central role in such a system for medical diagnostics, since it would service with decision support for physicians, as opposed to a decision automation, making high prediction accuracies insufficient for an adoption in clinical practice. For a real benefit from such a system, radiologist would need to know what exactly a certain diagnostic suggestion was based on, *e.g.*, which parts of an MRI.

The explainability of machine learning is not a serious point of concern for an application in medical diagnostic support, though. Broad research with different approaches and many promising developments are leading AI into an age of transparency and explainable versions of most machine learning techniques already exist in some form. A bigger obstacle for an effective machine-aided medical image interpretation framework is the construction of high-quality databases for training, an appropriate parametrization of acquisitions, and the definition of suitable metrics to assess similarity between measurements, especially from different vendors and hardware. Relevant technical questions concern appropriate feature extraction techniques, best length scales of signal comparisons, and the relative weighting of different aspects. Metrics should be sensitive enough to pathological alterations in all their heterogeneity, but flexible enough to tolerate physiological and anatomical variations between healthy patients. Clearly, there is still much work to be done on the path to such AI-based diagnostic tools in the described form, but the possibilities are yet greater.

A major advantage of machine-aided signal interpretation, which human physicians could not feasibly accomplish, is the possibility to classify and characterize signals from individual MRI voxels. Trained radiologists can only make sense of an MRI acquisition as a pixel matrix attained after image reconstruction from k-space (see section 1.2.2), by comparing the intensities of multiple pixels in an arrangement as a whole image. With machine learning, MRI signals can be interpreted directly in k-space, bypassing an image reconstruction. To include spatial information of possible anomalies, the reconstructed MRI signal can be processed on different length scales. Classically, entire images can be compared for anatomical irregularities on a computer vision basis, emulating what a radiologist would do. Additionally, machine learning and pattern recognition can be applied in a convolutional way exclusively to local voxel neighborhoods. Finally, in the special case of MRI, where each voxel can have multiple signal intensities based on the applied contrasts and acquisition settings, voxel signals can be interpreted individually without any information about spatial origin or voxel neighborhoods.

In this thesis, exhaustive preparations were made for such a voxel-wise signal interpretation approach. Its applicability for a detection of brain tumors was tested under

isolation of a specific signal component; the endogenous effect of microvascular geometry on transverse relaxation. Furthermore, automated quantifications of microvascular geometry and topology were implemented in a scalable way to process large datasets of ground-truth 3D architectures for the production of sufficient training, validation, and test data for machine learning. This way, dephasing effects of certain microstructures can be correlated directly with specific aspects of their geometry and topology. Either real anatomical data, as studied in the majority of this thesis, or different model architectures (see publication I and section 4.2), can serve as input to study the effects of different microstructural variations on the MRI voxel signal. For an effective use of machine learning, sufficient data availability or quick production abilities are essential.

Depending on the amount of available training data, different machine learning techniques can come into consideration for diagnostic decision support systems. With limited data availability of less than $\sim 10^4$ training samples, classical models like support vector machines or decision tree methods such as random forests are suitable. Such models require numerical feature vectors and cannot directly process raw image data, calling for efficient feature extraction methods. With very many tunable parameters and weights, neural networks, especially for deep learning, demand much more data in the order of at least 10^5 or 10^6 instances for sensible training (sometimes considerably more, depending on the network architecture). Deep neural networks with an increasing number of hidden layers usually have an astronomical number of weights and connections to be tuned and, in practice, the adaptation of pre-trained network architectures has proven efficient for many classification purposes [184].

An advantage of neural networks, of which there are many types, *e.g.*, convolutional neural networks, is their ability to autonomously identify sensible data parametrizations in their hidden layers (or latent space). This evades the need for feature definitions and enables direct end-to-end learning of input signals and output quantities or classifications. This is a major source of neural network flexibility and superior performance in many classification tasks. In the medical context, this advantage may alleviate the problem of finding appropriate similarity metrics of different acquisitions, but it would demand a coordination and maintenance of extremely large databases to be used for anomaly detection based on real training data. Such developments are conceivable in the far future, but several obstacles are currently in the way of an effective realization. Medical data processing is regulated individually by countries and the construction of a widely accessible infrastructure to share anonymized data would demand international cooperations on a political and administrative level. Also, general processing guidelines and normalization techniques for data from different scanners would be needed.

Recent years have seen machine learning invading virtually all areas of medical imaging, including numerous applications with MRI [185]. This is because the field

offers so many possibilities of data-based enhancement, the number of medical scans being conducted world-wide on a daily basis increases continuously, and the acquired data is already being archived in a digital format in most cases. Combining more of this data for a sophisticated interpretation of new acquisitions seems like a self-evident continuation, of course presuming complete data anonymization. A review of different use cases for AI in medical imaging would blow the scope of this thesis, but application areas include image reconstruction, artifact minimization, sequence design, image segmentation, and classification. For instance, the image reconstruction step, *i.e.*, the Fourier transformation in MRI, can be replaced by a deep neural network to map k-space data to image space, which can be trained incorporating signal noise and artifacts for increased resilience against such factors in comparison to traditional reconstruction [186]. In another image reconstruction example, undersampled k-space data can be Fourier transformed with k-space interpolation from machine learning [187].

The use of AI for disease detection based on MRI is still relatively rare, because it is a more complex issue with many degrees of heterogeneity on several levels. Details in anatomy and physiology can differ even among healthy humans. Influential factors are genetics, age, prior health problems, and life style [138]. Further, pathological phenotypes can differ substantially among individuals. A disease can appear in distinct facets and also depend on different conditions, individual predisposition, other personal factors as above, and mere chance. In some individuals, certain symptoms may evolve and in others they may not, just as combinations of different simultaneous conditions can influence particular pathological manifestations. This biological variance alone makes it difficult to generalize and automate diagnostic processes. Also, the hardware, protocols, and reconstruction steps of MRI can differ between vendors and devices, making a direct comparison of signal intensities difficult when planning to collect training and prediction data from different sites. Consequently, AI-aided diagnostics have recently been applied more with X-ray imaging, which does not have such sensitive soft-tissue contrasts [188, 189], and stained biopsies from histopathological examinations [190].

Quantitative MRI (qMRI) can generalize measurements across vendors and scanners by determining quantitative relaxation parameters for each imaging voxel. A great ambition of qMRI is to provide quantitative information about the degree of tissue malformations from certain diseases, as opposed to merely weighted images, which only reveal relative signal changes. A problem with this is the reasonable degree of variation of basic relaxation rates R_2 and R_2^* due to physiological dynamics such as the blood oxygen saturation [9, 191, 192] (cf. **Tab.** 1.1 in section 1.2.3). Certain value deviations often cannot be ascribed to invidivual microscopic conditions reliably. Phenomenological models can connect the blood oxygen saturation Y and field strength B_0 to relaxation times T_2 and T_2^* [193], but the quantitative relaxation times do not

enable an inference on the microvascular architecture on sub-voxel length scales without separate blood oxygenation measurements, *e.g.*, with quantitative susceptibility mapping (QSM) [194, 195] or quantitative BOLD [196–198]. For a voxel-wise characterization of capillary geometry, most methods fall back on susceptibility contrast with paramagnetic, intravascular contrast agents [30, 34] or at least hyperoxic/hypercapnic blood oxygen variations in more experimental methods [29]. Yet a common denominator remains to be the focus on relaxation rates attained from mono-exponential fitting of transverse relaxation and changes thereof on longer time-scales of seconds, sampled with the repetition time T_R.

The approach pursued for artificial MRI contrast definitions in this thesis, demonstrated with the tissue type classification in publication V, focuses on the more detailed form of transverse megnetization decay for different echo times $T_E < T_R$. In their early analytical treatments, Sukstanskii and Yablonskiy already predicted a Gaussian signal attenuation in the short-time regime and a Lorentzian form in the long-time regime, predicted for dephasing around arbitrarily oblate or prolate ellipsoidal susceptibility distributions [14]. This has been confirmed experimentally [44] and numerically in my simulations, showing good fit results assuming such functions.

Even better goodness of fit was achieved in publicaton V of this thesis using bi-exponential functions for the long-time dephasing regime. Such signal behavior is typically observed in multi-compartment tissues with different relaxation times of distinct spin pools (*e.g.* fat and water), but has also been observed in T_2-weighted acquisitions of the human brain with brain tumors and edema [199]. Interestingly, in publication V, we found that a bi-exponential T_2' evolution is also invoked in a single, extravascular spin pool by the microvasculature containing deoxygenated blood. This is expected to be a consequence of diffusion, because with longer echo times, small-scale field inhomogeneities are increasingly smeared, causing slower dephasing relaxation in the long-time regime. This effect was also observed in publication I.

In publication V, the goal of a more diverse parametrization of transverse relaxation within one repetition period T_R was to become independent of absolute relaxation rates, as determined in classical qMRI. The ambition was to achieve a sort of self-gauging by comparing the relations between different fit parameters in the short- and long-time dephasing regimes instead of relying on absolute relaxation strength. For support vector classification, each feature was scaled to the range $[-1, 1]$ to base predictions mainly on relative relations between individual fit model parameters. The hyperplane division implemented by SVMs was used to unveil how well-separated the healthy and pathological signals were in the scaled parameter space through relative positions along the different dimensions (scaled fit parameters). The improvement of classification accuracies with radial basis function kernels indicated a nonlinear distribution pattern

between tumor and healthy voxel signals, but the overall results and robustness to noise showed that dephasing attenuation shapes differ significantly and definitely enough for classification. With multiparametric fitting, robustness to noise was high compared to traditional DSC-based vessel characterizations [200], whereas a direct comparison is difficult because the binary tissue type classifications tested here fundamentally differ from the quantitative vessel size, blood volume, and vessel architectural estimations conducted in [200]. With the numerical framework developed throughout this project, further studies to correlate individual vessel properties (*e.g.*, the ones presented in publications II, III, and IV) with the associated dephasing curves (from publication V) should facilitate a better comparison with such established MRI methods.

A translation of the proposed voxel-wise signal interpretation from publication V, using machine learning to yield purpose-specific artificial MRI contrasts, to real, experimental MRI on humans is achievable, given ground-truth knowledge about the artificial contrast in a sufficiently large number of training and validation samples. Since training instances are given by individual voxels as opposed to entire image matrices, a considerable dataset size is quickly attainable for training. In the example of tumor detection or even grading, current gold-standard, contrast-enhanced MRIs could be used as the ground-truth for training AI models in a classification of co-registered voxels from MRIs without contrast enhancement, *e.g.*, from pre-bolus acquisitions. In a very recent preprint, contrast-enhanced T_1 and T_2 acquisitions, as well as diffusion-weighted measurements for the apparent diffusion coefficient (ADC) of each voxel, were combined with support vector classification in a similar approach to differentiate glioblastoma recurrence from edema in the peritumoral region [201]. Here, classifications were based on 270 radiomic features calculated from $5 \times 5 \times 5$ voxel neighborhoods from the above MRI acquisitions (with gadolinium enhancement) in a sliding window manner, also using entire regions of interest. This more classical radiomics approach was not only based on single-voxel contrast, but also incorporated surrounding voxel information, in analogy to texture analysis methods [202], which certainly improves classifications. Nonetheless, this study demonstrates the power of voxel-wise processing, since just ten glioblastoma patients yielded over half a million MRI voxels for classification [201].

Biomedical studies using animal models are subject to discussion in many communities, and justifiably so [203, 204]. In many animal studies, the question of how translatable the findings are to human medicine remains vaguely answered [205, 206]. Concerning the relevance of the results found in this thesis for a mouse model to human physiology, it was recently found that most intracranial microvascular properties pertaining to geometry, topology, and function are well translatable from mice to humans, with direct equivalence of topology and simple scaling rules for geometry and hemodynamics [207]. Thus, the provided proof-of-principle for voxel-wise tumor classifications should be valid

for humans as well. Further, the developed numerical tools for voxel-wise processing of large datasets, including automated relaxation fits, organization of intermediate results by predefined groups, optional matching with microstructural ground truth parameters, and machine learning for classification or regression of voxel properties, dubbed artificial contrasts, all packed in a highly scalable and parallelizable framework, can be readily applied to human data from experimental MRI acquisitions or other imaging techniques. Lastly, the custom-developed quantification tools demonstrated in publications II - IV, specialized for amorphous vessel networks of arbitrary size and shape, can be applied to segmented 3D data from virtually any imaging modality [208], including computed tomography [209], magnetic resonance angiography [210], and 3D digital subtraction angiography [211], as well as artificially constructed vessel networks [212–214].

The numerical developments in this thesis go beyond a mere proof-of-principle for voxel-wise tumor classifications based on endogenous T_2' contrast from variable echo time imaging, as provided in publication V. A large part of this project was dedicated to an extensive characterization of microvasculature within the healthy brain and glioblastoma multiforme. This is because the ultimate goal of this endeavor is to correlate specific vessel properties with voxel-level signal changes expected in MRI. The cylindrical vessel model described in section 1.2.4 oversimplifies realistic microvasculature by assuming parallel orientation, highly regular arrangement, and no interconnections between cylinders. Intracranial vessel networks have been found to contain systematic loops with functional purpose [215, 216] and a complex network structure made up of mesh-like capillaries, intertwined with arterioles and venoles with hierarchical branching into different generations of vessels with increasing calibers following certain scaling rules [217–220]. Further, complex microvascular geometry has been found to influence BOLD-based fMRI signals through its impact on T_2 and T_2^* significantly [221–223].

In publication I of this thesis, an extension of the well-studied SCM (presented in section 1.2.4) was attempted with a spatial regularity parametrization for a step towards more realistic capillary distributions. It was found that the cylindrical vessel model could not facilitate a bijective mapping of the transverse relaxation form (considering the density of states $\rho(\omega_L)$ of intra-voxel Larmor frequencies, *i.e.*, going beyond R_2') to underlying vessel characteristics when including distributive irregularity as a degree of freedom. Increasing vessel disorder was found to have the same effects on dephasing as an increasing variance in radius distributions or stronger diffusion. This led to the conclusion that more sophisticated vessel parametrizations are needed to describe realistic, amorphous and interconnected microvasculature and its effects on transverse relaxation. It is conjectured that a consideration of more vessel characteristics may solve degeneracies in the mapping from tissue microstructure to the macroscopic NMR signal. Therefore, a wide range of quantitative parameters was determined for real microvascular

networks in publications II, III, and IV, in order to identify some characteristics which are significantly altered by brain tumors on a large scale, as compared to the already intricate and interweaved cerebrovasculature of the healthy brain.

With the developed numerical framework, vascular magnetic resonance fingerprinting (vMRF) can also be conducted flexibly. Classical magnetic resonance fingerprinting (MRF) aims for an acceleration of multiparametric MRI and improved robustness to noise and artifacts in simultaneous, voxel-wise estimations of T_1, T_2, and T_2^* [224, 225]. Based on a simulated dictionary of signals associated with certain tissue properties and relaxation rates, the most probable property combination for each voxel is chosen based on a type of scalar-product between the simulated and measured signal vectors [224]. Diverse MRF techniques have arisen for image reconstruction [226], but specialized methods for microvascular characterizations have also been explored, usually referred to as vMRF or MR vascular fingerprinting [227, 228].

These methods have relied on signal dictionaries created with simulations based on idealized cylindrical vessel distributions, as studied analytically in section 1.2.4, with systematic variations of the cylindrical geometry and blood oxygenation. Mean vessel diameters R_C, tissue volume fractions η, and blood oxygen saturation are then predicted by vMRF for each voxel, based on dictionary matching [227]. Such an approach built on the cylindrical vessel model may be too idealized for the detection of disease-specific malformations, as these are not sufficiently parametrized by cylinders and demand properties such as tortuosity, distributive heterogeneity, and connectivity, as shown in publications II and IV. Also, the degeneracy of dephasing effects of the cylindrical vessel model uncovered in publication I of this thesis motivates an approach based on more realistic signal simulations.

Recently, real high-resolution angiograms have been used as the basis for vMRF dictionary construction with an analogous numerical approach taken in publication V of this thesis [229]. Still, the dictionary construction in vMRF generally demands systematic variations of vessel characteristics, which has, up to this point, only been achieved by artificial manipulations of angiograms, involving the deletion of certain vessels (ordered by size) and inflation of vessel radii, which ultimately again produces unnatural structures [229]. It is questionable whether such artificial vessel network manipulations produce angio-architectures comparable to what may be found, *e.g.*, in cancer tissue. Within this thesis, only natural vessel architectures were used to study the effects of microvascular geometry on spin dephasing. If necessary for dictionary construction, the findings concerning tumor-related alterations of vessel geometry and topology, presented in publications II - IV, could guide artificial network manipulations or constructions for vMRF studies in analogy to previous the approaches [227, 229].

I conjecture that it may be possible to refrain from artificial vessel modifications

and possibly focus more on building up dictionaries with different disease types in an MRF analogy. Even just including several disease types or a certain class of malignant tumors in a database seems like a worth-while endeavor. To limit the natural, physiological variability of the healthy signals, positional priors could be used with a voxel categorization, *e.g.*, using a brain atlas [230]. By differentiating brain regions, white and grey matter, or even cortical layers, a minimized variability of healthy tissue microstructure should be achieved [55, 223, 231–233]. With a clustering analysis, optionally unsupervised, the number of sensible tissue types to differentiate could be determined. By choosing the number of healthy tissue groups, the natural variance within each group could be tuned to minimize uncertainty of anomalous deviations for specific artificial contrasts. For instance, if the mean capillary radius is defined as the artificial contrast, the number of tissue groups could be set to the number of brain regions observed with significantly differing vessel calibers in a sensible range. This is expected to significantly improve the classification of pathological deviations of individual voxel signals.

Previous successes of MRI-based intra-voxel capillary characterization typically involved the intravascular administration of a super-paramagnetic contrast agent. The vMRF approaches discussed above were no exception to this [227–229]. The pass-through of a contrast agent bolus can reveal many local microvessel characteristics, with sensitivity to blood volume fraction, flow velocity, mean vessel diameter, vessel length density (see ρ_L in publications III and IV), and lumen permeability [34]. Further, with vessel architectural imaging (VAI), the relative abundance of underlying arterioles as compared to capillaries and venoles can be estimated for each MRI voxel when comparing simultaneous R_2 and R_2^* changes during contrast agent pass-through [36, 234]. This is enabled by the increased sensitivity of R_2^* to large vessels, while R_2 changes are stronger for small and intermediate vessel diameters (cf. **Fig.** 1.3 in section 1.2.4 or [74]). Despite the plethora of information it can reveal, the use of intravascular contrast agents should be limited to maximize patient comfort and minimize the risk of side effects like allergic reactions or long-term contrast agent depositions [117, 118]. Also, an interpretation of dynamic R_2/R_2^* changes for truly quantitative vessel characterizations requires the definition of an arterial input function, which models the contrast agent concentration as it passes and disperses through the vessel network [235, 236].

Alternative, endogenous approaches to vascular characterization based on MRI without contrast agents include ASL [119] and IVIM imaging [120] (briefly mentioned in section 1.2.5). In ASL, RF excitation is conducted outside of the imaging volume and arterial blood with transverse magnetization flows into the imaging region. Signal changes in comparison to reference acquisitions reveal local blood flow characteristics [237, 238]. DSC measurements have been shown to be replaceable by ASL for relative

cerebral blood flow estimation in the healthy brain [239] and high- and low-grade gliomas [240], although DSC allows for better glioma grading [241]. IVIM imaging is based on diffusion weighting and assumes quasi-undirected blood flow in capillaries to emulate a "pseudo-diffusion" with measurable diffusion coefficients $5 - 10$ times greater than what is observed from Brownian motion [120]. A two-component signal model allows the relative fraction of capillary volume to be estimated from IVIM. These imaging methods can also be simulated numerically with the developed `C++` code used in publication V with appropriate extension of an intravascular spin pool (more on this in section 4.2 about sensible continuations of this project).

The presented arguments make a data-driven approach of learning artificial MRI contrasts look like a promising starting point for a new branch of MRI, involving model-less interpretations of multiparametric acquisitions. Even though some pathologies can result in similar fundamental MRI contrast alterations, it is conceivable that a more detailed interpretation of single-voxel contrast combinations, *e.g.*, from multi-parametric or variable echo time imaging, may add an extra dimension to MRI that could solve some of these degeneracies. In any case, a better understanding of microvascular architecture on a quantitative basis will facilitate an improved capability to model and understand the effects thereof on macroscopic MRI signals. Also, with the presented microscopic imaging and processing framework, microstructural signatures of different neoplastic pathologies can be highlighted from new perspectives for a better understanding of system-wide functional alterations. This could, in turn, guide new approaches of tumor signal recognition, either through machine learning, direct physical modeling, or a combination of both, with hybrid modeling.

4.1 Reflection

As in any theoretical or numerical treatment of a real-world problem, models were used and approximations were made to capture certain aspects of reality. Publications I and II of this thesis adopted the cylindrical vessel model, which approximates capillaries by long, straight cylinders, cutting through a plane with parallel orientation to each other. This has been common practice in previous studies with similar aims of characterizing the vessel geometric influence on the dephasing process in NMR, of which an overview was provided in section 1.2.4. While the regular SCM may reasonably approximate myocardial and skeletal muscle tissue [71, 242, 243], its application to brain and tumor tissue is more difficult to justify. Intracranial vasculature is known to be relatively tortuous [168, 244] and convoluted with complex network structures [216, 245], while tumors have been found to additionally alter vessel tortuosity [146].

In publication I, the classical SCM introduced in section 1.2.4 was extended with the order parameter Γ to incorporate a continuous parametrization of distributional irregularity between the previously treated cases of a hexagonal crystal lattice and complete spatial randomness. In this study, the assumption of parallel vessel orientation was strictly enforced. The simulations and calculations were conducted for such idealized vessel systems in order to facilitate a systematic comparison of the effects of distribution irregularity with the previously studied properties, namely vessel radius R_C, tissue volume ratio η, blood susceptibility χ, and diffusion strength D. Starting with the SCM and a hexagonal lattice as a control, the effects of different arrangements were studied and compared to the impact of increasingly variable radius distributions and different diffusion coefficients. This study was meant to shed light on fundamental effects of singular aspects in an idealized setting. In consequence, a direct applicability of its results to real tissue is highly questionable, especially in the brain.

In publication II, the order parameter Γ was estimated for slices of tissue with $5\,\mu$m thickness, within which the vessel orientation was ignored. In this study, the 2D-OCP was not used to study artificial vessel distributions, but rather to attribute an order parameter to capillary constellations based on the positions of their centers within planes. By analyzing statistical distributions of Γ values, the model could be applied without enforcing parallelism of vessel segments. In this analysis, idealized tissue containing long, parallel cylinders would yield sharp peeks at individual Γ values (with correctly oriented planes for analysis). The shape and width of a Γ distribution from realistic tissue holds additional information about the degree of disorder beyond a single plane. Specifically, the variance of Γ values from the planes within a single MRI voxel can hold information about the degree of deviation from vessel parallelism. The variance of Γ distributions from different macroscopic voxels discloses the degree of heterogeneity on larger length scales throughout the tissue. A caveat of this parametrization is its dependence on the orientation of scanning planes in anisotropic tissue, but the implemented numerics offer an averaging of three perpendicular scanning plane directions.

Publication II revealed broad Γ distributions, both in U87 glioblastoma and healthy brain tissue. While statistically, the tissue types can be differentiated with sufficiently many Γ probes, the overlap is large (cf. **Fig. 4** of publication II). A contributing reason for this was presumably the non-selective placement of virtual voxels over different brain regions, incorporating partial volume effects from white and grey matter and generally broadening healthy tissue distributions. True for all analyses conducted in this thesis, an inclusion of additional spatial information and a categorization into different brain regions using a brain atlas, *e.g.*, from the Allen Institute for Brain Science (see brain-map.org/api/index.html), would certainly boost the distinguishability of tumors from healthy tissue (as suggested in the above discussion). This was demonstrated

in publication III with a differentiation of healthy cortex, basal ganglia, and corpus callosum. For MRI voxels lying on boundaries that overlap multiple tissue types, partial volume effects and an increased uncertainty of estimated parameters could be taken into account using a brain atlas registration.

Publication III showcases the flexibility of the developed quantification code in determining vessel geometry in arbitrarily shaped tissue regions. Binary masks can be used to include or exclude regions, allowing for combinations with flexible topological structure including holes. These masks could also be extracted from a brain atlas for further automation, but would require a reliable co-registration of the atlas to the microscopic data, which is a highly active research field in itself [246]. To complement the flexibility of the tailored vessel quantification program written within the course of this thesis, publication IV demonstrated its scalability. With over a million vessel segments per healthy brain hemisphere, to our knowledge, this work presented the most comprehensive geometric quantifications of cerebrovasculature to date.

Publication IV further introduced the largest network-topological quantifications of cerebrovasculature in healthy mammals and provided the first graph theoretical perspective on vessel remodeling in entire brain tumors with such detail. At the resolution of $3 - 5\,\mu$m, corresponding to the length scale of the smallest network constituents (capillaries), this study provided novel findings, revealing a very peculiar network structure in healthy and pathological tissue, which combines several paradigms of graph theory, which have, as far as we found, not been observed coinciding in real networks. Some properties were previously even assumed to rule each other out (see the discussion in publication IV). On larger length scales, the modular community analysis also suggested that vascular clusters form a small-world network throughout a healthy brain hemisphere, although a certain confirmation of this was not possible with the available data. A clear observation and major result in publication IV was the dramatic dismantling of modular vessel communities by glioblastoma.

Relatively new 3D microscopic imaging techniques with high resolution and large field-of-view, as well as recent advances in the availability of computational power and RAM have only enabled such analyses of real, large-scale vascular network connectivity. The computational load and challenges such analyses bear could only be handled with custom-developed numerical processing, resource-sparing coding, and the availability of high performance computing (HPC) machines, generously provided by the bwForCluster through the bwHPC and bwHPC-C5 projects of the state of Baden-Württemberg. The graph theoretical quantifications presented in publication IV significantly augmented previous topological characterizations of vascular networks, usually focused on particular brain regions and smaller tissue sections [55, 231, 232, 247, 248], suggesting that cerebrovascular networks at capillary resolution form a peculiar class of transport

networks with nontrivial property combinations. These findings remain to be verified in independent studies. In coming years, a better comprehension of vascular topology on different levels is expected to improve our understanding of complex pathological phenomena such as neurovascular uncoupling [26, 27].

Originally, the determination of mean capillary radii and fractional vessel volumes was meant to facilitate a comparison of the transverse relaxation predicted by the SCM (from section 1.2.4) with realistic parameter ranges found for healthy brain tissue and glioblastoma. Comparing tumor vasculature with healthy cerebrovasculature throughout the entire brain, it quickly became clear that vessel radii and cerebral blood volume were not sufficient to capture the main aspects of tumor-induced vessel remodeling (as demonstrated in publications II - IV and conform with previous literature discussed in these articles). Also, a segregation of the individual aspects of remodeling is not instructive in the context of treating the inverse problem of mapping dephasing characteristics to underlying vessel properties, as was shown in publication I; where spatial disorder, variance of radii, and diffusion turned out to have similar effects on transverse relaxation. This was an additional motivator to directly simulate the dephasing effects of realistic vessel geometries, as presented in publication V.

Despite real microvascular architectures being the substrate for the dephasing simulations, the numerical methodology in publication V was riddled with approximations and simplifying conditions, common in such studies [17, 18, 229]. For one, only extravascular signal contributions were considered in order to evade making assumptions about blood flow, a complex and computationally intense matter of its own (see section 4.2). Hematocrit, blood oxygen saturation, and the distribution of deoxyhemoglobin were modeled as constant throughout the vasculature within a virtual voxel, justifiable as a first approximation for short time scales of dephasing and small voxel dimensions below 1 mm. NMR signal was assumed to originate only from water protons, neglecting contributions from other hydrogen atoms. Additional susceptibility-relevant inclusions such as iron accumulations [249] and other sources of B_0 inhomogeneity were ignored. Excitation pulses were idealized with instantaneous effect and without B_1 inhomogeneities. Lastly, partial volume effects from white matter, gray matter, and cerebrospinal fluid were ignored and extravascular space was modeled as isotropic without additional diffusion barriers, with equal diffusion strength in all tissues to avoid introducing systematic variability and focus on differences induced by vascular geometry. Possible extensions towards more realistic conditions are discussed in section 4.2.

The segmentation of vessels from fluorescence microscopy presented a critical step in publications II - V. Imaging artifacts and different qualities of vessel labeling and tissue clearing add artificial variability to the datasets from different mice. Further, most of the quantified geometric parameters presented in publications III and IV strongly depend

on the vessel segmentation. The topological parametrizations presented in publications II and IV, on the other hand, are robust against segmentation variations, since these typically affect vessel thickness much more than the spatial distribution or network connectivity (with the exception of insufficient labeling effects). The segmentation toolkit used in this thesis (`ilastik` [157]) was chosen due to its generality, robustness to varying contrast intensities, and flexibility to include different features based on intensity, texture, and edge information, which could be tuned to the data [158]. This was helpful in segmenting out different forms of artifacts, such as shadow streaks from badly cleared tissue sections, which rarely occurred but could mimic very long, straight vessels. Many specialized tools have been developed incorporating different metrics and methods for vessel segmentation throughout the years [250]. Recently, convolutional neural networks have outperformed more classical methods, producing excellent vascular segmentations on large scales [251, 252]. The segmentations used in this thesis can readily be replaced with more specialized methods to further improve data quality.

Regardless of all the simplifications in publication V, making healthy and pathological tissue more similar than it would be in reality (*e.g.*, concerning diffusion coefficients and local blood oxygen saturations), the classification results based solely on single-voxel dephasing call for further studies in this direction. High classification accuracies of up to ∼95%, which could be achieved in publication V without using any voxel neighborhoods or information about the anatomical origin of a signal, are highly motivating, as they stand out in comparison to other studies with similar aim but far more elaborate MRI acquisitions, *e.g.*, with contrast enhancement, diffusion weighting, or spectroscopic imaging [201, 253]. Due to the computational complexity of further numerical refinements (see section 4.2), experimental analogies may be the more economic pathway now that a proof-of-principle for a pathology-specific artificial MRI contrast based on machine-aided dephasing interpretations has been provided.

A major open question remains for now, though: how well do the simulated differences of transverse relaxation in brain tumors shine through over all the other influences affecting the measurable signal in real MRI? Pertinent factors with an impact on the voxel signal intensity are manifold (see chapter 1). The cellular environment of extravascular space is far more complex than could be simulated, but has its own effects on T_2^* weighting [19], and in vivo physiology can be quite dynamic and difficult to model [18, 45], especially on large length scales, including breathing, pulsatile flow, and metabolic dynamics [46, 248]. Furthermore, hardware imperfections and patient movement, as well as physiological motion within the body complicate imaging with a voxel-level registration. Nonetheless, this is possible and imaging can be coordinated with the cardiac cycle and breathing to mitigate pulsatile blood flow effects [47] for better correspondence to simulated conditions through respiratory or cardiac gating.

A sensible continuation of this research project should involve a validation of the simulated dephasing effects from capillary blood in corresponding MRI experiments. Two-photon microscopy is a powerful method for in vivo imaging of blood vessel geometry, hemodynamics, and even oxygen saturation with sub-micrometer resolutions [254–256]. Recently, fMRI was performed in combination with this technique for microscopic blood oxygenation and flow information in mice for which a corresponding BOLD fMRI signal was acquired [257]. I have been involved with a closely collaborating research group in the development of a similar "correlated imaging" approach [49], which is meant to answer the above question and unveil differences and possible corrections between the simulated and truly measured relaxation.

4.2 Outlook

The research conducted within the course of this thesis paves the road to many avenues that can be pursued further to build on the attained insights and developed tools. As mentioned above, the microscopic data acquisition performed for the analyses in publications II - V, namely fluorescent light sheet microscopy [258], can be replaced by analogous high-resolution imaging techniques such as multi-photon microscopy [52], microCT [53, 150], or custom-built microscopy setups [259], ideally including hemodynamic information and blood oxygen saturation in live situations [255, 256]. Spatial variations of hematocrit and blood oxygenation could be implemented into the NMR simulations presented in publication V in a very straight-forward way. As tumors are known to have distinct metabolism, such an augmentation is expected to improve classification accuracies further. A correlation of topological connectivity features and measured blood property distributions would also be interesting and may provide valuable explanations for tumor-related neurovascular uncoupling [26].

If experimental imaging of the hemodynamics is not an available privilege, blood flow simulations could provide more realistic distributions of hematocrit, blood oxygenation and flow [260]. Numerous ways to go about this have been reported in literature, *e.g.*, [45, 235, 236, 247, 248, 261–263]. Recently, a hybrid approach was presented to combine individual models of the vasculature at different scales; specifically, the capillary bed and the arteriolar and venular vessel trees, with specialized coupling terms at the interface [139]. Such techniques offer an efficient way to model multiscale networks and account for the profound differences of structure and topology at different scales [220, 264], as well as complex rheological effects, such as the varying viscosity of blood depending on the capillary radius and dynamic vascular adaptation [261, 265]. A second spin pool for blood water could easily be added to the simulations with knowledge about blood flow. Specifically relevant for studies of tumor vasculature, variable vessel permeability

can be taken into account in hemodynamic and dephasing simulations, as tumors have been found to produce leaky vessels with a hyperpermeable lumen, which increases diffusion into and out of vessels [266]. Modeling of the extravascular compartment could be refined, *e.g.*, by implementing anisotropic diffusion along white matter tracts and differing proton densities in white and gray matter.

Furthermore, additional MRI contrasts can easily be implemented in the simulations of publications I and V. The fundamental contrasts with T_1 and intrinsic T_2, as described in section 1.2.3, obey exponential forms and can be multiplied on top of the more complex dephasing attenuation post-simulation. For an inclusion of diffusion effects in spin echo simulations, 180° pulses and imaging gradients have already been implemented numerically in the `C++` framework. Diffusion weighting can readily be achieved with the option of simulating arbitrary gradient pulse applications during dephasing. Since the magnetization magnitude and phase are both simulated, susceptibility mapping calculations from the simulated signal are already possible as well [195, 267]. With numerical variations of the blood susceptibility, BOLD and DSC simulations can be conducted with the `C++` code as well [17, 18, 229]. This could be combined with blood flow simulations for a more realistic evolution of dynamic contrast.

Especially with an extension to multiparametric MRI with several contrasts, fingerprinting in analogy to vMRF [227, 229] could be conducted in several ways. In combination with the quantification tools presented in publications II - IV of this thesis, geometric and topological properties of real angio-architectures could be matched with the MRI signals they are associated with. This could be done with a dictionary matching approach, as has been attempted before [227–229], or with the help of machine learning, as proposed in this thesis. To introduce systematic variations of vessel characteristics, similar to the classical dictionary building approaches in previous vMRF implementations, sophisticated vascular network models should be used to construct artificial architectures with geometric and topological properties matching real vasculature in the tissue types to be mimicked.

Recently, multifaceted models have been proposed that capture many aspects of microvasculature and allow for synthetic replications of a wide range of realistic properties [207]. Mathematical models specialized on tumor-characteristic vasculature are also available and could also be used for a large-scale production of numerical tumor phantoms for dictionary building [54, 151]. Such modeling approaches can be tested and refined with the developed toolkits from this research project by quantifying real microvasculature and transferring the results as inputs to the models. Further, the NMR dephasing effects of numerical phantoms built from different models can be simulated and compared to the effects of real vessel architectures in order to search for suitable models in the context of microvessel characterization based on voxel-wise MRI

processing. The most impactful aspects of microvascular geometry on MRI could be uncovered this way.
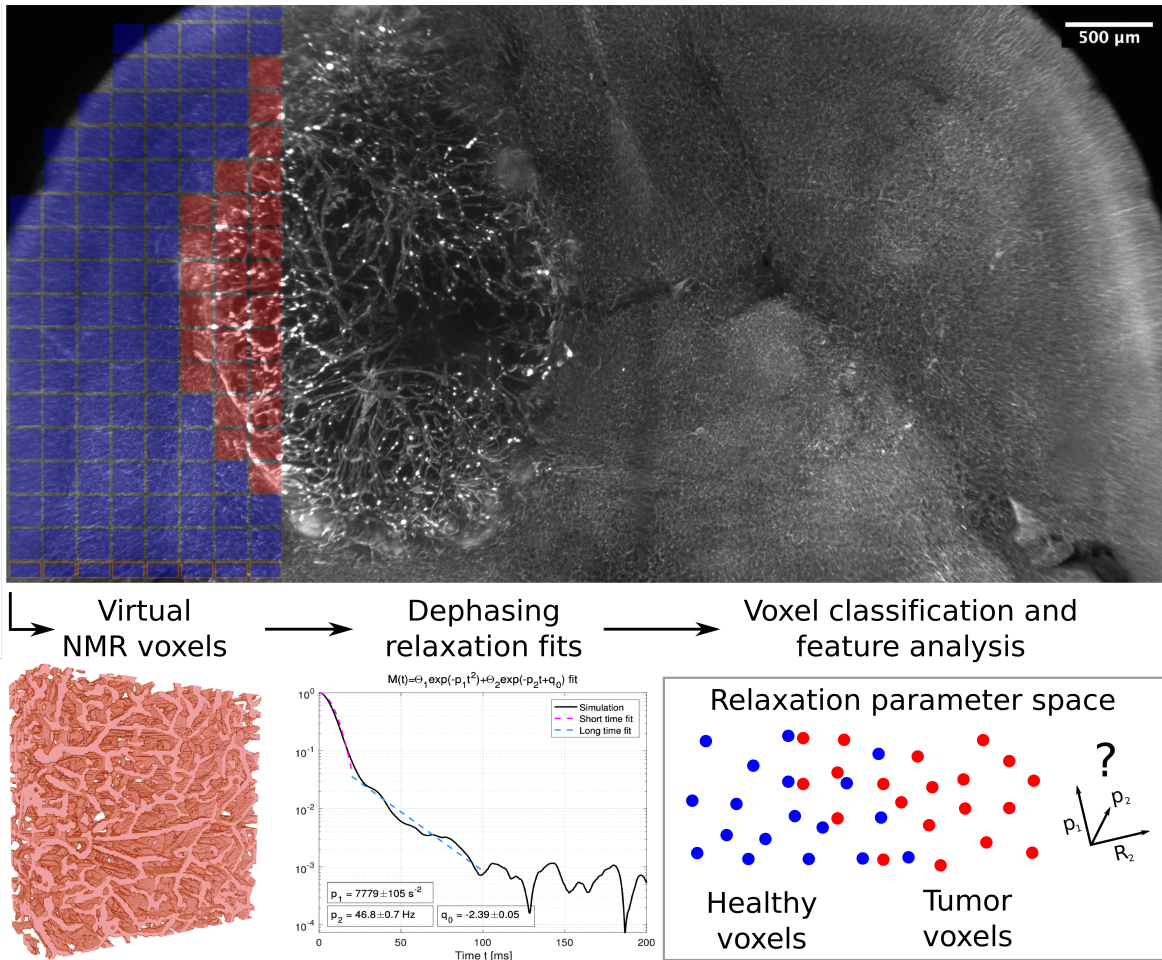

Figure 4.1: Conceptual depiction of the enabled development of an artificial MRI contrast, defined by a binary classification: healthy brain tissue vs. glioblastoma multiforme (as tested in the proof-of-principle in publication V). An average intensity projection of high-resolution fluorescence light sheet microscopy data of a mouse brain with U87 glioblastoma in the right hemisphere is partially overlaid with semitransparent, virtual NMR voxels to demonstrate the concept of artificial contrast; blue voxels correspond to healthy brain tissue and red voxels to tumor tissue. This classification is learned based on advanced dephasing parametrizations of numerically simulated transverse relaxation in virtual voxels with known tissue type, extracted from training samples, as introduced in publication V. The training data can be used to determine NMR feature importance, relations, and consequently, the most sensible settings for MRI sequences in analogous experimental acquisitions (*e.g.*, weighting schemes and echo times T_E to attain the most important relaxation features). With an increasing availability of training voxels, relaxation fitting could be bypassed using automated feature extraction or direct time series interpretations with artificial neural networks.

166

An advantage of simulating MRI numerically is the wide range of contrasts and imaging settings that can be emulated fast and cheap. Another aim of the developed numerical toolkit is to enable an optimization of MRI protocols for definitions of specific artificial contrasts. After simulating a large number of different imaging settings, machine learning algorithms or iterative reduction methods can reveal the most important acquisition types for a successful signal classification or regression. Feature importance and sensitivity analyses can reveal the relevant MRI contrasts and echo time regimes for a specific artificial contrast definition (see **Fig.** 4.1), guiding the design of an optimal MRI sequence for experimental translation with minimally required acquisitions. Ultimately, the numerical tools presented here can be used to investigate which vessel characteristics could be estimated from which MRI sequences in an idealized environment without other perturbing factors. This could be applied to diverse organs and pathologies in attempts to find reliable and useful artificial MRI contrasts based on organ- and contrast-specific sequences.

5 Summary

Many serious pathologies evolve with tissue-altering effects on the cellular length scale. This is why it is a great ambition of the medical imaging community to develop non-invasive microstructural imaging modalities, ideally sensitive to some microscopic aspects which are specifically modified by diseases. With a wide range of possible contrast settings in soft tissue and a fundamental sensitivity to the tissue microenvironment, MRI represents the ideal candidate for such developments. This thesis deals with the remodeling effects of brain tumors on microvasculature and in turn, its effects on transverse NMR relaxation. A comprehensive numerical framework was constructed for automated quantifications of real vascular structures and simulations of its effects on local NMR measurements. Both aspects can be correlated in this framework using machine learning.

Transverse relaxation is a fundamental process causing signal decay in all NMR and MRI measurements, which is influenced by magnetic field inhomogeneities within the signal-yielding volume (referred to as a voxel in imaging). The protein deoxyhemoglobin, contained in deoxygenated red blood cells, is paramagnetic with respect to the soft tissue environment. The presence of partially deoxygenated blood causes characteristic dipolar field distortions around vessels, which contributes to transverse relaxation. Theoretical treatments of this situation with idealized vessel models have shown well-defined effects of vessel geometry on the transverse relaxation, which may be used to make inferences about the microvasculature underlying MRI voxels with characteristic decay functions.

Although malignant tumors are known to remodel the vasculature of afflicted tissue, the resulting structures are difficult to describe with singular parameters and simple vessel models. There is high intra- und inter-tumoral heterogeneity concerning the resulting vascular structures, also depending on tumor type and grade. Despite a high variability of individual aspects, microvasculature associated with brain tumors deviates from its healthy counterpart from many perspectives. It can be suspected that the collective alterations of healthy vascular architectures by malignant brain tumors could influence transverse relaxation in a characteristic way, such that it can be used for tumor detection based in local NMR measurements.

This thesis begins with an introduction to the fundamentals of MRI and the mechanisms behind transverse relaxation, followed by an overview over classical model treatments of the vascular influence on transverse magnetization decay under different conditions concerning diffusion, blood susceptibility, and external field strength. To conclude the background information to this research project, different established cancer imaging techniques are briefly covered and the difficulties with endogenous signal

interpretations (without paramagnetic contrast agents) for microvascular characterization are examined. The introduction motivates a search for more elaborate vessel models to parametrize local and nonlocal alterations due to tumor growth, which could explain characteristic effects observed in MRI based on transverse relaxation, *e.g.*, BOLD fMRI.

Publication I extends the classical, well-studied cylindrical vessel model of transverse NMR relaxation by incorporating an order parameter which quantifies the spatial regularity of vessel distributions on a continuous range. It was found that this model is non-injective, concerning the effects of capillary regularity and geometry on transverse relaxation. An inverse mapping of transverse decay characteristics to microvascular disorder, radius distribution, and diffusion strength was difficult in this simplified model, but a definite correlation between transverse relaxation strength and the order parameter was found. In publication II, the regularity parametrization underlying publication I was applied to real microvasculature in brain tumors and healthy cerebrovascular networks in a mouse model. The ground-truth 3D vessel structure of entire brains was imaged with fluorescent light sheet microscopy and segmented for analysis. The order parameter showed high variance in both tissue types, but could allow for an identification of pathological tissue in large-scale statistical comparisons.

The difficulty of a reliable estimate of the order parameter from transverse relaxation and the large variance of this parameter in healthy brain tissue motivated a more extensive characterization of real microvasculature. Publication III demonstrated the quantification of a wide range of geometric vascular properties in a partitioned manner for cuboids reminiscent of MRI voxels in dimensions and arrangement (in a tiling box manner). The custom-developed quantifications were validated with model cylinders with known radii, different orientations and relations to the anisotropic 3D image resolution. Vessel quantifications were demonstrated in different brain regions and tumor core and periphery using custom masking with high flexibility. Different brain and tumor regions showed distinct microvascular characteristics.

In publication IV, the cerebrovascular networks were quantified in their entirety. Custom implementations of large-scale topological analyses of network connectivity were demonstrated and yielded novel findings concerning the network structure of the largest cerebrovascular networks analyzed this way to date. Studying two brain tumor models, it was found that glioblastoma multiforme had highly detrimental effects on large hierarchical clustering structures uncovered in the healthy brain vasculature. The graph theoretical parametrizations and the findings presented in tumors may contribute to a better understanding of the effects of brain tumors on the complex coupling between neuronal activity and hemodynamic response, known as neurovascular coupling. This may facilitate an improved interpretation of fMRI measurements based on transverse relaxation, and their peculiarities observed with brain tumors.

Finally, the focus returns to local effects of tumor growth on transverse magnetization decay in publication V. The real angio-architectures analyzed in publications II - IV were used as a substrate for NMR simulations to study the effects of real microvascular geometry on transverse relaxation. Without a confounding vessel geometrical model (as opposed to publication I), it was tested how well individual voxel signals could be differentiated between tumors and healthy brain tissue only based on the transverse decay as influenced by the local capillary geometry. A numerical framework to conduct large-scale MRI simulations using high performance computing for quick data generation was developed and introduced. Using support vector machines, motivating classification accuracies of 70-95% were reached without any consideration of voxel neighborhoods or anatomical signal origin. This provided a proof-of-principle for voxel-wise signal classifications for artificial contrast definitions, *e.g.*, tumor vs. healthy tissue classification, based on transverse relaxation with endogenous contrast and constant blood oxygenation. This may be a promising new approach for early tumor detection.

Microstructural imaging is expected to gain importance in clinical practice and become more specialized on diverse diseases. The combination of MRI and machine learning presents a promising pairing for this type of specialization. Dictionary-based techniques have been arising with different use cases, but mostly omitting machine learning up to this point. In this thesis, numerical tools were developed for the processing and analysis of large 3D microscopy or microCT datasets of real microvasculature and simulations of its effects in MRI, with automated tools incorporating machine learning to build a bridge between vessel geometry and associated NMR signal characteristics. This numerical framework represents the foundation for data-driven explorations of new microstructure-sensitive MRI sequences and NMR-assessable microvascular characteristics.

A Bibliography

[1] R. W. Brown, Y.-C. N. Cheng, E. M. Haacke, M. R. Thompson, and R. Venkatesan. *Magnetic resonance imaging: Physical principles and sequence design.* John Wiley & Sons Ltd, Chichester, UK, 2 edition, 2014.

[2] R. Pohmann, M. Von Kienlin, and A. Haase. Theoretical Evaluation and Comparison of Fast Chemical Shift Imaging Methods. *Journal of Magnetic Resonance*, 129(2):145–160, 1997.

[3] A. Kumar, R. R. Ernst, and K. Wüthrich. A two-dimensional nuclear Overhauser enhancement (2D NOE) experiment for the elucidation of complete proton-proton cross-relaxation networks in biological macromolecules. *Biochemical and Biophysical Research Communications*, 95(1):1–6, 1980.

[4] K. M. Jones, A. C. Pollard, and M. D. Pagel. Clinical applications of chemical exchange saturation transfer (CEST) MRI. *Journal of Magnetic Resonance Imaging*, 47(1):11–27, 2018.

[5] P. C. M. van Zijl, W. W. Lam, J. Xu, L. Knutsson, and G. J. Stanisz. Magnetization Transfer Contrast and Chemical Exchange Saturation Transfer MRI. Features and analysis of the field-dependent saturation spectrum. *NeuroImage*, 168:222–241, 2018.

[6] L. R. Buschle, F. T. Kurz, T. Kampf, S. M. F. Triphan, H.-P. Schlemmer, and C. H. Ziener. Diffusion-mediated dephasing in the dipole field around a single spherical magnetic object. *Magnetic Resonance Imaging*, 33(9):1126–1145, 2015.

[7] C. H. Ziener, W. R. Bauer, and P. M. Jakob. Transverse relaxation of cells labeled with magnetic nanoparticles. *Magnetic Resonance in Medicine*, 54(3):702–706, 2002.

[8] F. T. Kurz, T. Kampf, S. Heiland, M. Bendszus, H.-P. Schlemmer, and C. H. Ziener. Theoretical model of the single spin-echo relaxation time for spherical magnetic perturbers. *Magnetic Resonance in Medicine*, 71(5):1888–1895, 2014.

[9] D. A. Yablonskiy and E. M. Haacke. Theory of NMR signal behavior in magnetically inhomogeneous tissues: The static dephasing regime. *Magnetic Resonance in Medicine*, 32(6):749–763, 1994.

[10] V. G. Kiselev and S. Posse. Analytical theory of susceptibility induced NMR signal dephasing in a cerebrovascular network. *Physical Review Letters*, 81(25):5696–5699, 1998.

[11] W. R. Bauer and W. Nadler. Spin Dephasing in the Extended Strong Collision Approximation. *Physical Review E*, 65(6):066123, 2002.

[12] A. L. Sukstanskii and D. A. Yablonskiy. Gaussian approximation in the theory of MR signal formation in the presence of structure-specific magnetic field inhomogeneities. *Journal of Magnetic Resonance*, 163(2):236–247, 2003.

[13] C. H. Ziener, F. T. Kurz, and T. Kampf. Free induction decay caused by a dipole field. *Physical Review E*, 91(3):032707, 2015.

[14] A. L. Sukstanskii and D. A. Yablonskiy. Theory of FID NMR Signal Dephasing Induced by Mesoscopic Magnetic Field Inhomogeneities in Biological Systems. *Journal of Magnetic Resonance*, 151(1):107–117, 2001.

[15] F. T. Kurz, L. R. Buschle, A. Hahn, J. M. E. Jende, M. Bendszus, S. Heiland, and C. H. Ziener. Diffusion effects in myelin sheath free induction decay. *Journal of Magnetic Resonance*, 297:61–75, 2018.

[16] D. Ma, E. Y. Pierre, Y. Jiang, M. D. Schluchter, K. Setsompop, V. Gulani, and M. A. Griswold. Music-based magnetic resonance fingerprinting to improve patient comfort during MRI examinations. *Magnetic Resonance in Medicine*, 75(6):2303–2314, 2016.

[17] L. Gagnon, S. Sakadžić, F. Lesage, J. J. Musacchia, X. Lefebvre, Q. Fang, M. A. Yücel, K. C. Evans, E. T. Mandeville, J. Cohen-Adad, J. R. Polimeni, M. A. Yaseen, E. H. Lo, D. N. Greve, R. B. Buxton, A. M. Dale, A. Devor, and D. A. Boas. Quantifying the microvascular origin of bold-fMRI from first principles with two-photon microscopy and an oxygen-sensitive nanoprobe. *Journal of Neuroscience*, 35(8):3663–3675, 2015.

[18] É. Genois, L. Gagnon, J. Guilbert, S. Sakadžić, A. Devor, D. A. Boas, and M. Desjardins. First principle modeling of simultaneous VASO and BOLD fMRI with two-photon microscopy for optimal quantification of CBV changes in humans. In *Proceedings of SPIE*, volume 10864, page 108640V, 2019.

[19] X. Ulrich and D. A. Yablonskiy. Separation of cellular and BOLD contributions to T2* signal relaxation. *Magnetic Resonance in Medicine*, 75(2), 2016.

[20] S. Ogawa, T. M. Lee, A. R. Kay, and D. W. Tank. Brain magnetic resonance imaging with contrast dependent on blood oxygenation. *Proceedings of the National Academy of Sciences*, 87(24):9868–9872, 1990.

[21] G. J. M. The BOLD effect. *Methods in Molecular Biology*, 771:153–169, 2011.

[22] A. Gilead and M. Neeman. Dynamic remodeling of the vascular bed precedes tumor growth: MLS ovarian carcinoma spheroids implanted in nude mice. *Neoplasia*, 1(3):226–230, 1999.

[23] P. Carmeliet and R. K. Jain. Angiogenesis in cancer and other diseases. *Nature*, 407:249–257, 2000.

[24] R. K. Jain, E. di Tomaso, D. G. Duda, J. S. Loeffler, A. G. Sorensen, and T. T. Batchelor. Angiogenesis in brain tumours. *Nature Reviews Neuroscience*, 8:610–622, 2007.

[25] D. Fukumura, D. G. Duda, L. L. Munn, and R. K. Jain. Tumor Microvasculature and Microenvironment: Novel Insights Through Intravital Imaging in Pre-Clinical Models. *Microcirculation*, 17:206–225, 2010.

[26] R. W. Pak, D. H. Hadjiabadi, J. Senarathna, S. Agarwal, N. V. Thakor, J. J. Pillai, and A. P. Pathak. Implications of neurovascular uncoupling in functional magnetic resonance imaging (fMRI) of brain tumors. *Journal of Cerebral Blood Flow & Metabolism*, 37(11):3475–3487, 2017.

[27] S. Cai, Z. Shi, C. Jiang, K. Wang, L. Chen, L. Ai, and L. Zhang. Hemisphere-specific functional remodeling and its relevance to tumor malignancy of cerebral glioma based on resting-state functional network analysis. *Frontiers in Neuroscience*, 14:1410, 2021.

[28] T. H. Jochimsen, D. Ivanov, D. V. Ott, W. Heinke, R. Turner, H. E. Möller, and J. R. Reichenbach. Whole-brain mapping of venous vessel size in humans using the hypercapnia-induced BOLD effect. *NeuroImage*, 51(2):765–774, 2010.

[29] Y. Shen, I. M. Pu, T. Ahearn, M. Clemence, and C. Schwarzbauer. Quantification of venous vessel size in human brain in response to hypercapnia and hyperoxia using magnetic resonance imaging. *Magnetic Resonance in Medicine*, 69(6):1541–1552, 2013.

[30] C. C. Quarles, L. C. Bell, and A. M. Stokes. Imaging vascular and hemodynamic features of the brain using dynamic susceptibility contrast and dynamic contrast enhanced MRI. *NeuroImage*, 187:32–55, 2019.

[31] A. Romano, M. C. R. Espagnet, L. F. Calabria, V. Coppola, L. F. Talamanca, V. Cipriani, G. Minniti, A. Pierallini, L. M. Fantozzi, and A. Bozzao. Clinical applications of dynamic susceptibility contrast perfusion-weighted MR imaging in brain tumours. *Radiol Med*, 117(3):445–460, 2012.

[32] N. B. Semmineh, J. Xu, J. L. Boxerman, G. W. Delaney, P. W. Cleary, J. C. Gore, and C. C. Quarles. An efficient computational approach to characterize DSC-MRI signals arising from three-dimensional heterogeneous tissue structures. *PloS one*, 9(1):e84764, 2014.

[33] C. T. Farrar, W. S. Kamoun, C. D. Ley, Y. R. Kim, S. J. Kwon, G. Dai, B. R. Rosen, E. Di Tomaso, R. K. Jain, and A. G. Sorensen. In vivo validation of MRI vessel caliber index measurement methods with intravital optical microscopy in a U87 mouse brain tumor model. *Neuro-Oncology*, 12(4):341–350, 2010.

[34] I. Troprès, N. Pannetier, S. Grand, B. Lemasson, A. Moisan, M. Péoc'h, C. Rémy, and E. L. Barbier. Imaging the Microvessel Caliber and Density: Principles and Applications of Microvascular MRI. *Magnetic Resonance in Medicine*, 73(1):325–341, 2015.

[35] J. Dennie, J. B. Mandeville, J. L. Boxerman, S. D. Packard, B. R. Rosen, and R. M. Weisskoff. NMR imaging of changes in vascular morphology due to tumor angiogenesis. *Magnetic Resonance in Medicine*, 40:793–799, 1998.

[36] K. E. Emblem, K. Mouridsen, A. Bjornerud, C. T. Farrar, D. Jennings, R. J. H. Borra, P. Y. Wen, P. Ivy, T. T. Batchelor, B. R. Rosen, R. K. Jain, and A. G. Sorensen. Vessel architectural imaging identifies cancer patient responders to anti-angiogenic therapy. *Nature Medicine*, 19:1178–1183, 2013.

[37] I. Digernes, A. Bjørnerud, S. A. S. Vatnehol, G. Løvland, F. Courivaud, E. Vik-Mo, T. R. Meling, and K. E. Emblem. A theoretical framework for determining cerebral vascular function and heterogeneity from dynamic susceptibility contrast MRI. *Journal of Cerebral Blood Flow & Metabolism*, 37(6):2237–2248, 2017.

[38] S.-G. Kim and S. Ogawa. Biophysical and physiological origins of blood oxygenation level-dependent fMRI signals. *Journal of Cerebral Blood Flow & Metabolism*, 32:1188–1206, 2012.

[39] D. Attwell, A. M. Buchan, S. Charpak, M. Lauritzen, B. A. Macvicar, and E. A. Newman. Glial and neuronal control of brain blood flow. *Nature*, 468(7321):232–243, 2010.

[40] R. B. Buxton. Interpreting oxygenation-based neuroimaging signals: the importance and the challenge of understanding brain oxygen metabolism. *Frontiers in Neuroenergetics*, 2:8, 2010.

[41] R. B. Buxton. The physics of functional magnetic resonance imaging (fMRI). *Reports on Progress in Physics*, 76(9):96601, 2013.

[42] K. Zhang, S. D. Yun, S. M. F. Triphan, V. J. Sturm, L. R. Buschle, A. Hahn, S. Heiland, M. Bendszus, H.-P. Schlemmer, J. N. Shah, C. H. Ziener, and F. T. Kurz. Vessel architecture imaging using multiband gradient-echo/spin-echo EPI. *PLoS ONE*, 14(8), 2019.

[43] C. R. Fisel, J. L. Ackerman, R. B. Buxton, L. Garrido, J. W. Belliveau, B. R. Rosen, and T. J. Brady. MR contrast due to microscopically heterogeneous magnetic susceptibility: numerical simulations and applications to cerebral physiology. *Magnetic Resonance in Medicine*, 17(2):336–347, 1991.

[44] D. A. Yablonskiy. Quantitation of intrinsic magnetic susceptibility-related effects in a tissue matrix. Phantom study. *Magnetic Resonance in Medicine*, 39(3):417–428, 1998.

[45] A. R. Pries, T. W. Secomb, and P. Gaehtgens. Biophysical aspects of blood flow in the microvasculature. *Cardiovascular Research*, 32(4):654–667, 1996.

[46] S. Lorthois, F. Cassot, and F. Lauwers. Simulation study of brain blood flow regulation by intra-cortical arterioles in an anatomically accurate large human vascular network. part ii: Flow variations induced by global or localized modifications of arteriolar diameters. *NeuroImage*, 54(4):2840–2853, 2011.

[47] T. P. Santisakultarm, N. R. Cornelius, N. Nishimura, A. I. Schafer, R. T. Silver, P. C. Doerschuk, W. L. Olbricht, and C. B. Schaffer. In vivo two-photon excited fluorescence microscopy reveals cardiac- and respiration-dependent pulsatile blood flow in cortical blood vessels in mice. *American Journal of Physiology - Heart and Circulatory Physiology*, 302:H1367–H1377, 2012.

[48] M. O. Breckwoldt, J. Bode, F. T. Kurz, A. Hoffmann, K. Ochs, M. Ott, K. Deumelandt, T. Krüwel, D. Schwarz, M. Fischer, X. Helluy, D. Milford, K. Kirschbaum, G. Solecki, S. Chiblak, A. Abdollahi, F. Winkler, W. Wick, M. Platten, S. Heiland, M. Bendszus, and B. Tews. Correlated magnetic resonance imaging and ultramicroscopy (MR-UM) is a tool kit to asses the dynamics of glioma angiogenesis. *Elife*, 5:e11712, 2016.

[49] M. O. Breckwoldt, J. Bode, F. Sahm, T. Krüwel, G. Solecki, A. Hahn, P. Wirthschaft, A. S. Berghoff, M. Haas, V. Venkataramani, A. von Deimling, W. Wick, C. Herold-Mende, S. Heiland, M. Platten, M. Bendszus, F. T. Kurz, F. Winkler, and B. Tews. Correlated MRI and Ultramicroscopy (MR-UM) of Brain Tumors Reveals Vast Heterogeneity of Tumor Infiltration and Neoangiogenesis in Preclinical Models and Human Disease. *Frontiers in Neuroscience*, 12:1004, 2019.

[50] M. Osswald, E. Jung, F. Sahm, G. Solecki, V. Venkataramani, J. Blaes, S. Weil, H. Horstmann, B. Wiestler, M. Syed, L. Huang, M. Ratliff, K. Karimian Jazi, F. T. Kurz, T. Schmenger, D. Lemke, M. Gömmel, M. Pauli, Y. Liao, P. Häring, S. Pusch, V. Herl, C. Steinhäuser, D. Krunic, M. Jarahian, H. Miletic, A. S. Berghoff, O. Griesbeck, G. Kalamakis, O. Garaschuk, M. Preusser, S. Weiss, H. Liu, S. Heiland, M. Platten, P. E. Huber, T. Kuner, A. von Deimling, W. Wick, and F. Winkler. Brain tumour cells interconnect to a functional and resistant network. *Nature*, 528:93–98, 2015.

[51] E. E. Hoover and J. A. Squier. Advances in multiphoton microscopy technology. *Nature Photonics*, 7(2):93–101, 2013.

[52] C. Lefort. A review of biomedical multiphoton microscopy and its laser sources. *Journal of Physics D: Applied Physics*, 50(42):423001, 2017.

[53] A. C. Thompson, J. Llacer, L. Campbell Finman, E. B. Hughes, J. N. Otis, S. Wilson, and H. D. Zeman. Computed tomography using synchrotron radiation. *Nuclear Instruments and Methods In Physics Research*, 222(1-2):319–323, 1984.

[54] H. Rieger and M. Welter. Integrative models of vascular remodeling during tumor growth. *Wiley Interdisciplinary Reviews: Systems Biology and Medicine*, 7(3):113–129, 2015.

[55] F. Schmid, M. J. P. Barrett, P. Jenny, and B. Weber. Vascular density and distribution in neocortex. *NeuroImage*, 197:792–805, 2019.

[56] M. E. Peskin and D. V. Schroeder. *An Introduction to Quantum Field Theory*. Westview Press, Boulder, Colorado, USA, 1995.

[57] G. Schneider, A. Mooser, M. Bohman, N. Schön, J. Harrington, T. Higuchi, H. Nagahama, S. Sellner, C. Smorra, K. Blaum, Y. Matsuda, W. Quint, J. Walz, and S. Ulmer. Double-trap measurement of the proton magnetic moment at 0.3 parts per billion precision. *Science*, 358(6366):1081–1084, 2017.

[58] L. G. Hanson. Is quantum mechanics necessary for understanding magnetic resonance? *Concepts in Magnetic Resonance Part A*, 32A(5):329–340, 2008.

[59] L. Allen and J. H. Eberly. *Optical Resonance and Two-Level Atoms.* Dover Publications, Inc., New York, USA, 1987.

[60] F. Bloch. Nuclear Induction. *Phys. Rev.*, 70(7-8):460–474, 1946.

[61] D. J. Griffiths. *Introduction to Electrodynamics.* Pearson Education Inc, New Jersey, USA, 3 edition, 1999.

[62] S. F. Keevil. Spatial localization in nuclear magnetic resonance spectroscopy. *Physics in Medicine and Biology*, 51:579–636, 2006.

[63] K. Glunde, D. Artemov, M. F. Penet, M. A. Jacobs, and Z. M. Bhujwalla. Magnetic resonance spectroscopy in metabolic and molecular imaging and diagnosis of cancer. *Chemical Reviews*, 110(5):3043–3059, 2010.

[64] S. Posse, R. Otazo, S. R. Dager, and J. Alger. MR spectroscopic imaging: Principles and recent advances. *Journal of Magnetic Resonance Imaging*, 37(6):1301–1325, 2013.

[65] J. R. Brender, S. Kishimoto, H. Merkle, G. Reed, R. E. Hurd, A. P. Chen, J. H. Ardenkjaer-Larsen, J. Munasinghe, K. Saito, T. Seki, N. Oshima, K. Yamamoto, P. L. Choyke, J. Mitchell, and M. C. Krishna. Dynamic Imaging of Glucose and Lactate Metabolism by 13 C-MRS without Hyperpolarization. *Scientific Reports*, 9(1):1–14, 2019.

[66] E. L. Hahn. Spin echoes. *Physical Review*, 80(4):580–594, 1950.

[67] J. Gimsa and L. Haberland. Electric and magnetic fields in cells and tissues. In F. Bassani, G. L. Liedl, and P. Wyder, editors, *Encyclopedia of Condensed Matter Physics*, pages 6–14. Elsevier, Oxford, 2005.

[68] A. Krogh. The number and distribution of capillaries in muscles with calculations of the oxygen pressure head necessary for supplying the tissue. *The Journal of Physiology*, 52:409–415, 1919.

[69] C. H. Ziener, W. R. Bauer, and P. M. Jakob. Frequency distribution and signal formation around a vessel. *Magnetic Resonance Materials in Physics, Biology and Medicine*, 18:225–230, 2005.

[70] H. C. Torrey. Bloch equations with diffusion terms. *Physical Review*, 104:563–565, 1956.

[71] C. H. Ziener, T. Kampf, G. Reents, H.-P. Schlemmer, and W. R. Bauer. Spin dephasing in a magnetic dipole field. *Physical Review E*, 85(5):051908, 2012.

[72] C. H. Ziener, T. Kampf, G. Melkus, V. Herold, T. Weber, G. Reents, P. M. Jakob, and W. R. Bauer. Local frequency density of states around field inhomogeneities in magnetic resonance imaging: Effects of diffusion. *Physical Review E*, 76:031915, 2007.

[73] F. Oberhettinger. *Tables of Bessel Transforms*. Springer, Berlin, Germany, 1972.

[74] J. D. Dickson, T. W. J. Ash, G. B. Williams, A. L. Sukstanskii, R. E. Ansorge, and D. A. Yablonskiy. Quantitative phenomenological model of the BOLD contrast mechanism. *Journal of Magnetic Resonance*, 212:17–25, 2011.

[75] V. G. Kiselev and S. Posse. Analytical model of susceptibility-induced MR signal dephasing: Effect of diffusion in a microvascular network. *Magnetic Resonance in Medicine*, 41(3):499–509, 1999.

[76] A. L. Sukstanskii and D. A. Yablonskiy. Gaussian approximation in the theory of MR signal formation in the presence of structure-specific magnetic field inhomogeneities. *Journal of Magnetic Resonance*, 163:236–247, 2003.

[77] A. L. Sukstanskii and D. A. Yablonskiy. Gaussian approximation in the theory of MR signal formation in the presence of structure-specific magnetic field inhomogeneities. Effects of impermeable susceptibility inclusions. *Journal of Magnetic Resonance*, 167:56–67, 2004.

[78] W. R. Bauer, W. Nadler, M. Bock, L. R. Schad, C. Wacker, A. Hartlep, and G. Ertl. Theory of the BOLD Effect in the Capillary Region: An Analytical Approach for the Determination of T_2^* in the Capillary Network of Myocardium. *Magnetic Resonance in Medicine*, 41:51–62, 1999.

[79] W. R. Bauer, W. Nadler, M. Bock, L. R. Schad, C. Wacker, A. Hartlep, and G. Ertl. Theory of coherent and incoherent nuclear spin dephasing in the heart. *Physical Review Letters*, 83(20):4215–4218, 1999.

[80] W. R. Bauer and W. Nadler. Spin dephasing in the extended strong collision approximation. *Physical Review E*, 65:066123, 2002.

[81] C. Ziener, M. Rückl, T. Kampf, W. R. Bauer, and H.-P. Schlemmer. Mathieu functions for purely imaginary parameters. *Journal of Computational and Applied Mathematics*, 236:4513–4524, 2012.

[82] C. Ziener and H.-P. Schlemmer. The inverse Laplace transform of the modified Lommel functions. *Integral Transforms and Special Functions*, 24:141–155, 2013.

[83] J. R. Less, T. C. Skalak, E. M. Sevick, and R. K. Jain. Microvascular architecture in a mammary carcinoma: Branching patterns and vessel dimensions. *Cancer Research*, 51:265–273, 1991.

[84] P. Carmeliet and R. Jain. Angiogenesis in cancer and other diseases. *Nature*, 407:249–257, 2000.

[85] S. Nallanthighal, J. P. Heiserman, and D.-J. Cheon. The role of the extracellular matrix in cancer stemness. *Frontiers in Cell and Developmental Biology*, 7:86, 2019.

[86] D. Hanahan and R. A. Weinberg. Hallmarks of cancer: The next generation. *Cell*, 144(5):646–674, 2011.

[87] J. N. Kather, A. Marx, C. C. Reyes-Aldasoro, L. R. Schad, F. G. Zöllner, and C.-A. Weis. Continuous representation of tumor microvessel density and detection of angiogenic hotspots in histological whole-slide images. *Oncotarget*, 5:1–14, 2015.

[88] K. Schregel, N. Nazari, M. O. Nowicki, M. Palotai, S. E. Lawler, R. Sinkus, P. E. Barbone, and S. Patz. Characterization of glioblastoma in an orthotopic mouse model with magnetic resonance elastography. *NMR in Biomedicine*, 31(10):e3840, 2018.

[89] A. P. Pathak, S. McNutt, T. Shah, F. Wildes, V. Raman, and Z. M. Bhujwalla. In Vivo "MRI Phenotyping" Reveals Changes in Extracellular Matrix Transport and Vascularization That Mediate VEGF-Driven Increase in Breast Cancer Metastasis. *PLoS one*, 8(5):e63146, 2013.

[90] Y. Gordon, S. Partovi, M. Müller-Eschner, E. Amarteifio, T. Bäuerle, M.-A. Weber, H.-U. Kauczor, and F. Rengier. Dynamic contrast-enhanced magnetic resonance imaging: fundamentals and application to the evaluation of the peripheral perfusion. *Cardiovascular Diagnosis and Therapy*, 4(2):147–64, 2014.

[91] L. Zhang. Glioma characterization based on magnetic resonance imaging: Challenge overview and future perspective. *Glioma*, 3(2):61–66, 2020.

[92] R. García-Figueiras, S. Baleato-González, A. R. Padhani, J. A. V.-C. Antonio Luna-Alcalá, E. Sala, J. C. Vilanova, D.-M. Koh, M. Herranz-Carnero, and H. A. Vargas. How clinical imaging can assess cancer biology. *Insights into Imaging*, 10:28, 2019.

[93] E. O. Stejskal and J. E. Tanner. Spin diffusion measurements: Spin echoes in the presence of a time-dependent field gradient. *The Journal of Chemical Physics*, 42(1):288–292, 1965.

[94] D. K. Jones, editor. *Diffusion MRI - Theory, Methods and Applications.* Oxford University Press, Oxford, UK, 2010.

[95] J. H. Jensen and J. A. Helpern. MRI quantification of non-Gaussian water diffusion by kurtosis analysis. *NMR in Biomedicine*, 23(7):698–710, 2010.

[96] V. Brancato, C. Cavaliere, M. Salvatore, and S. Monti. Non-Gaussian models of diffusion weighted imaging for detection and characterization of prostate cancer: a systematic review and meta-analysis. *Scientific Reports*, 9:16837, 2019.

[97] D. S. Novikov, E. Fieremans, S. N. Jespersen, and V. G. Kiselev. Quantifying brain microstructure with diffusion MRI: Theory and parameter estimation. *NMR in Biomedicine*, 32(4):e3998, 2019.

[98] J. Veraart, D. Nunes, U. Rudrapatna, E. Fieremans, D. K. Jones, D. S. Novikov, and N. Shemesh. Noninvasive quantification of axon radii using diffusion MRI. *eLife*, 9:e49855, 2020.

[99] M. Haris, S. K. Yadav, A. Rizwan, A. Singh, E. Wang, H. Hariharan, R. Reddy, and F. M. Marincola. Molecular magnetic resonance imaging in cancer. *Journal of Translational Medicine*, 13:313, 2015.

[100] H. Mehrabian, S. Myrehaug, H. Soliman, A. Sahgal, and G. J. Stanisz. Quantitative Magnetization Transfer in Monitoring Glioblastoma (GBM) Response to Therapy. *Scientific Reports*, 8:2475, 2018.

[101] J. Virostko, A. G. Sorace, C. Wu, D. Ekrut, A. M. Jarrett, R. M. Upadhyaya, S. Avery, D. Patt, B. Goodgame, and T. E. Yankeelov. Magnetization Transfer MRI of Breast Cancer in the Community Setting: Reproducibility and Preliminary Results in Neoadjuvant Therapy. *Tomography*, 5(1):44–52, 2019.

[102] E. Vinogradov, A. D. Sherry, and R. E. Lenkinski. CEST: From basic principles to applications, challenges and opportunities. *Journal of Magnetic Resonance*, 229:155–172, 2013.

[103] B. Wu, G. Warnock, M. Zaiss, C. Lin, M. Chen, Z. Zhou, L. Mu, D. Nanz, R. Tuura, and G. Delso. An overview of CEST MRI for non-MR physicists. *EJNMMI Physics*, 3(1):19, 2016.

[104] D. Paech, J. Windschuh, J. Oberhollenzer, C. Dreher, F. Sahm, J. E. Meissner, S. Goerke, P. Schuenke, M. Zaiss, S. Regnery, S. Bickelhaupt, P. Bäumer, M. Bendszus, W. Wick, A. Unterberg, P. Bachert, M. E. Ladd, H. P. Schlemmer, and A. Radbruch. Assessing the predictability of IDH mutation and MGMT methylation status in glioma patients using relaxation-compensated multipool CEST MRI at 7.0 T. *Neuro-Oncology*, 20(12):1661–1671, 2018.

[105] M. Zaiss, J. Windschuh, S. Goerke, D. Paech, J. E. Meissner, S. Burth, P. Kickingereder, W. Wick, M. Bendszus, H. P. Schlemmer, M. E. Ladd, P. Bachert, and A. Radbruch. Downfield-NOE-suppressed amide-CEST-MRI at 7 Tesla provides a unique contrast in human glioblastoma. *Magnetic Resonance in Medicine*, 77(1):196–208, 2017.

[106] Y. Yang, X. Qu, Y. Huang, K. Afsar, G. Yan, G. Guo, and S. Duan. Preliminary application of 3.0 T magnetic resonance chemical exchange saturation transfer imaging in brain metastasis of lung cancer. *BMC Medical Imaging*, 20:4, 2020.

[107] G. Low, S. A. Kruse, and D. J. Lomas. General review of magnetic resonance elastography. *World Journal of Radiology*, 8(1):59–72, 2016.

[108] R. M. Sigrist, J. Liau, A. E. Kaffas, M. C. Chammas, and J. K. Willmann. Ultrasound elastography: Review of techniques and clinical applications. *Theranostics*, 7(5):1303–1329, 2017.

[109] A. Bunevicius, K. Schregel, R. Sinkus, A. Golby, and S. Patz. Review: MR elastography of brain tumors. *NeuroImage. Clinical*, 25:102109, 2020.

[110] K. Schregel, M. O. Nowicki, M. Palotai, N. Nazari, R. Zane, R. Sinkus, S. E. Lawler, and S. Patz. Magnetic Resonance Elastography reveals effects of antiangiogenic glioblastoma treatment on tumor stiffness and captures progression in an orthotopic mouse model. *Cancer Imaging*, 20(1):35, 2020.

[111] B. Türkbey, D. Thomasson, Y. Pang, M. Bernardo, and P. L. Choyke. The role of dynamic contrast-enhanced MRI in cancer diagnosis and treatment. *Diagnostic and Interventional Radiology*, 16(3):186–192, 2010.

[112] R. F. J. Barajas and S. Cha. Benefits of dynamic susceptibility-weighted contrast-enhanced perfusion MRI for glioma diagnosis and therapy. *CNS Oncology*, 3(6):407–419, 2014.

[113] A. Salem and J. P. O'Connor. Assessment of tumor angiogenesis: dynamic contrast-enhanced mr imaging and beyond. *Magnetic Resonance Imaging Clinics*, 24(1):45–56, 2016.

[114] C. Treutlein, A. Stollberg, C. Scherl, A. Agaimy, S. Ellmann, H. Iro, M. Lell, M. Uder, and T. Bäuerle. Diagnostic value of 3D dynamic contrast-enhanced magnetic resonance imaging in lymph node metastases of head and neck tumors: a correlation study with histology. *Acta Radiologica Open*, 9(8):1–8, 2020.

[115] M. Neeman and H. Dafni. Structural, functional, and molecular MR imaging of the microvasculature. *Annual Review of Biomedical Engineering*, 5:29–56, 2003.

[116] M. Baboli, J. Zhang, and S. G. Kim. Advances in Diffusion and Perfusion MRI for Quantitative Cancer Imaging. *Current Pathobiology Reports*, 7(4):129–141, 2019.

[117] A. Radbruch, H. Richter, S. Fingerhut, L. F. Martin, A. Xia, N. Henze, W. Paulus, M. Sperling, U. Karst, and A. Jeibmann. Gadolinium Deposition in the Brain in a Large Animal Model: Comparison of Linear and Macrocyclic Gadolinium-Based Contrast Agents. *Investigative Radiology*, 54(9):531–536, 2019.

[118] . M. W. J. Choi, J. W. Gadolinium Deposition in the Brain: Current Updates. *Korean Journal of Radiology*, 20(1):134–147, 2019.

[119] S. Haller, G. Zaharchuk, D. L. Thomas, K.-O. Lovblad, F. Barkhof, and X. Golay. Arterial spin labeling perfusion of the brain: emerging clinical applications. *Radiology*, 281(2):337–356, 2016.

[120] D. Le Bihan. What can we see with IVIM MRI? *NeuroImage*, 187:56–67, 2019.

[121] N. Fujima, K. Kudo, D. Yoshida, A. Homma, T. Sakashita, A. Tsukahara, K. K. Tha, Y. Zaitsu, S. Terae, and H. Shirato. Arterial spin labeling to determine tumor viability in head and neck cancer before and after treatment. *Journal of Magnetic Resonance Imaging*, 40(4):920–928, 2014.

[122] L. Kong, H. Chen, Y. Yang, and L. Chen. A meta-analysis of arterial spin labelling perfusion values for the prediction of glioma grade. *Clinical Radiology*, 72(3):255–261, 2017.

[123] A. Abdel Razek and N. Nada. Arterial spin labeling perfusion-weighted MR imaging: correlation of tumor blood flow with pathological degree of tumor differentiation, clinical stage and nodal metastasis of head and neck squamous cell carcinoma. *European archives of Oto-Rhino-Laryngology*, 275(5):1301–1307, 2018.

[124] Y. Li, X. Li, X. Yu, M. Lin, H. Ouyang, L. Xie, and Y. Shang. Investigating the value of arterial spin labeling and intravoxel incoherent motion imaging on diagnosing nasopharyngeal carcinoma in t1 stage. *Cancer Imaging*, 20:62, 2020.

[125] N. K. Logothetis and B. A. Wandell. Interpreting the BOLD signal. *Annual Review of Physiology*, 66:735–769, 2004.

[126] M. R. Metea and E. A. Newman. Interpreting the BOLD signal. *Journal of Neuroscience*, 26(11):2862–2870, 2006.

[127] E. S. Finn and R. Todd Constable. Individual variation in functional brain connectivity: implications for personalized approaches to psychiatric disease. *Dialogues in Clinical Neuroscience*, 18(3):277–287, 2016.

[128] R. E. Beaty, Y. N. Kenett, A. P. Christensen, M. D. Rosenberg, M. Benedek, Q. Chen, A. Fink, J. Qiu, T. R. Kwapil, M. J. Kane, and P. J. Silvia. Robust prediction of individual creative ability from brain functional connectivity. *Proceedings of the National Academy of Sciences*, 115(5):1087–1092, 2018.

[129] M. P. van den Heuvel and H. E. Hulshoff Pol. Exploring the brain network: A review on resting-state fmri functional connectivity. *European Neuropsychopharmacology*, 20(8):519–534, 2010.

[130] Y. Du, Z. Fu, and V. D. Calhoun. Classification and prediction of brain disorders using functional connectivity: Promising but challenging. *Frontiers in Neuroscience*, 12:525, 2018.

[131] J. J. Roelofs, T. Teodoro, and M. J. Edwards. Neuroimaging in Functional Movement Disorders. *Current Neurology and Neuroscience Reports*, 19(3):12, 2019.

[132] A. R. Pries and T. W. Secomb. Modeling structural adaptation of microcirculation. *Microcirculation*, 15(8):753–764, 2008.

[133] G. H. Glover. Spiral imaging in fMRI. *NeuroImage*, 62(2):706–712, 2012.

[134] K. Zhang, V. J. F. Sturm, L. R. Buschle, A. Hahn, S. D. Yun, J. N. Shah, M. Bendszus, S. Heiland, H.-P. Schlemmer, C. H. Ziener, and F. T. Kurz. Dual-contrast pCASL using simultaneous gradient-echo/spin-echo multiband EPI. *Magnetic Resonance Imaging*, 57:359–367, 2019.

[135] T. Q. Duong, D. S. Kim, K. Uğurbil, and S. G. Kim. Localized cerebral blood flow response at submillimeter columnar resolution. *Proceedings of the National Academy of Sciences*, 98(19):10904–10909, 2001.

[136] A. Devor, P. Tian, N. Nishimura, I. C. Teng, E. M. C. Hillman, S. N. Narayanan, I. Ulbert, D. A. Boas, D. Kleinfeld, and A. M. Dale. Suppressed neuronal activity

and concurrent arteriolar vasoconstriction may explain negative blood oxygenation level-dependent signal. *Journal of Neuroscience*, 27(16):4452–4459, 2007.

[137] D. A. Boas, S. R. Jones, A. Devor, T. J. Huppert, and A. M. Dale. A vascular anatomical network model of the spatio-temporal response to brain activation. *Neuroimage*, 40(3):1116–1129, 2008.

[138] M. D'Esposito, L. Y. Deouell, and A. Gazzaley. Alterations in the BOLD fMRI signal with ageing and disease: a challenge for neuroimaging. *Nature Reviews Neuroscience*, 4(11):863–872, 2003.

[139] M. Peyrounette, Y. Davit, M. Quintard, and S. Lorthois. Multiscale modelling of blood flow in cerebral microcirculation: Details at capillary scale control accuracy at the level of the cortex. *PLoS ONE*, 13(1), 2018.

[140] J. Holash, P. C. Maisonpierre, D. Compton, P. Boland, C. R. Alexander, D. Zagzag, G. D. Yancopoulos, and S. J. Wiegand. Vessel Cooption, Regression, and Growth in Tumors Mediated by Angiopoietins and VEGF. *Science*, 284:1994–1998, 1999.

[141] G. Bergers and L. E. Benjamin. Tumorigenesis and the angiogenic switch. *Nature Reviews Cancer*, 3:401–410, 2003.

[142] M. Welter, K. Bartha, and H. Rieger. Vascular remodelling of an arterio-venous blood vessel network during solid tumour growth. *Journal of Theoretical Biology*, 259(3):405–422, 2009.

[143] M. R. Owen, T. Alarcón, P. K. Maini, and H. M. Byrne. Angiogenesis and vascular remodelling in normal and cancerous tissues. *Journal of Mathematical Biology*, 58(4-5):689–721, 2009.

[144] F. Winkler. Hostile takeover: how tumours hijack pre-existing vascular environments to thrive. *The Journal of Pathology*, 242:267–272, 2017.

[145] J. R. Reichenbach and E. M. Haacke. High-resolution BOLD venographic imaging: A window into brain function. *NMR in Biomedicine*, 14(7-8):453–467, 2001.

[146] E. Bullitt, D. Zeng, G. Gerig, S. Aylward, S. Joshi, J. K. Smith, W. Lin, and M. G. Ewend. Vessel tortuosity and brain tumor malignancy: a blinded study. *Academic Radiology*, 12:1232–1240, 2005.

[147] S. R. McDougall, A. R. Anderson, and M. A. Chaplain. Mathematical modelling of dynamic adaptive tumour-induced angiogenesis: clinical implications and therapeutic targeting strategies. *Journal of Theoretical Biology*, 241(3):564–589, 2006.

[148] R. K. Jain. Normalizing tumor microenvironment to treat cancer: Bench to bedside to biomarkers. *Journal of Clinical Oncology*, 31(17):2205–2218, 2013.

[149] A.-L. Barabási. *Network Science.* Cambridge University Press, United Kingdom, 1 edition, 2016.

[150] R. Hlushchuk, D. Haberthür, P. Soukup, S. F. Barré, O.-Z. Khoma, J. Schittny, N. Haghayegh Jahromi, A. Bouchet, B. Engelhardt, and V. Djonov. High-resolution synchrotron-based X-ray microtomography as a tool to unveil the three-dimensional neuronal architecture of the brain. *Brain Structure and Function*, 225:2885–2895, 2020.

[151] H. Rieger, T. Fredrich, and M. Welter. Physics of the tumor vasculature: Theory and experiment. *The European Physical Journal Plus*, 131:31, 2016.

[152] R. Karch, M. Neumann, F. Neumann, R. Ullrich, J. Neumüller, and W. Schreiner. A gibbs point field model for the spatial pattern of coronary capillaries. *Physica A*, 369:599–611, 2006.

[153] A. Alastuey and B. Jancovici. On the classical two-dimensional one-component Coulomb plasma. *Journal de Physique*, 42(1):1–12, 1981.

[154] R. Karch, F. Neumann, R. Ullrich, J. Neumüller, B. K. Podesser, M. Neumann, and W. Schreiner. The spatial pattern of coronary capillaries in patients with dilated, ischemic, or inflammatory cardiomyopathy. *Cardiovascular Pathology*, 14:135–144, 2005.

[155] A. Ertürk, K. Becker, N. Jährling, C. P. Mauch, C. D. Hojer, J. G. Egen, F. Hellal, F. Bradke, M. Sheng, and H. U. Dodt. Three-dimensional imaging of solvent-cleared organs using 3DISCO. *Nature Protocols*, 7(11):1983–1995, 2012.

[156] J. Huisken, J. Swoger, F. D. Bene, J. Wittbrodt, and E. H. K. Stelzer. Optical sectioning deep inside live embryos by selective plane illumination microscopy. *Science*, 305(5686):1007–1009, 2004.

[157] C. Sommer, C. Straehle, U. Koethe, and F. A. Hamprecht. ilastik: Interactive Learning and Segmentation Toolkit. In *Proceedings of the IEEE International Symposium on Biomedical Imaging*, pages 230–233, 2011.

[158] S. Berg, D. Kutra, T. Kroeger, C. N. Straehle, B. X. Kausler, C. Haubold, M. Schiegg, J. Ales, T. Beier, M. Rudy, K. Eren, J. I. Cervantes, B. Xu, F. Beuttenmueller, A. Wolny, C. Zhang, U. Koethe, F. A. Hamprecht, and A. Kreshuk.

ilastik: interactive machine learning for (bio)image analysis. *Nature Methods*, 16(12):1226–1232, 2019.

[159] A. Okabe, B. Boots, K. Sugihara, and S. N. Chiu. *Spatial tessellations: concepts and applications of Voronoi diagrams*. Wiley, Chichester, 2 edition, 1999.

[160] J. C. Forster, W. M. Harriss-Phillips, M. J. J. Douglass, and E. Bezak. A review of the development of tumor vasculature and its effects on the tumor microenvironment. *Hypoxia*, 5:21–32, 2017.

[161] Y. Gazit, D. A. Berk, M. Leunig, L. T. Baxter, and R. K. Jain. Scale-invariant behavior and vascular network formation in normal and tumor tissue. *Physical Review Letters*, 75:2428, 1995.

[162] Y. Gazit, J. W. Baish, N. Safabakhsh, M. Leunig, L. T. Baxter, and R. K. Jain. Fractal Characteristics of Tumor Vascular Architecture During Tumor Growth and Regression. *Microcirculation*, 4(4):395–402, 1997.

[163] R. J. Gillies, P. A. Schomack, T. W. Secomb, and N. Raghunand. Causes and effects of heterogeneous perfusion in tumors. *Neoplasia*, 1(3):197–207, 1999.

[164] J. W. Baish and R. K. Jain. Fractals and Cancer. *Cancer Research*, 60:3683–3688, 2000.

[165] L. Risser, F. Plouraboué, A. Steyer, P. Cloetens, G. L. Duc, and C. Fonta. From homogeneous to fractal normal and tumorous microvascular networks in the brain. *Journal of Cerebral Blood Flow & Metabolism*, 27:293–303, 2007.

[166] J. W. Baish, T. Stylianopoulos, R. M. Lanning, W. S. Kamoun, D. Fukumura, L. L. Munn, and R. K. Jain. Scaling rules for diffusive drug delivery in tumor and normal tissues. *Proceedings of the National Academy of Sciences*, 108(5):1799–803, 2011.

[167] T. Mathivet, C. Bouleti, M. V. Woensel, F. Stanchi, T. Verschuere, L.-K. Phng, J. Dejaegher, M. Balcer, K. Matsumoto, P. B. Georgieva, J. Belmans, R. Sciot, C. Stockmann, M. Mazzone, S. D. Vleeschouwer, and H. Gerhardt. Dynamic stroma reorganization drives blood vessel dysmorphia during glioma growth. *EMBO Molecular Medicine*, 9:1629–1645, 2017.

[168] E. Bullitt, G. Gerig, S. M. Pize, W. Lin, and S. R. Aylward. Measuring tortuosity of the intracerebral vasculature from MRA images. *IEEE Transactions on Medical Imaging*, 22:1163–1171, 2003.

[169] V. D. Blondel, J.-L. Guillaume, R. Lambiotte, and E. Lefebvre. Fast unfolding of communities in large networks. *Journal of Statistical Mechanics*, 8, 2008.

[170] L. Clarke, I. Glendinning, and R. Hempel. The MPI Message Passing Interface Standard. In *Programming Environments for Massively Parallel Distributed Systems*, pages 213–218. Birkhäuser Basel, Basel, 1994.

[171] K. M. Koch, X. Papademetris, D. L. Rothman, and R. A. de Graaf. Rapid calculations of susceptibility-induced magnetostatic field perturbations for in vivo magnetic resonance. *Physics in Medicine & Biology*, 51(24):6381, 2006.

[172] A. P. Pathak, B. D. Ward, and K. M. Schmainda. A novel technique for modeling susceptibility-based contrast mechanisms for arbitrary microvascular geometries: The finite perturber method. *NeuroImage*, 40(3):1130–1143, 2008.

[173] A. Brun and E. Englund. A white matter disorder in dementia of the alzheimer type: a pathoanatomical study. *Annals of Neurology*, 19(3):253–262, 1986.

[174] K. L. Davis, D. G. Stewart, J. I. Friedman, M. Buchsbaum, P. D. Harvey, P. R. Hof, J. Buxbaum, and V. Haroutunian. White matter changes in schizophrenia: evidence for myelin-related dysfunction. *Archives of General Psychiatry*, 60(5):443–456, 2003.

[175] R. J. Ward, F. A. Zucca, J. H. Duyn, R. R. Crichton, and L. Zecca. The role of iron in brain ageing and neurodegenerative disorders. *The Lancet Neurology*, 13(10):1045–1060, 2014.

[176] D. S. Novikov, V. G. Kiselev, and S. N. Jespersen. On modeling. *Magnetic Resonance in Medicine*, 79(6):3172–3193, 2018.

[177] A. Lasocki and F. Gaillard. Non-contrast-enhancing tumor: A new frontier in glioblastoma research. *American Journal of Neuroradiology*, 2019.

[178] J. Soares, P. Marques, V. Alves, and N. Sousa. A hitchhiker's guide to diffusion tensor imaging. *Frontiers in Neuroscience*, 7:31, 2013.

[179] Y. K. Mariappan, K. J. Glaser, and R. L. Ehman. Magnetic resonance elastography: A review. *Clinical Anatomy*, 23(5):497–511, 2010.

[180] A. Horská and P. B. Barker. Imaging of brain tumors: MR spectroscopy and metabolic imaging. *Neuroimaging Clinics of North America*, 20(3):293–310, 2010.

[181] V. Rieke and K. B. Pauly. MR thermometry. *Journal of Magnetic Resonance Imaging*, 27(2):376–390, 2008.

[182] G. Montavon, W. Samek, and K.-R. Müller. Methods for interpreting and understanding deep neural networks. *Digital Signal Processing*, 73:1–15, 2018.

[183] W. Samek, G. Montavon, S. Lapuschkin, C. J. Anders, and K. R. Müller. Explaining deep neural networks and beyond: A review of methods and applications. *Proceedings of the IEEE*, 109(3):247–278, 2021.

[184] J. Fang, Y. Sun, K. Peng, Q. Zhang, Y. Li, W. Liu, and X. Wang. Fast neural network adaptation via parameter remapping and architecture search. In *International Conference on Learning Representations*, 2020.

[185] A. S. Lundervold and A. Lundervold. An overview of deep learning in medical imaging focusing on mri. *Zeitschrift für medizinische Physik*, 29(2):102–127, 2019.

[186] B. Zhu, J. Z. Liu, S. F. Cauley, B. R. Rosen, and M. S. Rosen. Image reconstruction by domain-transform manifold learning. *Nature*, 555(7697):487–492, 2018.

[187] Y. Han, L. Sunwoo, and J. C. Ye. k-space deep learning for accelerated mri. *IEEE Transactions on Medical Imaging*, 39(2):377–386, 2020.

[188] A. Park, C. Chute, P. Rajpurkar, J. Lou, R. L. Ball, K. Shpanskaya, R. Jabarkheel, L. H. Kim, E. McKenna, J. Tseng, J. Ni, F. Wishah, F. Wittber, D. S. Hong, T. J. Wilson, S. Halabi, S. Basu, B. N. Patel, M. P. Lungren, A. Y. Ng, and K. W. Yeom. Deep Learning–Assisted Diagnosis of Cerebral Aneurysms Using the HeadXNet Model. *JAMA Network Open*, 2(6):e195600–e195600, 2019.

[189] R. Pranav, A. Park, J. Irvin, C. Chute, M. Bereket, M. Domenico, C. P. Langlotz, M. P. Lungren, A. Y. Ng, and B. N. Patel. AppendiXNet: Deep Learning for Diagnosis of Appendicitis from A Small Dataset of CT Exams Using Video Pretraining. *Scientific Reports*, 10(1), 2020.

[190] S. Zhou, H. Marklund, O. Blaha, M. Desai, B. Martin, D. Bingham, G. J. Berry, E. Gomulia, A. Y. Ng, and J. Shen. Deep learning assistance for the histopathologic diagnosis of helicobacter pylori. *Intelligence-Based Medicine*, 1-2:100004, 2020.

[191] M. J. Silvennoinen, C. S. Clingman, X. Golay, R. A. Kauppinen, and P. C. M. Van Zijl. Comparison of the dependence of blood R2 and R2* on oxygen saturation at 1.5 and 4.7 Tesla. *Magnetic Resonance in Medicine*, 49(1):47–60, 2003.

[192] J. M. Zhao, C. S. Clingman, M. J. Närväinen, R. A. Kauppinen, and P. C. Van Zijl. Oxygenation and hematocrit dependence of transverse relaxation rates of blood at 3T. *Magnetic Resonance in Medicine*, 58(3):592–597, 2007.

[193] K. Uludağ, B. Müller-Bierl, and K. Uğurbil. An integrative model for neuronal activity-induced signal changes for gradient and spin echo functional imaging. *NeuroImage*, 48(1):150–165, 2009.

[194] E. M. Haacke, S. Liu, S. Buch, W. Zheng, D. Wu, and Y. Ye. Quantitative susceptibility mapping: current status and future directions. *Magnetic Resonance Imaging*, 33(1):1–25, 2015.

[195] C. Liu, H. Wei, N.-J. Gong, M. Cronin, R. Dibb, and K. Decker. Quantitative Susceptibility Mapping: Contrast Mechanisms and Clinical Applications. *Tomography*, 1(1):3–17, 2015.

[196] T. Christen, B. Lemasson, N. Pannetier, R. Farion, C. Segebarth, C. Rémy, and E. L. Barbier. Evaluation of a quantitative blood oxygenation level-dependent (qBOLD) approach to map local blood oxygen saturation. *NMR in Biomedicine*, 24(4):393–403, 2011.

[197] T. Christen, D. S. Bolar, and G. Zaharchuk. Imaging brain oxygenation with MRI using blood oxygenation approaches: methods, validation, and clinical applications. *American Journal of Neuroradiology*, 34(6):1113–1123, 2013.

[198] D. A. Yablonskiy, A. L. Sukstanskii, and X. He. Blood oxygenation level-dependent (BOLD)-based techniques for the quantification of brain hemodynamic and metabolic properties - theoretical models and experimental approaches. *NMR in Biomedicine*, 26(8):963–86, 2013.

[199] L. R. Schad, G. Brix, I. Zuna, W. Härle, W. J. Lorenz, and W. Semmler. Multiexponential proton spin-spin relaxation in MR imaging of human brain tumors. *Journal of Computer Assisted Tomography*, 13(4):577–587, 1989.

[200] I. Digernes, L. B. Nilsen, E. Grøvik, A. Bjørnerud, G. Løvland, E. Vik-Mo, T. R. Meling, C. Saxhaug, r. Helland, K. D. Jacobsen, O. Geier, and K. E. Emblem. Noise dependency in vascular parameters from combined gradient-echo and spin-echo DSC MRI. *Physics in Medicine and Biology*, 65(22):225020, 2020.

[201] A. Dasgupta, B. Geraghty, P. J. Maralani, N. Malik, M. Sandhu, J. Detsky, C.-L. E. Tseng, H. Soliman, S. Myrehaug, Z. Husain, J. Perry, A. Lau, A. Sahgal, and G. Czarnota. Quantitative mapping of individual voxels in the peritumoral region of glioblastoma to distinguish between tumor infiltration and edema. *Research Square*, 2021.

[202] X. Chen, X. Wei, Z. Zhang, R. Yang, Y. Zhu, and X. Jiang. Differentiation of true-progression from pseudoprogression in glioblastoma treated with radiation

therapy and concomitant temozolomide by GLCM texture analysis of conventional MRI. *Clinical Imaging*, 39(5):775–780, 2015.

[203] M. B. Bracken. Why animal studies are often poor predictors of human reactions to exposure. *Journal of the Royal Society of Medicine*, 102(3):120–122, 2009.

[204] H. B. van der Worp, D. W. Howells, E. S. Sena, M. J. Porritt, S. Rewell, V. O'Collins, and M. R. Macleod. Can Animal Models of Disease Reliably Inform Human Studies? *PLoS Medicine*, 7(3):e1000245, 2010.

[205] K. Lenting, R. Verhaak, M. ter Laan, P. Wesseling, and W. Leenders. Glioma: Experimental models and reality. *Acta Neuropathologica*, 133:263–282, 2017.

[206] P. Pound and M. Ritskes-Hoitinga. Is it possible to overcome issues of external validity in preclinical animal research? Why most animal models are bound to fail. *Journal of Translational Medicine*, 16:304, 2018.

[207] A. F. Smith, V. Doyeux, M. Berg, M. Peyrounette, M. Haft-Javaherian, A. E. Larue, J. H. Slater, F. Lauwers, P. Blinder, P. Tsai, D. Kleinfeld, C. B. Schaffer, N. Nishimura, Y. Davit, and S. Lorthois. Brain capillary networks across species: A few simple organizational requirements are sufficient to reproduce both structure and function. *Frontiers in Physiology*, 10:233, 2019.

[208] B. Laviña. Brain vascular imaging techniques. *International Journal of Molecular Sciences*, 18(1):70, 2017.

[209] D. J. Murphy, A. Aghayev, and M. L. Steigner. Vascular CT and MRI: a practical guide to imaging protocols. *Insights into Imaging*, 9(2):215–236, 2018.

[210] M. P. Hartung, T. M. Grist, and C. J. François. Magnetic resonance angiography: Current status and future directions. *Journal of Cardiovascular Magnetic Resonance*, 13(1):19, 2011.

[211] W. J. van Rooij, M. Sprengers, A. N. de Gast, J. Peluso, and M. Sluzewski. 3D rotational angiography: the new gold standard in the detection of additional intracranial aneurysms. *American Journal of Neuroradiology*, 29(5):976–979, 2008.

[212] M. Scianna, C. G. Bell, and L. Preziosi. A Review of Mathematical Models for the Formation of Vascular Networks. *Journal of Theoretical Biology*, 333:174, 2013.

[213] H. Perfahl, B. D. Hughes, T. Alarcón, P. K. Maini, M. C. Lloyd, M. Reuss, and H. M. Byrne. 3D hybrid modelling of vascular network formation. *Journal of Theoretical Biology*, 414:254–268, 2017.

[214] P. M. Cogswell, M. A. Rischall, A. E. Alexander, H. J. Dickens, G. Lanzino, and J. M. Morris. Intracranial vasculature 3D printing: review of techniques and manufacturing processes to inform clinical practice. *3D Printing in Medicine*, 6(1):18, 2020.

[215] C. B. Schaffer, B. Friedman, N. Nishimura, L. F. Schroeder, P. S. Tsai, F. F. Ebner, P. D. Lyden, and D. Kleinfeld. Two-photon imaging of cortical surface microvessels reveals a robust redistribution in blood flow after vascular occlusion. *PLoS Biology*, 4:22, 2006.

[216] P. Blinder, A. Y. Shih, C. A. Rafie, and D. Kleinfeld. Topological basis for the robust distribution of blood to rodent neocortex. *Proceedings of the National Academy of Sciences*, 107:12670–12675, 2010.

[217] C. D. Murray. The Physiological Principle of Minimum Work: I. The Vascular System and the Cost of Blood Volume. *Proceedings of the National Academy of Sciences*, 12(3):207–214, 1926.

[218] M. P. Wiedeman, R. F. Tuma, and H. N. Mayrovitz. *An Introduction to Microcirculation*. Elsevier Academic Press, New York, 1981.

[219] F. Cassot, F. Lauwers, C. Fouard, S. Prohaska, and V. Lauwers-Cances. A Novel Three-Dimensional Computer-Assisted Method for a Quantitative Study of Microvascular Networks of the Human Cerebral Cortex. *Microcirculation*, 13:1–18, 2006.

[220] S. Lorthois and F. Cassot. Fractal analysis of vascular networks: Insights from morphogenesis. *Journal of Theoretical Biology*, 262:614–633, 2010.

[221] E. Rostrup, I. Law, M. Blinkenberg, H. Larsson, A. Born, S. Holm, and O. Paulson. Regional differences in the cbf and bold responses to hypercapnia: a combined pet and fmri study. *Neuroimage*, 11(2):87–97, 2000.

[222] R. V. Harrison, N. Harel, J. Panesar, and R. J. Mount. Blood capillary distribution correlates with hemodynamic-based functional imaging in cerebral cortex. *Cerebral cortex*, 12(3):225–233, 2002.

[223] B. M. Ances, O. Leontiev, J. E. Perthen, C. Liang, A. E. Lansing, and R. B. Buxton. Regional differences in the coupling of cerebral blood flow and oxygen metabolism changes in response to activation: implications for bold-fmri. *Neuroimage*, 39(4):1510–1521, 2008.

[224] D. Ma, V. Gulani, N. Seiberlich, K. Liu, J. L. Sunshine, J. L. Duerk, and M. A. Griswold. Magnetic Resonance Fingerprinting. *Nature*, 495(7440):187–192, 2013.

[225] J. I. Hamilton, Y. Jiang, Y. Chen, D. Ma, W.-C. Lo, M. Griswold, and N. Seiberlich. MR fingerprinting for rapid quantification of myocardial T1, T2, and proton spin density. *Magnetic Resonance in Medicine*, 77(4):1446–1458, 2017.

[226] J. Assländer. A Perspective on MR Fingerprinting. *Journal of Magnetic Resonance Imaging*, 53(3):676–685, 2020.

[227] T. Christen, N. A. Pannetier, W. W. Ni, D. Qiu, M. E. Moseley, N. Schuff, and G. Zaharchuk. MR vascular fingerprinting: A new approach to compute cerebral blood volume, mean vessel radius, and oxygenation maps in the human brain. *NeuroImage*, 89:262–270, 2014.

[228] B. Lemasson, N. Pannetier, N. Coquery, L. S. B. Boisserand, N. Collomb, N. Schuff, M. Moseley, G. Zaharchuk, E. L. Barbier, and T. Christen. MR Vascular Fingerprinting in Stroke and Brain Tumors Models. *Scientific Reports*, 6:37071, 2016.

[229] P. Pouliot, L. Gagnon, T. Lam, P. K. Avti, C. Bowen, M. Desjardins, A. K. Kakkar, E. Thorin, S. Sakadzic, D. A. Boas, and F. Lesage. Magnetic resonance fingerprinting based on realistic vasculature in mice. *NeuroImage*, 149:436–445, 2017.

[230] L. Swanson. *Brain maps: structure of the rat brain.* Gulf Professional Publishing, 2004.

[231] B. Weber, A. L. Keller, J. Reichold, and N. K. Logothetis. The microvascular system of the striate and extrastriate visual cortex of the macaque. *Cerebral cortex*, 18(10):2318–2330, 2008.

[232] S. Hirsch, J. Reichold, M. Schneider, G. Székely, and B. Weber. Topology and hemodynamics of the cortical cerebrovascular system. *Journal of Cerebral Blood Flow & Metabolism*, 32:952–967, 2012.

[233] X. Ji, T. Ferreira, B. Friedman, R. Liu, H. Liechty, E. Bas, J. Chandrashekar, and D. Kleinfeld. Brain microvasculature has a common topology with local differences in geometry that match metabolic load. *Neuron*, 109(7):1168–1187.e13, 2021.

[234] M. Kim, J. E. Park, K. Emblem, A. Bjørnerud, and H. S. Kim. Vessel type determined by vessel architectural imaging improves differentiation between early

tumor progression and pseudoprogression in glioblastoma. *American Journal of Neuroradiology*, 42(4):663–670, 2021.

[235] K. Sommer, R. Schmidt, D. Graafen, H.-C. Breit, and L. M. Schreiber. Contrast Agent Bolus Dispersion in a Realistic Coronary Artery Geometry: Influence of Outlet Boundary Conditions. *Annals of Biomedical Engineering*, 42:787–796, 2014.

[236] J. Martens, S. Panzer, J. van den Wijngaard, M. Siebes, and L. M. Schreiber. Influence of contrast agent dispersion on bolus-based mri myocardial perfusion measurements: A computational fluid dynamics study. *Magnetic Resonance in Medicine*, 84(1):467–483, 2020.

[237] R. B. Buxton, L. R. Frank, E. C. Wong, B. Siewert, S. Warach, and R. R. Edelman. A general kinetic model for quantitative perfusion imaging with arterial spin labeling. *Magnetic Resonance in Medicine*, 40(3):383–396, 1998.

[238] E. C. Wong. Quantifying CBF with pulsed ASL: technical and pulse sequence factors. *Journal of Magnetic Resonance Imaging*, 22(6):727–731, 2005.

[239] M. A. Weber, M. Günther, M. P. Lichy, S. Delorme, A. Bongers, C. Thilmann, M. Essig, I. Zuna, L. R. Schad, J. Debus, and H.-P. Schlemmer. Comparison of arterial spin-labeling techniques and dynamic susceptibility-weighted contrast-enhanced MRI in perfusion imaging of normal brain tissue. *Investigative Radiology*, 38(11):712–718, 2003.

[240] C. Warmuth, M. Gunther, and C. Zimmer. Quantification of blood flow in brain tumors: comparison of arterial spin labeling and dynamic susceptibility-weighted contrast-enhanced MR imaging. *Radiology*, 228(2):523–532, 2003.

[241] A. Arisawa, Y. Watanabe, H. Tanaka, H. Takahashi, C. Matsuo, T. Fujiwara, M. Fujiwara, Y. Fujimoto, and N. Tomiyama. Comparative study of pulsed-continuous arterial spin labeling and dynamic susceptibility contrast imaging by histogram analysis in evaluation of glial tumors. *Neuroradiology*, 60(6):599–608, 2018.

[242] G. Liu, A. A. Qutub, P. Vempati, F. Mac Gabhann, and A. S. Popel. Module-based multiscale simulation of angiogenesis in skeletal muscle. *Theoretical Biology and Medical Modelling*, 8(6), 2011.

[243] G. M. Fraser, S. Milkovich, D. Goldman, and C. G. Ellis. Mapping 3-D functional capillary geometry in rat skeletal muscle in vivo. *American journal of physiology. Heart and circulatory physiology*, 302(3):H654–H664, 2012.

[244] S. Lorthois, F. Lauwers, and F. Cassot. Tortuosity and other vessel attributes for arterioles and venules of the human cerebral cortex. *Microvascular Research*, 91:99–109, 2014.

[245] P. Blinder, P. S. Tsai, J. P. Kaufhold, P. M. Knutsen, H. Suhl, and D. Kleinfeld. The cortical angiome: an interconnected vascular network with noncolumnar patterns of blood flow. *Nature Neuroscience*, 16:889–897, 2013.

[246] M. A. Viergever, J. Maintz, S. Klein, K. Murphy, M. Staring, and J. Pluim. A survey of medical image registration - under review. *Medical Image Analysis*, 33:140–144, 2016.

[247] J. Reichold, M. Stampanoni, A. L. Keller, A. Buck, P. Jenny, and B. Weber. Vascular graph model to simulate the cerebral blood flow in realistic vascular networks. *Journal of Cerebral Blood Flow & Metabolism*, 29:1429–1443, 2009.

[248] S. Lorthois, F. Cassot, and F. Lauwers. Simulation study of brain blood flow regulation by intra-cortical arterioles in an anatomically accurate large human vascular network: Part i: Methodology and baseline flow. *NeuroImage*, 54(2):1031–1042, 2011.

[249] B. Yao, T. Li, P. Gelderen, K. Shmueli, J. Dezwart, and J. Duyn. Susceptibility contrast in high field MRI of human brain as a function of tissue iron content. *NeuroImage*, 44(4):1259–1266, 2009.

[250] S. Moccia, E. De Momi, S. El Hadji, and L. S. Mattos. Blood vessel segmentation algorithms - Review of methods, datasets and evaluation metrics. *Computer Methods and Programs in Biomedicine*, 158:71–91, 2018.

[251] M. Haft-Javaherian, L. Fang, V. Muse, C. B. Schaffer, N. Nishimura, and M. R. Sabuncu. Deep convolutional neural networks for segmenting 3D in vivo multi-photon images of vasculature in Alzheimer disease mouse models. *PLoS ONE*, 14(3), 2019.

[252] M. I. Todorov, J. C. Paetzold, O. Schoppe, G. Tetteh, S. Shit, V. Efremov, K. Todorov-Völgyi, M. Düring, M. Dichgans, M. Piraud, B. Menze, and A. Ertürk. Machine learning analysis of whole mouse brain vasculature. *Nature Methods*, 17:442–449, 2020.

[253] S. C. Thust, M. J. van den Bent, and M. Smits. Pseudoprogression of brain tumors. *Journal of Magnetic Resonance Imaging*, 48(3):571–589, 2018.

[254] S. Sakadžić, E. Roussakis, M. A. Yaseen, E. T. Mandeville, V. J. Srinivasan, K. Arai, S. Ruvinskaya, A. Devor, E. H. Lo, S. A. Vinogradov, and D. A. Boas. Two-photon high-resolution measurement of partial pressure of oxygen in cerebral vasculature and tissue. *Nature Methods*, 7:755–759, 2010.

[255] J. Lecoq, A. Parpaleix, E. Roussakis, M. Ducros, Y. G. Houssen, S. A. Vinogradov, and S. Charpak. Simultaneous two-photon imaging of oxygen and blood flow in deep cerebral vessels. *Nature Medicine*, 17:893–898, 2011.

[256] D. G. Lyons, A. Parpaleix, M. Roche, and S. Charpak. Mapping oxygen concentration in the awake mouse brain. *Elife*, 5:e12024, 2016.

[257] M. Desjardins, K. Kılıç, M. Thunemann, C. Mateo, D. Holland, C. G. L. Ferri, J. A. Cremonesi, B. Li, Q. Cheng, K. L. Weldy, P. A. Saisan, D. Kleinfeld, T. Komiyama, T. T. Liu, R. Bussell, E. C. Wong, M. Scadeng, A. K. Dunn, D. A. Boas, S. Sakadžić, J. B. Mandeville, R. B. Buxton, A. M. Dale, and A. Devor. Awake mouse imaging: From two-photon microscopy to blood oxygen level-dependent functional magnetic resonance imaging. *Biological Psychiatry: Cognitive Neuroscience and Neuroimaging*, 4(6):533–542, 2019.

[258] P. A. Santi. Light sheet fluorescence microscopy: A review. *Journal of Histochemistry and Cytochemistry*, 59(2):129–138, 2011.

[259] J. Senarathna, H. Yu, C. Deng, A. L. Zou, J. B. Issa, D. H. Hadjiabadi, S. Gil, Q. Wang, B. M. Tyler, N. V. Thakor, and A. P. Pathak. A miniature multi-contrast microscope for functional imaging in freely behaving animals. *Nature Communications*, 10(99), 2019.

[260] G. Hartung, C. Vesel, R. Morley, A. Alaraj, J. Sled, D. Kleinfeld, and A. Linninger. Simulations of blood as a suspension predicts a depth dependent hematocrit in the circulation throughout the cerebral cortex. *PLoS Computational Biology*, 14(11), 2018.

[261] A. R. Pries, T. W. Secomb, P. Gaehtgens, and J. F. Gross. Blood flow in microvascular networks. Experiments and simulation. *Circulation Research*, 67(4):826–834, 1990.

[262] T. W. Secomb, R. Hsu, N. B. Beamer, and B. M. Coull. Theoretical simulation of oxygen transport to brain by networks of microvessels: effects of oxygen supply and demand on tissue hypoxia. *Microcirculation*, 7(4):237–247, 2000.

[263] Q. Fang, S. Sakadžić, L. Ruvinskaya, A. Devor, A. M. Dale, and D. A. Boas. Oxygen advection and diffusion in a three dimensional vascular anatomical network. *Optics express*, 16(22):17530, 2008.

[264] A. R. Pries, T. W. Secomb, and P. Gaehtgens. Design principles of vascular beds. *Circulation Research*, 77(5):1017–1023, 1995.

[265] A. R. Pries and T. W. Secomb. Microcirculatory Network Structures and Models. *Annals of Biomedical Engineering*, 28:916–921, 2000.

[266] D. M. McDonald and P. Baluk. Significance of blood vessel leakiness in cancer. *Cancer Research*, 62(18):5381–5385, 2002.

[267] A. M. Halefoglu and D. M. Yousem. Susceptibility weighted imaging: Clinical applications and future directions. *World Journal of Radiology*, 10(4):30–45, 2018.

B List of Own Publications

Book chapters

- <u>A. Hahn</u> and F. T. Kurz. Chapter 8: Advanced imaging/MRI for tissue engineering in *Tissue Engineering Using Ceramics and Polymers, 3ed*, edited by Aldo R. Boccaccini, Peter X. Ma, and Liliana Liverani. Elsevier, Woodhead Publishing Series (appearing September 1, 2021). ISBN 9780128205082

Peer-reviewed publications as first author

1. <u>A. Hahn</u>, J. Bode, T. Krüwel, G. Solecki, S. Heiland, M. Bendszus, B. Tews, F. Winkler, M. O. Breckwoldt, and F. T. Kurz. Glioblastoma multiforme restructures the topological connectivity of cerebrovascular networks. Scientific Reports 9:11757 (2019). https://doi.org/10.1038/s41598- 019-47567-w

2. <u>A. Hahn</u>, J. Bode, T. Krüwel, L. R. Buschle, V. J. F. Sturm, K. Zhang, B. Tews, H.-P. Schlemmer, S. Heiland, M. Bendszus, C. H. Ziener, M. O. Breckwoldt, and F. T. Kurz. Gibbs point field model quantifies disorder in microvasculature of U87-glioblastoma. Journal of Theoretical Biology 494:110230 (2020). https://doi.org/10.1016/j.jtbi.2020.110230

3. <u>A. Hahn</u>, J. Bode, A. Alexander, K. Karimian-Jazi, K. Schregel, D. Schwarz, A. C. Sommerkamp, T. Krüwel, A. Abdollahi, W. Wick, M. Platten, M. Bendszus, B. Tews, F. T. Kurz, and M. O. Breckwoldt. Large-scale characterization of the microvascular geometry in development and disease by tissue clearing and quantitative ultramicroscopy. Journal of Cerebral Blood Flow & Metabolism 271678X20961854 (2020). https://doi.org/10.1177/0271678X20961854

4. <u>A. Hahn</u>, J. Bode, S. Schuhegger, T. Krüwel, V. J. F. Sturm, K. Zhang, J. M. E. Jende, B. Tews, S. Heiland, M. Bendszus, M. O. Breckwoldt, C. H. Ziener, and F. T. Kurz. Brain tumor classification of virtual NMR voxels based on realistic blood vessel-induced spin dephasing using support vector machines. NMR in Biomedicine e4307 (2020). https://doi.org/10.1002/nbm.4307

Peer-reviewed publications as co-author

5. F. T. Kurz, C. H. Ziener, M. Rückl, <u>A. Hahn</u>, V. J. F. Sturm, K. Zhang, L. R. Buschle, M. Bendszus, S. Heiland, H.-P. Schlemmer, W. R. Bauer, and T. Kampf. The influence of spatial patterns of capillary networks on transverse relaxation. Magnetic Resonance Imaging 40:31–47 (2017). https://doi.org/10.1016/j.mri.2017.03.012

6. L. R. Buschle, C. H. Ziener, K. Zhang, V. J. F. Sturm, T. Kampf, <u>A. Hahn</u>, G. Solecki, F. Winkler, M. Bendszus, S. Heiland, H.-P. Schlemmer, and F. T. Kurz. Vessel radius mapping in an extended model of transverse relaxation. Magnetic Resonance Materials in Physics, Biology and Medicine 31:531–551 (2018). https://doi.org/10.1007/s10334-018-0677-9

7. F. T. Kurz, L. R. Buschle, <u>A. Hahn</u>, J. M. E. Jende, M. Bendszus, S. Heiland, and C. H. Ziener. Diffusion effects in myelin sheath free induction decay. Journal of Magnetic Resonance 297,61–75 (2018). https://doi.org/10.1016/j.jmr.2018.10.001

8. P. Wirthschaft, J. Bode, A. E. M. Simon, E Hoffmann, R. van Laack, T. Krüwel, F. Dietrich, D. Bucher, <u>A. Hahn</u>, F. Sahm, M. O. Breckwoldt, F. T. Kurz, T. Hielscher, B. Fischer, N. Dross, C. Ruiz de Almodovar, A. von Deimling, C. Herold-Mende, C. Plass, S. Boulant, B. Wiestler, G. Reifenberger, P. Lichter, W. Wick, and B. Tews. A PRDX1-p38α heterodimer amplifies MET-driven invasion of IDH-wildtype and IDH-mutant gliomas. International Journal of Cancer 143(5), 1176–1187 (2018). https://doi.org/10.1002/ijc.31404

9. K. Zhang, V. J. F. Sturm, L. R. Buschle, <u>A. Hahn</u>, S. D. Yun, N. J. Shah, M. Bendszus, S. Heiland, H.-P. Schlemmer, C. H. Ziener, and F. T. Kurz. Dual-contrast pCASL using simultaneous gradient-echo/spin-echo multiband EPI. Magnetic Resonance Imaging 57:359–367 (2019). https://doi.org/10.1016/j.mri.2018.11.018

10. M. O. Breckwoldt, J. Bode, F. Sahm, T. Krüwel, G. Solecki, <u>A. Hahn</u>, P. Wirthschaft, A. S. Berghoff, M. Haas, V. Venkataramani, A. von Deimling, W. Wick, C. Herold-Mende, S. Heiland, M. Platten, M. Bendszus, F. T. Kurz, F. Winkler, and B. Tews. Correlated MRI and Ultramicroscopy (MR-UM) of Brain Tumors Reveals Vast Heterogeneity of Tumor Infiltration and Neoangiogenesis in Preclinical Models and Human Disease. Frontiers in Neuroscience 12:1004 (2019). https://doi.org/10.3389/fnins.2018.01004

11. J. M. E. Jende, J. B. Groener, C. Rother, Z. Kender, <u>A. Hahn</u>, T. Hilgenfeld, A. Juerchott, F. Preisner, S. Heiland, S. Kopf, M. Pham, P. P. Nawroth, M. Bendszus,

and F. T. Kurz. Association of Serum Cholesterol Levels With Peripheral Nerve Damage in Patients With Type 2 Diabetes. JAMA Network Open 2(5):e194798 (2019). https://doi.org/10.1001/jamanetworkopen.2019.4798

12. K. Zhang, S. D. Yun, S. M. F. Triphan, V. J. F. Sturm, L. R. Buschle, A. Hahn, S. Heiland, M. Bendszus, H.-P. Schlemmer, N. J. Shah, C. H. Ziener, and F. T. Kurz. Vessel architecture imaging using multiband gradient-echo/spin-echo EPI. PLoS ONE 14(8):e0220939 (2019). https://doi.org/10.1371/journal.pone.0220939

13. J. M. E. Jende, J. B. Groener, Z. Kender, A. Hahn, J. Morgenstern, S. Heiland, P. P. Nawroth, M. Bendszus, S. Kopf, and F. T. Kurz. Troponin T parallels structural nerve damage in type 2 diabetes - a cross-sectional study using magnetic resonance neurography. Diabetes db191094 (2020). https://doi.org/10.2337/db19-1094

14. J. M. E. Jende, J. B. Groener, Z. Kender, C. Rother, A. Hahn, T. Hilgenfeld, A. Juerchott, F. Preisner, S. Heiland, S. Kopf, P. P. Nawroth, M. Bendszus, and F. T. Kurz. Structural Nerve Remodeling at 3-T MR Neurography Differs between Painful and Painless Diabetic Polyneuropathy in Type 1 or 2 Diabetes. Radiology 294:405–414 (2020). https://doi.org/10.1148/radiol.2019191347

15. J. M. E. Jende, Z. Kender, C. Rother, L. Alvarez-Ramos, J. B. Groener, M. Pham, J. Morgenstern, D. Oikonomou, A. Hahn, A. Juerchott, J. Kollmer, S. Heiland, S. Kopf, P. P. Nawroth, M. Bendszus, and F. T. Kurz. Diabetic Polyneuropathy Is Associated With Pathomorphological Changes in Human Dorsal Root Ganglia: A Study Using 3T MR Neurography. Frontiers in Neuroscience 14:570744 (2020). https://doi.org/10.3389/fnins.2020.570744

16. J. M. E. Jende, Z. Kender, C. Mooshage, J. B. Groener, L. Alvarez-Ramos, J. Kollmer, A. Juerchott, A. Hahn, S. Heiland, P. P. Nawroth, M. Bendszus, S. Kopf, and F. T. Kurz. Diffusion Tensor Imaging of the Sciatic Nerve as a Surrogate Marker for Nerve Functionality of the Upper and Lower Limb in Patients With Diabetes and Prediabetes. Frontiers in Neuroscience 15:642589 (2021). https://doi.org/10.3389/fnins.2021.642589

Conference contributions

Talks as first author and presenter

1. <u>A. Hahn</u>, K. Zhang, G. Solecki, M. O. Breckwoldt, L. R. Buschle, S. Heiland, C. H. Ziener, M. Bendszus, F. Winkler, and F. T. Kurz. *Correlated quantitative assessment of glioblastoma-angiogenesis by T2-mapping and in vivo multiphoton microscopy.* 25th Annual meeting of the International Society for Magnetic Resonance in Medicine (ISMRM), Honolulu, Hawaii, USA (April 2017).

2. <u>A. Hahn</u>, T. Krüwel, J. Bode, B. Tews, S. Heiland, M. Bendszus, C. H. Ziener, and F. T. Kurz. *Einfluss realer Gefäßarchitekturen in Glioblastom und gesundem Hirngewebe auf die transversale Relaxation.* 52nd Annual meeting of the German Society for Neuroradiology (DGNR), Cologne, Germany (October 2017).

3. <u>A. Hahn</u>, K. Zhang, K. Deumelandt, T. Krüwel, J. Bode, V. Sturm, L. Buschle, M. O. Breckwoldt, B. Tews, M. Platten, S. Heiland, M. Bendszus, C. H. Ziener, and F. T. Kurz. *Transversale Relaxation in Glioblastom- und gesundem Hirngewebe und deren Kapillarverteilungen im Gibbs Entropiemodell.* 20th Annual meeting of the German section of the ISMRM, Göttingen, Germany (November 2017).

4. <u>A. Hahn</u>. *Statistical super-resolution imaging: Towards microstructure estimates based on endogenous contrast and machine learning.* 9th Young scientists academy for medical technology of the German Research Foundation (9. Nachwuchsakademie Medizintechnik (NAMT) der Deutschen Forschungsgemeinschaft (DFG)) about "Quantitative MRI as key technology in life sciences", Berlin, Germany (September 2019).

5. <u>A. Hahn</u>, J. Bode, S. Schuhegger, V. J. F. Sturm, M. O. Breckwoldt, S. Heiland, C. H. Ziener, M. Bendszus, and F. T. Kurz. *In silico proof-of-principle for reproducible brain tumor predictions on individual NMR voxels based on endogenous microvascular susceptibility effects using support vector machine classification.* 36th Annual scientific meeting of the European Society for Magnetic Resonance in Medicine and Biology (ESMRMB), Rotterdam, Netherlands (October 2019).

6. <u>A. Hahn</u>, S. Schuhegger, J. Bode, V. J. F. Sturm, M. O. Breckwoldt, S. Heiland, C. H. Ziener, M. Bendszus, and F. T. Kurz. *Numerical feasibility study of voxel by voxel signal classifications to detect glioblastoma multiforme in mice based on endogenous static BOLD contrast using random forests.* 36th Annual scientific meeting of the ESMRMB, Rotterdam, Netherlands (October 2019).

7. <u>A. Hahn</u>, J. Krüwel-Bode, Y. Seemann, S. Schuhegger, J. M. E. Jende, A. Hohmann, V. J. F. Sturm, K. Zhang, S. Heiland, M. Bendszus, M. O. Breckwoldt, C. H. Ziener, and F. T. Kurz. *Proof-of-principle for endogenous signal classification towards voxel-wise tumor detection using statistical machine learning.* 28th Annual meeting of the ISMRM, planned for Sydney, Australia, May 2020 (moved online due to Covid-19, August 2020).

Talks as co-author

8. L. R. Buschle, T. Kampf, F. T. Kurz, V. J. F. Sturm, <u>A. Hahn</u>, H.-P. Schlemmer, and C. H. Ziener. *Quantitative Suszeptibilitätsbildgebung von Mikrogefäßen.* 20th Annual meeting of the German section of the ISMRM, Göttingen, Germany (November 2017).

9. K. Zhang, S. D. Yun, V. J. F. Sturm, S. M. F. Triphan, L. R. Buschle, <u>A. Hahn</u>, S. Heiland, M. Bendszus, H.-P. Schlemmer, C. H. Ziener, and F. T. Kurz. *A high resolution Gradient-Echo/Spin-Echo EPI sequence for vessel architectural imaging.* 34th Annual Scientific Meeting of ESMRMB, Barcelona, Spain (October 2017).

10. K. Zhang, S. M. F. Triphan, V. J. F. Sturm, L. R. Buschle, <u>A. Hahn</u>, S. D. Yun, S. Heiland, M. Bendszus, H.-P. Schlemmer, C. H. Ziener, and F. T. Kurz. *Vessel Architectural Imaging mit einer hochaufgelösten Gradienten-Echo/Spin-Echo EPI Sequenz.* 52nd Annual meeting of the DGNR, Cologne, Germany (October 2017).

Conference posters

1. L. R. Buschle, C. H. Ziener, M. O. Breckwoldt, <u>A. Hahn</u>, J. Bode, B. Tews, M. Bendszus, H.-P. Schlemmer, and F. T. Kurz. *Quantitative susceptibility mapping: phase images and microstructure.* 25th Annual meeting of the ISMRM, Honolulu, Hawaii, USA (April 2017).

2. K. Zhang, S. D. Yun, S. M. F. Triphan, V. J. F. Sturm, L. R. Buschle, <u>A. Hahn</u>, S. Heiland, M. Bendszus, H.-P. Schlemmer, N. J. Shah, C. H. Ziener, and F. T. Kurz. *A High Resolution Gradient-Echo/Spin-Echo EPI Sequence for Vessel Architecture Imaging.* 26th Annual meeting of the ISMRM, Paris, France (June 2018).

3. K. Zhang, F. T. Kurz, L. R. Buschle, V. J. F. Sturm, <u>A. Hahn</u>, S. D. Yun, H.-P. Schlemmer, and C. H. Ziener. *Dual-Contrasts pCASL using simultaneous Gradient-Echo/Spin-Echo EPI.* 34th Annual scientific meeting of the ESMRMB, Barcelona, Spain (October 2017).

4. <u>A. Hahn</u>, T. Krüwel, J. Bode, L. R. Buschle, B. Tews, S. Heiland, M. Bendszus, C. H. Ziener, and F. T. Kurz. *Vascular-induced spin dephasing in real vascular networks reveals useful decay characteristics to differentiate glioblastoma from healthy brain tissue.* 26th Annual meeting of the ISMRM, Paris, France (June 2018).

5. F. T. Kurz, L. R. Buschle, <u>A. Hahn</u>, M. Bendszus, S. Heiland, C. H. Ziener, and J. M. E. Jende. *Anisotropy and diffusion effects in myelin water imaging.* 53rd Annual meeting of the DGNR, Frankfurt, Germany (October 2018).

6. L. R. Buschle, C. H. Ziener, K. Zhang, V. J. F. Sturm, T. Kampf, <u>A. Hahn</u>, G. Solecki, F. Winkler, M. Bendszus, S. Heiland, H.-P. Schlemmer, and F. T. Kurz. *Vessel radius mapping for realistic vascular architecture in a U87-glioblastoma xenograft model.* 53rd Annual meeting of the DGNR, Frankfurt, Germany (October 2018).

7. <u>A. Hahn</u>, J. Senarathna, V. J. F. Sturm, S. Heiland, M. Bendszus, F. T. Kurz, and A. P. Pathak. *Physiologically accurate simulations of endogenous susceptibility-based contrast in cancer reveal the importance of intravascular oxygen variations on transverse relaxation.* 27th Annual meeting of the ISMRM, Montréal, Quebec, Canada (May 2019).

8. K. Zhang, J. M. E. Jende, V. J. F. Sturm, L. R. Buschle, <u>A. Hahn</u>, S. Heiland, H.-P. Schlemmer, M. Bendszus, O. Sedlaczek, C. H. Ziener, and F. T. Kurz. *Measurement of peripheral nerve perfusion using FAIR PRESS.* 27th Annual meeting of the ISMRM, Montréal, Quebec, Canada (May 2019).

9. J. M. E. Jende, S. Kopf, Z. Kender, <u>A. Hahn</u>, J. Morgenstern, P. P. Nawroth, M. Bendszus, and F. T. Kurz. *Troponin T is a potential indicator for nerve damage in Type 2 Diabetes - results from Diffusion Tensor Imaging of the sciatic nerve.* 28th Annual meeting of the ISMRM, planned for Sydney, Australia, May 2020 (moved online due to Covid-19, August 2020).

Acknowledgments

Explanation

I hereby assure that I composed this work by myself and did not use any other than the listed resources.

Heidelberg, April 26, 2021 . . . .

Artur Hahn